TEXTURE AND GROWTH PARAMETERS IN SEMISOLID PROCESSING OF $Ba_2YCu_3O_{7-y}$

Anacleto M. de Figueiredo

Ph.D. Thesis
Department of Materials Science and Engineering
Massachusetts Institute of Technology
Cambridge, MA
June 1993

(copy # 6)

TEXTURE AND GROWTH PARAMETERS IN SEMISOLID PROCESSING OF $Ba_2YCu_3O_{7-x}$

by

ANACLETO MARTIM DE FIGUEREDO

Engenheiro de Minas, Universidade de São Paulo
(1978)
S.M., Universidade de São Paulo
(1983)

Submitted to the Department of Materials Science and Engineering
in Partial Fulfillment of the Requirements for the Degree of

DOCTOR OF PHILOSOPHY
in Metallurgy

at the

MASSACHUSETTS INSTITUTE OF TECHNOLOGY
June, 1993

Signature of Author ..... A M Figueredo
Department of Materials Science and Engineering
April 30, 1993

Certified by .....
Michael J. Cima
Norton Associate Professor of Ceramics
Thesis Supervisor

Accepted by .....
Linn W. Hobbs
John F. Elliott Professor of Materials
Chair, Departmental Committee on Graduate Students

TEXTURE AND GROWTH PARAMETERS IN
SEMISOLID PROCESSING OF $Ba_2YCu_3O_{7-y}$

by

ANACLETO MARTIM DE FIGUEREDO

Submitted to the Department of Materials Science
and Engineering on April 30, 1993 in Partial Fulfillment of the
requirements for the Degree of Doctor of Philosophy
in Metallurgy

ABSTRACT

Directional solidification of the peritectic superconducting compound $Ba_2YCu_3O_{7-y}$ (Y) was investigated by the laser-heated floating zone technique. Materials and solidification parameters were systematic varied and correlated to growth morphologies. Materials parameters included chemical composition, structure and nature of the constituent phases of the polycrystalline precursors. Solidification parameters included growth rate, maximum temperature in the zone, temperature gradient and oxygen partial pressure. Solidification morphologies and other structural features were examined in quenched specimens.

Depending on oxygen partial pressure and growth rate, different types of growth morphologies were identified. In the high oxygen partial pressure range, at 1.27 atm O_2, the observed growth morphologies were "faceted plane front", "cellular", "dendritic" and "quenched". Steady-state solidification of single-crystalline filaments was achieved with planar front at rates near the transition from planar to cellular/dendritic growth. Cellular or dendritic morphologies led to the growth of textured, multiphase polycrystalline specimens. The temperature gradient had only a small effect on the maximum velocity for planar growth. This velocity increased by only a factor of 3 when the temperature gradient was increased by two orders of magnitude. A solidification model was used to interpret experimental observations. The model assumes limited diffusion of solute in the liquid during the growth of the superconducting phase. The model shows, in agreement with experiment, that growth rate of the low temperature solid phase has a strong effect on ability to obtain the desired faceted plane front, and that thermal gradient has only a small effect. Interparticle spacing of the high-temperature phase is also predicted to have a strong effect.

Rather unusual growth morphologies were obtained in directional melting and solidification of γ in low oxygen partial pressures. Incongruent melting of the lower temperature phase [γ or α (BaY_2CuO_5] resulted in aligned growth of rods or plates of a high temperature phase, ε (BaY_2O_4) in the liquid phase, *on heating*. The following sequences of peritectic reactions were observed on melting in compositions near γ:

$\gamma \rightarrow \alpha + L \rightarrow \delta + L$ ($P_{O_2} > 10^3$ Pa)

$\gamma \rightarrow \alpha + L \rightarrow \varepsilon + L \rightarrow \delta + L$ (8 Pa < $P_{O_2} < 10^3$ Pa)

$\gamma \rightarrow \varepsilon + L \rightarrow \delta + L$ ($P_{O_2} < 8$ Pa)

In the above reactions, α and δ (Y_2O_3) phases comprised equiaxed particles. Rod like ε was formed upon incongruent melting of α at 8 Pa < $P_{O_2} < 10^3$ Pa. At oxygen pressures below about 8 Pa, α was no longer formed and the oriented ε phase formed directly from γ, and was plate-like in morphology. The reactions $\alpha \rightarrow \varepsilon + L$ and $\gamma \rightarrow \varepsilon + L$ were not observed in the system Ba-Y-Cu-O prior to this work. Temperature-P_{O_2} conditions for the stability of γ, α, ε, and δ were determined from metallographic, X-ray diffraction, and EPMA analysis of quenched and as-solidified specimens. This information provided a qualitative overall picture of the P_{O_2}-dependent changes in the related pseudo-binary phase diagrams, and of the expected growth morphologies in the pressure range between 8 and ~10^6 Pa.

Directional growth of ε was modelled in a simple way. The α particles ahead of the ε interface dissolve in the superheated liquid and solute transport for ε growth is assumed to be limited by diffusion along the growth direction over distances equal to half the rod or plate spacing. A relation between superheating at the growth interface and growth rate was derived from the present model. Composite filaments produced by directional growth of ε on heating were succesfully used as precursors for the growth of the superconducting phase γ. It is demonstrated that by means of suitable changes in P_{O_2} directional solidification can be used for interconversion of the low temperature phases according to $\gamma + \alpha \leftrightarrow \alpha + L \leftrightarrow \varepsilon + \beta$, where β represents the $BaCu_2O_2$ phase. The sequence of reactions from right to left, led to growth of γ crystals containing very fine α particles.

In the planar front regime, higher solidification velocities produced γ+α filaments with higher critical current densities. A sharp decrease in critical current density occurred at the transition from planar to cellular/dendritic growth. Within the latter regime, the critical current density decreased as the solidification velocity increased. Direct, as well as indirect current density measurements yielded current density values along the ab planes in excess of 10^5 A/cm^2 at 77.3 K. Current densities increased rapidly with decreasing temperature, reaching values in excess of 10^6 A/cm^2 at low fields, below about 30K. At T ≤ 50 K, single-grained filaments displayed good flux pinning characteristics, manifested by the weak field dependence of the critical current density. At 77.3 K, a rapid decrease of the current density with applied field, over the entire field interval investigated, revealed a decrease in flux pinning strength. However, at 77.3K, the critical current of LHFZ filaments exceeded that of good polycrystalline materials by more than 2 orders of magnitude at low fields, and by more than 3 orders of magnitude at 1 T applied field.

Thesis Supervisor: Michael J. Cima
Title: Norton Associate Professor of Ceramics

Contents

List of Tables

List of Figures

Chapter 2

Chapter 3

Chapter 4

Chapter 5

Chapter 6

Chapter 7

ACKNOWLEDGEMENTS

I consider myself very fortunate for having had the opportunity to meet many outstanding and interesting persons at M.I.T. To them, my sincere thanks.

I thank my advisor, Prof. Michael J. Cima for giving me the opportunity to work in his group and for his advice during the execution of this work. I thank Prof. Merton C. Flemings for being so generous with his time, for his many suggestions, constant help, and for showing me how interesting solidification is. I thank Dr. John S. Haggerty for his invaluable expertise and constant help with the equipment, as well as for always being in a good mood, even when I forgot a chopper in the laser beam path.

I sincerely thank Profs. Linn W. Hobbs, Nicholas J. Grant and Stuart B. Brown for helping me along the way. The commitment of Prof. John F. Elliott to graduate education was still vigorous during the last semester he taught 3.50. I thank him very much for teaching the way he did. I also thank Prof. Donald R. Sadoway for his participation in my thesis committee and for his suggestions. Thanks are also due to Prof. Kenneth C. Russell for his advice earlier in the program.

Dr. Wendell Rhine provided the expertise necessary to prepare polymer solutions. Dr. Joe Patchett helped me in the early stages of this work and was always there with a friendly smile and a word of encouragement.

Mr. John Centorino and Mr. Leonard Rigione provided assistance in the lab in many opportunities. Thanks to Michael Jercinovic for his invaluable and very competent help with the microprobe. Thanks are also due to Dr. Julia Sigalovsky for his friendship. It was nice to have her around. Micki Lifhtfoot also helped me to find my way around. Barry Millsap was always friendly, courteous and helpful. Thanks also to Dr. Xiao-Ping Jiang for his help and for the many discussions we had on the subject of this work. Thanks to Barbara Layne for being so kind. Sally Gregg was also very helpful.

Thanks to my officemates, Simone Peterson, Bryan Backwell, Karina Rigby, Man-Fai Ng, Jae-Dok Yoo, Susi Ferrell, and others from 12-096, for helping me whenever I needed. I thank Paul McIntyre for taking some TEM pictures for me.

I would like to thank my mother and my family for their support.

I could not complete this work without the support of Neuza. She was instrumental to help me navigate through periods of crises. Her constant encouragement throughout this work was invaluable. We have many, many beautiful memories from the five years we lived in Cambridge. I thank Neuza for her love and for being such a brave woman. Thanks to Maria for being so precious. She is a huge driving force for everything we do.

I acknowledge the financial support of Fundação de Amparo a Pesquisa do Estado de São Paulo, Conselho Nacional de Pesquisas and IPEN/Comissão Nacional de Energia Nuclear-SP, Brazil. This work has been funded by Tokyo Electric Power Co.

Chapter 1
Introduction

1.1 Objectives

The high-temperature superconductor $YBa_2Cu_3O_{7-\delta}$ (123) first synthesized in 1987, possesses high intra-granular critical current densities at very high magnetic fields at low temperatures and in moderate fields at high temperatures. In addition, the flux pinning strength of 123, and hence, its current density, can be markedly enhanced by the controlled introduction of crystalline defects. However, in the polycrystalline form, this material suffers from the so called "electrical weak-link" problem, which is associated primarily to the poor electrical properties displayed by most types of grain boundaries in 123.

This work is concerned with directional solidification structures obtained in 123 and their relation to the weak-link problem. The investigation reported here was primarily aimed at the relations between growth parameters, growth structures and critical current density capacity of directionally solidified 123.

1.2 Thesis Organization

This thesis is organized in nine chapters. The literature is reviewed in Chapter 2. Some normal state and superconducting properties of 123, considered relevant from the materials processing standpoint, are briefly reviewed. Also reviewed are relations between microstructure and properties, with emphasis on intragranular current densities. The nature of phase equilibria in the system Y-Ba-Cu-O and their relation to oxygen partial pressure is the subject of the remaining portion of Chapter 2.

Sample preparation is described in Chapter 3, which presents experimental procedures employed in the fabrication of superconducting polycrystalline filaments of 123.

Chapter 4 is concerned with the stability of semisolid mixtures formed by incongruent melting of 123. This aspect is considered relevant for the

processing of this material, since adequate microstructures and reproducible properties cannot be obtained by semisolid floating zone solidification if the zone is not stable.

Chapters 5 and 6 are concerned with the relations between microstructure and growth parameters in semisolid processing of $YBa_2Cu_3O_{7-\delta}$ by the laser-heated floating zone technique. The results discussed in Chapter 5 are for ambient or higher oxygen partial pressures. Solidification microstructures are discussed in relation with superconductivity. A model for peritectic solidification of $YBa_2Cu_3O_{7-\delta}$ from semisolid melts is presented in this chapter to aid in the interpretation of the experimental results.

Chapter 6 describes novel solidification structures obtained at low oxygen partial pressures. Directional melting and solidification of 123 in low oxygen partial pressures is reported in this chapter. This is the first report of directional phase formation on melting in oxide systems. Data on phase equilibria obtained from solidification experiments is also presented and compared to the literature. The data revealed the existence of two previously unreported invariant reactions in the system Y-Ba-Cu-O. An adaptation of the model presented in Chapter 5 is applied to the solidification morphologies obtained at low P_{O_2}. Experiments on 123 growth from the solidification structures obtained at low oxygen partial pressures are also reported.

Chapter 7 reports on electrical and magnetic properties of LHFZ filaments solidified with planar front. Conclusions are presented in Chapters 8. Finally, processing alternatives with potential for the production of 123 with enhanced intragranular critical current density are presented in Chapter 9 as suggestions for future work.

A Note About Compound Notation

In this work, the notation adopted for the superconducting compound is $YBa_2Cu_3O_{7-\delta}$ or 1:2:3. This notation is incorrect, but it is now so entrenched in the literature that the use of correct notations is often leads to confusion. The tetragonal and orthorhombic phases will be denoted by $YBa_2Cu_3O_{6+\delta}$ and $YBa_2Cu_3O_{7-\delta}$, respectively. The correct notation consist in listing the oxides in order of their cation radii, largest first. Thus the proper notation for the superconducting compound is $Ba_2YCu_3O_{7-\delta}$ or 2:1:3.

Chapter 2
Background

2.1 *High-Temperature Superconducting Materials*

Some complex ternary oxides contained copper and rare earths such as $La_{4-2x}Ba_{2+2x}Cu_{2-x}O_{10-2x}$,[1] $(La,Nd)_{4-2x}Ba_{2+2x}Zn_{2-x}O_{10-2x}$,[2] and A_2BaCuO_5 (A = Y, Sm, Eu, Gd, Dy, Ho, Er, Yb).[3] were isolated and characterized by Michel, Raveau and co-workers in 1981. Early in 1985, the same group reported good metallic conduction in the oxygen deficient perovskite $BaLa_4Cu_5O_{13+\delta}$.[4] About a year later, Bednorz and Müller discovered superconductivity above 30 K in the oxide $(La_{2-x}A_x)CuO_4$ (A = Ba, Sr or Ca).[5] The report of Bednorz and Müller triggered an unprecedent research activity in "high-temperature superconductivity", which led to the discovery of superconductivity above 90 K in the system Ba-Y-Cu-O (Wu and co-workers,[6] 1987), and above 100 K in the systems Bi-Ca-Sr-Cu-O (Maeda an co-workers,[7] 1988) and Tl-Ca-Ba-Cu-O (Sheng and Hermann,[8] 1988).

Fig. 2.1 shows the significant increase in the critical temperature of superconducting materials brought by the advent of cuprate superconductors. Unfortunately, the upward trend in the critical temperature of these novel materials stalled at the end of 1989.[10] Presently, finding ways to increase the critical current density of these materials is one of the main focus of the research in superconductivity. Most of the work in the area of superconductivity has been concentrated on the Y, Bi and Tl families of superconducting oxides, which are listed with other systems in Table 2.1, from Burns[9].

All compounds of table 2.1, especially the ones pertaining to the three main families of high-temperature superconductors are plagued by low critical current densities, particularly when they are in the polycrystalline form.[11] The increase of the critical current densities (J_c) of these materials, which are type-II superconductors, depends on the improvement of both intragranular and intergranular J_c. However, it is unlikely that a process can be found that increases the superconducting properties, and hence the intragranular current

densities of all the grain boundaries that act as weak links. Therefore, the material has either to be textured or freed from grain boundaries. Processing techniques capable of introducing structural defects close to the atomic scale are also required to enhance the intragranular current densities of 123.

Table 2.1. A partial list of the high-temperature superconductors. The chemical formulae are the ideal ones. Values of T_c are the higher ones reported. n is the number of the immediately adjacent Cu-O planes in the unit cell (or the number of Cu-O planes per primitive cell). (From Burns[9]).

Formula	T_c (K)	n	Notations
$(La_{2-x}Sr_x)CuO_4$	38	1	La (n=1); 214
$(La_{2-x}Sr_x)CaCu_2O_6$	60	2	La (n=2)
$Tl_2Ba_2CuO_6$	0-80	1	2-Tl (n=1); Tl2201
$Tl_2Ba_2CaCu_2O_8$	108	2	2-Tl (n=2); Tl2212
$Tl_2Ba_2Ca_2Cu_3O_{10}$	125	3	2-Tl (n=3); Tl2223
$Bi_2Sr_2CuO_6$	0-20	1	2-Bi (n=1); Bi2201
$Bi_2Sr_2CaCu_2O_8$	85	2	2-Bi(n=2); Bi2212
$Bi_2Sr_2Ca_2Cu_3O_{10}$	110	3	2-Bi (n=3); Bi2223
$(Nd_{2-x}Ce_x)CuO_4$	30	1	Nd (n=1); T'
$YBa_2Cu_3O_7$	92-95	2	Y123; Y213; YBCO; 123
$YBa_2Cu_4O_8$	86	2	Y124
$Y_2Ba_4Cu_7O_{14}$	91	2	Y247; Y123.5
$TlBa_2CuO_5$	0-50	1	1-Tl (n=1); Tl1201
$TlBa_2CaCu_2O_7$	80	2	1-Tl (n=2); Tl1212
$TlBa_2Ca_2Cu_3O_9$	110	3	1-Tl (n=3); Tl1223
$TlBa_2Ca_3Cu_4O_{11}$	122	4	1-Tl (n=4); Tl1234
(Nd,Ce,Sr)CuO_4	30	1	T*
$(Ba_{0.6}K_{0.4})BiO_3$	30	-	BKBO

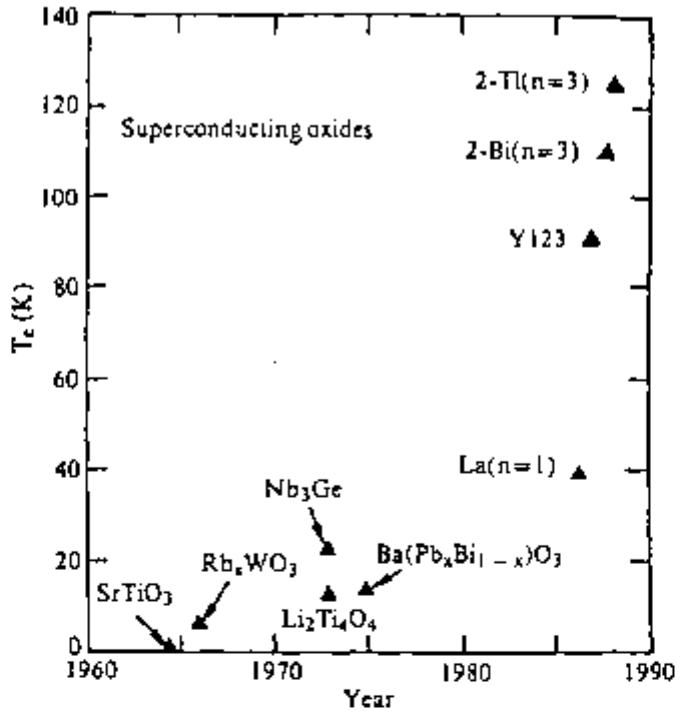

Fig. 2.1. Critical temperature vs. the year of discovery of the superconducting compound. The notations are the same given in Table 2.1 (From Burns[10]).

The compound 123 has high intragranular (intrinsic) current density in very high fields at low temperatures, and in moderate fields of a few tesla at 77 K. The weak-link problem is less serious in the Bi based compounds than in 123. However, the intrinsic current density of these materials decrease very rapidly with temperature, so their use will be apparently limited to temperatures below 30 or 40 K. The weak-link problem seems also to be less severe in Tl- than in Y-based materials.[11] Tl compounds also may be useful at higher temperatures than the Bi family, but their investigation is still at an early stage. Intense research has been conducted on 123 because of its high J_c at high temperatures and fields.

2.2 *The Superconducting Oxide $YBa_2Cu_3O_{7-\delta}$*

2.2.1 *Crystallographic Structures*

The basic structural features of $YBa_2Cu_3O_{7-\delta}$ are shown in Fig. 2.2. The unit cell is related to a cubic perovskite structure with one of the cube axes tripled. The structure is complicated by variable oxygen content and the presence of two different types of square planar coordination of copper and oxygen ions.

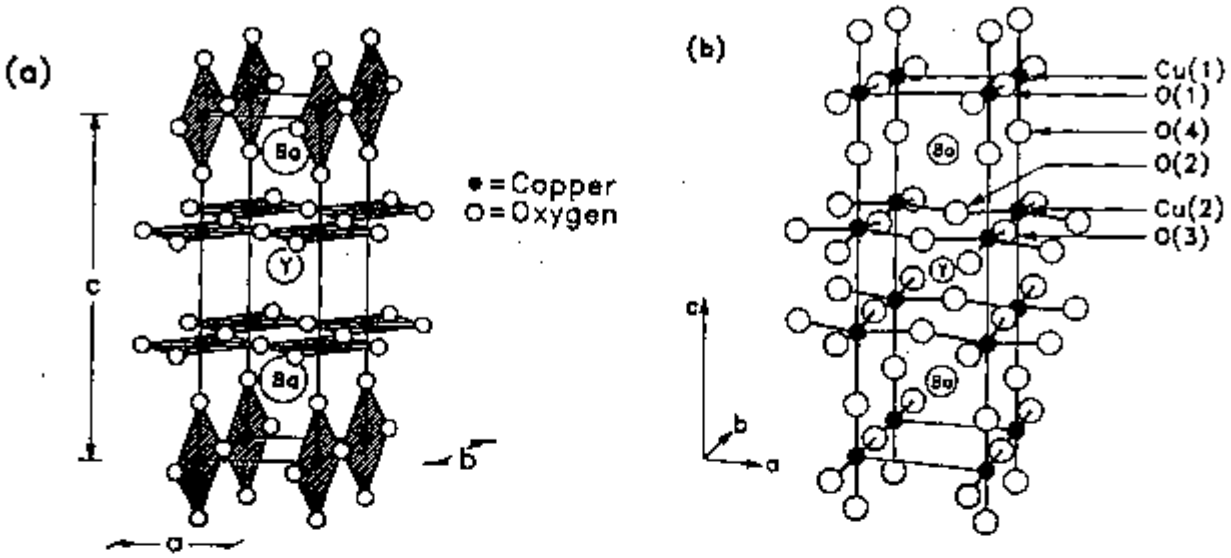

Fig. 2.2. The structure of $YBa_2Cu_3O_{7-\delta}$ (a) Location of copper-oxygen planes and chains in the structure. (b) Oxygen site designations (From Beyers and Shaw [12]).

Copper atoms are labeled Cu(2) and Cu(1) to indicate that they belong to the two closely spaced Cu-O planes and the Cu-O chains, respectively. The Cu-O planes extend indefinitely in two directions (the *ab* plane), while the Cu-O chains extend indefinitely in only one direction (the *b*-axis direction). Five different types of oxygen sites exist. Oxygen sites labeled O(2) and O(3) are in the Cu-O planes and those labeled O(1) and O(4) in the Cu-O chains. The last site, O(5) is largely unoccupied. $YBa_2Cu_3O_{7-\delta}$is orthorhombic because of the presence of the site O(1).

At 297 K, the lattice parameters of orthorhombic $YBa_2Cu_3O_{6.91}$ are a = 0.3820 nm, b = 0.3885 nm and c = 1.1683 nm.[12] $YBa_2Cu_3O_7$ ($\delta = 0$) is only obtained if the sample is slowly cooled in oxygen. If oxygen is removed, the structure undergoes an orthorhombic-to-tetragonal phase transformation. The structure of $YBa_2Cu_3O_6$ is obtained by removing the O(1) anion from $YBa_2Cu_3O_7$. A sample of $YBa_2Cu_3O_{6.06}$, for example, has lattice parameters $a = b$ = 0.386 nm and c= 1.182 nm.[13] The dependence of lattice constants on oxygen partial pressure is given in Fig. 2.3, which also shows that the orthorhombic to tetragonal transformation temperature decreases with oxygen pressure.

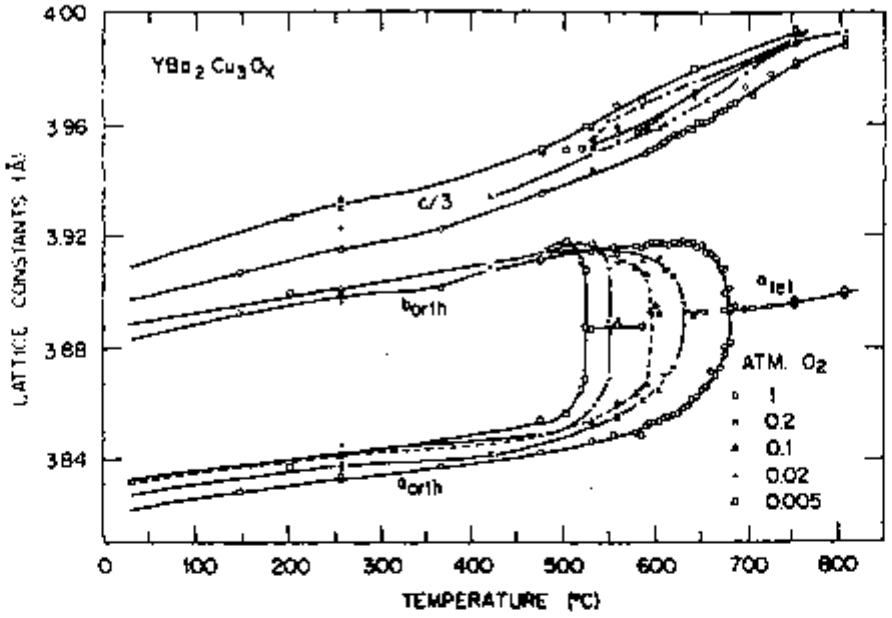

Fig. 2.3. Variation of the lattice constants of $YBa_2Cu_3O_y$ with oxygen pressure and temperature (From Specht *et al.* [13])

During slow cooling, the oxygen stoichiometry in 123 follows the isobaric lines shown in the upper portion of Fig. 2.4.[14] The lower portion of that figure corrresponds to the pseudo-binary diagram $YBa_2Cu_3O_6$-$YBa_2Cu_3O_7$.[15] According to the data of Fig. 2.4, the orthogonal to orthorhombic transformation starts at about 680°C when the material is slowly cooled in 1 atm O_2.

2.2.2 *Normal State Properties*

Measurements of high temperature *dc* resistivity in a single crystal of $YBa_2Cu_3O_{7-\delta}$ (Fig. 2.5) have shown that this property is highly directional.[17] Over the measured range in Fig. 2.5, the resistivity dependence is of the type $\rho = A + BT$. All of the three curves, ρ_a, ρ_b and ρ_c, exhibit the same temperature dependence found in metals at elevated temperatures. Therefore, the compound $YBa_2Cu_3O_{7-\delta}$ may be regarded as a highly anisotropic three-dimensional metal, rather than a two-dimensional metal. The ratio of ρ_a to ρ_b is equal to 2.2 and is approximately temperature-independent, suggesting that the Cu-O chains make a large contribution to the conductivity in the *ab*-plane.[18]

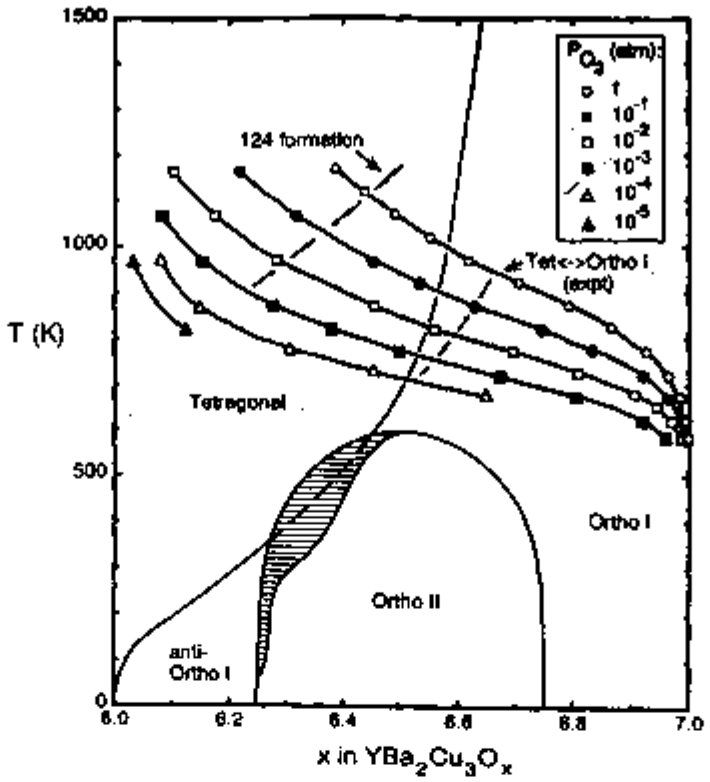

Fig. 2.4. Pseudo-binary phase diagram for 123. [14,15,16]

Depending on the value of δ, $YBa_2Cu_3O_{7-\delta}$ may be metallic, superconductor of anti-ferromagnetic. This is shown in Fig. 2.6.[19] The value of T_c for $\delta \approx 0$ is about 93 K and is essentially constant in the range $0 < \delta < 0.2$. At $\delta \approx 0.65$, a metal-insulator phase transition occurs and the tetragonal material becomes anti-ferromagnetic.

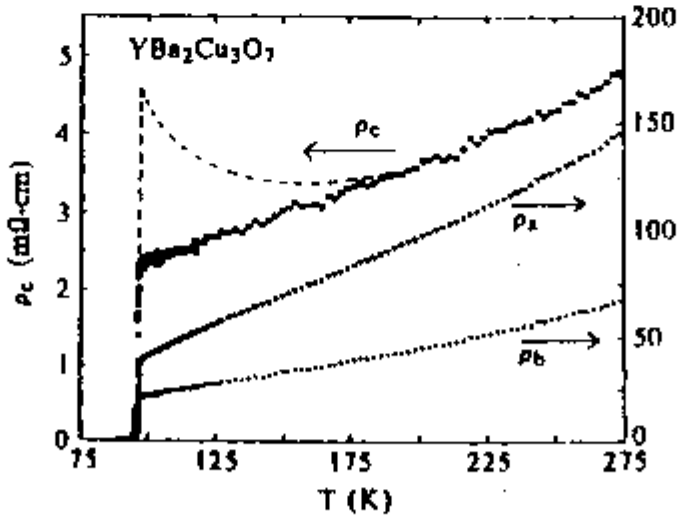

Fig. 2.5. Resistivity of 123 along the crystallographic directions *a*, *b*, and *c*. [17]

The plateau at $T_c \approx 60$ K and $\delta \approx 0.5$ has been related to an ordered oxygen structure, called Ortho-II. Prior to the work of Beyers *et al*,[16] it was commonly believed that the 60 K plateau corresponded to a single phase region. The former investigators have shown that the changes in superconducting properties with oxygen content in 123 cannot be explained by two separate and distinct superconducting phases. They found more than one type of diffraction pattern in samples with $\delta = 0.35$ and $\delta = 0.1$ and proposed that phase separation between ordered structures with only small differences in oxygen content may be occurring at these average stoichiometries. According to their view, the region between the two plateaus corresponds to a progression of ordered structures with only small differences in oxygen content and not to a mixture of two distinct phases.

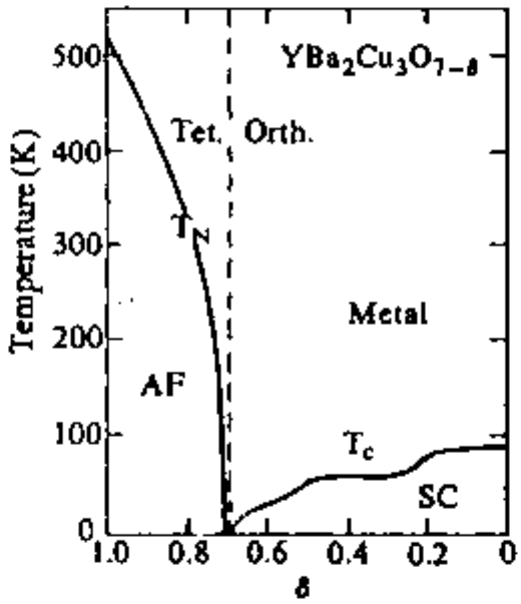

Fig. 2.6. Temperature versus composition showing the tetragonal and orthorhombic fields, the anti-ferromagnetic (AF) region, the Néel temperature T_N, and the superconductor region of 123.[19]

2.2.3 *Superconducting Properties*

Some aspects of superconductivity in 123 will be briefly presented in this section along with some measured properties to illustrate the complexities associated to the processing of this material.

All high-T_c oxides are type-II superconductors. Fig. 2.7 shows a schematic magnetic phase diagram for a type-II superconductor. A sample of a type-II material is normal at fields higher than $H_{c2}(T)$. For $H_{c1} < H < H_{c2}$, the superconductor is in the so-called vortex state. In this portion of the H-T space the surface energy of a domain between a superconducting and a normal region is negative.[20] Because of negative surface energy, the normal-state, flux bearing regions, will subdivide until a single fluxoid quantum passes through in the otherwise superconducting sample. This subdvision of the flux lines results in a decrease in the overall free energy of the material. The fluxoid quantum is usually called a flux or vortex line. As the external field is increased, the density of flux lines increases until H_{c2} is reached and the field penetrates the material uniformly, making it normal. At fields below $H_{c1}(T)$, the magnetic flux is completely expelled from the bulk as in a type-I superconductor. This state is commonly referred to as the Meissner state.

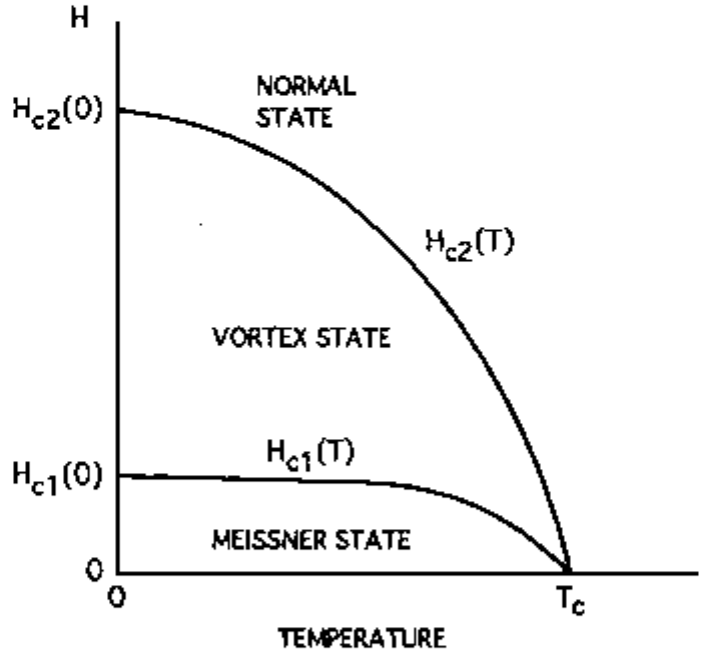

Fig. 2.7. Magnetic phase diagram for type-II superconductors (schematic).

Two important length scales in superconductors are the coherence length (ξ) and the magnetic penetration depth (λ). The first is a measure of the spatial extent of superconductivity and the second a measure of the depth of penetration of an external magnetic field. Below H_{c1}, the circulation of a

persistent supercurrent in a surface region of thickness equal to the penetration depth, induces a field that exactly cancels the applied field inside the sample. This current is commonly called shielding current.

The length scales λ and ξ are related to the critical fields H_{c1} and H_{c2} by $H_{c1} = \Phi_0/\pi\lambda^2$ and $H_{c2} = \Phi_0/\pi\xi^2$ where Φ_0 is the fluxoid quantum.[20] Therefore, small coherence lengths mean large H_{c2} values, or vice-versa. Measured values of λ [21] and H_{c1} [24] for the compound 123 are given in Fig. 2.8. The plot of Fig. 2.8 (a)[22] is a schematic, but qualitatively correct representation of the temperature dependence of the penetration depth (λ) and coeherence length (ξ).

Direct evidence of the electronic anisotropic behavior of 123 is also provided by magnetization hysteresis curves.[23] The two magnetization loops of Fig. 2.9, which correspond to fields applied parallel and perpendicular to the *c*-

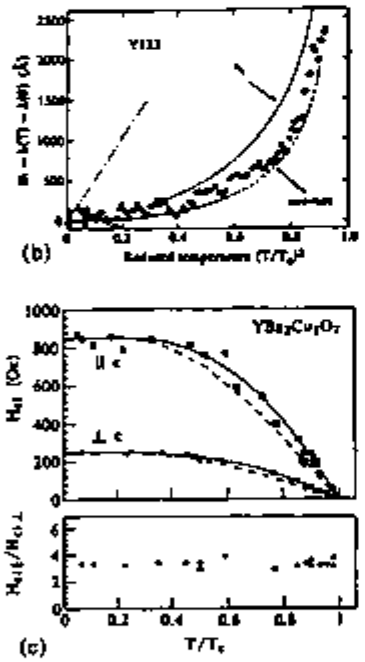

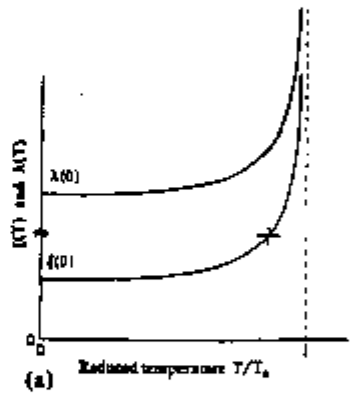

Fig. 2.8. (a) Schematic temperature dependence of the penetration depth and coherence length (ref. 22). (b) The magnetic penetration depth as a function of the reduced temperature (ref. 21). (c) Lower critical field for H parallel and perpendicular to the c-axis of single crystal 123 (ref. 24).

axis, illustrate well the anisotropic behavior of this material. In these curves, the lower critical field H_{c1} corresponds to the point in the initial part of the loop where departure from linearity (perfect diamagnetism) begins. The critical field determined for $H \perp ab$, Fig. 2.9 (b), is larger than that determined

for $H \parallel ab$, Fig. 2.9 (a), by a factor of more than 30. If the applied field is parallel to the *ab* plane, the induced screening currents flow perpendicular to the *ab* plane. For this case, the initial portion of the magnetization curve of Fig. 2.9 (a) shows a sharp departure from linearity, as the field increases above H_{c1}. A gradual departure of the magnetization curve from perfect diamagnetism occurs when the screening currents are induced along the direction of the *ab* planes ($H \parallel c$), as shown in Fig. 2.9 (b). This indicates that the (intrinsic) pinning of flux lines is stronger in the orientation perpendicular to the *ab* planes.

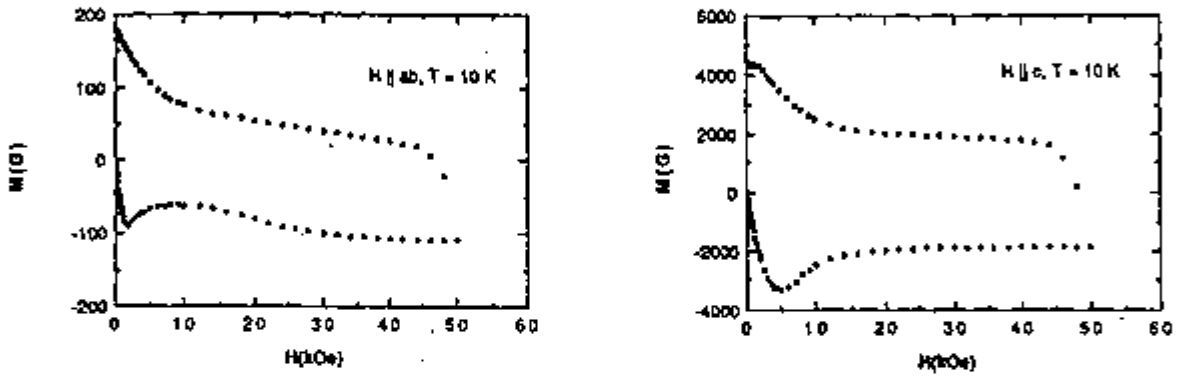

Fig. 2.9. Magnetization loops of a twinned 123 crystal at 10 K for fields applied perpendicular and parallel to the *c* axis. From Welp *et al.*[23]

Compared to conventional type-II superconductors, the compound 123 has extremely large values of H_{c2}, which are very anisotropic (Fig. 2.10). $H_{c2}(0)$ can be estimated from the $H_{c2}(T)$ data of Fig. 2.9.[25] The estimated values are very high: 670 T in the *ab* plane and 120 T along the *c* direction.[26] Thus, the above relation between the upper critical field and coherence length yields very small values of ξ, i.e., $\xi_c(0) \approx 0.3$ nm and $\xi_{ab}(0) \approx 1.6$ nm. However, Fig. 2.8 shows that ξ becomes very large close to T_c. This means that high-T_c oxides also need to contain relatively large defects to pin the flux lines at high temperatures.

Another characteristic of high-T_c materials is the occurrence of reversible magnetization and resistive behavior in some temperature range immediately below T_c. Cooling the material in the absence of an applied field, then applying a field $H > H_{c1}$ and measuring the magnetization with increasing temperature produces the curve labeled ZFC in Fig. 2.11. The curve labeled FC is obtained when the magnetization is measured in the presence of an applied field, on cooling. Fig. 2.11 shows that there is a temperature above which the magnetization is reversible, i.e., the FC and ZFC results are the same above

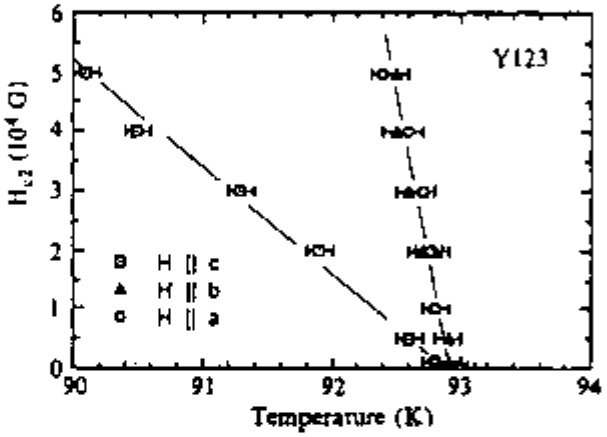

Fig. 2.10. Experimental values for the upper critical field. The critical fields along the a direction and along the b direction are the same within the experimental error (From ref. 26).

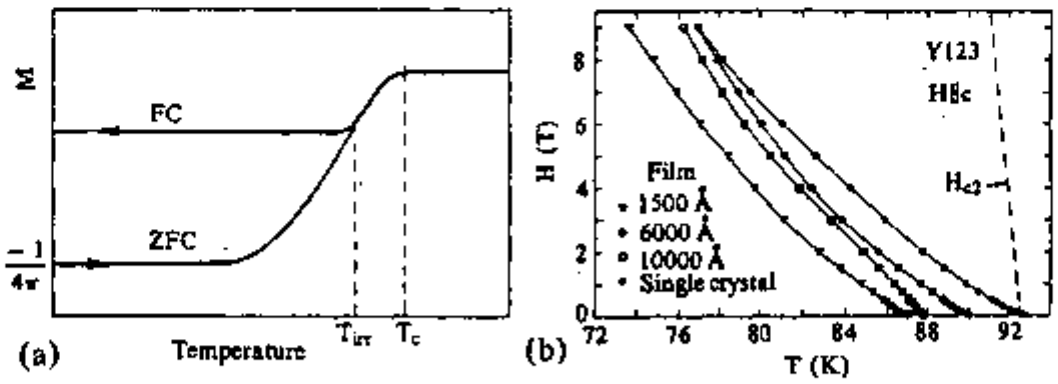

Fig. 2.11. (a) Temperature dependence of the magnetization when measured in a field H, for a sample cooled in zero field (ZFC), and when the sample is cooled with H applied (FC). (b) Irreversibility temperature of 123 films of different thicknesses (From ref. 27)

that temperature. Performing similar measurements at different fields allows one to determine $T_{irr}(H)$, the irreversibility line of Fig. 2.11 (b). This line defines a boundary in the phase diagram H-T above which J_c becomes very small or vanishes.[27] The occurrence of a phenomenon called giant flux creep is related to the existence of the irreversibility line. In the proximity of this line, the supercurrents in high-T_c superconductors have thermal relaxation rates that are orders of magnitude larger than in conventional superconductors .

Calculated values for the maximum current that 123 can carry (the depairing current) range from 10^8 to 10^9 A/cm^2 at 4 K, and from 10^7 to 10^8 A/cm^2 at 7 K.[28]

Flux Pinning and Intra-granular Critical Current Densities

In the mixed or vortex state ($H_{c1} < H < H_{c2}$) "tubes" of flux bearing, normal state material, called vortices, are present in 123.[11] Currents circulate around these vortices, screening the superconducting surroundings from the normal-state vortex core. Because of the Lorentz force ($\mathbf{J} \times \mathbf{H}$), these vortices repel each other. In isotropic superconductors, this repulsion causes the flux lines to arrange in two-dimensional, hexagonal close-packed lattice, called flux lattice or Abrikosov lattice.

When a current J flows in a mixed-state superconducting sample along a direction normal to H, the individual vortices will be again subjected to the action of a Lorentz force, and will be pushed in the $\mathbf{J} \times \mathbf{H}$ direction.[29] The motion of flux lines results in the development of an electric field parallel to J, which absorbs energy from the circuit and appears as an electrical resistance[30]. Therefore, in the mixed state, the vortices have to be strongly pinned if resistive losses are to be avoided in type-II superconductors. Technological applications require type-II superconductors with large current-carrying capability, and this is conditioned to the existence of large forces in the region of the vortex core, which oppose the Lorentz force, impeding the motion of flux lines by "pinning" them in their position.

The superconducting state has a lower free energy than the normal state. The difference in the energy of the two states per unit volume is called the "condensation energy". Since the core of a flux line is normal, the introduction of a flux line in a superconducting region causes an increase in the free

energy by an amount equal to the condensation energy times the core volume. This energy increase will be maximum if the order parameter of the superconducting region is 1. Smaller increases in free energy will result if the normal vortex core "sit" on microstructural features that have a lower superconducting order parameter, and, consequently, a lower condensation energy. Such features can be arrays of point, linear or planar crystalline defects and, possibly, interfaces between superconducting and non-superconducting regions. The minimum increase in free energy will result when the vortex core is located in a normal region, such as a non-superconducting second-phase precipitate. Therefore, the free energy of the material is lowered when flux lines are attracted to crystalline defects of inclusions.

The pinning force per unit length of flux line is expressed by $f_p = \partial U / \partial x$, where U is the pinning energy and x is in the direction of the Lorentz force. The magnitude of this force can be approximated by $\Delta U / \ell$, where ΔU is the difference between the free energy of the superconducting and defect regions, and ℓ is the interaction length over which U can change. Therefore, at microstructural features with sharp boundaries, ℓ will be small and the resulting pinning force will be large. The characteristic length ℓ is estimated to be of the order of the coherence length, ξ, since the latter is the minimum length scale over which electronic properties can change in a superconductor[11]. Thus, to be effective, a pin needs to have dimensions of the order of ξ in the direction of the Lorentz force. The effectiveness of such a pinning center will be further enhanced if its dimension parallel to H is made very large in order to increase the volume of core pinned.[11]

In summary, the critical current density of high-temperature superconductors is determined by intrinsic and extrinsic properties. Intrinsic properties include the thermodynamic critical field and the coherence length. Extrinsic properties are related to the size, distribution, density and other characteristics of microstructural features. Grain boundaries are also included in this category and are discussed in section 2.4.1. Due to the highly anisotropic nature of the electronic properties of high-temperature superconductors, the geometry of the pinning centers depends on the current direction as well as on the direction of the applied magnetic field. Moreover, the large increases in coherence length that occur close to the critical temperature suggest that pinning centers of larger dimensions may also become effective just below T_c.

2.3 Other Superconducting Phases in the System Y-Ba-Cu-O

Two additional superconducting phases have been identified in the system Ba-Y-Cu-O in high oxygen pressures, $YBa_2Cu_4O_8$ (124) and $Y_2Ba_4Cu_7O_{14-\delta}$ (123.5). With $YBa_2Cu_3O_{7-\delta}$ they constitute the series of homologous superconducting compounds $Y_2Ba_4Cu_{6+n}O_{14+n}$ (n = 0, 1, 2), which include the compound $YBa_2Cu_3O_{7-\delta}$ (n = 0). The 124 structure is formed by inserting an extra Cu-O layer between de Ba-O layers in every 123 unit cell. This compound was first identified as an intergrowth in 123.[31] Subsequently, it was also observed as an ordered structure in films annealed in 1 atm oxygen.[32] Bulk synthesis of this compound was achieved in the high-temperature, high-oxygen pressure experiments of Karpinski *et al.*[33-36] and Morris *et al.*[37,38] These studies also confirmed the existence of 123.5. Later, numerous investigators[39-45] were able to synthesize the phase 124 at ambient oxygen pressure and lower temperatures. These phases may play a key role in the critical current density enhancement of $YBa_2YCu_3O_{7-\delta}$, since their interconversion (section 2.5) can be exploited for the introduction of flux pinning centers in 123 (section 2.4.2).

2.4 Microstructure and Critical Current Densities in Bulk $YBa_2Cu_3O_{7-\delta}$

The electrical weak link and the flux pinning problems are so complex that they have been researched almost separately. Many of the complexities are of intrinsic nature and have been discussed in the preceding sections. Others may arise by virtue of the myriad of processes used in the fabrication of samples, which certainly contain important unidentified microstructural features.

In Fig. 2.12, from the work of Jin and Graebner,[46] the transport current density is plotted against the applied field for different categories of 123 samples. At 1 T, for example, grain boundary alignment by melt-texturing results in an average increase in J_c of more than 4 orders of magnitude over the average values measured in polycrystalline samples. This example illustrates the severity of the weak-link electrical behavior of grain boundaries in polycrystalline 123.

An encouraging trend in the current density of melt-processed materials is revealed when recent results[243,244,252] are included in the original plot of Jin and Graebner. These results are indicated by dashed lines in Fig. 2.12 and show that, at low fields, the critical current density of melt-processed 123 is approaching the values previously obtained in irradiated samples.

2.4.1 *The Grain Boundary Problem in $YBa_2Cu_3O_{7-\delta}$*

Bulk, polycrystalline 123 consolidated by sintering techniques has extremely low current densities (J_c), even in the absence of applied magnetic fields. At 77 K, J_c displays a marked dependence on applied field, practically dropping to zero at fields as low as 0.1 T. Most potential applications of high-temperature superconductors are associated with the presence of much stronger magnetic fields, i.e., orders of magnitude higher than the previous value. Attempts to increase the transport properties of polycrystalline 123 have all produced insignificant results. This is because of the so called "weak-link" electrical behavior displayed by the grain boundaries.

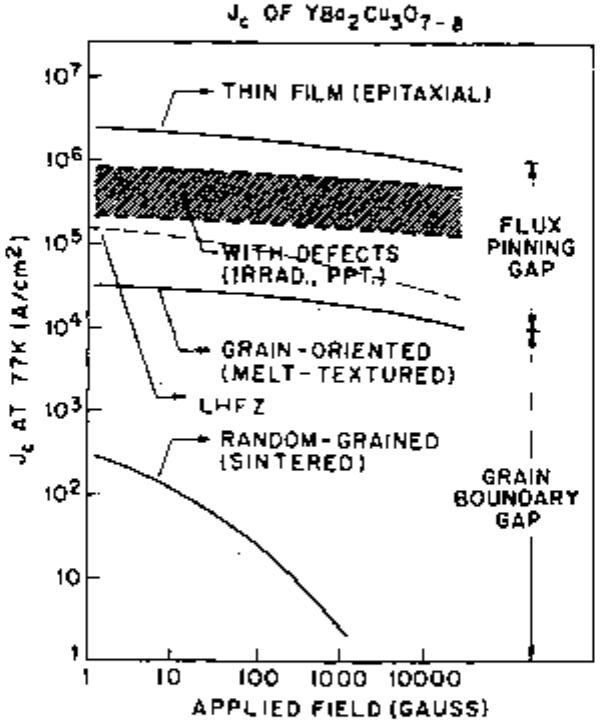

Fig. 2.12. Transport current density versus applied field in 123. Very high current densities are obtained in this material by the controlled introduction of flux pinning defects.[46]

Many of the microstructural features that control the current density in bulk, polycrystalline 123 are related to the intrinsic and extrinsic characteristics of the grain boundaries. The first category includes structural variations, such as dislocations and coherence of CuO_2 planes at the boundaries, deviations in the cation and oxygen stoichiometry, and inherent

anisotropy of the superconducting properties.[11] Structural variations are likely to alter the local electronic structure, particularly the Cu-O bond distance and angle. Small changes in the Cu-O bonds are known to cause suppression or loss of superconductivity in high-T_c superconducting oxides. The anisotropy in superconductivity is responsible for weak connection at large-angle grain boundaries. The extrinsic factors are related to the synthesis and processing techniques and comprise chemical variations at the boundaries. Carbonaceous compounds, insulating layers, and segregated impurities have been identified by Auger spectroscopy and electron microscopy along 123 grain boundaries[11].

Stringent control over the starting composition and the processing conditions is required to prevent the formation of secondary phases at the grain boundaries, as well as to enhance the intergranular current density. However, direct and indirect critical current densities measurements in materials with clean grain boundaries still indicated low intergranular to intragranular J_c ratios. These ratios also decrease rapidly with applied field, becoming practically zero at very low fields.[47] This behavior is primarily associated with the small coherence lengths of 123, which also depend on the crystallographic direction. At 0 K, the values for 123 are ξ_c (0) ~ 0.3 nm and ξ_{ab} (0) ~ 1.6 nm.[46] Supercurrents cannot flow through grain boundaries thicker than the coherence length without showing weak-link characteristics.[48,51] In conventional superconductors, ξ (0) typically varies from ~50 nm to 10^3 nm.[46] Thus, grain refinement is an effective way of increasing the critical current density in these materials.

Dimos, Chaudhari and Mannhart[47] have demonstrated that all grain boundaries in 123, except those misoriented by less than 5°, behave as Josephson junctions or Josephson-type weak-links (across a Josephson superconducting-insulator-superconducting junction, a current is observed to flow at zero voltage)[49] Fig. 2.13 from the work of Dimos, Chaudhari and Mannhart shows the pronounced dependence of the misorientation angle of two adjacent 123 grains on the critical current density ratio, expressed by $J_c^{g.b.} / J_c^{grain}$. This ratio was observed to saturate to a value of about 1/50 at large misorientation angles.

Babcock *et al.*[50,51] have demonstrated that the weak-link behavior is not common to all high-angle grain boundaries, as one would expect from the results of Dimos, Chaudhari and Mannhart. They found some naturally occur-

ing grain boundaries in flux grown bicrystals that did not display weak-link behavior, even when the Cu-O planes of one grain were almost perpendicular to the Cu-O planes of the other grain. Babcock *et al.*[50] argued that the tendency of flux-grown bicrystals to self-select low-energy configurations as they grow could make them to behave differently from the artificially made epitaxial thin film bicrystals of Dimos et. al. The former authors proposed that the grain boundary properties may also be influenced by a number of

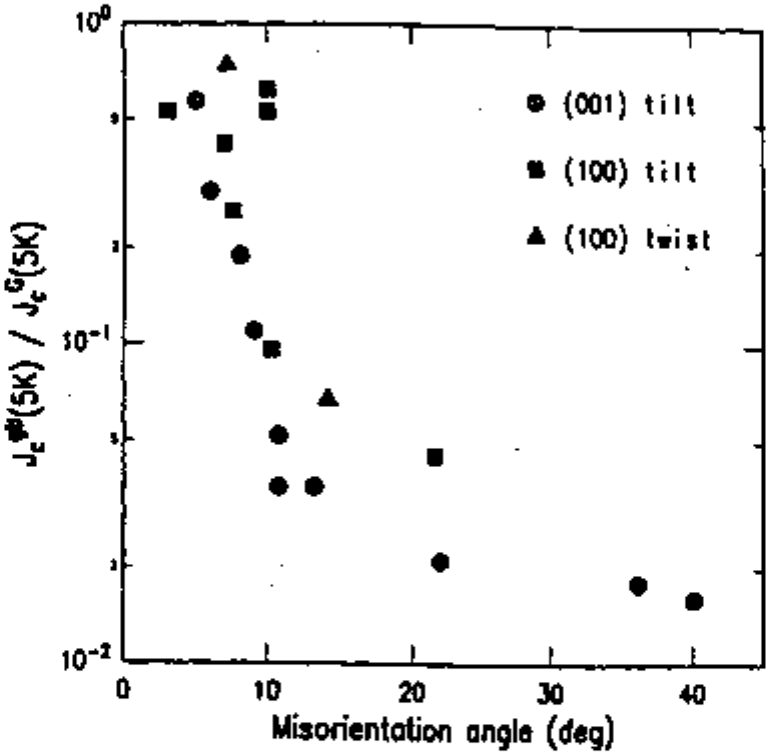

Fig. 2.13. Intergranular critical current density as a function of the misorientation angle.[47]

factors, such as boundary plane, character of segregation, or the presence of impurities.

Alexander *et al.*[52] have investigated grain boundary compositions in 123 and found that in stoichiometric materials, the grain boundaries were rich in copper. In addition, the levels of segregation in a given material varied from boundary to boundary. The presence of CuO along grain boundaries has also been detected by a number of authors.[53-56]

Other important factors in the superconducting properties of 123 are microcracking due to thermal and phase transformation stresses and the lack of an adequate density of flux pinning sites within grains.

2.4.2 *Intragranular Current Densities: Flux Pinning*

Jin and Graebner[46] observed that, while the weak-link problem of polycrystalline materials can be removed by melt-processing, the high-field values of J_c are apparently limited to the lower range of the interval 10^4 - 10^5 A/cm². They proposed that a low density of flux-pinning sites in bulk melt-processed materials is likely to limit the current density to ~ 10^4 A/cm² at 1 T, since in non-weak linked epitaxial thin films, which are known to contain a large density of pinning centers, J_c exceeds 10^6 A/cm² at 77 K and 1 T.

Better theoretical understanding of flux pinning, as well as practical techniques for introducing pinning centers in bulk materials are required to increase the current density in bulk materials. The progress in the former areas has been very stimulating. Important information about flux pinning mechanisms has been gained from irradiation experiments and the phase decomposition technique[46], apparently meets the practical requirements for introduction of pinning centers in 123.

Irradiation-Enhanced Flux Pinning

Although it is likely that irradiation will not be the technique of choice for flux pinning enhancement in high-T_c materials, because of its inherent drawbacks, it has provided researchers with valuable information about the relations among type and number density of pinning sites and critical current density.

Flux pinning defects have been succesfully introduced in 123 single crystals by fast neutron[56,57] proton[58] and heavy ion irradiation.[56] Magnetization current densities as high as 20 MA/cm² have been measured in proton-irradiated 123 at 3 K and H < 1 T by Civale *et al.*[58] At 77 K and H = 1 T, irradiated crystals usually display current densities between 4-6 x 10^5 A/cm².[57,58] These values are very close to those measured in epitaxial thin films.

Recent studies by Civale *et al.*[58] on 123 single crystals irradiated by proton and tin ions have provided important insights concerning the flux pinning capability of two pin geometries, as well as their effectiveness in displacing the irreversibility line to higher temperatures and higher fields. Fig. 2.14, reproduced from their work, shows the dependence of the critical current

density on the applied field at 5 K and 77 K for samples irradiated with protons and tin ions. As shown by the plots, both types of particles improved the flux pinning by more than two orders of magnitude at 77 K, in the low field region, relatively to the unirradiated sample. The increase in flux pinning due to irradiation was not so large at 5 K because at low temperatures unirradiated 123 has a large density of effective pinning centers.

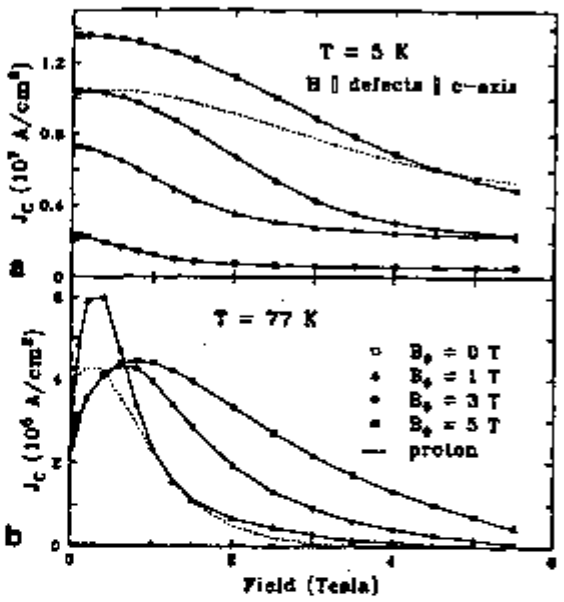

Fig. 2.14. Critical current density of irradiated 123 single crystals. (a) With 580 MeV Sn ions at an angle of 2 degrees from the c axis at doses that produce defect densities equal to the vortex density at fields of 1 T, 3 T, and 5 T. Best results for a proton irradiated crystal and an unirradiated crystal are shown for comparison. From ref. 58.

The intrinsic pinning in 123 may be related to the perovskite structure itself, oxygen or vacancy order-disorder effects[46,59] Proton irradiation produces basically point defects, which have an effective, albeit localized pinning action. Since each point defect confines a small portion of the vortex core, the pinning energy is small and the thermal relaxation effects ("flux creep") are pronounced. Thus, proton irradiation yields only marginal current density increases in the high temperature regime. Irradiation with 580 MeV Sn ions produced columnar defects about 5 nm in diameter and 10 nm apart, which were capable of pinning much larger volumes of vortex core.[58] As a consequence of their large pinning energy, these defects caused larger increases in the current density of single crystals in the high temperature region, even at high magnetic fields, as illustrated in Fig. 2.14. At low

temperatures and high fields, the effects of both types of particles were similar.

Creation of Flux Pinning Sites by Phase Decomposition

The phase decomposition technique has been investigated by several authors.[60,61] Their approach consisted in heating the 124 phase to the stability field of 123 (above 920°C) for a short time, followed by rapid cooling to 700-750°C to retain the defects induced by phase transformation. These defects are distributed in a very fine scale in the transformed material, which displays 123 characteristics, indicated by a transition temperature of about 90 K, when it is oxygenated at low temperatures. With this technique, current densities of about 10^5 A/cm^2 were obtained at 0.9 T. This value represents an increase of about one order of magnitude over the values obtained in typically processed 123 (including melt-processed materials). The defects, identified by transmission electron microscopy, consisted of stacking faults 1 to 3 nm thick and fine twins, spaced by 10 - 50 nm. Non-flux pinning defects, like copper oxide particles with average diameter of about 250 nm, were also identified. Jin *et al.*[60] attributed the improved flux pinning in 123 obtained by phase decomposition to the presence of the lower T_c stacking defects and the associated dislocations.

Flux Pinning by Dislocations

The superconducting order parameter is lower in the vicinity of dislocations, because the lattice is distorted by these defects.[46] Dislocation densities as high as 10^9 cm^{-2}, have been observed in in epitaxial thin films as well as in melt-processed 123.[46] The higher critical currents of epitaxial thin films have been related to the presence of screw dislocations associated with spiral growth as well as defects in low angle boundaries between the spirals. In order to be efficient pins, the dislocations need to be properly oriented with respect to the direction of the applied field.

Several possible causes for the high dislocation density in melt-processed 123, have been cited by Jin.[62] They include accomodation of lattice parameters in the presence of local cation concentration gradients that occur during crystal growth, relief of internal stresses generated by local temperature gradients, strains caused by the encounter of parallel 123 platelets with slightly

different orientations or by bending of platelets close to inclusions, and thermal mismatch between the 123 matrix and the 211 particles. However, the current density reported by Jin *et al.* for melt processed 123 containing dislocation densities between 10^9 and 10^{10} cm^{-2} was still two orders of magnitude lower than in high-J_c thin films with similar dislocation densities. According to Jin *et al.* the above dislocation spacings in both the thin films and melt-processed materials appear to be far greater than the vortex spacing in high magnetic fields ($H \geq 1$ T). Therefore, dislocations alone cannot account for the high degree of flux pinning in thin films.[62]

Synthesis and processing techniques capable of producing materials with controlled dislocation densities are required to determine the actual contribution of dislocations to flux pinning in 123.

Flux Pinning by Second Phase Particles

There are many reports in the literature concerning the effects of second phase additions on the critical current density of 123. Additions comprise the high-temperature, non-superconducting phase Y_2BaCuO_5(211), which participates in the peritectic reaction m1 with 123, and a number of other phases that do not belong to the system Y-Ba-Cu-O. These phases can be either elemental metals, such as silver[63-77], platinum[78], gold[79] or oxides, such as $BaSnO_3$,[80-81] $BaTiO_3$,[82-83] Sb_2O_3,[84] Ag_2O.[85]

Several authors have claimed that the 211 particles may enhance flux pinning in melt processed 123. This seems improbable, since the particles are orders of magnitude larger than the coherence length. Even crystalline defects such as dislocations, stacking faults and other regions with depressed order parameters, such as the interfaces between non-superconducting inclusions and the superconducting matrix, are not sufficiently numerous or do not have the right geometry to contribute effectively to flux pinning. This point has been demonstrated for the 211 by Jin *et al.*[86,87] These investigators employed aerosol techniques to sinthesize 123 containing a dispersion of fine 211 particles. The particles remained very fine (~800 nm) after melt processing the composite material, but the increase in current density due to their presence was not significant.

Magnetization results for melt-processed 123 samples containing excess 211 in the form of fine particles have also been reported by Sagdahl *et al.*.[88] These

investigators found that the irreversibility line in those samples was much steeper and shifted to considerably higher temperatures compared to single crystal 123. In disagreement with previous results, they found a significant increase of about one order of magnitude in the effective pinning energy of their samples.

Probably, the current density of 123 containing excess 211 particles is higher because these particles contribute to the formation of microstructural features that apparently enhance intra-domain connectivity (see section 5.3.7). In addition, fine 211 particles contribute to improve the kinetics of the peritectic reaction and the stability of the semisolid melts from which 123 is grown (Chapter 5). Jin *et al.*[87] have also observed that the 123 platelet spacing decreases linearly with 211 particle size. Other significant microstructural characteristics observed in composite materials containing excess of 211 in the form of fine particles[i] are the absence of microcracks and cleaner platelet or low-angle grain boundaries.[88,89] Therefore, fine 211 particles contribute not only to develop the 123 platelet structure but also to improve the fracture toughness of these materials reducing the extent of intragranular and low-angle boundary microcracking .[11,87]

Finer 211 particles has been observed in melt processed 123 containing Pt or $BaSnO_3$ additions.[78,80,81] If these additions have a real effect on the current density, the effect is likely to be indirect, that is, it is caused by the reduction of 211 particle size by the impurities, which in turn may affect the structure of the melt-processed superconducting phase. Silver may increase the fracture resistance of 123, since higher fracture toughness have been measured in 123 - Ag composites.[76]

2.5 *Phase Equilibria and Phase Stability in the System Y-Ba-Cu-O*

Numerous studies of phase equilibria in the system Y-Ba-Cu-O have been published since the discovery of the superconducting compound 123.[16,38,90-115] The existence of a large number of phases and the marked oxygen partial pressure dependence of all invariant reactions,[91,94,95,104,105,109] make the phase equilibria in this system quite complex. Phase equilibria studies are further complicated by the chemical reactivity of Y-Ba-Cu-O liquids, which interact strongly with most container materials and substrates, and also by the affinity for carbon manifested by some compounds of this system, including the

superconducting phases.[117-122] Phase diagrams for high-T_c superconductors published before 1991 have been compiled and reviewed by Whitler and Roth[116] Significant discrepancies are still found among published results for phase equilibria in the system Y-Ba-Cu-O, especially at high and low oxygen partial pressures. Under atmospheric conditions, pseudo-ternary sections and temperature-composition cuts determined by several authors are in qualitative agreement with respect to the boundaries of two- and three-phase equilibria fields.

The oxygen partial pressure has a marked influence on the phase equilibria in the Y-Ba-Cu-O system. Beyers and Ahn[16] pointed out that, indeed, one of the principal causes of the many conflicts on the structure and physical properties of superconducting oxides is the failure to control or monitor the oxygen partial pressure during oxyde synthesis.

2.5.1 *Phase Equilibria in The System Y-Ba-Cu-O in Air*

The pseudo-ternary and temperature-composition sections determined in air by Roth *et al.*[92] seem to be more complete and will be briefly discussed here. Their results were obtained with Y-Ba-Cu-O pellets sintered on MgO single crystal tablets, to minimize contamination, and from quenching experiments, performed in 70 Ag - 30 Pd tubes. Later, Verkouteren[123] found that Ag-Pd alloys also react with liquid Y-Ba-Cu-O phases.

The pseudo-ternary section BaO-1/2(Y_2O_3)-CuO was determined by Roth *et al.*[92] at 875°C (Fig. 2.15) and by a number of other investigators[116] in the temperature range 800°C - 900°C. Published results are in general agreement concerning the phase relations at barium contents below about 50 mol %. Two ternary compounds exist in this region, the superconducting phase $YBa_2Cu_3O_{6+\delta}$ and the "green phase" Y_2BaCuO_5, which is non-superconducting and was identified in 1982 by Michel and Raveau.[3] However, the exact nature of the pseudo-ternary section close to the BaO corner is still unclear.

Some investigators[95,104,109] found the presence of a perovskite type phase, identified as $YBa_3Cu_2O_{6+\delta}$ (132) in the barium-rich corner of the composition triangle. Subsequent studies of quaternary phase relations at low oxygen pressures have also proposed that the former phase participates in two invariant reactions near the 123 composition. In the study of Roth *et al.*[92] it was concluded that this phase was, in fact, a single phase region of solid

solution bounded by, but not including, the compositions 1:3:2, 1:4:2 and 1:5:3. These authors observed that none of the latter compositions could be prepared as a single phase and that they contained Y_2BaCuO_5, $BaCuO_2$, and probably hydrates. However, specimens with the nominal formula $Y_{0.8}Ba_{3.2}Cu_{2-x}O_{6.4-\delta}$ prepared from $\delta = 0$ to $\delta = 0.3$ were entirely single phase. Moreover, this single phase could only be prepared with barium carbonate. Carbonate-free specimens prepared with barium oxide in oxygen atmospheres contained only $BaCuO_2$, Y_2BaCuO_5 and Ba_2CuO_3 and also unidentified X-ray diffraction peaks. Such specimens were easily attacked by atmospheric moisture, unlike the samples prepared from barium carbonate in air. From these observatins, Roth *et al.*[92] concluded that the so-called "other perovskite" phase in the system BaO-Y_2O_3-CuO was chemically and structurally an oxy-carbonate.

In Fig. 2.16 (a) the compound Y_2BaCuO_5 was found to melt incongruently (in Ag-70 Pd containers) at 1275 ± 25°C into Y_2O_3 plus liquid. The compound

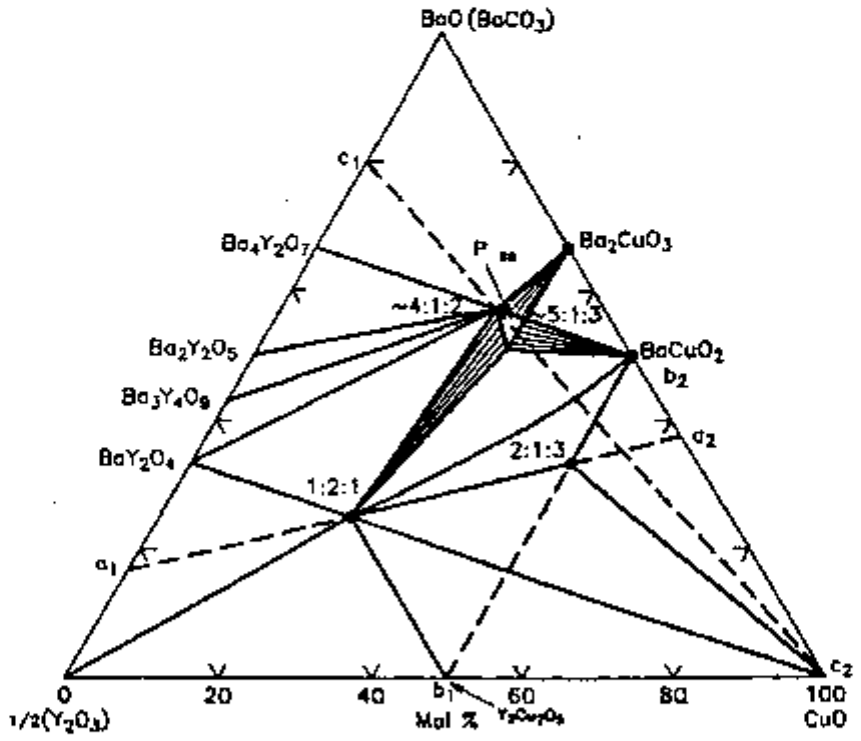

Fig. 2.15. Pseudo-ternary section of the system $1/2(Y_2O_3)$-BaO-CuO in air, at temperatures around 850°C. [92]

123 decomposed into 211 plus liquid at 1002 ± 2°C and then became fully liquid at 1258 ± 2°C. Other researchers in the field found considerably larger

liquidus temperature .[116] In a revision of their work, which is presented in Fig. 2.16 (b), Roth *et al.*[116] concluded that the temperature of 1258°C merely corresponded to the reaction 211 + L → 200 + L, and estimated a value of 1475°C for the true liquidus temperature of the composition 123. Therefore, the position of the liquidus line is actually to the right of that shown in Fig. 2.16 (a), in agreement with determinations by Murakami[124] and Aselage and Keefer.[91] When contained in MgO single crystals, the composition 123 was found to melt at relatively higher temperatures (1015°C).[116] This difference is probably caused by contamination from the Ag-Pd container materials that were used by Roth *et al.*[92]

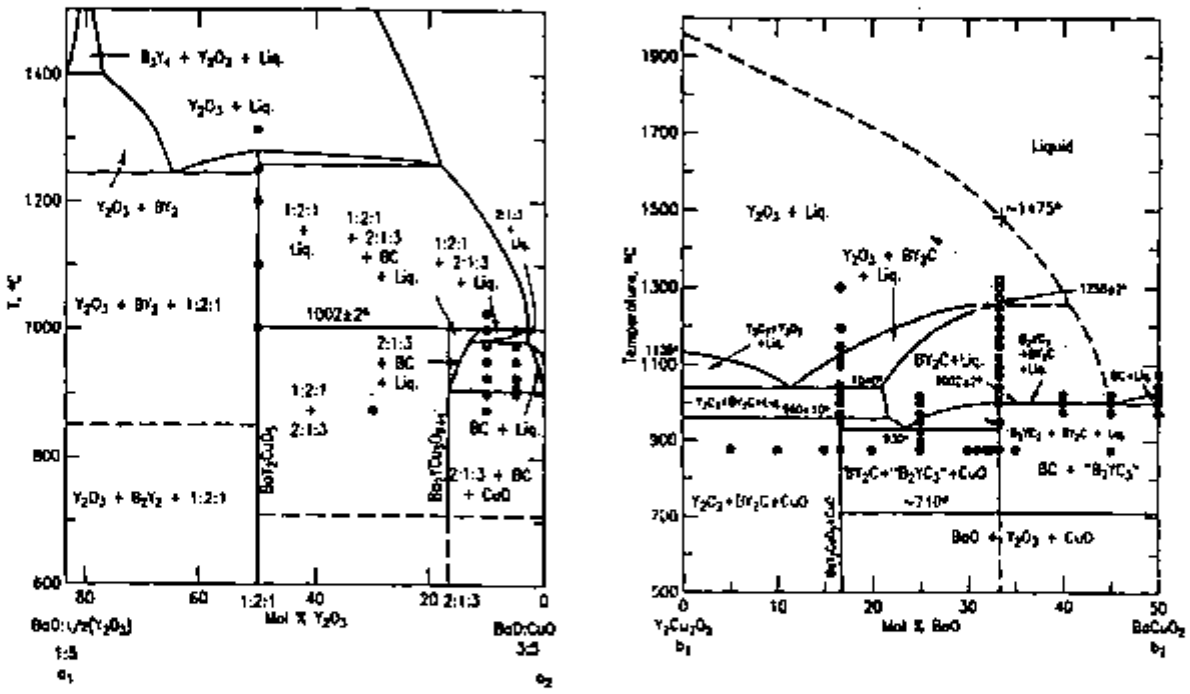

Fig. 2.16. Temperature-composition sections corresponding to the lines a1-a2 and b1-b2 of the ternary section shown in Fig. 2.15. [92,116]

2.5.2 *Invariant Reactions in the System Y-Ba-Cu-O*

In a study of liquidus relations in the system Y-Ba-Cu-O in air, Aselage and Keefer[91] determined 11 invariant reactions in the compositional region near 123. The results of their work are summarized in Table 2.2, where eutectics are denoted by "e", pseudo-peritectics by "p" and peritectics by "m". Aselage and Keefer have also determined the liquidus diagram in the CuO corner of

the composition triangle, which was later modified by Lay and Renlund,[105] who used the results of Oka *et al.*[93] . and their own to obtain the diagram presented in Fig. 2.17 (b). The compositions studied by Lay and Renlund included 211, 123, a composition between CuO and 123 and three compositions along the extension of the line from 211 through 123. The modified liquidus diagram, in agreement with the results of Roth *et al.*,[92] indicates a very narrow primary phase field for the 123 compound, which is located at very low yttrium concentrations. Lindemer *et al.*[109] have determined a value of 3 mol % for the the solubility of yttrium in the liquid m_1 at pressures above 94 Pa. This low solubility value is expected to play a major role in the kinetics of solidification of the 123 compound.

Ahn, Lee and Beyers used coulometric titration of oxygen and microanalysis to determine quaternary phase relations near the composition 123 at 850°C in reduced oxygen pressures.[96,104] Under these conditions, they identified nine invariant points, including e_1 of Table 2.2, the CuO/Cu_2O reaction, and the following reaction:

$$7\ YBa_2Cu_3O_6 \rightarrow 3\ Y_2BaCuO_5 + YBa_3Cu_2O_{6+\delta} + 8\ BaCu_2O_2 + (5\text{-}y)/2\ O_2 \qquad (2.1)$$

The above equilibrating reaction was considered by Ahn *et al.* to establish the minimum oxygen pressure for the thermodynamic stability of the compound 123. However, they did not determine the cation and oxygen stoichiometry for the phase identified as $YBa_3Cu_2O_5$ or "132" Variations in the X-ray peak positions for that phase were also mentioned by Ahn *et al.*, but they did not support Roth's conclusion that the "132" phase is actually an oxycarbonate. The reasons for the disagreement were not stated in their report.

2.5.3 *Oxygen Pressure Dependence of the Temperature of Invariant Reactions in the System Y-Ba-Cu-O*

Lay and Renlund[105] have also determined the dependence on oxygen pressure of some invariant reactions in the sytem Y-Ba-Cu-O (Fig. 2.17). The line labeled c_1 in Fig. 2.17 corresponds to incongruent melting of the compound 211 in a sample with overall composition 123, the line m_4 is for incongruent melting of phase pure 211, and the lines c_3 and c_2 for incongruent melting of 123 and 211 in a sample of overall composition between 123 and CuO. Also,

Table 2.2. Temperature of invariant reactions near 123 compositions in air.[91]

TEMPERATURE (°C)	INVARIANT POINT	REACTION
890	e1	$YBa_2Cu_3O_{6+\delta} + BaCuO_2 + CuO \rightarrow L$ (e1)
920	e2	$BaCuO_2 + CuO \rightarrow L$ (e2)
940	p1	$YBa_2Cu_3O_{6+\delta} + CuO \rightarrow Y_2BaCuO_5 + L$ (p1)
975	p2	$Y_2BaCuO_5 + CuO \rightarrow Y_2Cu_2O_5 + L$ (p2)
1000	e3	$Y_2BaCuO_5 + BaCuO_2 \rightarrow L$ (e3)
1000	p3	$YBa_2Cu_3O_{6+\delta} + BaCuO_2 \rightarrow BaY_2CuO_5 + L$ (p3)
1015	m1	$YBa_2Cu_3O_{6+\delta} \rightarrow Y_2BaCuO_5 + L$ (m1)
1015	m2	$BaCuO_2 \rightarrow L$ ($BaCuO_2$)
1026	-	$CuO \rightarrow Cu_2O$
1110	e4	$Y_2Cu_2O_5 + Cu_2O \rightarrow L$ (e4)
1122	m3	$Y_2Cu_2O_5 \rightarrow Y_2O_3 + L$ (m3)
1270	m4	$Y_2BaCuO_5 \rightarrow Y_2O_3 + L$ (m4)

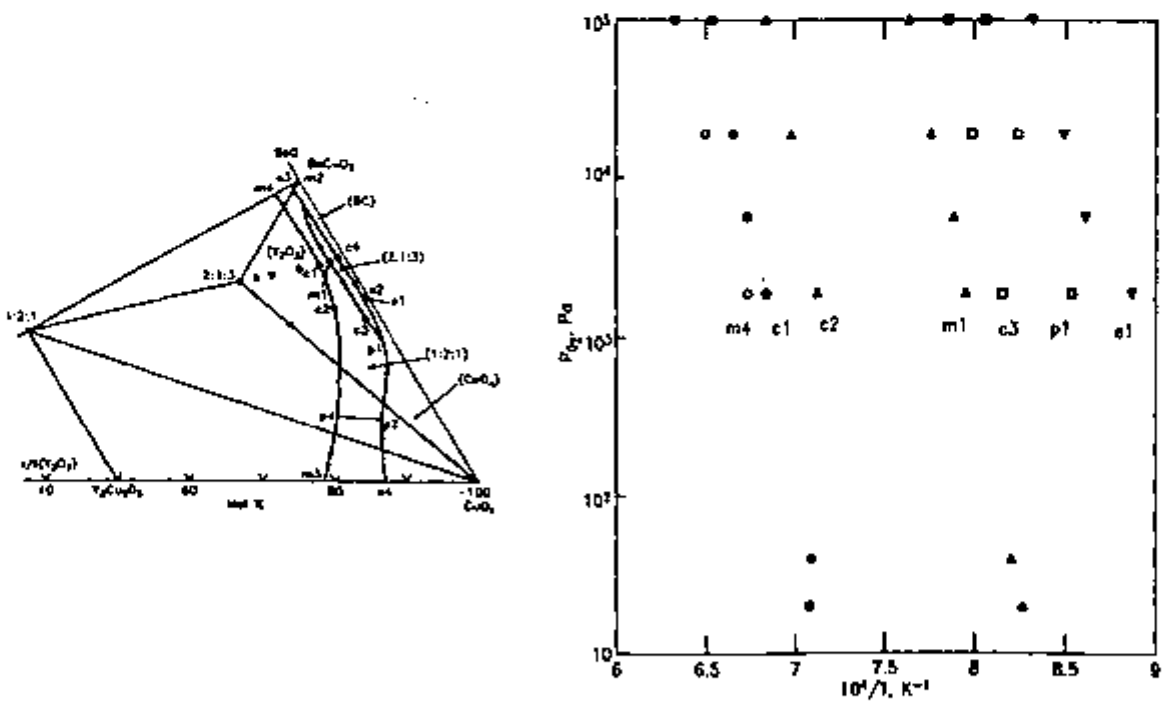

Fig. 2.17. (a) Oxygen pressure dependence of invariant reactions in the system Y-Ba-Cu-O for the liquidus compositions shown in (b). [105]

the intersection of lines m_4 and c_1 at approximately 10^3 Pa in Fig. 2.17 suggest a change in the nature of phase relations below 10^3 Pa O_2.

2.5.4 *Thermodynamic Stability of Phase Pure* $YBa_2Cu_3O_{7-\delta}$

Studies of the decomposition of phase pure $YBa_2Cu_3O_{7-\delta}$ have been performed over several decades of oxygen pressure.[1] The study of Lindemer *et al.*[109] reports that, at oxygen pressures below 94 Pa, the decomposition of pure 123 proceeds by reaction 2.1, in agreement with Ahn *et al.*[95,104] They determined temperature and oxygen pressure conditions for the previous reaction and also for the reaction m_1. With these determinations and literature results for the low temperature region, they proposed a field for thermodynamic stability of phase pure 123, which is reproduced in Fig. 2.18.

2.5.5 *Phase Equilibria in the System Y-Ba-Cu-O at High Oxygen Pressures*

The thermodynamic stability of the superconducting compounds $YBa_2Cu_4O_8$ and $Y_2Ba_4Cu_7O_{14-\delta}$ has been the subject of considerable interest. Soon after the discovery of these compounds it was realized that the controlled decomposition of 123.5 to 124 and then to 123 plus CuO could provide a

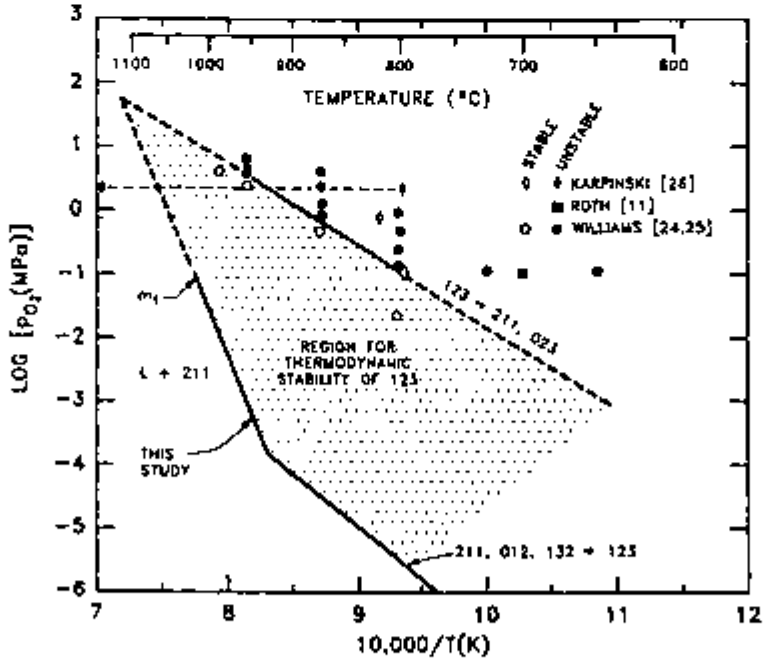

Fig. 2.18. Temperature-P_{O_2} conditions for the thermodynamic stability of phase pure 123, as determined by Lindemer *et al.*[109]

practical technique for increasing flux pinning in 123.[40,60,126] Short times at 900°C cause the decomposition of these materials and the precipitation of very thin platelets of CuO. The intragranular critical current densities after decomposition are one order of magnitude higher than those for typical sintered materials. However, the weak-link problem still persists in the decomposed material, since the randomly oriented grain structure of the precursors is retained in the 123 that forms. In order to fully exploit the benefits of enhanced flux pinning in these materials, the weak link problem must be eliminated by some method.

Fig. 2.19 reproduces the 123 - CuO polythermal section of the pseudo-ternary BaO-Y_2O_3- CuO phase diagram, which was proposed by Lindemer *et al.* [109] for oxygen pressures below 0.1 MPa. At these pressures, the diagram show complicated melting relations, which involve at least two solid phases. The diagram also shows the existence of the field 123 plus CuO, between 879°C and 964°C, over the entire composition range. At the point p_1, 123 and CuO are formed by the reaction of 211 with liquid.

Recently, Karpinski *et al.*[111] have published results on the stability of the compounds 123, 123.5, and 124 over a range of oxygen pressures from 10^{-2} MPa to 1000 MPa (0.1 to 10,000 atm). Their results, which are reproduced in Figure

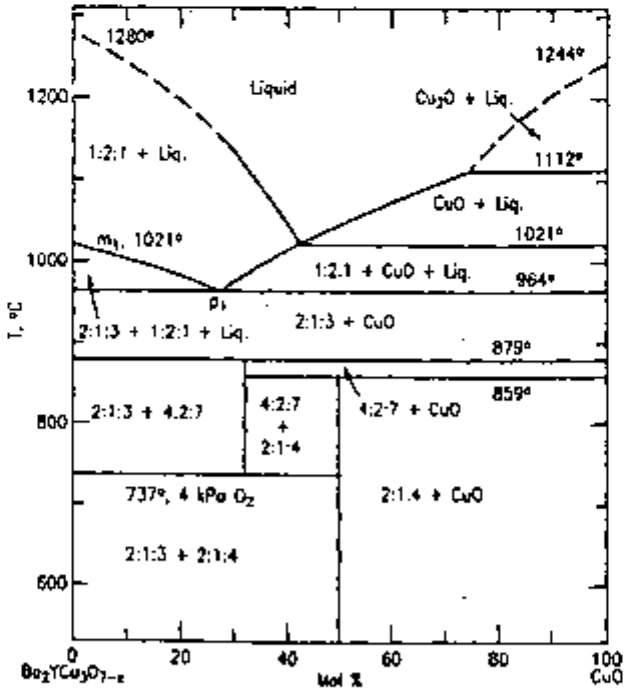

Fig. 2.19. 123-CuO polythermal section proposed by Lindemer *et al.*[109] The 123 liquidus line should be displaced to higher temperatures (see Fig. 2.17).

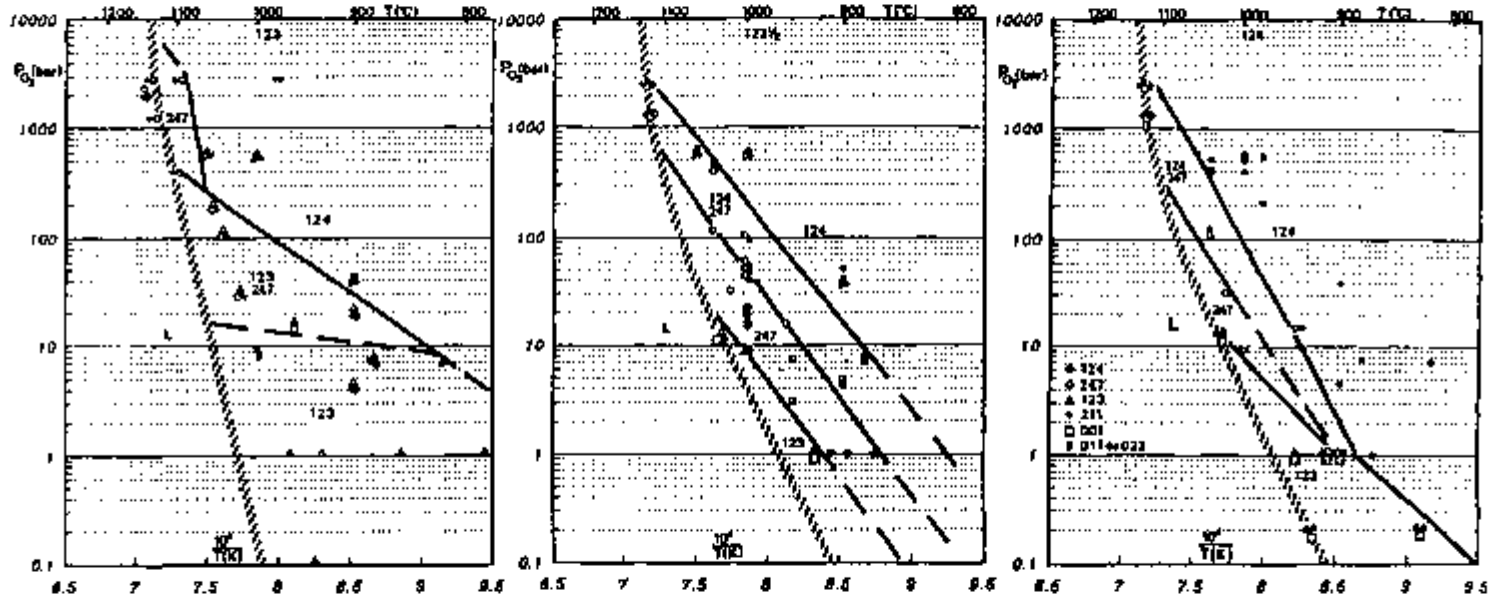

Fig. 2.20. Log PO_2-1/T sections of the P-T-X phase diagram for compositions 123, 123.5 and 124. From Karpinski *et al.*[111]

2.20, indicate that the phase 123.5 decomposes incongruently above about 1 MPa O_2 at the stoichiometric composition (2 MPa O_2 at the 124 composition. Their P_{O_2}-temperature conditions suggest that, as the oxygen pressure increases, the 123 plus CuO field in Fig. 2.19 becomes narrower, and eventually disappears.

2.6 *$YBa_2Cu_3O_{6+\delta}$ Crystal Growth*

2.6.1 *Flux Growth*

Small 123 single crystals can be grown from melts containing low yttrium concentrations, in the absence of convection, by a technique called "flux growth". The schematic pseudo-binary phase diagram of Fig. 5.1 indicates that crystals with the approximate composition 123 can be grown from liquid of composition c_{L_p}. This is a simple binary representation of the flux growth method.

Details about specific procedures for flux growth of 123 are given in a number of reports.[127-142] Compositions around $Y_3Ba_{30}Cu_{67}O_x$ are homogenized at 1010-1020°C for a few hours. Following homogenization, the crystallization of $YBa_2Cu_3O_x$ is achieved upon slow cooling through the peritectic temperature. The very thin, plate-like crystals that form are recovered by either pumping out the residual liquid flux from the crucible or by extraction from the solidified mass that results if the flux is allowed to solidify.

The habit of flux grown 123 crystals is tabular to platy (001) with (010) and (100) side faces[133]. Under very low or very high cooling rates, other lateral faces may develop. At cooling rates below 0.5°C/h, Wolf *et al.*[132,136] found that (101) and (011) were also present in some crystals. At fast cooling rates, the same authors observed non-equilibrium morphologies, where the edge of the (001) face of the thin platelets developed a serrated pattern. This pattern was formed by small facets parallel to the *c*-axis, apparently of the (110) type. These experimentally observed habits are supported by the theoretical investigations of Sun *et al.*[133]

Surface morphology studies by Sun and Schmid[133] revealed that the growth mechanisms of the lateral (100)/(010) faces consist of two-dimensional nucleations, which start at the crystal corners and edges. The basal (001) faces grow by the screw dislocation mechanism or spiral growth. Scheel and

Niedermann[145] were able to explain the two-dimensional mechanism using a combination of STM and SEM to study the growth features near edges and corners of natural {100} and {001} faces.

Wolf[136] reported that the growth velocity along the c-axis is about 10^{-3} μm/s and does not depend on experimental conditions, such as melt composition, crucible type, procedures and melt supersaturation. In contrast, the growth velocities along the *a*-axis could be increased from 5.6×10^{-4} μm/s to more than 0.56 μm/s, i.e., more than three orders of magnitude, by increasing the supersaturation of the melt. This investigator attributed the difference in growth velocities to different growth mechanisms of the (100) and (001) faces.

2.6.2 *Solidification Processing of* $YBa_2Cu_3O_{6+\delta}$

Investigations on solidification processing of 123 begun soon after this superconducting oxide was first isolated in 1986.[146] Alignment of 123 grains or elimination of 123 grain boundaries has been succesfully achieved by several solidification techniques, directional or not.[147] These processes usually produce melt-textured crystals with higher critical current density than polycrystalline materials and are all based on solidification from a semisolid melt.[148-175] In a typical melt-texture technique, the 123 compound is heated for a short time above the peritectic temperature (m1) to form a semisolid mixture of 211 and copper-rich liquid, which is slowly cooled through the peritectic reaction for nucleation and growth of the tetragonal 123 phase. The transformation of the solidified tetragonal crystals to the orthorhombic, superconducting phase is achieved either upon slow cooling to temperatures below about 400°C or by isothermal annealing at a temperature in the range 400-500°C. Because the growth rate of 123 crystals is much higher in the *a* or *b* direction than in the *c* direction, the solidified material crystallizes in the form of thin parallel plates, with wide *ab* faces and stacked along the *c*-direction. Such growth morphologies occur even in the absence of a temperature gradient.

Another common feature to solidification-processed 123 is that the peritectic reaction during the cooling step through the m1 temperature does not go to completion. As a result, the 123 grains always contain a dispersion of particles of the high temperature phase Y_2BaCuO_5 (211). The amount of residual 211

will depend on a number of factors, such as the structure and composition of the precursor, temperature, temperature gradient, and growth rate.

Apart from the common characteristics just cited, the solidification techniques that have been investigated so far differ with respect to temperature schedule, cooling rates, temperature gradients and composition of the precursor materials. They may be grouped into two distinct categories, according to the temperature gradient, since distinct microstructures are produced in the low and high-temperature gradient ranges.

Isothermal or Low Temperature Gradient Techniques

If the temperature gradient is low or negligible, the solidification microstructures consist of multiple domains of 123 plates. These domains are randomly oriented, and thus contain large-angle grain boundaries. The thin 123 plates inside a domain, however, are very wide and separated by low-angle, non weak-linked grain boundaries. The transport critical current density of these materials is low if measured across the large-angle grain boundaries. The intra-domain J_c, however, is large and the number of weak-links is considerably reduced in comparison with polycrystalline materials. Such structures may possibly find practical uses in magnetic bearings or microwave cavity applications[147] because they have much large magnetic hysteresis, and Meissner effect. Other common characteristics to samples pertaining to this category are the presence of cracks and residual copper oxide and barium cuprate inclusions, particularly along large-angle grain boundaries, in addition to the excess 211 particles. In addition, copper oxide is lost by evaporation because of the long solidification times required.[86] Contamination caused by the reaction of the liquid phase with the crucible materials is also a problem. Some techniques pertaining to this category are briefly described below.

The so-called "melt-textured growth" or MTG technique employed by Jin *et al.*[148] yields very dense and preferentially aligned microstructures. It consists basically in heating the 123 compound to temperatures around 1050°C and subsequent cooling to 900°C in temperature gradients of at least 50°C/cm. Transport current densities of 1.7×10^4 A/cm^2 at zero field and ~4×10^3 A/cm2 at 1T and 77 K were obtained in materials processed according to this

schedule. In addition, the field dependence of J_c in these samples was greatly attenuated.

The technique reported by Salama *et al.*[154] consisted of rapidly heating 123 precursor samples above the peritectic temperature to avoid the formation of low temperature eutectic liquid. The sample was kept at 1100°C for 10 min to allow for complete incongruent melting of 123 to 211 and liquid, then rapidly cooled to 1030°C, and finally slowly cooled at a rate of 1°C/h to 980°C, in order to allow the crystallization of the tetragonal 123 phase. No temperature gradients were employed and the whole sample solididified uniformly upon cooling through the peritectic temperature. Long 123 plate domains, oriented over wide areas were observed in the microstructure of the solidified samples, and transport current densities in excess of 3.7×10^3 A/cm^2 were measure at 77 K and 0.6 T. Refinements of this technique have produced materials with critical current densities of 10^3 A/cm^2 at 77 K and 30 T.[242] The "quench-melt-growth" or QMG process developed by Murakami *et al.*[151], is similar to the technique of Jin *et al.*[148] In Murakami's process, however, the precursor semisolid material from which 123 is grown, i.e., 211 + L, is obtained by rapidly heating 123 above 1200°C for short times to decompose the 211particles to very fine Y_2O_3 particles and liquid. The latter semisolid material is then quenched to room temperature. The quenched material is then finely ground and pressed into pellets, which finally constitute the precursor for 123 growth. Upon melting these pellets, the fine and homogeneously dispersed Y_2O_3 particles react with the liquid phase nucleating very fine, needle-like 211 particles. The sole purpose of the previous steps is to produce a semisolid, 211 plus liquid material containing micrometer-sized 211 particles, which is then cooled through the peritectic temperature under an applied temperature gradient of 10-20°C/cm, to form high-J_c 123 crystals. The J_c values of Murakami's samples exceeded 10^4 A/cm^2 at 1 T and 77 K. The multiple-step nature of this process, which also requires handling of very reactive liquids at high temperatures is a serious obstacle when pratical applications are considered. In addition, fine size-scale 211 + L mixtures can be produced by other ceramics processing techniques like sol-gel processing, to cite one.

High-Temperature Gradient Techniques: Zone Melting

Several investigators have used the zone melting process of Pfann,[176] or modifications of the Bridgeman technique to obtain highly-textured microstructures in both the Y-Ba-Cu-O[89,153,155,156,167,172,175] and Bi-systems.[177-182] This technique is particularly suited to the production of filaments, wires and rods, single-grained or containing continuous grains aligned parallel to the growth direction. Due to the small dimensions of the hot zone, temperature gradients in this process are typically higher than 100°C/cm.[167,169] For fibers with diameters below 300 μm, the temperature gradients can be larger than 10^4°C/cm.[89,177-181]

There are several ways by which heat is supplied to the hot zone in floating-zone growth. The most commonly employed are based on localized resistive elements placed inside resistive furnaces,[152,155,164,167,168,171,175] focussed halogen lamps,[157] and CO_2 laser beams.[89,177-182] In the latter case, two variations of the zone-melting process have been succesfully used to grow textured fibers and rods of 123 and $Bi_2Sr_2CaCu_2O_y$, the so-called laser-heated floating zone technique (LHFZ)[89,180,182] and the laser pedestal growth (LPG).[177-179,181]

The laser-heated techniques are ideal for processing highly reactive molten oxides. In addition to being crucibleless, the atmosphere of the crystal grower chamber is at room-temperature, can be easily changed and is not limited by the heat source. The latter characteristic allows easier crystal growth in vacuum or at high pressures. Perhaps, one of the most important characteristics of laser processing of filaments is that laser beams can be shaped into a number of forms through the use of appropriate optics. This leaves very interesting processing possibilities to be explored in complex materials such as 123. For example, temperature profiles can be greatly varied in magnitude and shape over length scales of a hundred micrometers. This allows the experimenter to control not only the nature of the phases within a given location in the semisolid zone, but also the lifetime of a given phase. It is conceivable that such complexities could be used for purposes of microstructural control. The laser-heated technique has also a great potential for the continuous production of high-J_c superconducting filaments or wires.

Steady-state crystal growth of materials that melt incongruently such as $Bi_2Sr_2CaCu_2O_y$ and 123 has been demonstrated by a number of researchers.[177-182] In floating zone growth, the average composition of the liquid ahead of the

freezing interface will adjust so that the solidified material has the same average composition as the feed rod.[182]

One of the difficulties encountered by Lu *et al.*,[181] during growth of extended lengths of single-crystal fibers of $Bi_2Sr_2CaCu_2O_y$ was posed by the peritectic nature of the material. In their work, the effects of the growth rate and fiber diameter on the structure of laser-pedestal grown $Bi_{2.1}Sr_{1.8}Ca_{1.1}Cu_2O_8$ were studied. These authors concluded that there was a maximum growth rate above which single-crystals could not be obtained and that the maximum growth rate for planar front growth was dependent on fiber diameter, smaller diameters tolerating higher growth rates. Their observed transitions from single-crystal to single-phase, multigrained fibers were consistent with the concepts of constitutional supercooling and interface stability.[183]

Directional growth of 123 crystals from fully molten zones has not been achieved so far. This is because the very low viscosity of fully molten 123 precludes the formation of stable zones. Another complicating factor is the nature of the Y-Ba-Cu-O phase diagram itself. Assume that a stable zone composed by a liquid of composition 1:2:3 is achieved. On cooling, Y_2O_3 precipitates as fine particles, which will coarsen very rapidly, before they react with the surrounding liquid to form the 211 phase. The large 211 particles will not be able to hold the liquid within the zone by capillarity and inadequate microstructures will form because the liquid will migrate out of the zone. For the above reasons, floating zone growth of 123 crystals is presently restricted to partially molten zones.

Chapter 3
Polycrystalline Superconducting Filaments

3.1 Introduction

Superconducting 123 filaments have been fabricated either by conventional techniques, such as plastic extrusion, or by methods that make use of organometallic precursors. In the former processes,[184,185] ceramic oxide powders are combined with high molecular weight organic polymers, dispersants and surfactants. Such mixtures are mechanically homogenized at the melting temperature of the binder and hot extruded through capillary dies. Alternatively, the ceramic oxides can also be mixed with a solution of the organic components in a volatile solvent to form a slurry. Selective evaporation of solvent from the resultant slurry yields a plastic mass with adequate rheological properties for extrusion.[186] The chemical routes rely on the use of organometallic precursors such as metal carboxylates[187] or modified metal alkoxides[188] preceramics to form spinnable gels with high oxide content. Hot extrusion of 123 powder in metal canisters[189] and electrophoretic deposition of 123 particles on metallic wires followed by electrophoretic silver coating,[190] and dry spinning of solutions of acetates of Y, Ba and Cu[191] are also examples of techniques that have been used to fabricate metal-clad wires and filaments.

Superconducting filaments for this study were initially purchased from a commercial vendor (CPS Superconductor Co., Milford, MA) and latter fabricated at M.I.T. The solidification experiments required bare filament samples with diameter between 250 and 400 μm and maximum length of about 10 cm. Therefore, due to its simplicity, the binder solution technique was the most appropriate to meet the former specimen requirements.

The processes employed in the fabrication of polycrystalline filaments used in the present study are described in the following sections. Despite the use of different starting materials, as well as somewhat different processes, the microstructure of the composite filaments fabricated in the laboratory was very similar to the microstructure of the commercial filaments.

3.2 *Commercial Filaments*

In the filament extrusion process, developed by CPSS,[184-192] mixtures of 123 and 211 powders, produced by calcination of appropriate ratios of $BaCO_3$, CuO and Y_2O_3 were mixed by milling in cyclohexane using a dispersant. The powder mixture, collected after drying the slurry at room temperature was combined with a proprietary binder and extruded into green filaments with 250 or 300 μm diameter. Specific details about binder removal and sintering procedures are not available. The nominal 211 content and porosity of the filaments were 22.8 wt.% 211 and 30 vol%, respectively. The low density, as well as the microstructure of the sintered polycrystalline filaments suggested that they were sintered at temperatures below 950°C.

3.3 *Development of a Process for the Fabrication of Polycrystalline Precursor Filaments*

A simple extrusion process was developed specifically to fabricate polycrystalline precursors for this study, and was used to fabricate phase pure 123 filaments or composite filaments containing 123 plus 20 wt.% 211. The latter consisted of an inter-dispersion of fine grains of the two component phases. Processing variables and techniques were empirically optimized to reproduce the characteristics and microstructure of the filaments supplied by the commercial vendor.

3.4 *Experimental*

3.4.1 *Selection of Ceramic Powders*

Undesirable amounts of secondary phases and contaminants are usually present in superconducting powders synthesized by repeatedly calcining and grinding mixtures of yttrium oxide, copper oxide and barium carbonate. Contaminants are inevitably introduced in the calcination steps due to the highly reactive nature of most of the oxides of barium in the system Y-Ba-Cu-O, as well as in the milling process, due to wear of the milling media.
Commercial $YBa_2Cu_3O_y$ and 211 powders (*SSC, Inc, Woodinville, WA*) synthesized by a spray pyrolysis process were selected to minimize potential problems associated to chemical impurities, such as reduced T_c. The process used by the fabricant consisted basically in properly mixing the metal ions,

which were in the form of nitrates, with an organic component, whose function was to control the viscosity of the solution. 20 to 50 μm diameter droplets were then produced by atomization of the viscous solution. After drying, the diameter of the droplets decreased to 10 to 20 μm. A cyclone separator then concentrated and directed the dry spherical particles to a tube furnace, where they explode upon ignition, forming 2 μm diameter particles. The resulting particles are composed by an intimate mixture of the yttrium oxide, copper oxide and barium carbonate. These mixtures were rapidly converted to the superconducting 123 phase during calcination. Agglomerates resulting from the calcination process were broken by jet-milling, instead of conventional ball-milling. Because the oxides were mixed in a very fine scale, shorter conversion times were required to synthesize 123. Finer, more homogeneous 123 particles with no secondary phases and lower levels of contaminants were produced by this process.

As-received 123 powder fabricated by the above process had nominal particle size (d_{50}) between 2 and 3 μm and surface area (BET) of 1.30 m^2/g. Examination of the powder in the SEM revealed almost equiaxed particles, with diameters below 5 μm, as shown in Fig. 3.1. Secondary phases or impurities were not detected by X-ray diffraction [Fig. 3.2 (a)]. Splitting of the high-angle peaks was observed after treating the as-received powder at 900°C in air, for 4 h [Fig. 3.2 (b)]. Therefore, the as-received powder was not fully orthorhombic. As-received 211 powders consisted of agglomerates, shaped like hollow spheres and were composed by small, mostly sub-micrometric globular particles (Fig. 3.3). The powders were very fine, with a nominal BET surface area of 1.75 m^2/g.

3.4.2 Selection of Organic Components (Binders, Plasticizers and Solvents)

Experiments with PMMA (poly-methyl metacrylate), PIB (poly-isobutylene) and PVB (poly-vinylbutyral) as binders, and toluene as solvent, indicated that better slurries were formed by the addition of a solution of poly-vinyl butyral (Average molecular weight 36,000, d = 1.083) to the ceramic powders. However, because the rate of evaporation of toluene was faster than desired, it was difficult to prevent the polymer solution from becoming too concentrated during the solvent removal step. For this reason, other solvents were tried. Solutions of PVB in octanol yielded excellent results, due to the

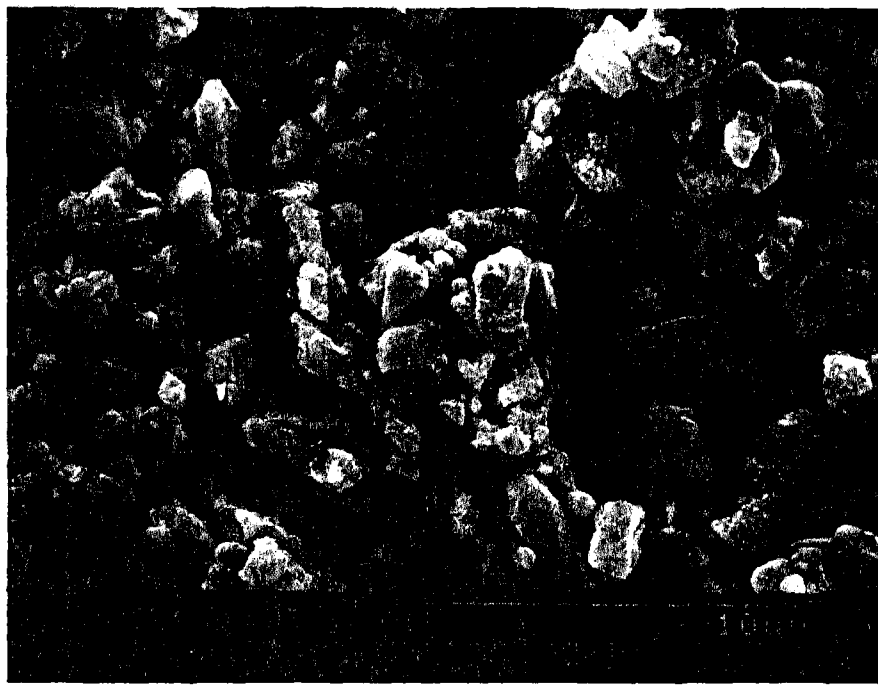

Fig. 3.1. Morphology of 123 particles from as-received type B (SSC) powder.

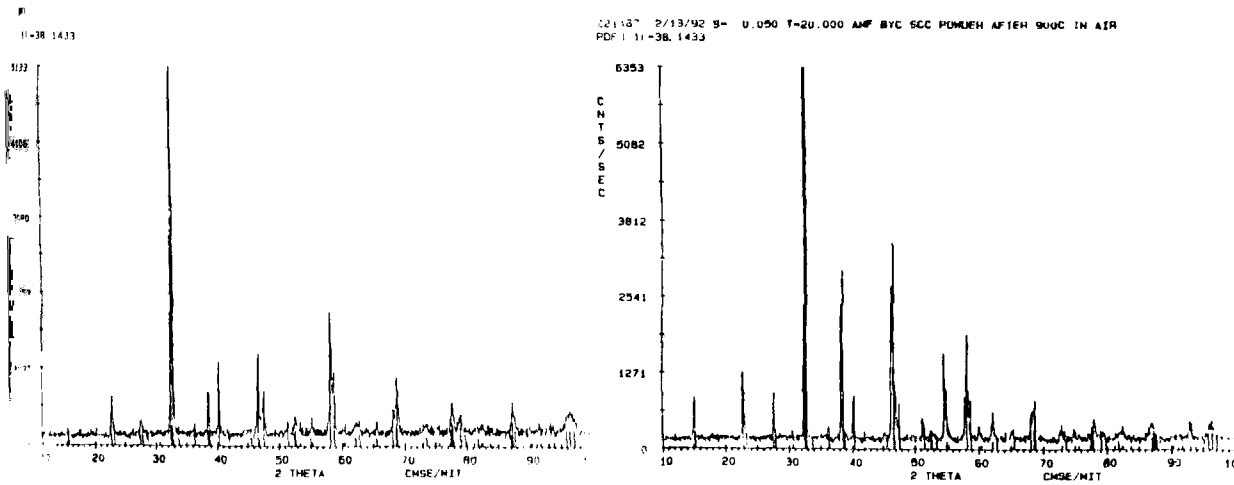

Fig. 3.2. X-ray diffraction patterns of (a) as-received 123 powder, and (b) as-received powder treated at 900°C in air, for 4 h.

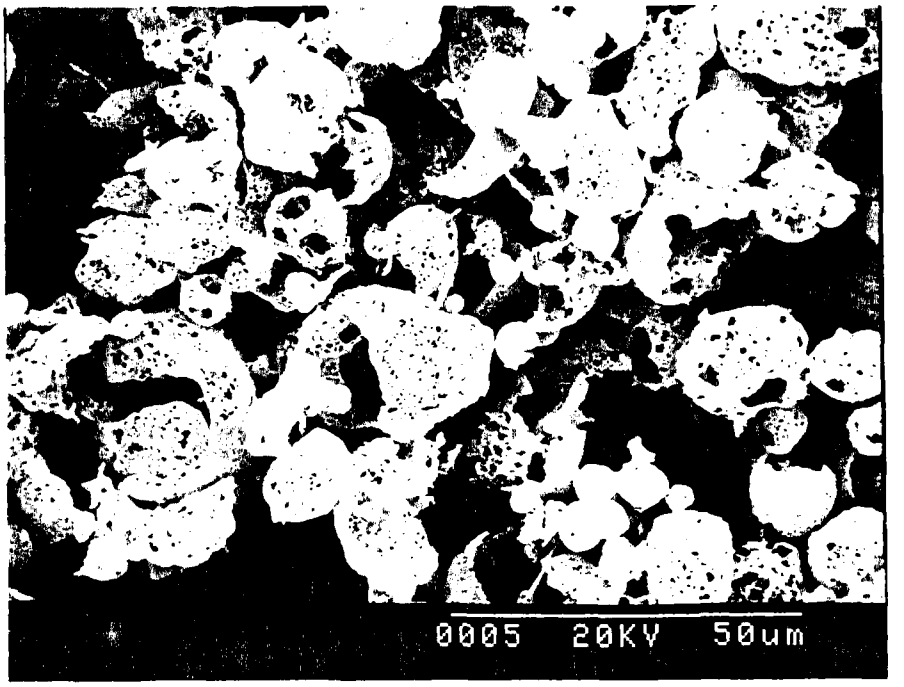

Fig. 3.3. 211 powder morphology (as-received). Spherical shells were formed by the agglomeration of submicrometric, globular 211 particles.

high boiling point (196°C) and also higher viscosity of the latter solvent, when compared to toluene. DBP (Di-butyl phtalate, molecular weight 278.35, m.p. -35 °C, *b.p.* 340°C, d=1.043) was used as a plasticizer, since it is routinely employed to plasticize PVB polymers.

3.4.3 Filament Preparation

123 and 211 powders were weighed in the desired proportions and transferred to an agate mortar. Octanol was added until the powder was completely wetted. Using the pestle, the powders were mixed and grinded in the presence of solvent for about 30 min, to break particle agglomerates. A solution previously prepared by dissolving 2 g of PVB and 1 g of DBP in 12 ml of octanol was then added to the dispersed powders. The correct volume of solution was measured so as to obtain the proper volume fraction of PVB in the mixture PVB plus ceramics (dry basis). By trial and error it was found that a PVB content between 25 and 30 vol.% resulted in fibers with satisfactory

green strength and adequate microstructure after sintering. A very viscous slurry was obtained by adding the polymer solution to the powder slurry. This slurry was then transferred to a pyrex container and the excess solvent was slowly evaporated on a hot-plate to produce a clay-like mixture. The mixture was then extruded to 300 - 400 μm filaments, on top of glass plates. If the wet filaments adhered to the glass plates, the stock mixture was heated again to increase its viscosity by decreasing the solvent content. The glass plates with the wet filaments were placed in a vacuum oven at - 30 mm Hg for 24 h at room-temperature to remove most of the solvent while preventing sagging. The temperature of the oven was then increased to 120 - 150 °C to remove the remaining solvent and increase the green strength of the filaments. Green filaments were placed along grooves formed by placing alumina rods side by side in the bottom of magnesia boat. The boat was then transferred to a high-temperature furnace, where the filaments were sintered in flowing oxygen. The heating schedule consisted of two steps, one for binder burn-out and one for sintering. Binder burn-out was performed by heating slowly at 1°C/min, holding at 300°C for 5 h, heating at 1°C/min to 500°C and holding for 5 h. The sintering step consisted of heating from 500°C at 1°C/min to temperatures between 920-950°C, and holding at the maximum temperature for 10 to 12 hours. After sintering, the filaments were furnace cooled.

3.4.4 *Results*

The process described above yielded straight filaments of phase pure 123 and composite, 123 plus 20 wt.% 211. Filament lengths and diameters varied from 50 to 100 mm and 300 to 400 μm. Relative densities of 70% and 100% were obtained for the composite and phase pure filaments, respectively.

Figs. 3.4, 3.5, and 3.6 show longitudinal sections of commercial filaments and filaments fabricated at M.I.T. by the process described above. The filament of Fig. 3.4 was sintered in air by a modified heating schedule, which consisted in eliminating the 300°C from the above schedule. Relatively large spherical voids formed in the filament after this sintering schedule. It is likely that the binder was burned out too fast, leaving relatively large pores in the microstructure. On sintering, these pores coalesced forming the voids shown in Fig. 3.4. The number of voids was drastically reduced by the

introduction of a 5 h plateau at 300°C, as shown in Fig. 3.6. Dense spots like that indicated in Fig. 3.6 were observed in some filaments. The microstructures of the filaments fabricated for the present work was very similar to the microstructure of the filaments received from the commercial vendor.

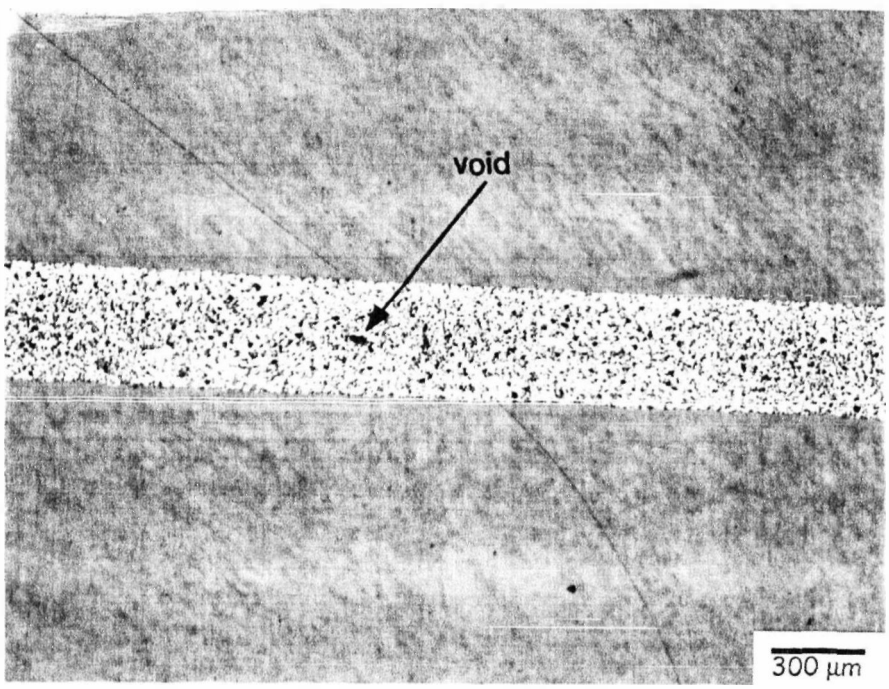

Fig. 3.4 Microstructure of filaments sintered in air following a heating schedule of 500°C for 5 h and 950°C for 10 h, with 1°C/min heating ramps.

Fig. 3.7 shows the longitudinal section of a sintered, phase pure 123 filament. The 123 grains in the phase pure filaments are larger than in the composite filaments by more than one order of magnitude. In the composite filaments, grain growth did not occur, probably because of the presence of small high-temperature phase particles (211) along 123 grain boundaries. The microstructure of phase pure 123 filaments also revealed some degree of grain orientation along the extrusion direction, as shown in Fig. 3.7.

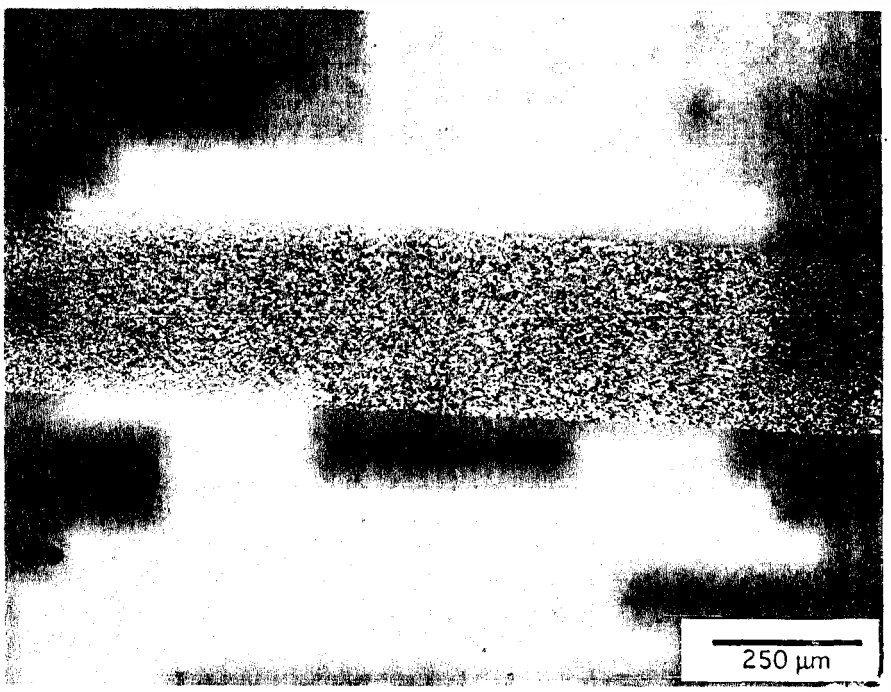

Fig. 3.5 Microstructure of a commercial filament.

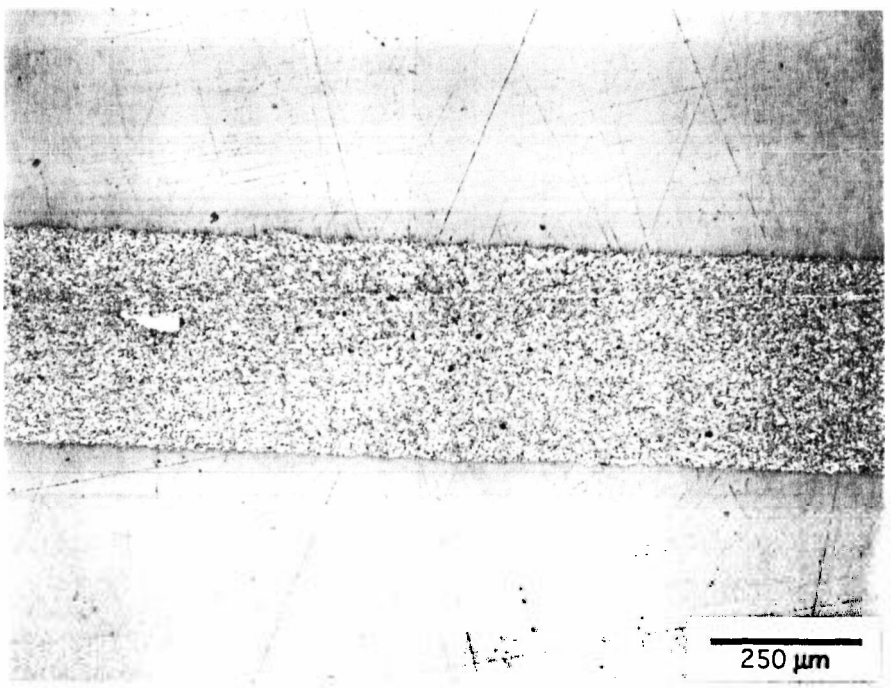

Fig. 3.6 Filament fabricated by the process described in section 3.4.3.

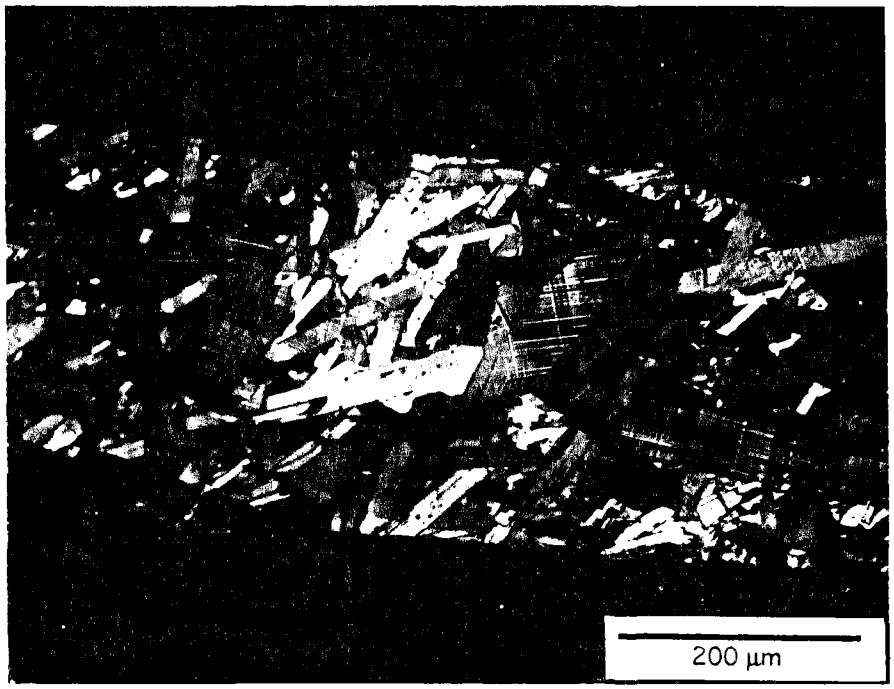

Fig. 3.7. Microstructure of fully dense, phase pure 123 filaments fabricated by the process described in section 3.4.3.

Fig. 3.8. Fracture surface of a filament containing 20 wt.% fabricated by the extrusion process.

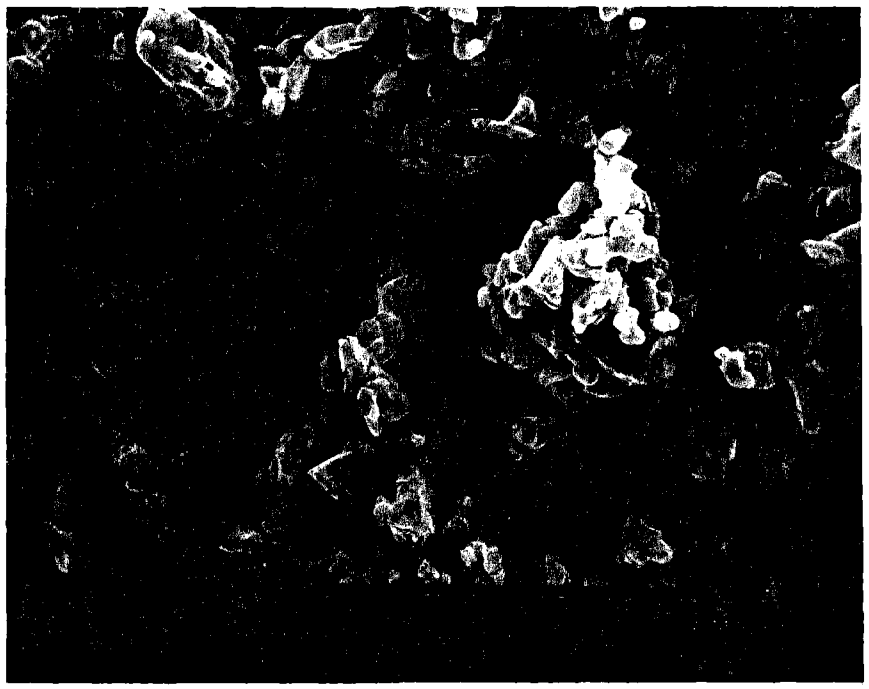

Fig. 3.9. Fracture surface of the commercial filament.

Fracture surfaces are presented in Fig. 3.8 and 3.9, to show that the filaments fabricated in the laboratory were also similar to the commercial filaments with respect to grain size and porosity. The small, globular particles surrounding the larger particles in Fig. 3.8 correspond to the 211 phase. Fig. 3.8 also shows a hollow, spherical agglomerate of 211 particles that survived the filament fabrication process. This problem was corrected in subsequent lots by increasing the mixing time.

3.5 Summary

Superconducting precursor filaments were fabricated by plastic extrusion. Extrudates were prepared by adding octanol-based solutions of a binder (polyvinil butyral), and a plasticizer (di-butyl phtalate) to previously mixed

powder slurries. The optimum binder content was empirically determined to fall between 25 and 30% by volume (dry basis). Full density was only achived in phase pure 123 filaments. The average density of the filaments containing 211 was about 70 %. The microstructure of the filaments prepared by the PVB route was similar to that of the commercial filaments.

Chapter 4
Microstructural Evolution of Semisolid Mixtures Formed by Incongruent Melting of $YBa_2Cu_3O_{6+\delta}$

4.1 Introduction

The objective of this chapter is to call attention to two important phenomena related to the growth of 123 crystals from semisolid melts: particle coarsening and the associated morphological evolution. The experiments reported here were performed with the purpose of gaining qualitative insights, as well as to provide guidance for the design of directional solidification experiments.

The high-temperature phase particles that form at the melting interface during floating-zone growth stay in contact with the liquid phase for a period of time equal to the zone length divided by the growth rate, before they reach the solidification interface and react with the liquid to form the superconducting compound. During their residence time in the zone, the 211 particles increase in size and also undergo morphological changes, because the occurrence of coarsening. Therefore, due consideration has to be given to these phenomena if materials with optimum characteristics and properties are to be fabricated.

Some aspects of particle ripening in concentrated solid-liquid mixtures are presented in the following sections. The effects of volume fraction and convection on the rate constant and the morphological evolution during particle coarsening are also briefly discussed. Experimental observations of microstructural development and evolution in semisolid mixtures of Y_2BaCuO_5 (211) plus liquid, are presented and discussed. The size-scale refinement that results from the addition of platinum to the semisolid 211 + L mixtures is discussed just as an example of possible alternatives that might be used to prevent the undesirable reduction of interfacial 211/L area during directional solidification of 123.

4.2 *Ostwald Ripening in Solid-Liquid Mixtures*

A polydisperse mixture of two phases of nearly equilibrium compositions and volume fractions is not in thermodynamic equilibrium. The energy of the two-phase system will be higher than that for thermodynamic equilibrium because of the presence of a non-zero interfacial energy and the nature of the mixture itself. When one of the phases is fluid, elastic stresses are absent and the system will move towards its thermodynamic equilibrium state by reducing its excess interfacial area. The process of interfacial area reduction is called coarsening or Ostwald ripening when it proceeds by diffusional mass transfer from regions of high interfacial curvature to regions of low interfacial curvature. During the coarsening process, significant morphological changes occur and the average size-scale of the two-phase mixture (or particle size) increases with time.[193]

4.2.1 *Diffusion Controlled Particle Coarsening in Non-zero Volume Fraction Systems*

The classical theory of particle coarsening, commonly known as LSW theory, was laid out by Greenwood,[194] Lifshitz and Slyozov,[195] and Wagner.[196] The LSW theory, developed for the limit $\varphi \to 0$, where φ is the volume fraction of the coarsening phase, was later extended by a number of authors to account for the volume fraction effects on the coarsening kinetics.[198-202] Such theories have been reviewed by Fischmeister and Grimvall,[197] and more recently by Vorhees.[193] They all result in kinetic equations with the same form of that given by the LSW theory. All theories also predict an increase in the rate constant with the volume fraction, but they disagree with respect to the form of the dependence of the rate constant on the volume fraction.

The theoretical work mentioned above and the accumulated experimental evidence support a kinetic equation of the form

$$[\bar{r}(t)]^n - [\bar{r}(0)]^n = K(\varphi,t)t \tag{4.1}$$

were the rate constant, K, is defined as*

$$K(\varphi,T) = \frac{\alpha(\varphi)Dc_i^{\infty}\gamma V_m^2}{RT}, \tag{4.2}$$

where $\alpha(\varphi)$ is a parameter that depends on the volume fraction of the coarsening phase, γ is the interfacial energy, V_m is the molar volume of the coarsening phase, D is the diffusion coefficient, c_i^∞ is the solubility of the rate controlling species in the matrix for an inifinite radius of curvature, R is the gas constant, and T is the temperature.

Considering the case of compound precipitates, examination of eq. (4.2) indicates that the coarsening process is controlled by the component with the smallest product of diffusivity and concentration. This case was analyzed in detail by Bhattacharyya and Russell[203] and by Fischmeister and Grimwall[197] in the dilute limit. These authors argued that, in the case of no mass transfer with the environment, one could retard the coarsening process by introducing an excess of the faster diffusing constituent. This excess depresses the concentration of the slower diffusing species in the matrix and, depending on its magnitude, the coarsening rate could be significantly reduced. Bhattacharyya and Russell considered the case of compound precipitates composed by elements sparingly soluble in the matrix and concluded that a fraction of a weight percent could decrease the rate constant by several orders of magnitude.

Fischmeister and Grimwall also pointed out that the coarsening rate could be reduced by the addition of alloying elements that lower the interfacial energy when adsorbed at the phase boundary between the coarsening phase and the matrix.

4.2.2 Particle Coarsening in the Presence of Convection

Akaiwa, Hardy and Vorhees[204] have studied the effects of convection on Ostwald ripening in Sn-Pb alloys over a wide range of Sn volume fraction. Some of their results are reproduced in Fig. 4.1 to illustrate the combined effects of convection and volume fraction on the rate constant for coarsening. Fig. 4.1 (a) shows the results obtained in the absence of convection. The data for the systems Fe-Cu and Co-Cu was normalized to the data of Pb-Sn at a volume fraction of 0.6. The data of Fig. 4.1 (a) shows that the rate constant increases significantly with volume fraction. The combined effects of convection and volume fraction are shown in Fig. 4.1 (b) for the system Sn-Pb. For solid volume fractions up to 0.6, convection increased the rate constant by a factor between 3 and 4. Above 0.6, skeletal structures developed and convec-

tion had no effect on the rate constant for coarsening. At a volume fraction solid of 0.02, the coarsening exponent changed from its classical value of 3 to 2.7. At intermediate volume fractions the classical value of 1/3 was obtained, in agreement with other reports for concentrated systems.[196-201, 206]

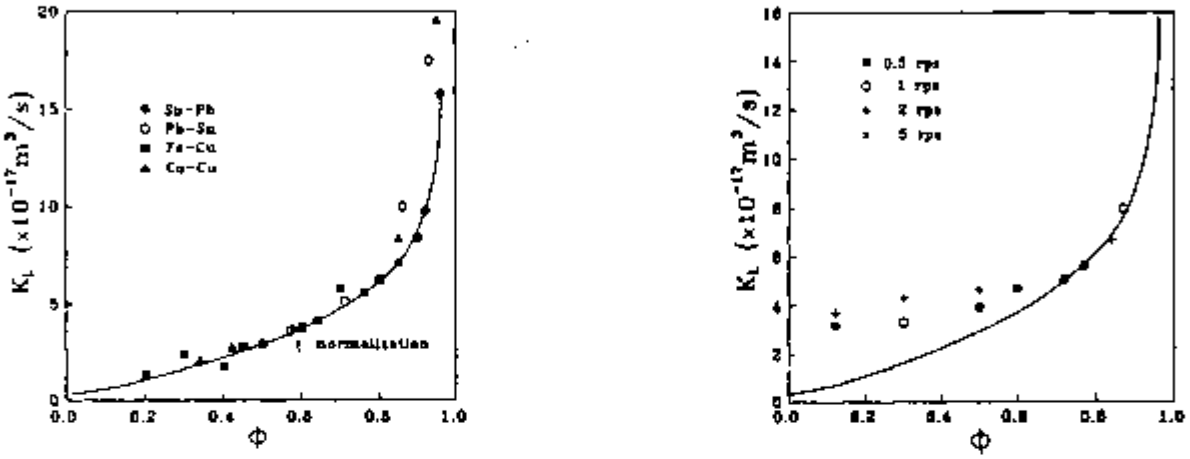

(a) (b)

Fig. 4.1. Coarsening rate constants determined in metallic solid-liquid systems by Akaiwa et al.[204] (a) In the absence of convection. (b) In the presence of convection.

4.2.4 *Morphological Development During Particle Coarsening*

Recent computer simulations of morphological development during Ostwald ripening have been performed by Voorhees *et al.*[206] The authors claimed that particle migration may be induced by strong diffusional interactions at small interparticle separations. They found a correlation between such motion and the spatial distribution of the particles and suggested that particle motion is a generic aspect of the ripening process at high volume fractions of the coarsening phase. Fig. 4.2 (a), from the work of the above authors, shows the calculated normal interfacial velocities for a collection of particles. The direction and magnitude of the interfacial velocities are indicated by lines drawn perpendicular to the interface, inwardly and outwardly, to indicate positive and negative interfacial velocities, respectively. Fig. 4.2 (b) shows morphological changes that occurred in a group of four initial circular particles. The morphological distortion of the larger growing particles was caused by the devel-

opment of flat interfaces in the region between them. Interfacial velocities between the larger particles were nearly zero due to the screening effect caused by the flat interfaces.

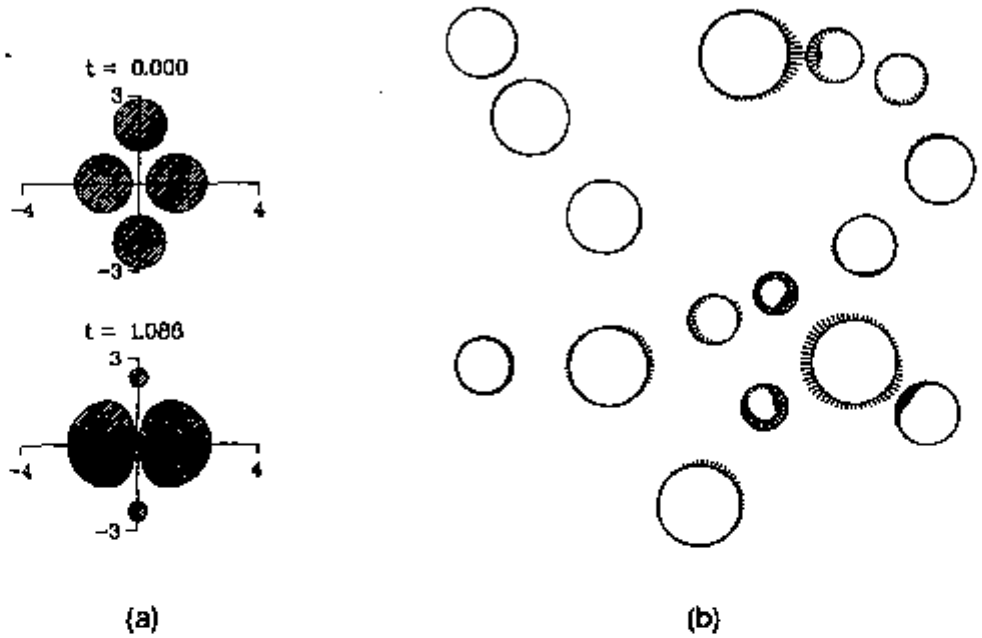

Fig. 4.2. Morphological changes during particle coarsening. (a) Interfacial velocities calculated by Voorhees et al.[206] The figure shows a random spatial distribution of particles at an area fraction of 11%. The lines drawn represent the magnitude and direction of the normal interface velocity. The lines are drawn inwardly when the particle is shrinking and outwardly when the particle is growing. The non-uniform interfacial velocities can result in morphological changes as well as motions of the centers of mass of the particles. (b) Morphological evolution of four circular particles arranged such that the two growing particles are close together. The smaller particles have a dimensionless radius of 0.9 and the larger particles have a dimensionless radius of 1.

4.3Experimental

4.3.1 Sample Preparation

123 powders from two different vendors were used in the sample preparation. Powder A was supplied by CPSS, Inc., Milford, MA, and powder B from SSC, Inc., Woodinville, WA. 2 mm green rods were fabricated by isopressing these powders in isoprene molds at 40,000 psi. Dense polycrystalline samples with elongated, plate-like 123 grains (Fig. 4.3) were obtained after sintering the green rods in flowing oxygen at 950°C for 6 h. Some rods were also prepared by adding 1.1 wt.% Pt (99.9% purity, nominal average particle size 0.38 μm) to

type-A powder. Samples for the experiments were obtained by sectioning 2 mm sintered rods into 3 mm long pieces.

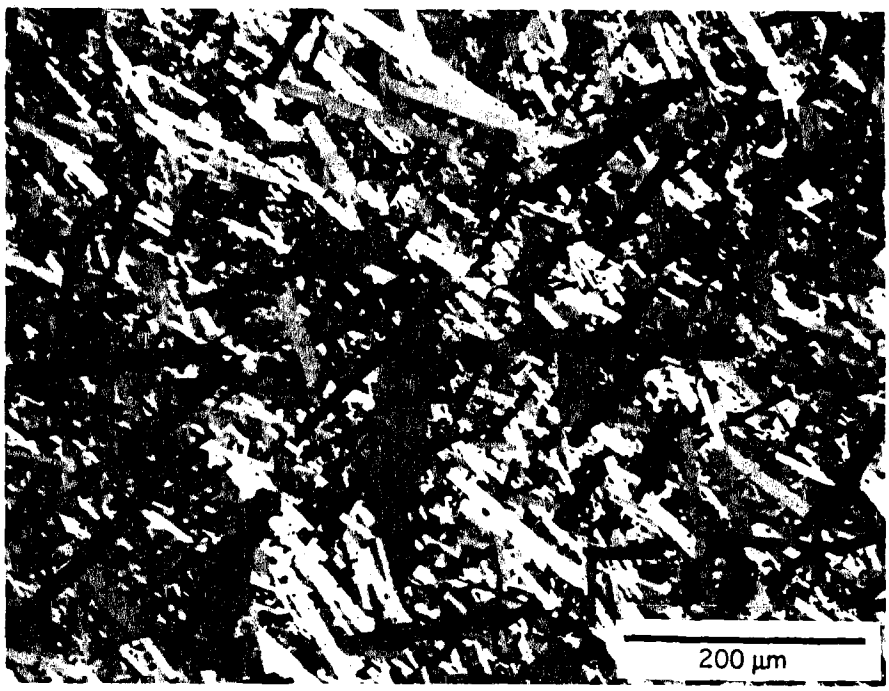

Fig. 4.3. Microstructure of the sintered 123 rods (type B powder) used in the quenching experiments (type-B 123 powder).

4.3.2 *Quenching Experiments*

Small 123 samples were placed inside a platinum basket previously lined with MgO single crystal plates obtained by cleaving MgO single crystal blocks. This was done to prevent direct contact of the samples with the metallic basket. The baskets were attached to the end of a thin thermocouple tube, as close as possible to the thermocouple bead, taking care to avoid contact between thermocouple and sample. The volumes of the thermocouple bead and sample did not differ very much. The whole assembly was then lowered in a vertical furnace maintained at 1094°C. Temperature readings were taken immediately after the introduction of the sample into the furnace. It took about 1 min to equilibrate the sample with the furnace temperature. After holding the samples at the temperature for pre-determined periods of time, they were quickly removed from the furnace, quenched in water, and immediately dried. All samples retained their shape upon incongruent melting,

and were easily detached from the MgO plates. Signs of reaction between the samples and the MgO plates were not detected even after 5 hours at 1094°C.

Quenched samples were cut in two halves. One half was used for metallographic sectioning and the other to extract the Y_2BaCuO_5 particles from the eutectic $BaCuO_2$ - CuO matrix.

4.3.3 *Particle Extraction*

The extraction of 211 particles from the quenched samples was performed in de-ionized water at room-temperature. Quenched samples were placed in a small beaker and ultra-sonicated for about 1 hour. After a few minutes in the ultrasonicator, green clouds started to emanate from the samples, indicating that the 211 particles were being liberated by the disintegration of the eutectic matrix, caused by dissolution of barium cuprate. The extraction process resulted in an aqueous suspension of fine particles of copper oxide (debris) and 211 particles. The 211 particles were collected by filtration for further morphological observation. The filtrate was washed several times to eliminate most of the fine debris (CuO). An alternative and simpler procedure to collect the particles consisted of stirring the suspension and allowing the 211 particles to settle directly on an SEM stub placed in the bottom of the becker.

Metallographic sections were prepared by mounting quenched samples in resin, grinding in oil to avoid corrosion of the eutectic matrix and fine polishing down to 0.25 μm with diamond paste.

4.4 *Microstructural Changes in Solid-Liquid Mixtures Formed by Incongruent Melting of $YBa_2Cu_3O_{6+\delta}$*

4.4.1 *Microstructures of Samples Quenched from the Semisolid State*

Samples quenched from the semisolid state contained cracks but no shrinkage voids. The corrosive action of the quenching medium (water) was limited to a superficial layer less than 100 μm thick.

The structure of the semisolid material which resulted from incongruent melting of 123 was well preserved by quenching, that is, the reaction between the liquid phase and the high-temperature particles to form the superconducting compound was supressed upon cooling. The resulting microstructure is shown in Fig. 4.5, and consisted of rod-like particles of the

high-temperature phase, Y_2BaCuO_5, randomly dispersed in an eutectic matrix of barium cuprate and copper oxide, formed upon the solidification of the liquid phase

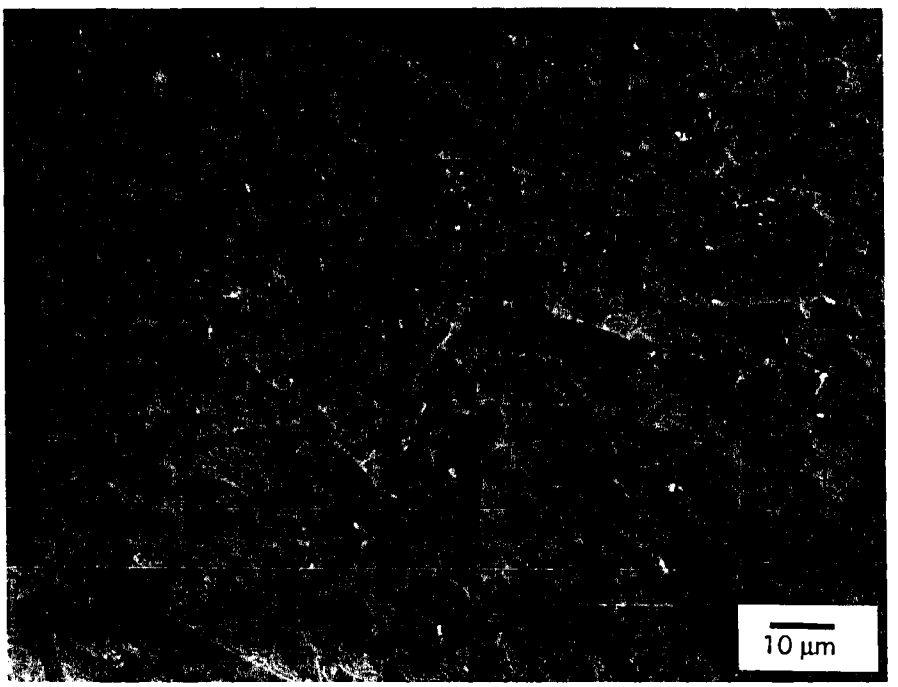

Fig. 4.4. Characteristic microstructure of quenched semisolid mixtures of 211 and liquid.

in the semisolid material. The light gray phase in the eutectic matrix corresponds to copper oxide, which normally appears white when viewed in the optical microscope.

4.4.2 Effect of 123 Precursor History on 211 Particle Size

General observations of quenched samples prepared from powder A and powder B revealed that both the 211 coarsening rate and morphology were influenced by the history of the 123 powder. The differences are shown in the micrographs of Figs. 4.5 and 4.6, which are from quenched samples originated from powder A and powder B, respectively. In both cases, elongated particles were formed upon incongruent melting of 123. However, smaller particles were produced by the decomposition of type A 123 powder.

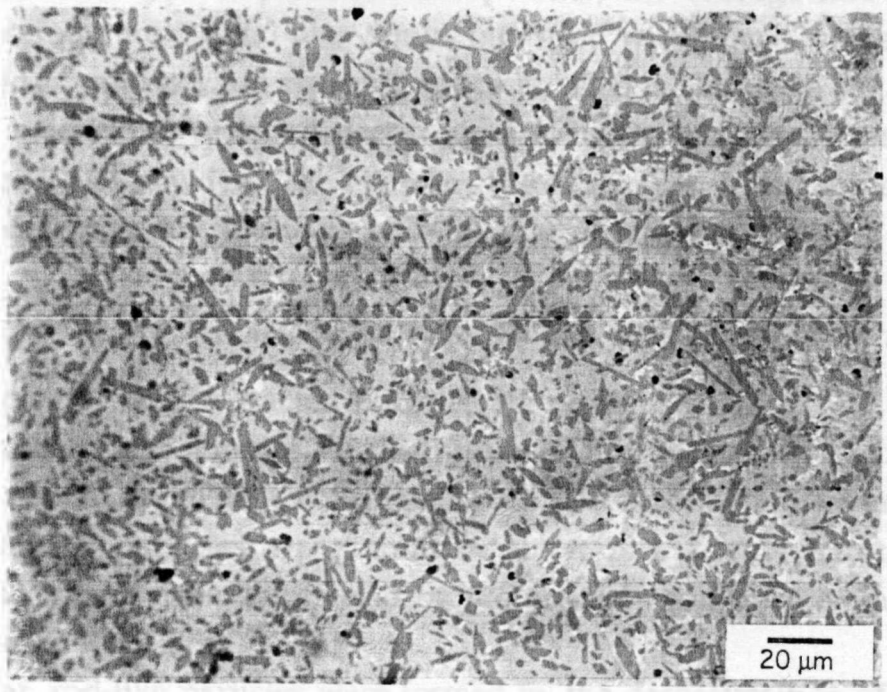

(a) (211 + L) semisolid mixture held at 1094° for 30 min, then quenched in water.

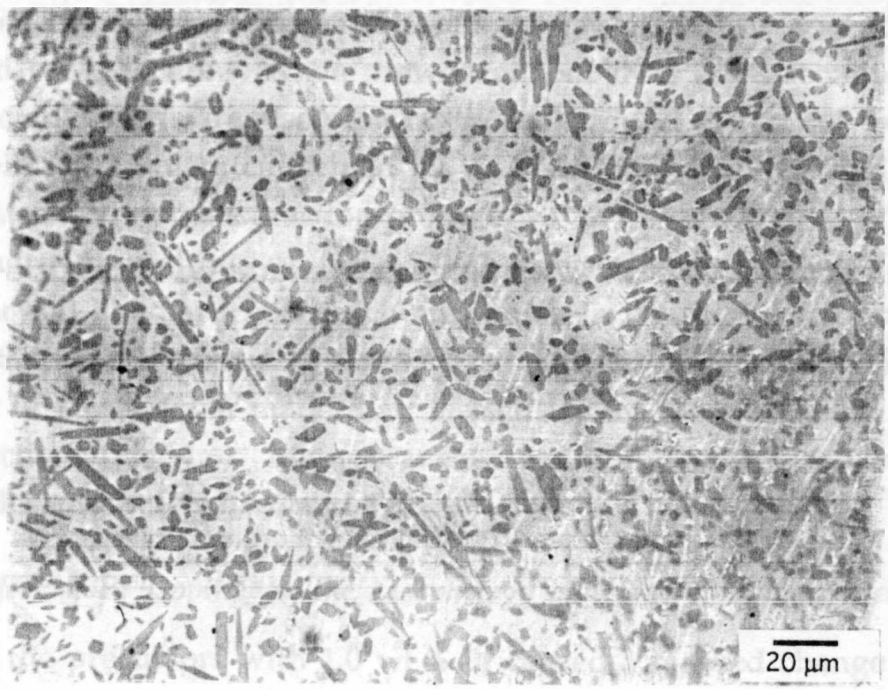

(b) (211 + L) semisolid mixture held at 1094°C for 266 min, then quenched in water.

Fig. 4.5. Microstructures of quenched mixtures of 211 and L produced by incongruent melting of type-A 123 in air.

For the same type of precursor 123 powder, the average size-scale of the two-phase mixture, 211 (s) plus liquid, increased with time, i.e., the particles coarsened by an Ostwald ripening process. This is shown in Fig. 4.5 for the samples made from type-A 123 powder, and in Fig. 4.6 for the samples made from type-B 123 powder. The microstructures also suggested some anisotropy in the coarsening rate, particularly in the case of type-B samples.

4.4.3 *Effect of 123 Precursor History on the Morphology of 211 Particles*

SEM micrographs of extracted particles are presented in Figs. 4.7 and 4.8, for type-A and type-B samples, respectively. Highly faceted 211 particles were formed upon incongruent melting of both precursors. However, when the two kinds of particles were compared, it is evident that the particle morphology was strongly affected by the processing history of the precursor 123 powders.

Regular, rod-like particles were formed by the decomposition of type-A 123 powder, as shown in Figs. 4.5 and 4.7. Higher magnification views, like the one shown in Fig. 4.7 (bottom) revealed that the lateral surface of the particles is formed by a large number of facets, giving an impression of circular or rounded cross-sections, when viewed on polished cross-sections. Eutectic copper oxide debris are also seen in the background of Fig. 4.7 (bottom) with sponge-like agglomerates formed by the reaction of eutectic barium cuprate with water during the extraction process.

Incongruent melting of type B-123 samples also formed faceted, but irregular rod-like particles, which are shown in the SEM micrographs of Fig. 4.8. In this case, the lateral surfaces of the particles were bounded by a smaller number of facets, what made their faceted nature more apparent in polished cross-sections (Fig. 4.6). Many branched and hollow particles were observed in type-B samples (Figs. 4.6 and 4.8).

4.4.4 *Effect of Pt Doping on the Morphology and Size of 211Particles*

Doping the precursors with 1.0 wt.% Pt caused a marked change in both the morphology and size of the 211 particles formed upon incongruent melting of 123. This is shown in Figs. 4.9 (a) and (b), where microstructures of non-dopped and dopped samples are compared. Both samples were prepared from

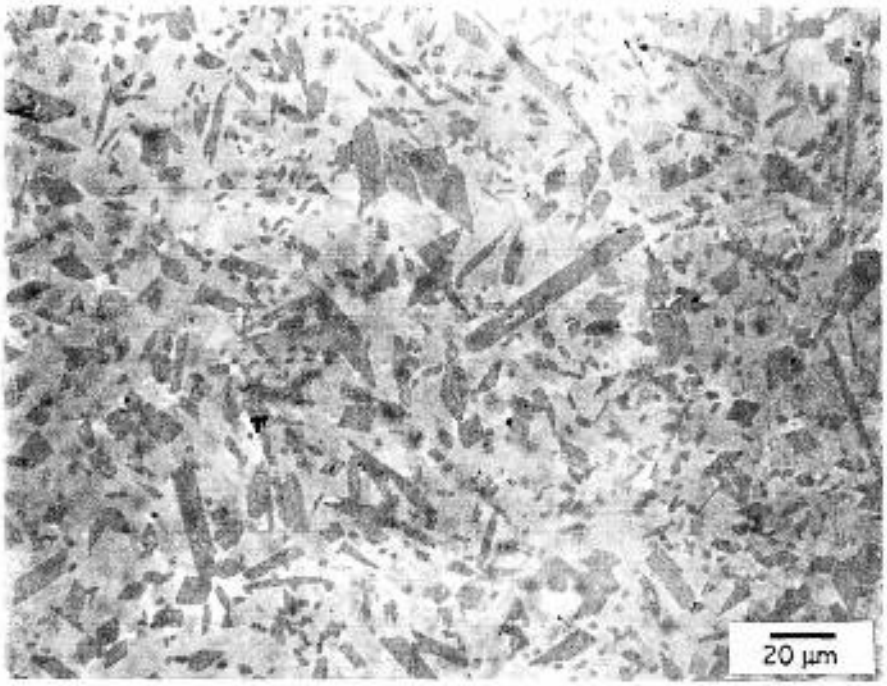

(a) Type B (211 + L) semisolid mixture held at 1094°C for 3 min, then quenched in water.

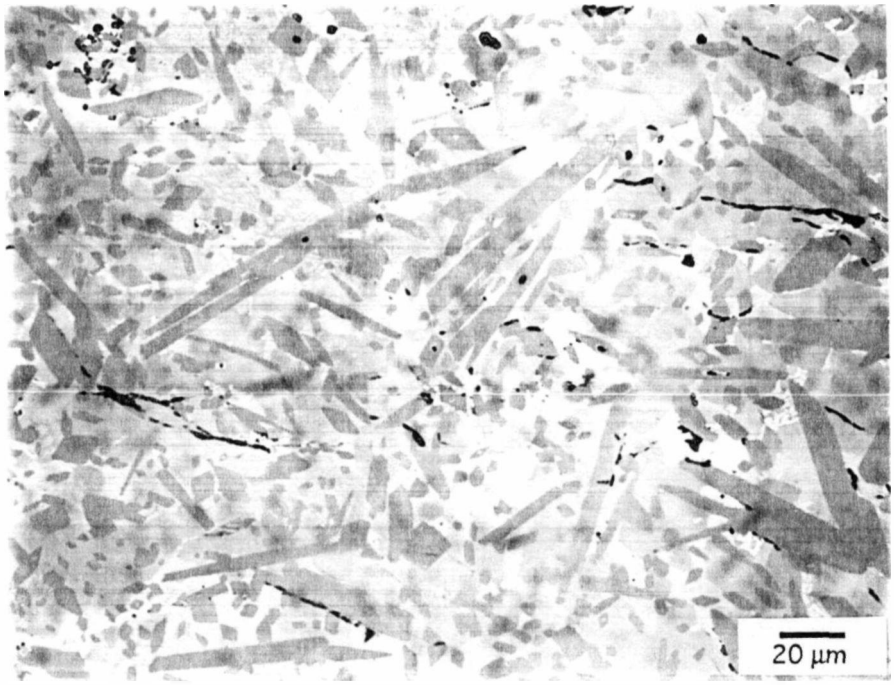

(b) Type B (211 + L) semisolid mixture held at 1094°C for 180 min, then quenched in water.

Fig. 4.6. Microstructures of quenched mixtures of 211 and L produced by incongruent melting of type-B 123 in air. Highly faceted, as well as hollow particles are observed. Comparison with 4.6 shows that larger 211 particles resulted from type-B 123 samples.

Fig. 4.7. SEM micrographs of 211 particles extracted from quenched semisolid mixtures formed by incongruent melting of type A 123 samples. Samples held at 1094°C, in air, for 10 min, and then quenched in water. Particles extracted by ultrasonicating the quenched samples in de-ionized water for 1 h. The faceted nature of the particles is shown with more detail in the bottom micrograph.

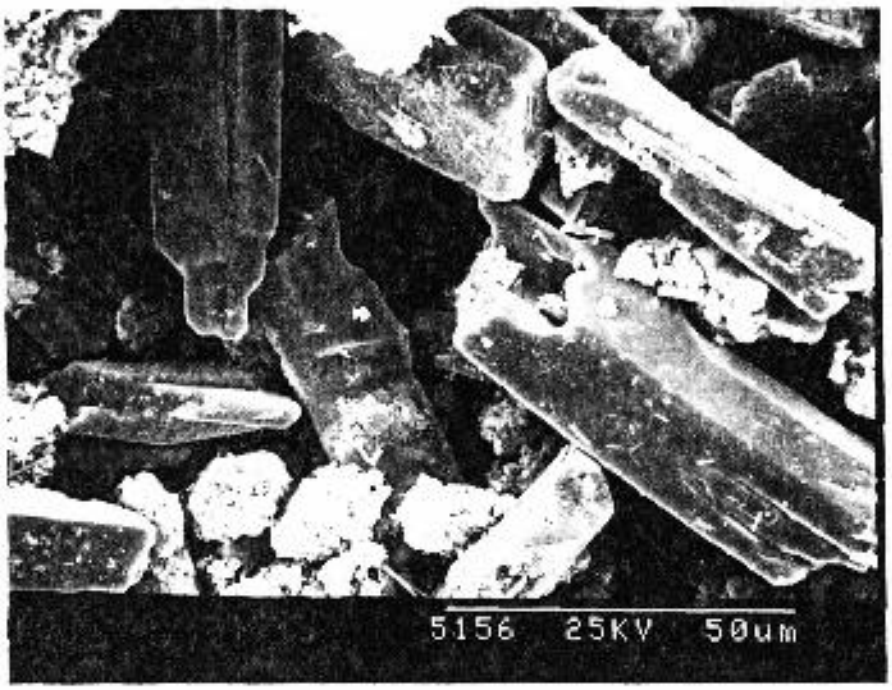

Fig. 4.8. SEM micrographs of 211 particles extracted from quenched semisolid mixtures formed by incongruent melting of type B 123 samples. Sample held at 1094°C, in air, for 30 min, and then quenched in water. Particles extracted by ultrasonicating the quenched sample in de-ionized water for 1 h. The 211 particles were also faceted, but more irregular than the type A particles. Hollow and branched particles were commonly observed in these samples.

type-A 123 powder. Fig. 4.9 suggests that the coarsening kinetics was significantly retarded by the addition of platinum. The dopped sample shown in Fig. 4.9 (bottom) was held at 1094°C for 301 min and still contained finer particles than the non-dopped sample, Fig. 4.9 (top), which was held at 1094°C for 100 min. Close inspection of Fig. 4.9 revealed that the finer size-scale in the platinum-dopped samples was was due to a decrease in the transversal, not longitudinal dimension of the particles.

The morphology of the particles formed upon the decomposition of platinum-dopped samples was very peculiar. Needle-like particles were present in those samples in place of the rod-like particles previously seen in the non-dopped samples. In Fig. 4.10, particles from samples containing no Pt are compared to the needle-like particles that resulted from the addition of Pt to 123. Dopping caused a marked increase in the aspect ratio of the particles, as shown in Fig. 4.10. In addition, the 211 needles from dopped samples did not occur isolated but in clusters, which can be seen in Fig. 4.10 (bottom). Isolated clusters are shown in Fig. 4.11. In these clusters, the needles radiate from what appears to be a common nucleation center.

4.5 Discussion

The syntheses and processing histories of both 123 powders used in this study were discussed in Chapter 3. Powder A (CPSS) was fabricated by repeated calcination and grinding of individual or intermediate component metal oxides. As pointed out in Chapter 3, this process introduces significant levels of contaminants in the superconducting powders, usually at the 1 wt.% level. These contaminants are likely to come from the wear of milling media and, to a lesser extent, from ceramic crucibles used for the calcination steps. Therefore, complex oxides with higher melting points than 123 may be formed by reaction of the contaminants with the later. If it is assumed that the former oxides act as heterogeneous nucleation centers for the precipitation of 211, the size-scale of the semisolid mixture formed upon incongruent melting of 123 should decrease as the level of contamination increases. Because the repeated grinding steps used to synthesize type A powder were eliminated in the synthesis of type B 123 powder by the solution technique, this powder was cleaner. Therefore it is tempting to attribute the coarser size-scale of the semisolid mixture formed upon decomposition of

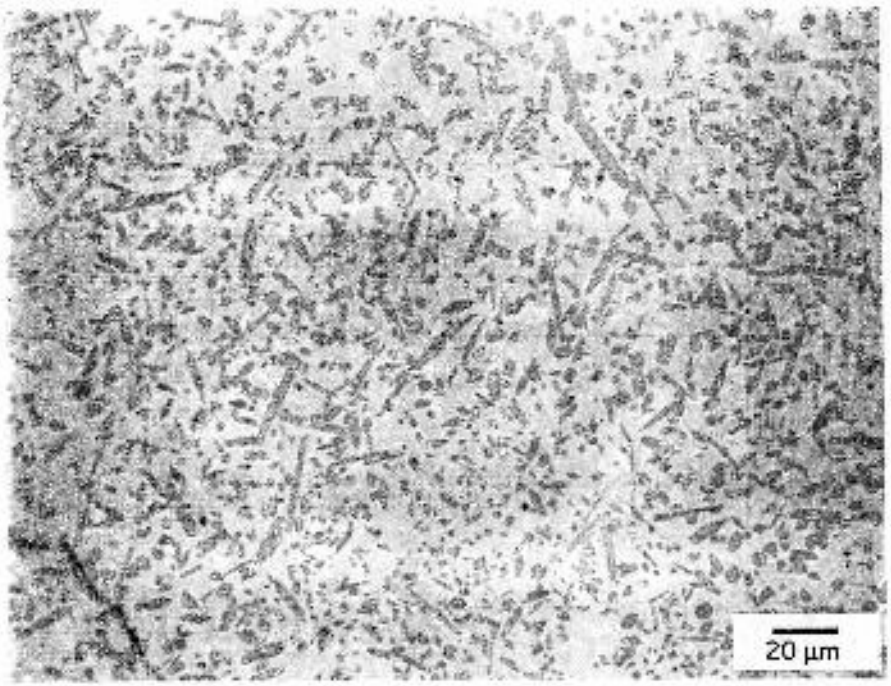

(a) Sample heated at 1094°C for 266 min, then quenched in water. No Pt added.

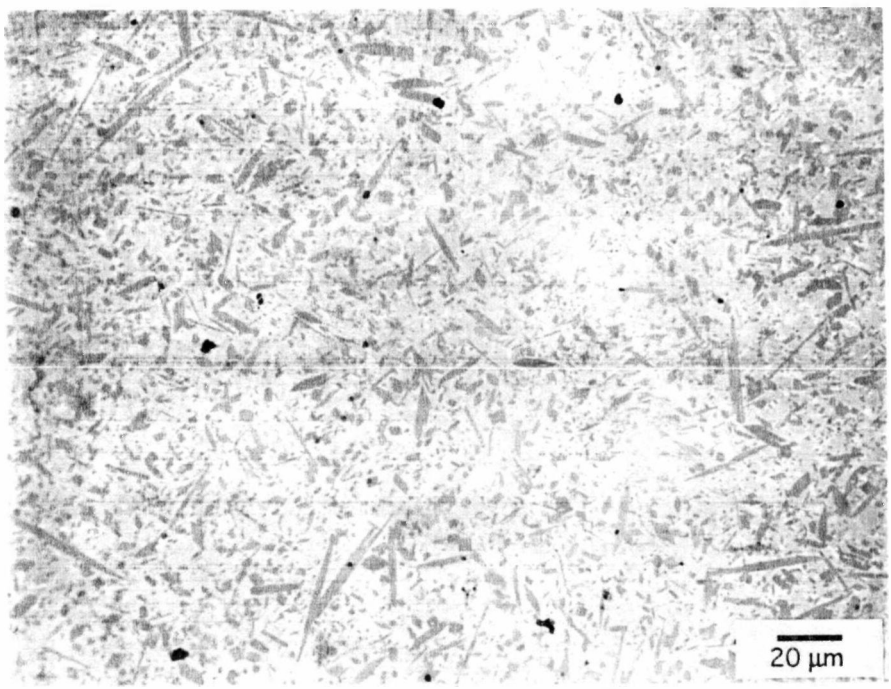

(b) Sample heated at 1094°C for 301 min, then quenched in water. 1.1 wt.% Pt added.

Fig. 4.9. Microstructures of quenched samples originated from type-A powder.

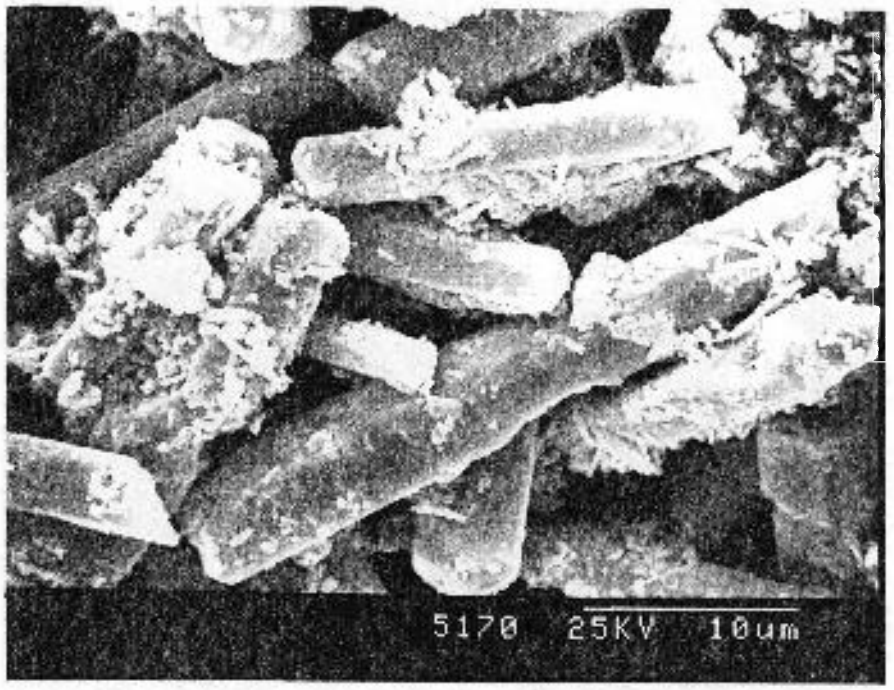

(a) No Pt added

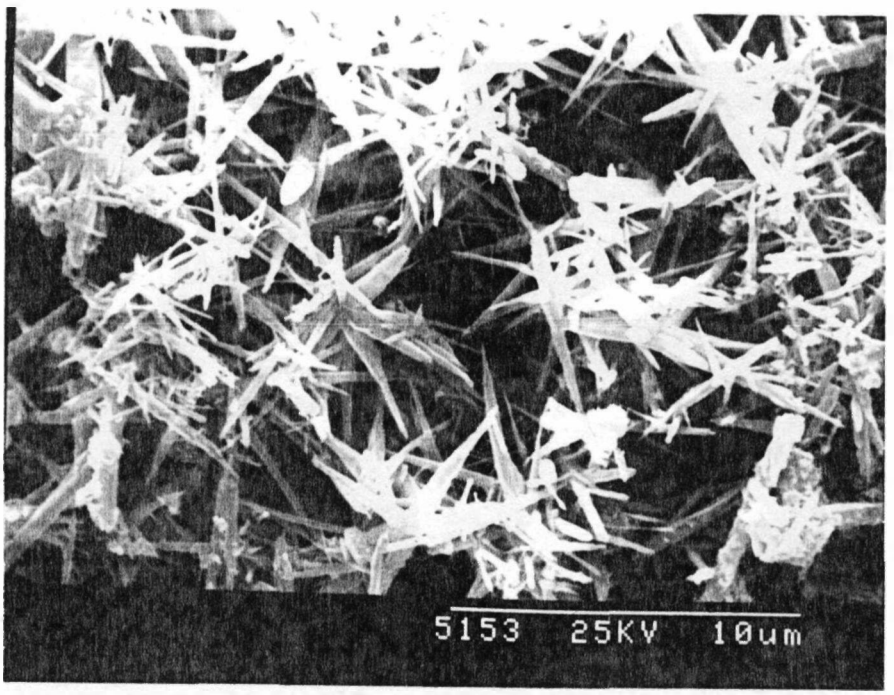

(b)1.1 wt.% Pt added

Fig. 4.10. Effect of Pt on the morphology and size of 211 particles produced by decomposing type-A 123 powder and holding the decomposed mixture at 1094°C for 30 min.

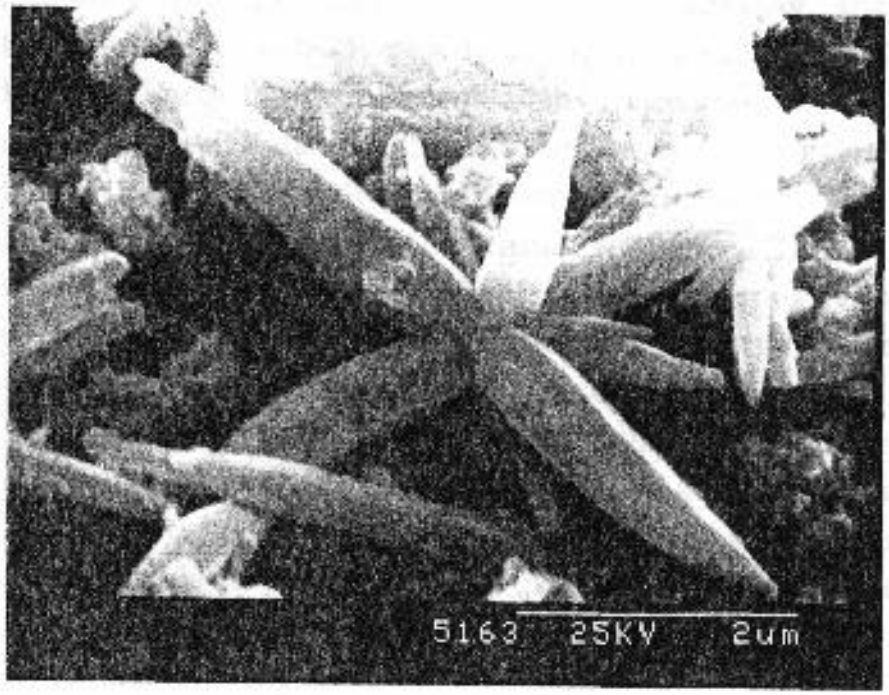

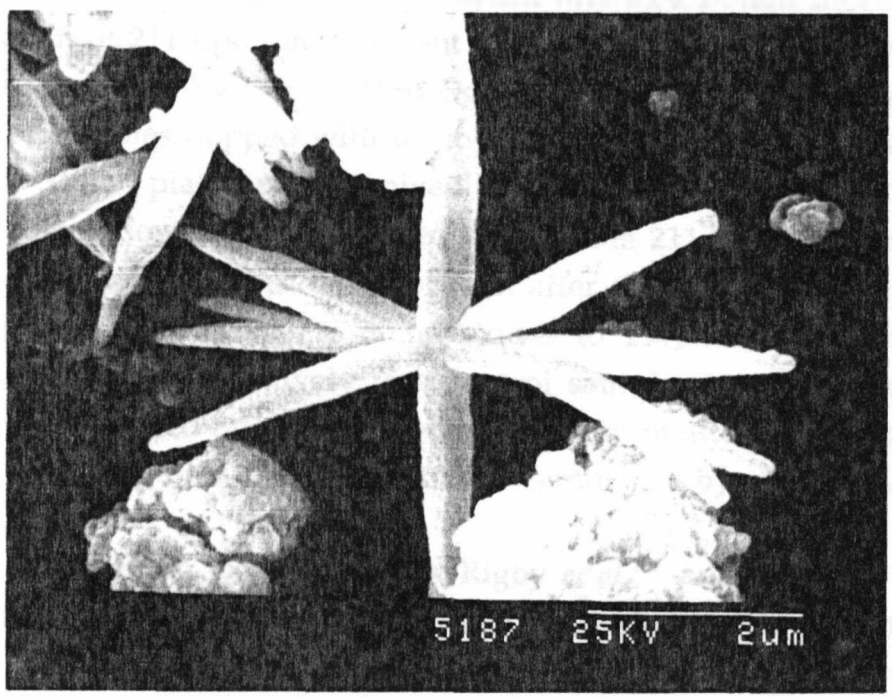

Fig. 4.11. 211 needle formations. These shapes were produced by the decomposition of type-A 123 powder containing 1.1 wt.% Pt.

type-B powder to the lower impurity content or lower density of heteregeneous nucleation centers of the latter. However, analyses of the impurities contained in both powders are not available and without a detailed knowledge of the kind, as well as the concentration of the impurity it is difficult to substantiate the above information. If a certain dissolved impurity has negative activity interaction coefficient its presence in the semisolid melt may also depress the yttrium solubility. This will contribute to increase the coarsening resistance of 211. The coarsening resistance of 211 will also increase if the solid-liquid interfacial energy is decreased by impurities adsorbed at the solid-liquid interface..

The origins of the Pt dopping effects on particle size and morphology are not clear. The star-like shapes formed by assemblages of 211 needles apparently suggest that they all nucleated on a common site, probably composed by some complex oxide of platinum. Such complex oxides have been recently observed in the experiments of Rigby *et al.*,[207] which are similar to those reported here. The association of many nucleation events on the same site with the highly anisotropic growth of 211 could cause the observed needle formations. These star-like shapes were not observed in undoped samples.

Without respect to details about possible mechanisms to explain the resulting morphologies, it is clear that platinum acts as a potent inoculant for the precipitation of 211 upon incongruent melting of 123. This hypothesis is apparently supported by the work of Ogawa et. al.[78] They prepared polycrystalline 211 samples dopped with up to 5.0 wt.% platinum using two different methods. When platinum was mixed with the individual metal oxides prior to their calcination, a marked dependence of the 211 grain size on platinum content was observed. Adding platinum after the calcination step, i.e., after conversion of the individual metal oxides to 211, did not result in any change in grain size relatively to a control sample containing no platinum. Therefore, they ruled out the possibility of platinum altering the grain growth kinetics and concluded that it affected the grain size by enhancing the nucleation of 211 grains.

Recent coarsening experiments by Rigby *et al.*[207] and Izumi *et al.*[208] have indicated that in semisolid melts formed by the peritectic decomposition of 123, the presence of small amounts of platinum did not affect the temporal exponent. In both dopped and "undopped" samples, their experimentally determined exponent agreed with the value of 1/3 predicted by the LSW

theory for zero volume fraction of the coarsening phase, as in the solid-liquid metallic systems.

Similar effects on the 211 particle size have also been obtained by other authors [80,81] through addition of barium stannate to 123.

4.6 Summary and Conclusions

The morphology of Y_2BaCuO_5 (211) particles formed upon incongruent melting of $YBa_2Cu_3O_{6+\delta}$ (123) was investigated in samples prepared by heating sintered 123 samples above the peritectic temperature and quenching the resulting semisolid mixture in water. Sintered samples were prepared from powders sinthesized by two different techniques and containing different levels of contaminants.

The morphology and size of the 211 particles varied in the two powders investigated. The decomposition of 123 in samples prepared with the powder containing lower nominal levels of contaminants resulted in coarser 211 particles.

The addition of 1 wt. % Pt to the precursors resulted in significant morphological changes in the 211 particles formed upon decomposition of 123. In dopped samples, the 211 particles occurred as needles radiating from what appears to be a common nucleation center, forming star-like clusters.

The small addition of platinum demonstrated to be very effective in refining the particle size of 211 in semisolid melts formed by the peritectic decomposition of 123. Platinum was also found to be effective in increasing the coarsening resistance of 211 particles.

Finally, an important conclusion in the context of solidification processing of 123 is that the microstructure of the semisolid melts can be altered through suitable changes in the chemistry of the precursor materials, as well as through additions of foreign phases. However, more thermochemical data concerning the behavior of impurities in the Y-Ba-Cu-O system is needed in order to optimize processing parameters, as well as to further clarify mechanisms.

Chapter 5
Semisolid Solidification of $YBa_2Cu_3O_{6+\delta}$

5.1 Introduction

5.1.1 Objectives

The weak-link electrical behavior in polycrystalline 123 is associated primarily with high-angle grain boundaries. Thus, single-crystal microstructures or microstructures with oriented and continuous grains are desirable for applications requiring large amounts of current. In recent years, a number of directional solidification techniques have been succesfully applied to the production of bulk 123 containing large grains with a preferred orientation.[147-175] Little is known, however, about the kinetic limitations for growth of $YBa_2Cu_3O_{6+\delta}$. The study reported herein was undertaken as an effort to understand the relations between growth parameters and microstructure in directionally solidified 123.

5.1.2 Growth of $YBa_2Cu_3O_{6+\delta}$ Crystals

Flux Growth

Small 123 single crystals can be grown from melts containing low yttrium concentrations, in the presence of convection, by a technique called "flux growth".[127-145] The schematic pseudo-binary phase diagram of Fig. 5.1 indicates that crystals with the approximate composition 123 can be grown from liquid of composition c_{L_p}. This is a simple binary representation of the flux growth method.

Semisolid Solidification

Solidification processing of high-temperature superconductors is complicated by the tendency of ceramic materials to facet during solidification and by incongruent melting of the superconducting compounds. In air, the peritectic reaction which occurs at the $YBa_2Cu_3O_{6+\delta}$ solidification interface can be written more appropriately as:[109]

$$0.437\ Y_3BaCuO_5 + 4.225\ [Y_{0.03}Ba_{0.37}Cu_{0.60}O_{0.872}]_{(l)} + 0.165\ O_2 = YBa_2Cu_3O_{6.2} \qquad (5.1)$$

Thus, solidification of 123 occurs by reaction of a copper-rich liquid with the solid compound Y_2BaCuO_5. Plane front growth of 123 must occur under conditions where the liquid composition at the solidification front is greatly different from the composition of the solidified crystal.

The solidification of binary alloys having a peritectic reaction has been discussed by many authors. Few studies report the implications of the peritectic solidification theory on 123 crystal growth. Fig. 5.1 is a schematic pseudo-binary diagram of the type frequently used to describe phase equilibria for the Y-Ba-Cu-O system in the melting range. The peritectic reaction considered is that at approximately 1015°C

$$\alpha + L = \gamma, \tag{5.2}$$

where approximate compositions of the three terms in Eq. (5.2) are given by α, c_{L_p} and γ. In dendritic solidification, peritectic reactions such as this usually proceed by the γ phase surrounding the primary α phase. Subsequent reaction can then only occur by diffusion through the solid. As a result, the reaction rarely goes to completion.[183,209-210] An exception is the iron carbon system where the high diffusivity of carbon in the solid results in complete transformation during (or after) solidification. Dendritic solidification of ternary alloys involving a peritectic system has also been studied, for example in the Fe-C-X system where one element (carbon) diffuses rapidly and the other slowly,[211,212] and in the Ti-Al-B system where little solid diffusion occurs.[212]

In recent years, a number of studies have been conducted on directional solidification of peritectic alloys with controlled temperature gradient, G, and growth rate, R.[183,210-215] Microstructures obtained at high G/R are of particular interest in alloys that would be two phase, $\alpha + \gamma$, at equilibrium. Several investigators have proposed that at sufficiently high G/R and absence of convection, it should be possible to solidify a hypoperitectic alloy with a plane front directly from a liquid of the same composition. The solid forming would consist of a composite of $\alpha + \gamma$ with the amount of the high temperature solid phase, α, becoming vanishingly small as initial composition approaches the peritectic composition.[183,214,215] The two phases would form directly from the liquid at approximately the peritectic temperature. Recently, Boettinger[213] adpated the Jackson-Hunt[216] analysis of eutectic growth to peritectics and concluded that coupled growth of α and

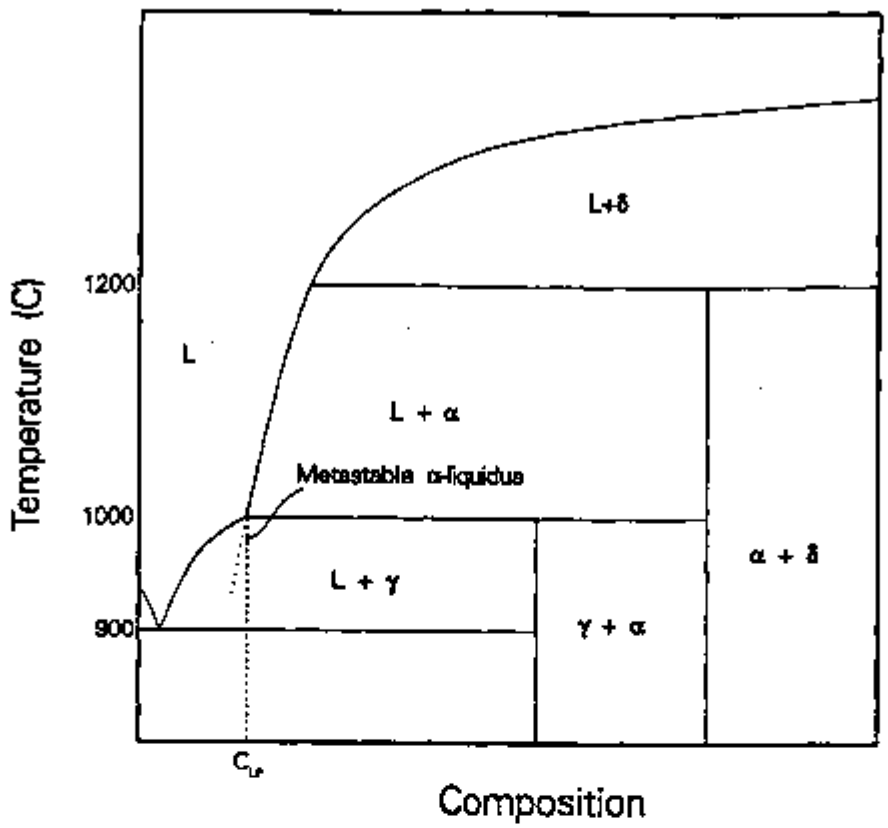

Fig. 5.1. Schematic binary phase diagram containing a peritectic reaction $L + \alpha \rightarrow \gamma$.

γ phases is inherently unstable.[213] Later, Hillert[217] arrived at the same conclusion by using thermodynamic arguments. Boettinger *et al.*[213] and Oliver and Kamad[218] have found banded microstructures in directionally solidified Ti-Al alloys. Their results apparently support Boettinger's conclusion.

In the absence of convection it is found that 123 (γ of Fig. 5.1) can be grown from a semisolid two phase material consisting of α [$Y_2BaCuO_5(s)$] and liquid. It will be shown herein that the mechanism for accomplishing this is quite different from the "surrounding" and solid diffusion mechanism that is commonly observed in metals.

High-temperature superconducting compounds are extremely reactive in the molten state. The floating zone[176] is, therefore, an appropriate technique to study the solidification of these compounds, since no crucible is required. Among all floating zone methods, the most suitable one is the laser-heated floating zone (LHFZ).[219] This technique allows easy control of temperature gradients and growth atmospheres, as well as the establishment of very short

zones in filamentary samples. This is an important advantage, since compositional steady state can then be obtained in a matter of minutes. For these reasons, the LHFZ technique was used in the present study in conjunction with filamentary samples.

Table 5.1. Precursor filaments for the laser-heated floating zone experiments.

Filament Origin	Composition	Diameter (μm)	Density (% TD)
CPSS, Inc.	123 + 7.5 wt.% 211	250 and 300	~77
CPSS, Inc.	123 + 22.8 wt.% 211	250	~70
MIT	123	300 to 400	70 - 100
MIT	123 + 20.0 wt.% 211	300 to 400	~70
MIT	123 + 30.0 wt.% 211	300 to 400	~70

5.2 *Experimental*

5.2.1 *Materials*

Polycrystalline precursor filaments were used as feed materials for the LHFZ process. Filament origin, composition and diameter are given in Table 5.1. Fabrication processes and other filament characteristics are described in detail in chapter 3.

5.2.2 *Laser-Heated Floating Zone Solidification Apparatus*

The laser-heated floating zone (LHFZ) apparatus used in this study is shown in Fig. 5.2. It consists of a 100-W CO_2 laser, two-beam heating optics, and a controlled atmosphere crystal grower with a cold wall chamber, operated at pressures ranging from ~5 Pa to 1.3×10^5 Pa (5×10^{-2} torr to 1.3 atm). The upper and lower pulling heads in the crystal grower can be translated and rotated independently. Usually the specimen is rotated to homogeneize the temperature in the hot zone, but this was not done in this study, since the samples were solidified from partially molten zones with high solid content.

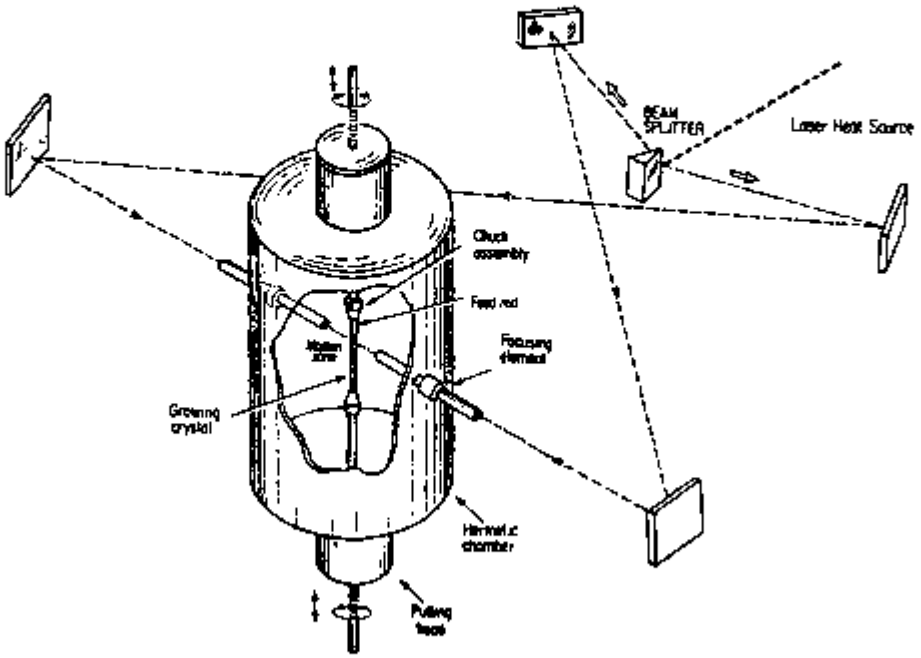

Fig. 5.2. Sketch of the laser-heated floating zone (LHFZ) furnace.

5.2.3 *Solidification Techniques*

Precursor filaments were cut into pieces several centimeters long and mounted in chucks with two axes of rotation and two axes of triangulation. The chuck with the filament was transferred to an aligning device consisting of a vertical rod and a telescope with cross-hairs. The chuck's micrometers were repeatedly adjusted until the vertical axes of both the sample and the supporting rod coincided.

The chucks with aligned filaments were then attached to the upper and lower pulling heads of the crystal grower. The heads were moved towards each other to position the filament tips within the laser focal region. At this point, the chamber was closed, evacuated to about 27 Pa (~200 mtorr) and pressurized with oxygen to 1.27 atm.

Two opposite laser beams (Fig. 5.2) were then focused onto the filament to produce a spot size of 900 or 1500 μm. Typical molten zone lengths of 1 or 2 filament diameters were established in this way. The filaments were pulled

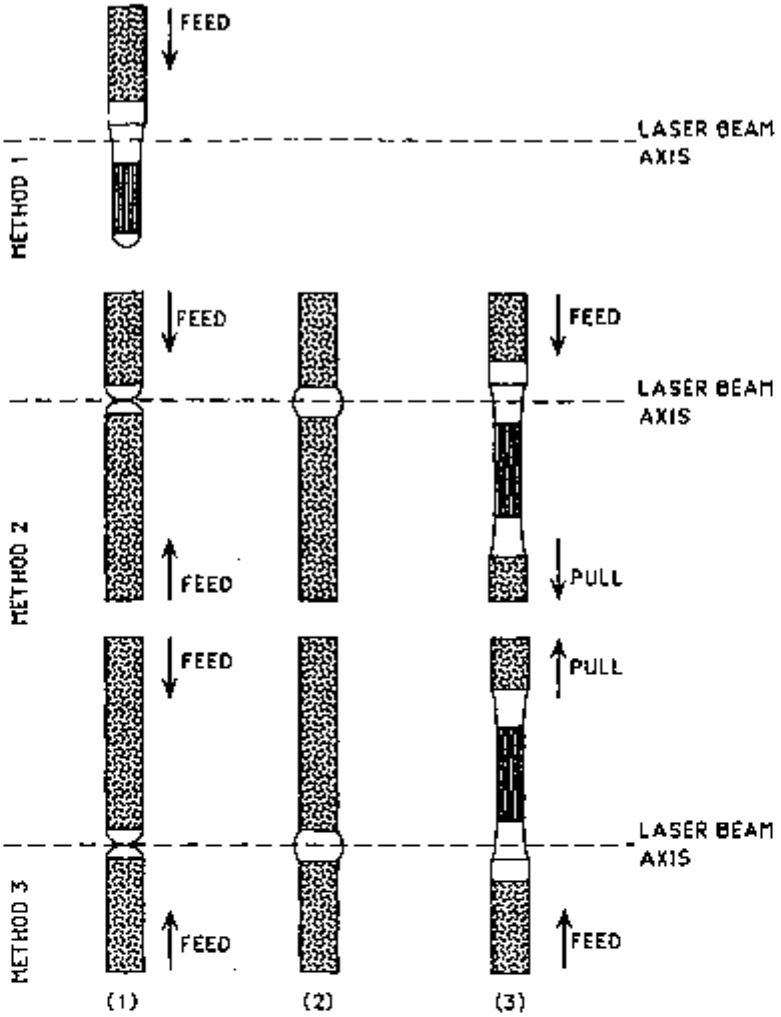

Fig. 5.3. LHFZ techniques used in this work for directional solidification of 123 filaments.

through the hot zone using three different methods (Fig. 5.3). In method 1, Fig. 5.3 (a), the filament was gripped only from above and passed through the hot zone in a downward direction. In methods 2 and 3, the filament was gripped from above and below. The upper and lower heads were slowly moved towards each other until the filament tips were fused in the hot spot. The direction of movement of one of the heads was then immediately reversed. In method 2, Fig. 5.3 (b), the connected segments were moved in the downward direction, and in method 3, Fig. 5.3 (c), the pulling direction was upwards. Small reductions in the diameter of the growing filament could be obtained in methods 2 and 3 by varying the relative translational velocity of the upper and lower chucks.

As soon as the zone became stable, it was scanned with a micropyrometer to locate the maximum temperature position. The pyrometer's target area was estimated to be about 50×50 μm^2. Temperature readings were not corrected for emissivity. The hottest region was always in the center of the semisolid (211 plus liquid) region, unless the sample had not been properly aligned. Maximum temperatures during growth were set in the range 1100 to 1160°C by adjustments of the laser power. Very low laser power was needed because of the small filament cross-section and relatively low melting temperature of $YBa_2Cu_3O_{6+\delta}$. Since the necessary power values, between 1 and 2 W, were in the very bottom of the scale, temperature fluctuations occurred. Better temperature stability was achieved by increasing the primary beam power and placing a chopper in the beam path to obtain the desired power level. The chopper reduced the power to 33% of its nominal value.

Filaments were grown at nominal rates from 1.1 to 13.9 μm/hs (4 to 50 mm/h). After the desired lenght (4 to 5 cm) was obtained, the growth was interrupted by simultaneously closing the beam shutter and stopping the movement of the pulling heads. This essentially quenched and preserved the integrity of the partially molten zone for subsequent metallographic examination. The hot zone became dark within less than a second after closing the beam shutter. This observation suggested that the quenching rate is of the order of 10^3 °C/s. Table 5.2 summarizes the characteristics of most of the runs.

5.2.4 Sample Preparation and Observation

As-grown filaments were segmented in three pieces. The sections containing the quenched semisolid zone and the initial portion to solidify were mounted in resin for metallographic preparation. The length of the piece containing the quenched material varied from a few to about 30 filament diameters. The other segments were about 30 to 50 diameters long. Magnetic and electrical property measurements (chapter 7) were performed on the last portion to solidify, in order to avoid initial compositional transients.

Longitudinal sections were prepared by grinding the mounted samples onto silicon carbide paper or diamond-impregnated metal disk, until their mid-section was exposed. Polishing was performed with diamond paste down to 1/4 μm using metallographic cutting fluid as lubricant. Polished

sections were observed in a conventional optical microscope equiped with polarizing filters and differential interference contrast (Nomarski).

Estimates of temperature gradients were made by measuring the zone length in metallographic sections of quenched filaments. The gradient in the liquid was taken to be the temperature difference between the maximum measured temperature and the peritectic temperature (1000°C) divided by half the zone length. Values around 10^6 °C/m were obtained for all samples.

Intragranular structures were observed by scanning electron microscopy on transversal fracture surfaces of single-grained and multi-grained filaments. Backscattered electron micrographs were employed for measuring the 211 particle size within quenched zones. The SEM was provided with chemical analysis capability (EDAX), which was used for phase identification in metallographic sections. Electron microprobe analysis (Superprobe 733, Jeol USA, Inc., Peabody, MA) was used for phase identification and chemical composition measurements.

5.3 *Results*

5.3.1 Influence of Growth Parameters on the Morphology of Semisolid Zones

The morphological stability of the semisolid zone filaments was observed to depend on temperature, growth rate, growth method, composition, density and microstructure of the precursor. The importance of a stable zone cannot be overstated, since its morphology controls the macroscopic characteristics, the microstructure, and hence the properties of LHFZ grown filaments.

The maximum temperatures used in the present study are much higher than the peritectic temperature of 123. Such high temperatures were necessary to achieve the desired zone length of about 1 diameter. During growth, small (~20 μm) displacements from the axial position may occur due to a number of factors, such as imperfect alignment, vibrations in the crystal grower, fluctuations in growth rate, and longitudinal density variations in the precursor. The power delivered to the sample by the laser beam falls off rapidly if the filament moves out of focus, and may not be sufficient to melt the sample core. This is exemplified by the sample shown in Fig. 5.12 (a). Because of progressive misalignment, the melting and solidification interfaces were about to coincide at the time of quenching. This would have resulted in a single-grained filament with a polycrystalline core.

Table 5.2. Growth parameters, diameter and morphology of LHFZ filaments grown in 1.27 atm O_2.

Sample #	wt.% 211	Growth method[a]	Growth rate (μm/s)	Max. temp. (°C)	Temp. Gradient (°C/μm)	Beam diam. (μm)	Zone Length (μm)	Diameter (μm)		Inter-face type[b]	Number of grains
								Feed	Filament		
061	7.5	3	1.11	1100	1.11	900	180	250	195	a2	4
062	7.5	3	1.11	1150	1.71	900	175	250	150	a3	5
020	22.8	1	1.39	1150	0.90	900	330	300	325	a3	2
009	22.8	1	1.39	1120	1.14	900	210	300	300	a3	3 to 5
010	22.8	1	1.39	1135	1.29	900	210	300	300	a3	3 to 5
023	22.8	1	1.67	1140	2.33	900	120	300	290	a3	2
022	22.8	1	2.22	1150	0.97	900	310	300	290	a2	1
026	22.8	2	2.22	1140	2.33	900	120	300	290	a1	1
080	22.8	3	2.64	1140	1.29	900	216	250	200	a1	1
076	22.8	2	2.64	1125	2.53	900	100	250	210	a1	1
036	22.8	2	2.78	1100	0.49	1500	410	250	200	a1	1
038	22.8	1	2.78	1150	0.55	1500	550	250	220	a3	>10[c]
039	22.8	2	2.78	1150	0.55	1500	550	250	220	a3	10[c]
017	22.8	1	2.78	1140	0.80	900	350	300	240	a3	6[c]
056A	22.8	1	2.78	1115	1.00	900	230	210	203	a1	1
086	30.0	2	2.78	1150	1.08	900	276	461	421	a2	2[e]
139	20.0	2	2.78	1135	1.11	900	243	295	230	a2	2[e]
056D	22.8	1	2.78	1150	1.11	900	269	256	190	a1	1
085	20.0	2	2.78	1150	1.13	900	263	474	408	a1	1
121[d]	20.0	2	2.78	1150	1.17	900	256	354	308	a1	1
091	20.0	2	2.78	1145	1.22	900	236	269	197	a1	1
138	20.0	2	2.78	1140	1.25	900	223	374	321	a2	2[e]
012	22.8	1	2.78	1140	1.27	900	220	300	280	a2	1
029	22.8	2	2.78	1140	1.27	900	220	300	260	a2	1
136	20.0	2	2.78	1145	1.40	900	164	393	328	a2	2[e]
130	20.0	2	2.78	1140	1.42	900	197	400	308	a1	1
129	20.0	2	2.78	1115	1.52	900	151	295	256	a2	2
033	22.8	2	2.78	1150	1.88	900	160	300	280	a2	1
077	22.8	2	2.78	1120	2.01	900	118	224	211	a1	1
134	20.0	2	3.11	1120	1.40	900	170	393	302	a2	2[e]
083	0.0	2	2.78	1050	0.42	900	236	367	262	b1	X
019	22.8	2	3.33	1150	0.86	900	350	300	300	b1	X
048	22.8	2	3.33	1150	1.36	900	210	250	180	b2	X
039	22.8	2	4.17	1150	0.66	1500	550	250	220	b2	X
014	22.8	1	4.17	1140	1.08	900	260	300	300	b2	X
015	22.8	1	4.17	1140	1.12	900	270	300	280	b2	X
042	22.8	3	5.00	1150	1.20	900	250	300	225	b2	X
043	22.8	3	5.56	1150	0.91	900	330	300	225	b2	X
013	22.8	1	5.56	1150	1.03	900	290	300	300	b2	X
044	22.8	3	6.94	1150	1.00	900	300	300	230	b2	X
051	22.8	2	8.33	1150	0.86	900	350	250	175	b2	X
054	22.8	2	13.89	1150	1.05	900	285	225	155	d	

(a) Growth Method: See text for explanation.
(b) See Fig. 5.11 for explanation.
(c) Non-steady state (short filament).
(d) 210 + 012 precursor (feed).
(e) 2 grains parallel to the growth direction.
(X) Textured, polycrystalline sample.

At growth rates rates below 1.4 μm/s (5 mm/h), poor quality filaments were obtained because of extensive liquid migration down the temperature gradient and in the direction of the precursor. This problem became more severe in compositions containing less 211. An extreme case of liquid migration is typified by the quenched sample shown in Fig. 5.4, which contained 7.5 wt.% 211, and was grown at 1.1 μm/s at a relatively low temperature of 1100°C. The upper portion of the micrograph corresponds to the quenched semisolid zone and the lower portion to the growing crystal. In that sample, pronounced liquid migration caused the formation of a large crown on top of the zone, which was also very irregular. Such a zone morphology led to the growth of an irregular crystal with a very poor microstructure, composed of large and blocky 211 particles dispersed in the 123 grains. Lower temperatures and higher growth rates were necessary to counteract the deleterious effects of liquid migration. Fig. 5.15 (b) shows that stable zones could be obtained in phase pure 123 samples by reducing the temperature to 1050°C and increasing the growth rate to 2.78 μm/s (10 mm/h). However, these conditions led to cellular, instead of planar front growth, which is the desired morphology.

Increasing the volume fraction of 211 in the precursor to values between 20 and 30 wt.% resulted in the stabilization of the semisolid zone at growth rates above 1.4 μm/s and temperatures as high as 1160°C. This is shown in Fig. 5.5 for a filament containing 30 wt.% 211. Three different interfaces are visible in the filament of Fig. 5.5, as one moves from the top to the bottom of the micrograph. The first interface separates the precursor (darker region) from the hot zone. Below this interface, intergranular liquid coexists with 123 and 211 grains. At the second interface, the semisolid zone is formed by the incongruent melting of 123 to 211 plus liquid. The third interface is the solidification interface, where 123 is formed by the peritectic reaction of 211 and liquid.

A close view of the fully dense region which precedes the semisolid zone, is shown in Fig. 5.6. Fig. 5.6 (a) and (b) are from samples containing 30 and 22.8 wt.% 211, respectively. Optical microscopy and SEM revealed that this region was composed by fine grains of 123 and 211 plus an intergranular liquid, determined to be rich in copper by EDAX. The amount of intergranular liquid in this region was very small for the 30 wt% composition [Fig. 5.6 (a)] compared to the 22.8 wt.% composition [Fig. 5.6 (b)]. Fig. 5.6 shows

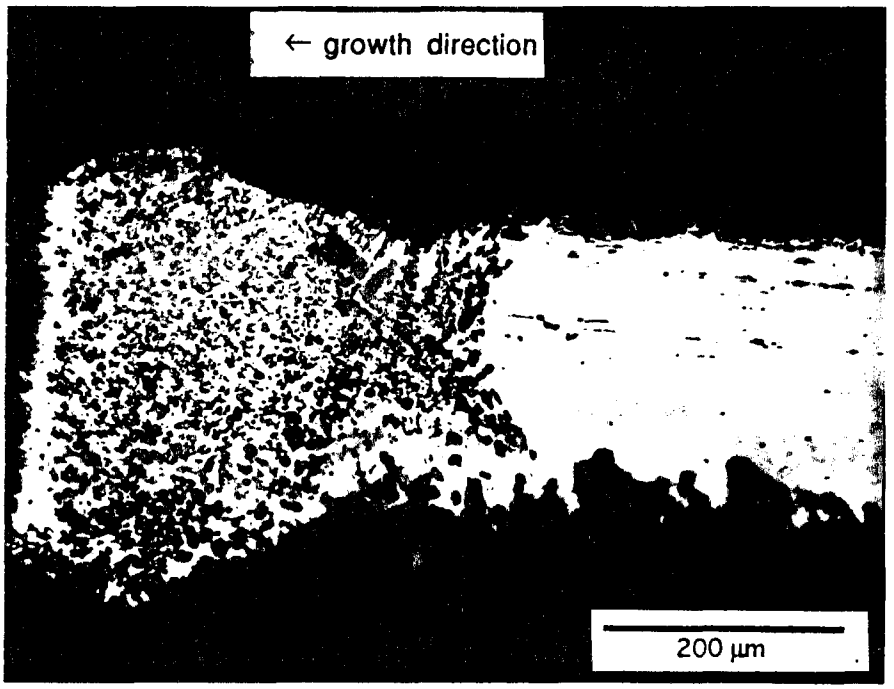

Fig. 5.4. Quenched zone of a filament containing 7.5 wt.% 211. R = 1.1 μm/s; T = 1100°C; P_{O_2} = 1.27 atm. Under these growth conditions, the amount of 211 in the sample was insufficient to hold the liquid within the zone by capillarity, preventing its migration towards the precursor. This resulted in poor microstructures, as shown. Sample 061. Ordinary light.

the presence of white spots inside the zone. These spots are rich in copper, as determined by EDAX and EPMA, and were present in most of the LHFZ samples. The foregoing observations point to significant variations in the chemical composition of the semisolid material inside the zone.

Longitudinal composition profiles were measured by EPMA across quenched semisolid zones, using incremental steps of 20 or 30 μm and a probe diameter of 30 μm (at 15 kV), to assure that average compositions were measured at each point. Scans were run within a single grain, near the axis of the filaments.

The resulting scans and optical micrographs of the samples from which they were originated are shown in Figs. 5.7 (a) and 5.12 (d); 5.7 (b) and 5.12 (c); 5.8 and 5.13 (b). All samples were quenched during steady state growth. In Figs. 5.7 and 5.8, the initial and final plateaus correspond to points in the precursor and in the solidified material, respectively. Measurements between these two plateaus correspond to the semisolid material. The measured

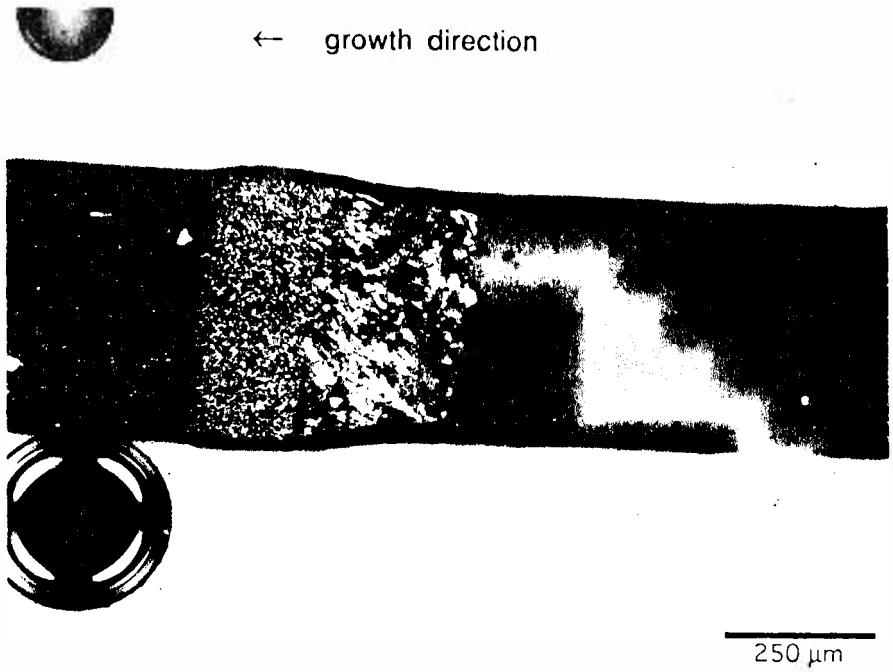

Fig. 5.5. Longitudinal section across the quenched zone of a sample containing 30 wt. % 211. R = 2.78 μm/s; T = 1150°C; P_{O_2} = 1.27 atm. This sample shows the stabilizing effect of higher 211 content in the semisolid zone. Dark spots in the growing grains are precursor voids that survived the passage of the semisolid zone. The microstructure of the region indicated by the arrow is shown in Fig. 5.6 (a).

average compositions of both the precursor and the solidified material were in good agreement with the nominal composition of the polycrystalline filaments, indicated in the plots by horizontal dashed lines.

Figs. 5.7 and 5.8 show that the distribution coefficient is less than 1 for CuO, greater than 1 for BaO and slightly less than 1 for Y_2O_3. Thus, copper oxide is rejected into the zone at the solidification interface. As the semisolid zone travels along the filament, the copper-rich liquid infiltrates into the precursor, forming the bulged, intermediate region described above. Within that region, 123 coexists with 211 and the liquid rich in copper. The average compositions measured in the bulged region are consistent with liquid contents of 40 to 45 vol%. Such concentrations are larger than the porosity of the precursor by 10 to 15 vol%. This is so, because the liquid content in the bulged region can be increased by the reaction of 123 with Ba-Cu oxides at the precursor/zone interface (Table 2.2, reaction e1). The existence of plateaus in the profiles of yttrium, barium and copper was taken as evidence that the other invariant reactions described in Table 2.2 also occurred in the semisolid

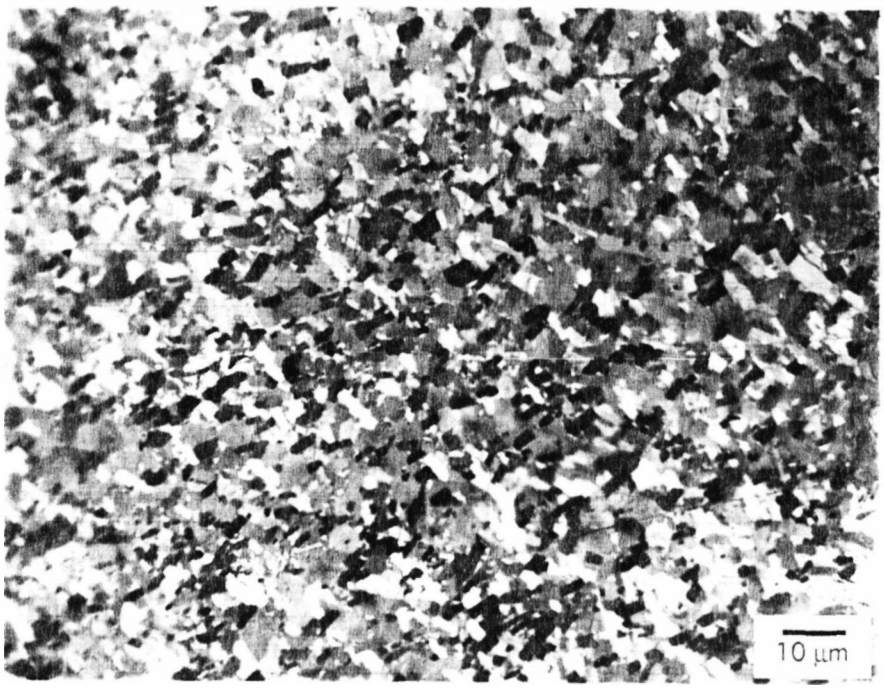

(a)

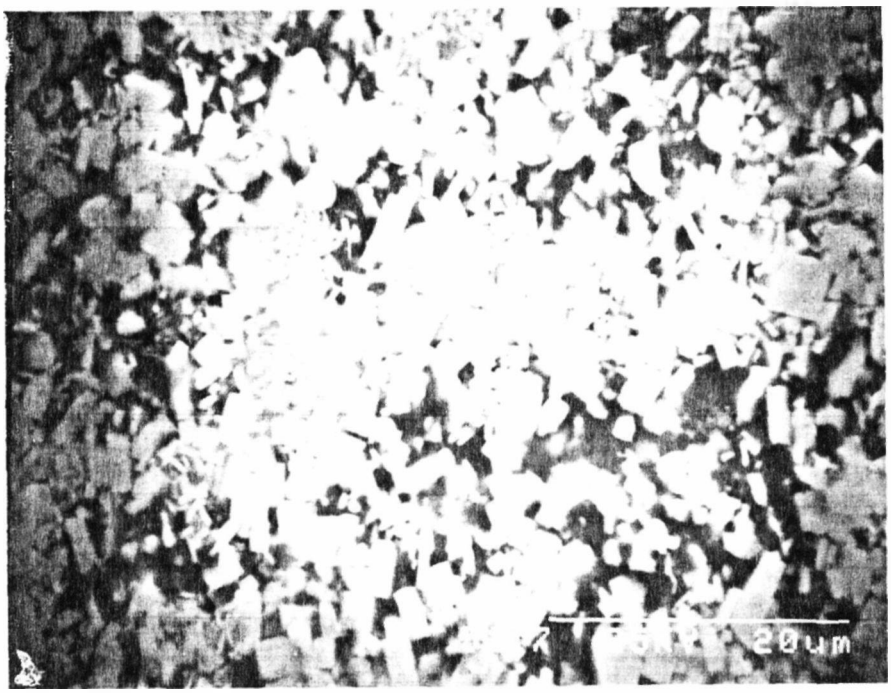

(b)

Fig. 5.6. Microstructures of the material located between the precursor and the semisolid zone: (a) is from sample 086, which contained 30 wt.% 211 (optical) and (b) is from sample 039 which contained 22.8 wt.% 211 (backscattered SEM image). The small 211 grains can be easily distinguished from the larger, blocky 123 grains in (b). The small amount of liquid in (a) actually promoted liquid-phase sintering. In (b) the liquid concentration was large enough to form a semisolid material.

material before solidification of 123 took place. Therefore, it is likely that minor amounts of other solid phases, like $Y_2Cu_2O_5$ and Y_2O_3 coexist with 211 and liquid in the semisolid zone. Figs. 5.7 (a) shows that at positions where the temperature was above 1100°C, singularities occurred in the copper and yttrium profiles, but the barium concentration remained virtually unchanged. Indeed, in this temperature range, table 2.2 list two invariant reactions that do not involve barium, namely e4 and m3.

Figs. 5.7 (a) and 5.7 (b) are for samples of same composition (22.8 wt.% 211), grown under similar conditions, except that the sample of Fig. 5.7 (b) was pulled in the upward direction (method 3). Comparison of both figures reveals that the concentration profiles within the semisolid material varied with the pulling direction. The copper and yttrium profiles levelled off to lower values when the growth direction was reversed. When the filament is pulled upwards, segregation of copper oxide occurs at the top of the zone. Since CuO (Cu_2O) is the densest material in the zone, it will tend to sink as it is segregated at the solidification interface. The downward flow of copper oxide will result in a more homogeneous semisolid material, as indeed observed.

Fig. 5.8 shows that when the maximum temperature in the zone was reduced to 1115°C, the quenched zone contained less barium and more copper than the zones from samples grown at higher temperatures. The composition profiles of Fig. 5.8 resulted in the solidification of a sample with a large density of copper oxide inclusions, as shown in Fig. 5.24 (c). Further reductions in the maximum temperature caused the profiles to level off again and the disappearance of the copper oxide inclusions.

The bulged polycrystalline region described above did not form when fully dense precursors were used in the LHFZ growth of 123 . This is shown in Fig. 5.9. In the micrograph of Fig. 5.9, the upper, intermediate and lower regions correspond to the polycrystalline precursor, the quenched semisolid zone and the 123 crystal, respectively. The fully dense precursor was obtained by melting and solidifying a porous polycrystalline filament at a relatively high growth rate of 6.94 μm/s (25 mm/h). The resulting zone morphology is similar to that obtained in LHFZ growth of oxides that melt congruently.

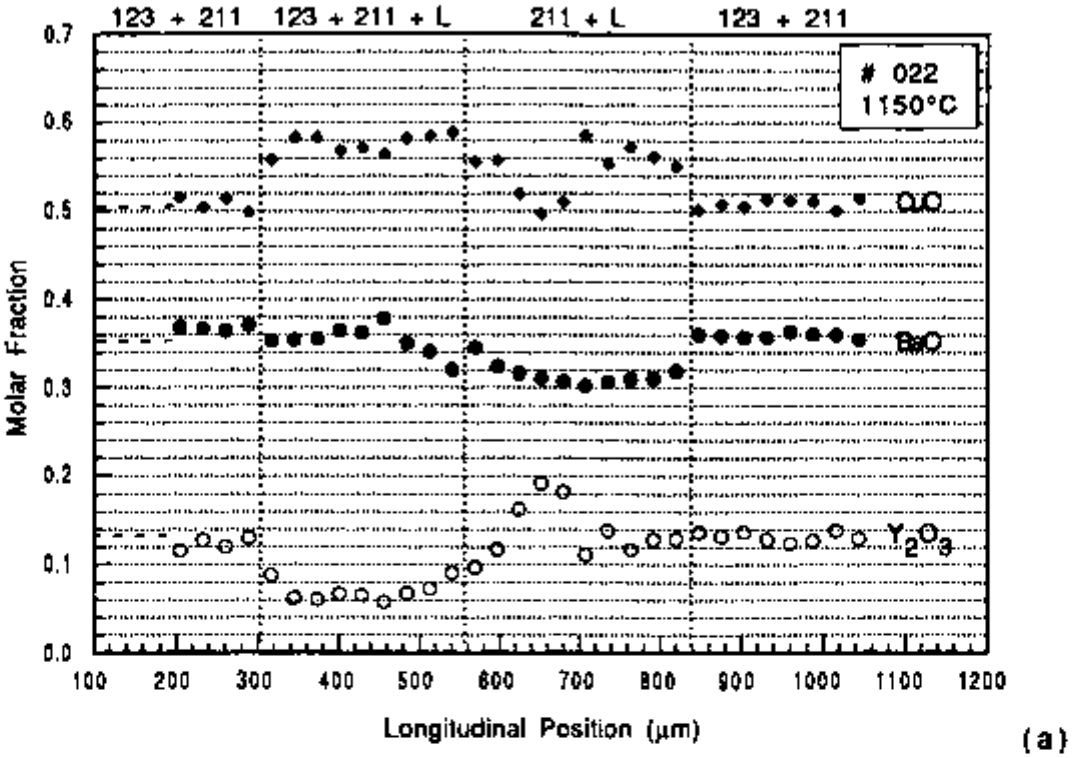

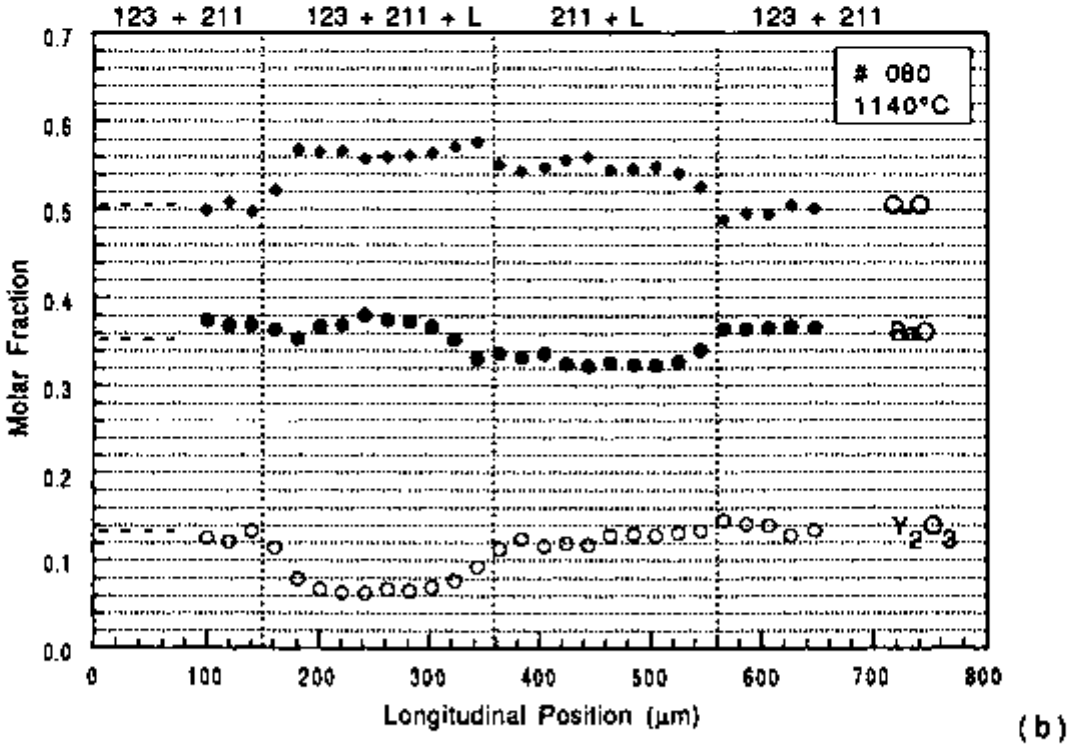

Fig. 5.7. Zone composition profiles of samples solidified by (a) method 2 and (b) method 3. The nominal composition of both samples was 123 + 22.8 wt.% 211. Zone micrographs of samples 022 and 080 are shown in Figs. 5.12 (c) and 5.12 (d), respectively.

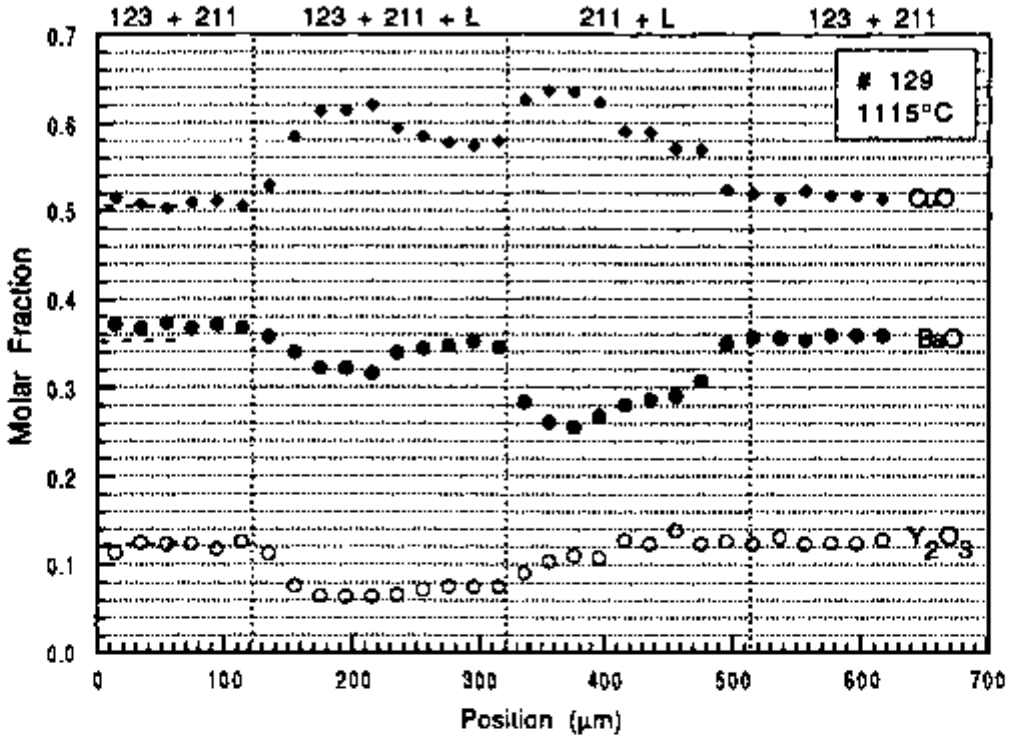

Fig. 5.8. Zone composition profile of a sample solidified by method 2 at a relatively low temperature of 1115°C. The 211 content of the precursor was 20 wt.%. The zone micrograph of sample 129 is shown in Fig. 5.13 (b).

5.3.2 *General Observations of Quenched Interfaces*

Fig. 10 summarizes the interface morphologies observed in directional solidification of 123 samples. The high temperature gradient data is from present results and the low temperature gradient points correspond to the results of Cima et al.[89] Recently, additional data have been published that are in basic agreement with the present results.[220] Four different regimes were revealed when the interface morphologies are plotted on a graph of temperature gradient, G, versus growth rate, R. The four types of interfaces are termed "faceted/plane front", "cellular/dendritic", "equiaxed blocky" and "quenched". The last designation corresponds to the term "mushy" assigned by Izumi *et al.*[167] to samples where a clear distinction of $YBa_2Cu_3O_y$/liquid interfaces was not possible. Here, the designation "quenched" was attributed when 123 did not form due to reaction kinetics limitations. The microstructure of these samples was composed by a dispersion of 211 particles in a quenched liquid matrix, which is an eutectic of $BaCuO_2$ and CuO.

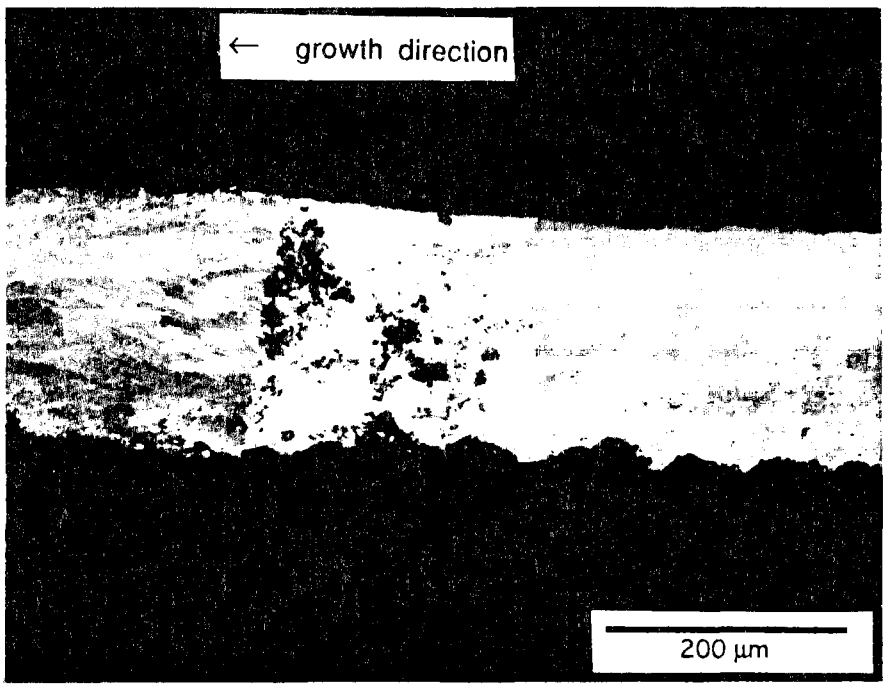

Fig. 5.9. Typical appearance of the quenched zone (middle) of an essentially single-grained filament (bottom) growing from a fully dense polycrystalline precursor (top). The precursor was previously grown from a sintered filament at a higher speed (6.94 μm/s). This micrograph confirmed that the 211 + 123 + L region in between the polycrystalline precursor and the 123 melting interface was indeed formed by reaction of the precursor with the copper-rich liquid from the zone. Sample 056A.

In Fig. 5.10, the temperature gradient axis spans almost three orders of magnitude while the growth rate has a linear axis. A one hundred-fold increase in temperature gradient, from 10^4 °C/m to 10^6 °C/m, increased the critical growth rate for faceted crystals by only a factor of two.

The four terms describing interface morphology are explained by the schematic illustration of the 123 interface in the quenched specimens shown in Fig. 5.11. The first and second categories in Fig. 5.11 comprise different types of structures, termed a1, a2, a3, and b1, b2, b3, b4, respectively. These designations correspond to the experimental observations reported in Table 5.2. The structures b3, b4, and the blocky/equiaxed structure have been reported in the literature[89,169] but did not occur under the conditions of the present experiments.

Polished sections of representative quenched interfaces are shown in Fig. 5.12 to 5.16. Structures obtained under planar front conditions are illustrated

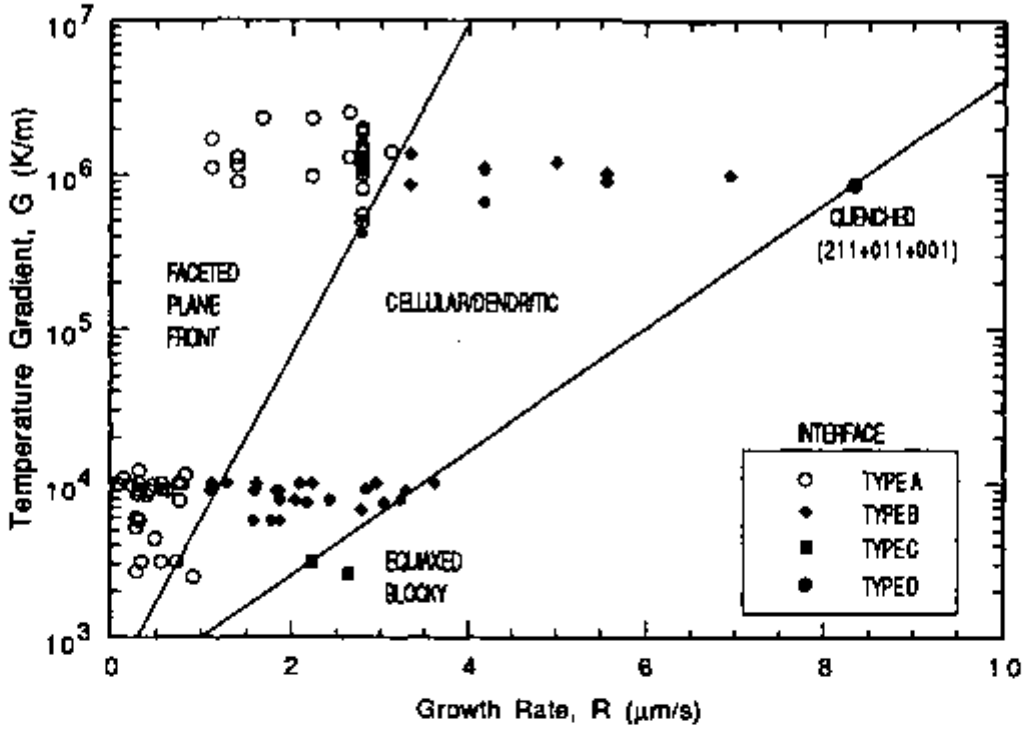

Fig. 5.10. Combined effect of temperature gradient and growth rate on the morphology of the solidification interface. Low temperature gradient data are from Cima *et al.*[89]

in Figs. 5.12 (type a1), 13 (type a2) and 14 (type a3). Dendritic and cellular structures (type b1) are illustrated in Fig. 5.15 (a) and (b). The dendritic structure (type b1) is illustrated in Figs. 5.15 (a) and 5.20 (a). The cellular (type b2) structure is shown in Figs. 5.15 (b), 5.20 (b), and 5.20 (c). The "quenched" structure is shown in Figs. 5.16 and 5.21.

Type "a" morphologies led to the growth of single-grained filaments by natural grain selection. In this process, the growth of misaligned grains is progressively terminated as they intercept the filament's surface. An example is given in Fig. 5.5, where the left grain was growing towards the filament's surface at the time of quench. The orientation of the surviving grain is dictated by the fast growth direction of the 123 crystal, which is parallel to the basal, or *ab* plane. Experimental observations indicated that the growth of at least 30 filament diameters was necessary before a single-grained sample could be obtained by grain selection. If the surviving grains are oriented such as that their *ab* planes are nearly parallel to the growth direction, much longer lengths have to be travelled by the zone before only one grain remains.

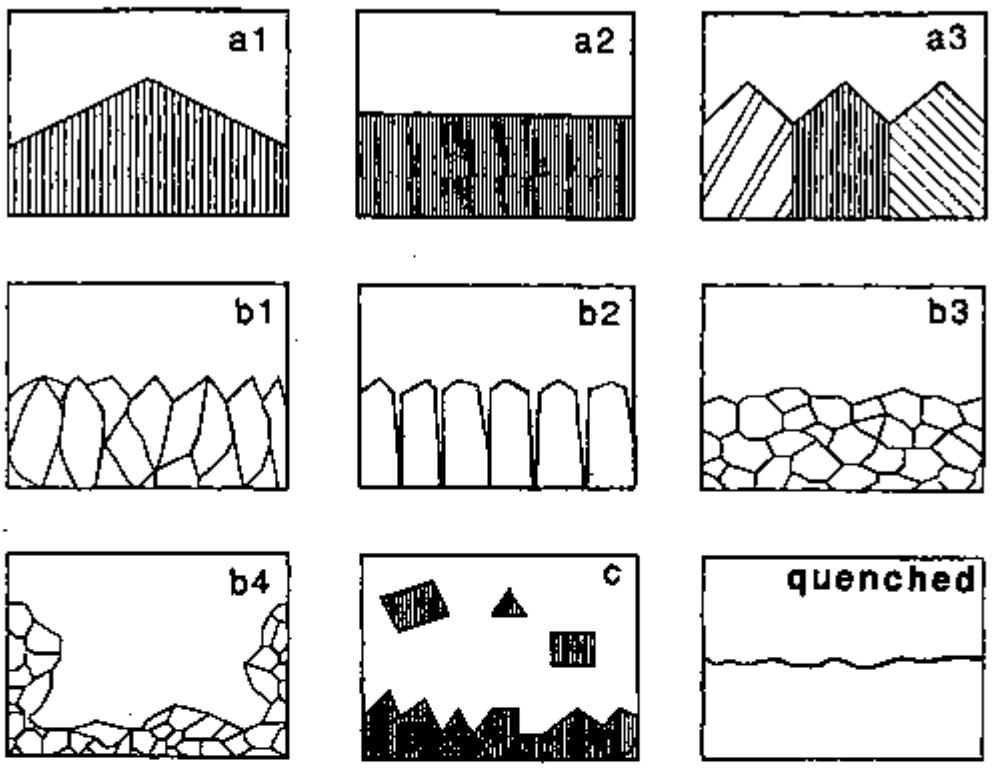

Fig. 5.11. Schematic illustration of interface morphologies. Types b3, b4 and blocky did not occur at high temperature gradients (LHFZ).

Faceted solidification interfaces were observed in LHFZ filaments at low and intermediate growth rates, as shown in Figs. 5.12, 5.13 and 5.14. The microstructures were observed to vary in a systematic way with growth rate, with a gradual transition from faceted/planar and faceted interfaces to celullar/dendritic interfaces with increasing growth rate. Cellular interfaces were clearly identified in phase pure 123 samples, but not in filaments containing excess 211.

Some of the filament solidification interfaces appeared flat or faceted with single crystal growth of 123 occurring in the solidified material, as determined by optical microscopy with polarizing filters. These grains are continuous, indicating that secondary nucleation is relatively infrequent. Single-crystal filaments were produced at intermediate growth rates (Table II). A number of grains (three or four) were observed in fibers prepared at the slower rates.

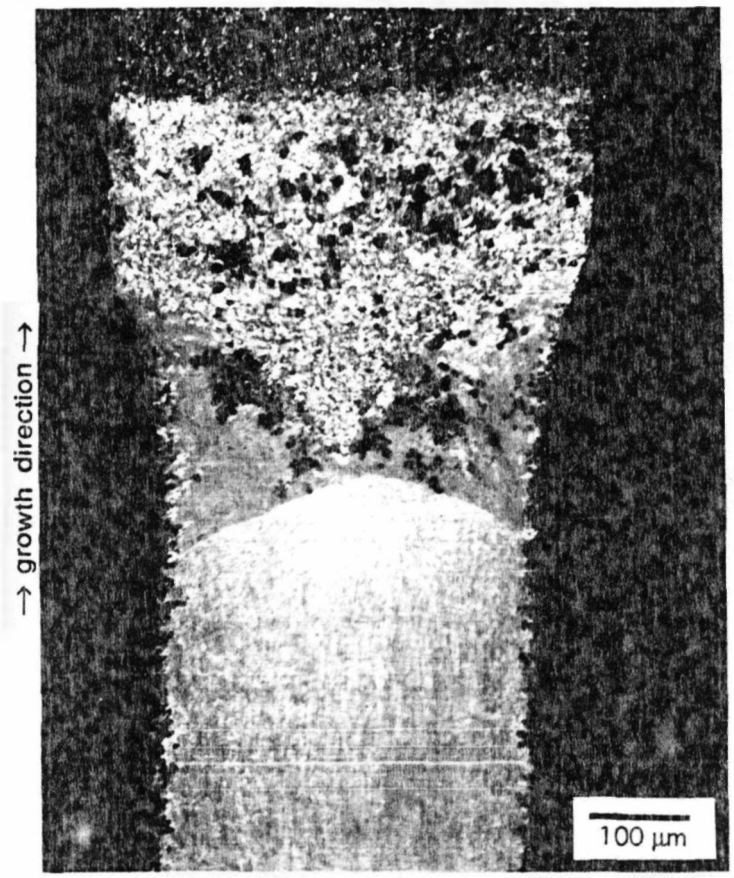

Fig. 5.12 (a). Longitudinal section of a quenched filament grown in the planar front regime with faceted, type a1 interface. R = 2.78 µm/s; G ~ 1.4°C/µm; Sample 130 (20 wt.% 211). Interference contrast revealed incipient twinning in the solidified material (bottom).

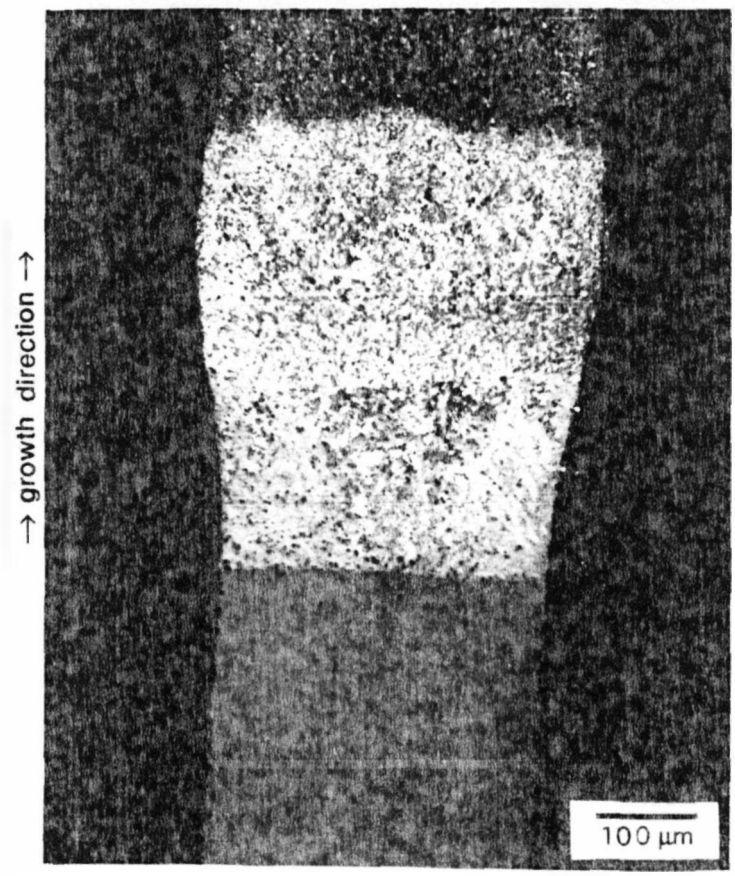

Fig. 5.12 (b). Longitudinal section of a quenched filament grown in the planar front regime with faceted, type a1 interface. R = 2.78 µm/s; G = 1.88 °C/µm; Sample 033 (22.8 wt.% 211). Polarized light.

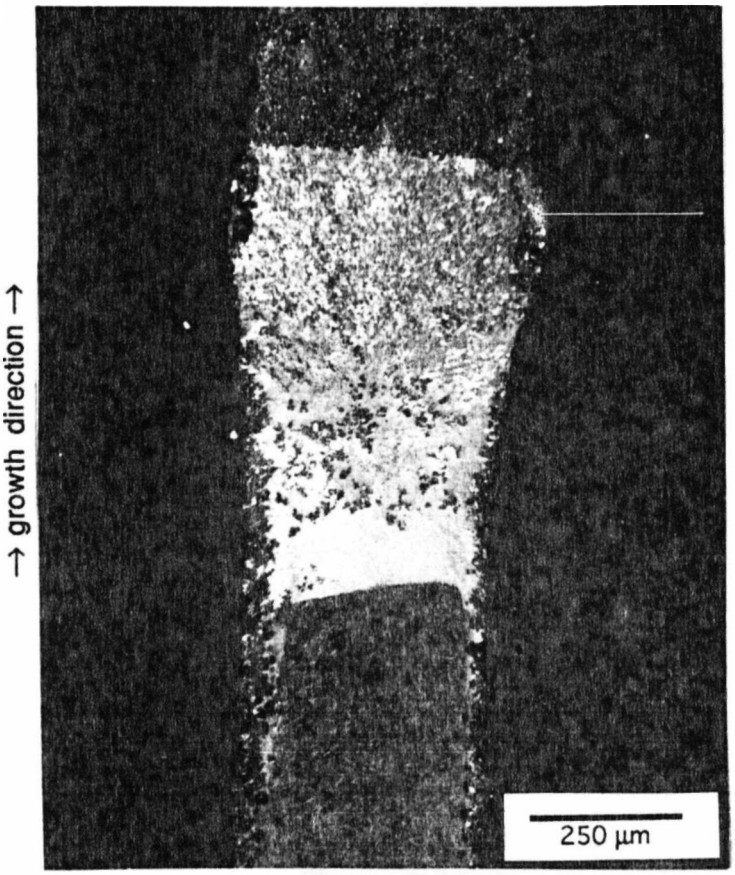

Fig. 5.12 (c). Longitudinal section of a quenched filament grown in the planar front regime with faceted, type a1 interface. R =2.64 μm/s; G=1.29°C/μm; Sample 080 (22.8 wt.% 211). Polarized light.

Fig. 5.12 (d). Longitudinal section of a quenched filament grown in the planar front regime with faceted, type a1 interface. R=2.22 μm/s; G=0.97 °C/μm; Sample 022 (22.8 wt.% 211). Polarized light.

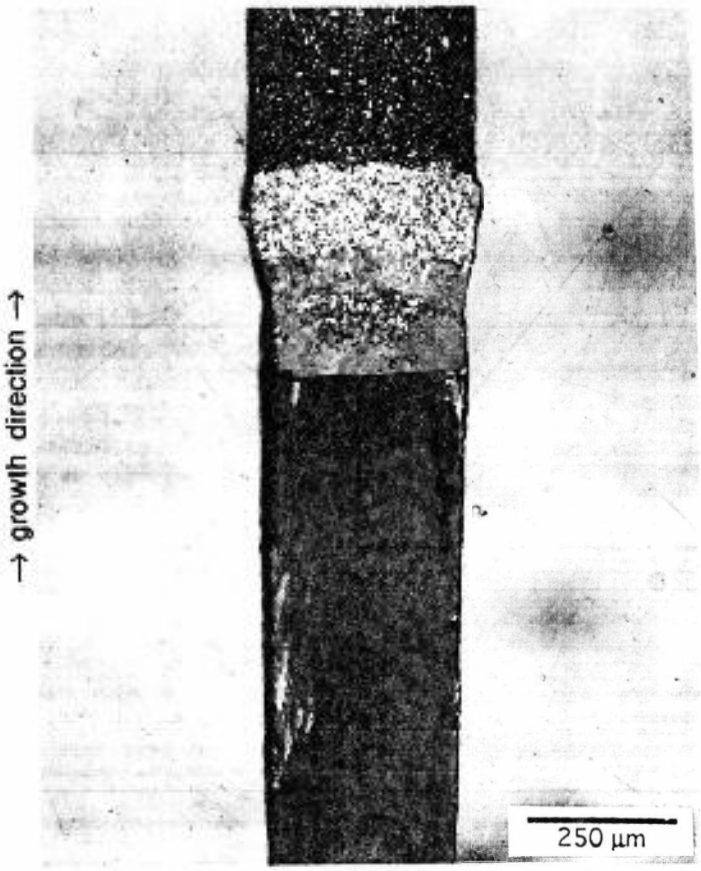

Fig. 5.13 (a). Longitudinal section of a quenched filament grown in the planar front regime with faceted, type a2 interface. R=2.78 µm/s; G=1.25 °C/µm; Sample 138 (20.0 wt.% 211). Secondary nucleation close to the surface. Polarized light light.

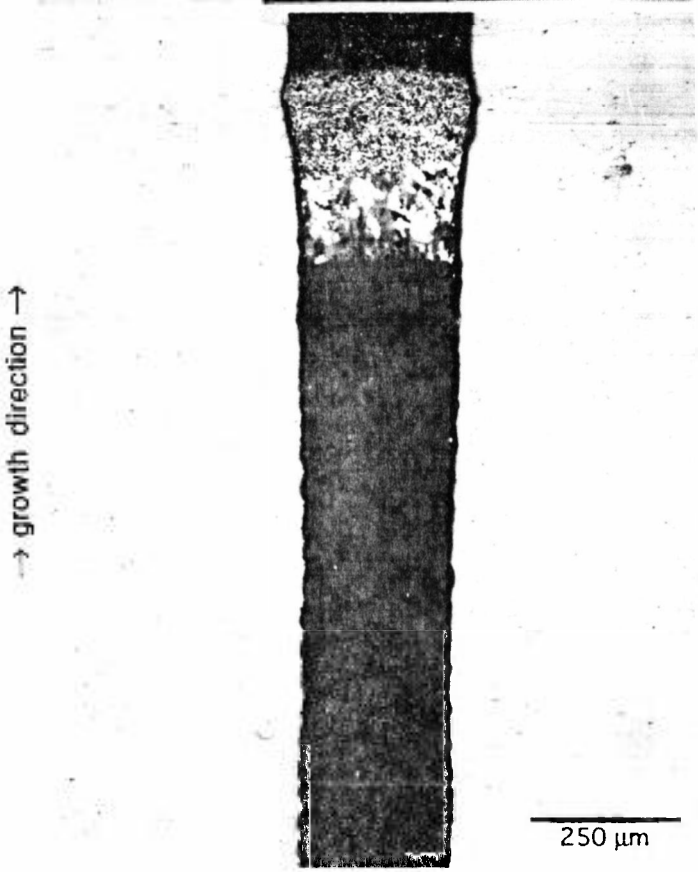

Fig. 5.13 (b). Longitudinal section of a quenched filament grown in the planar front regime with faceted, type a2 interface. R = 2.78 µm/s; G = 1.52°C/µm; Sample 129 (20.0 wt.% 211). 2 grains parallel to the growth direction. Polarized light.

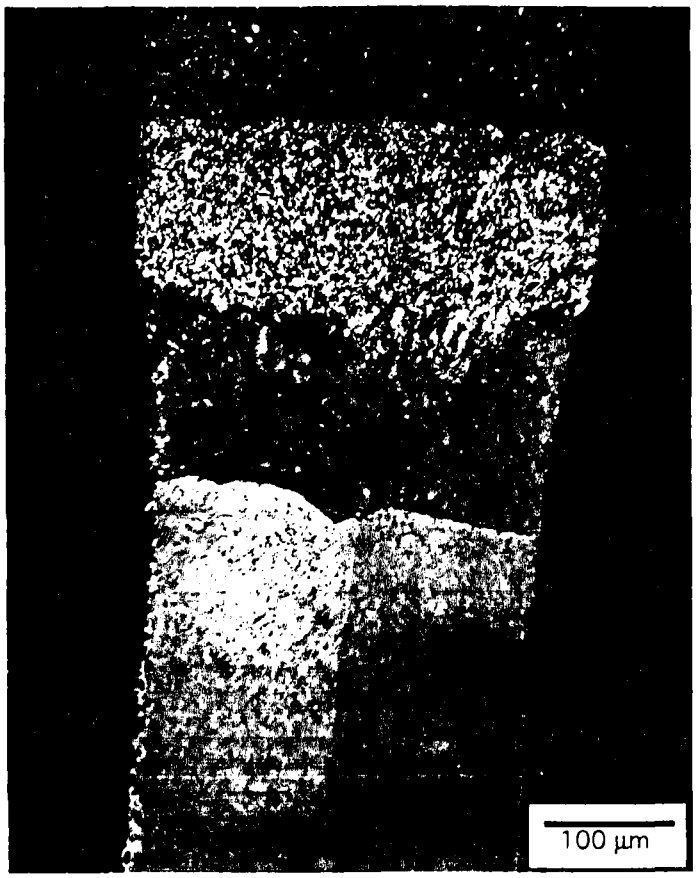

Fig. 5.13 (c). Longitudinal section of a quenched filament grown in the planar front regime with faceted, type a2 interface.
R = 2.78 μm/s; G = 1.40°C/μm;
Sample 136 (20.0 wt.% 211).
Two grains parallel to the growth direction.
Polarized light.

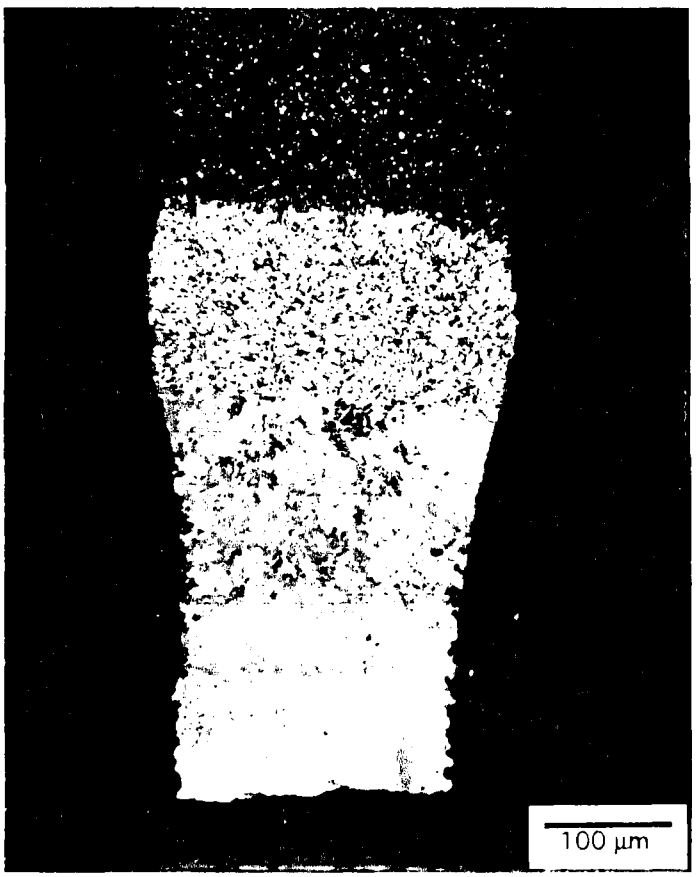

Fig. 5.13 (d). Longitudinal section of a quenched filament grown in the planar front regime with faceted, type a2 interface.
R = 2.78 μm/s; G = 1.11°C/μm;
Sample 139 (20.0 wt.% 211).
Polarized light.

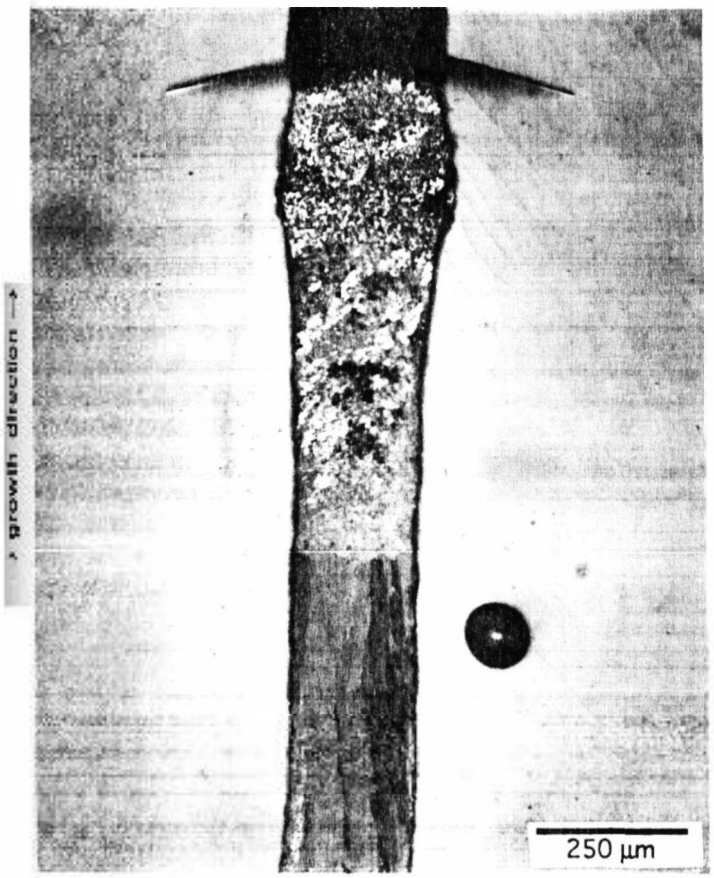

Fig. 5.14 (a). Longitudinal section of a quenched filament grown in the planar front regime with faceted, type a3 interface. R = 2.78 µm/s; G = 0.55°C/µm; Sample 039 (22.8 wt.% 211). The microstructure of region (1) is shown in Fig. 5.6 (b) and that of region (2) in Figs. 5.17 (a) and (b). Polarized light.

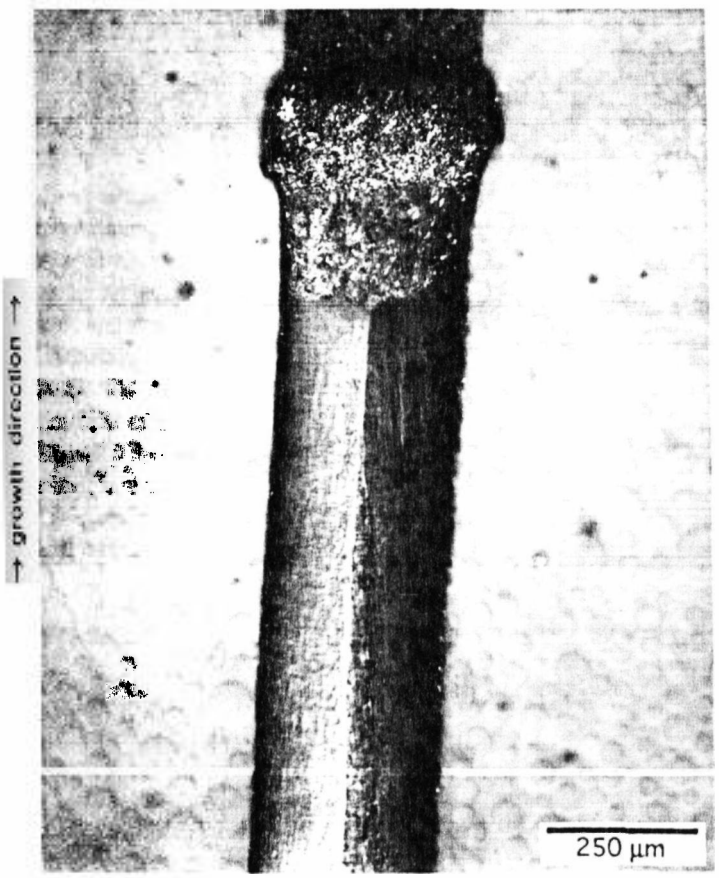

Fig. 5.14 (b). Longitudinal section of a quenched filament grown in the planar front regime with faceted, type a3 interface. R = 2.78 µm/s; G = 1.29°C/µm; Sample 010 (22.8 wt.% 211). Incipient twinning (tweed microstructure) in the solidified material revealed by interference contrast (bottom).

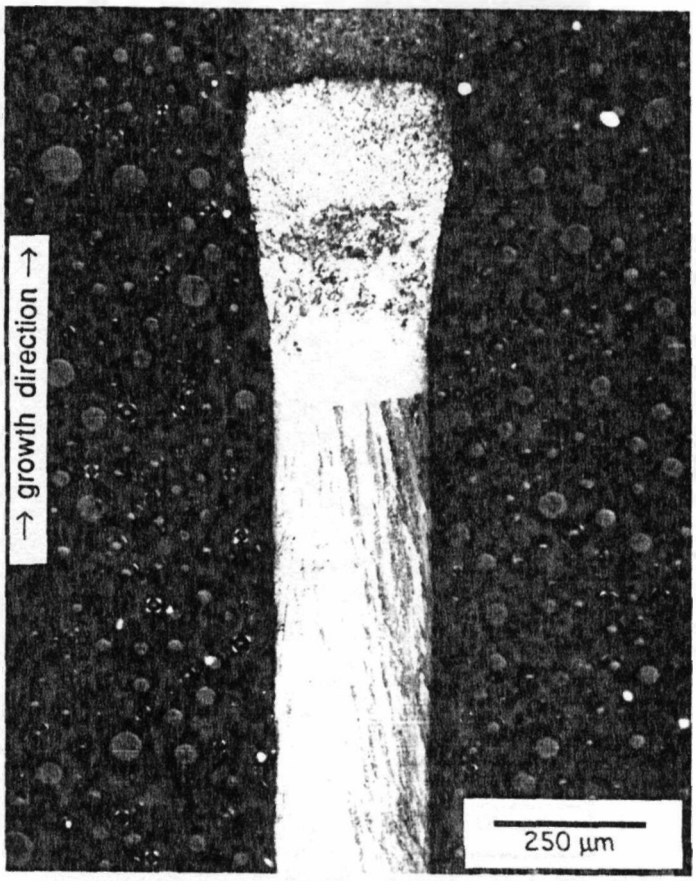

Fig. 5.15 (a).
Longitudinal section of a quenched filament grown in the dendritic regime.
Type b1 interface.
Sample 019
(22.8 wt.% 211)
R =3.33 µm/s;
G = 0.86 °C/µm.
Polarized light.

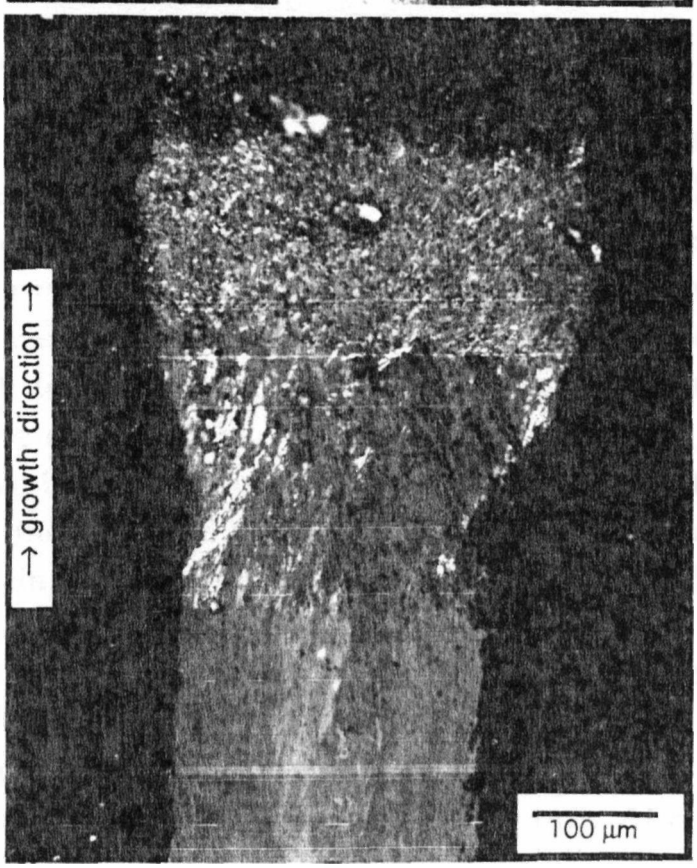

Fig. 5.15 (b).
Longitudinal section of a quenched filament grown in the cellular regime.
Type b1 interface.
Sample 083
(Phase pure 123)
R =2.78 µm/s;
G = 0.42°C/µm.
Polarized light.

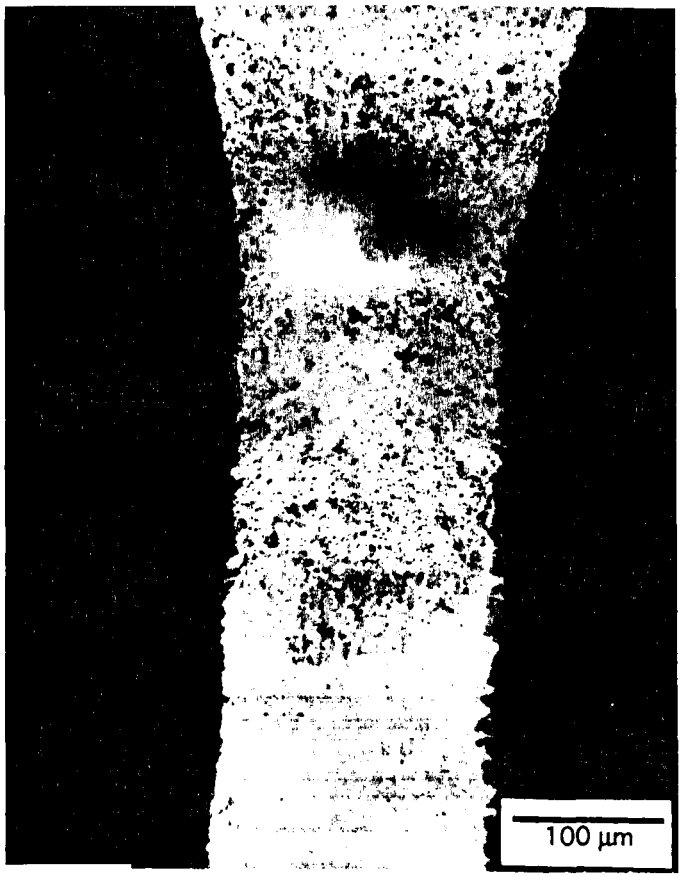

Fig. 5.16. When the growth rate exceeded 8 μm/s, the highly undercooled semisolid mixture of 211 + L was simply quenched at the growth interface and 123 did not form. Sample 051 (22.8 wt. % 211). R = 8.33 μm/s; G = 0.86°C/μm. Type-d interface. The microstructure of the solidified material (bottom region) is shown in Fig. 5.21. Polarized light.

The effect of the peritectic reaction on 211 particle size is shown in the micrographs of Fig. 17, which correspond to a sample solidified under planar front conditions. The plane of polishing is longitudinal, so that the microstructure on both sides of the quenched interface can be resolved. The figure clearly demonstrates that the peritectic reaction occurs largely or entirely in a region very close to the solidification interface. An abrupt decrease occurs in the volume fraction of the 211 particles when they are engulfed by the growing 123 crystal. The 211 content in the semisolid zone and in the solidified material was measured near the solidification interface by a point counting method,[221] in micrographs similar to those of Figs. 17 (a) and 17 (b).

The average volume fraction of 211 in the semisolid side of the solidification interface was 62.6 ± 5.2 % and did not depend on growth rate. Fig. 18 shows that the amount of 211 consumed by the peritectic reaction decreases linearly with increasing growth rate. At zero growth rate the

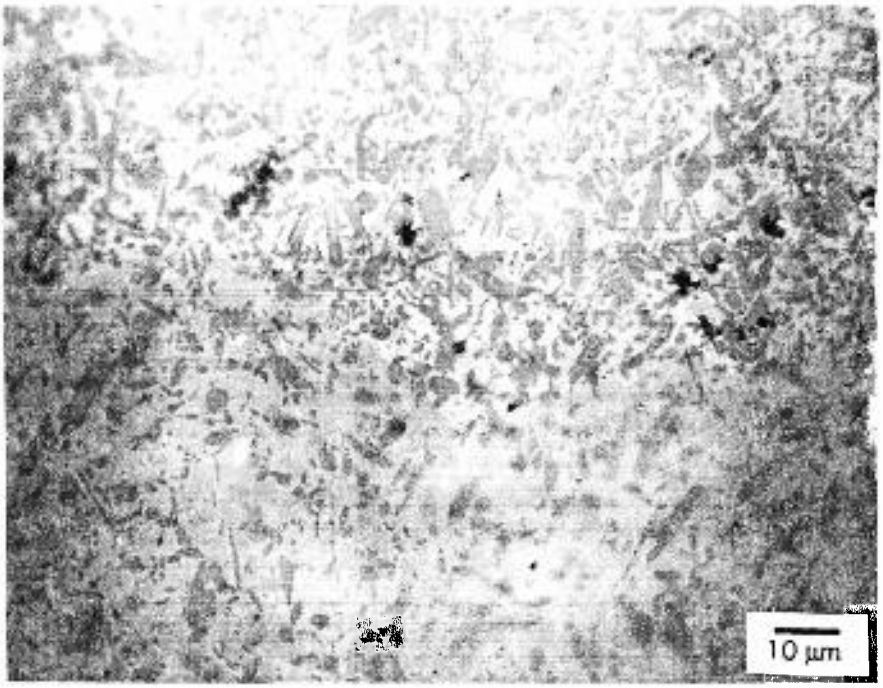

(a)

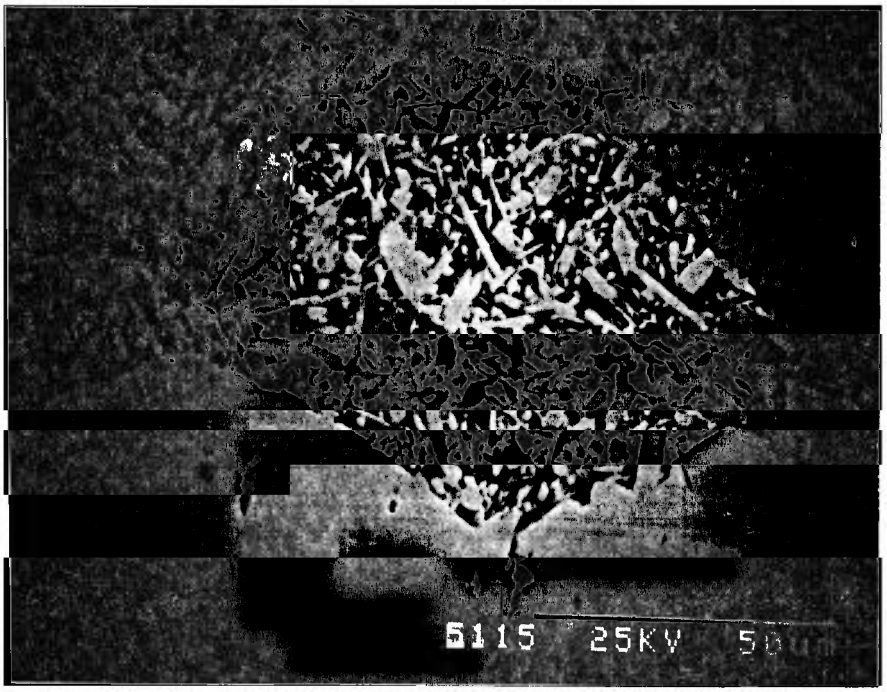

(b)

Fig. 5.17. High magnification views of a plane front, faceted solidification interface . (a) Optical micrograph showing the abrupt decrease that occurs in the volume fraction of 211 tas the growth front advances. (b) SEM back scattered view of the same sample. The optical micrograph was prepared after the SEM micrograph, with a repolishing step in between.

experimental line intersects the axis at about 22 vol.%, a value very close to the nominal composition of the filaments (23.2 vol.%). At high growth rates, the experimental curve intersects the horizontal dashed line at a growth rate near the value determined for the cellular/dendritic-to-mushy transition. Past this intersection point, the cooling rates are sufficiently high to prevent any reaction between the liquid and the 211 phase, and the semisolid material is effectively quenched.

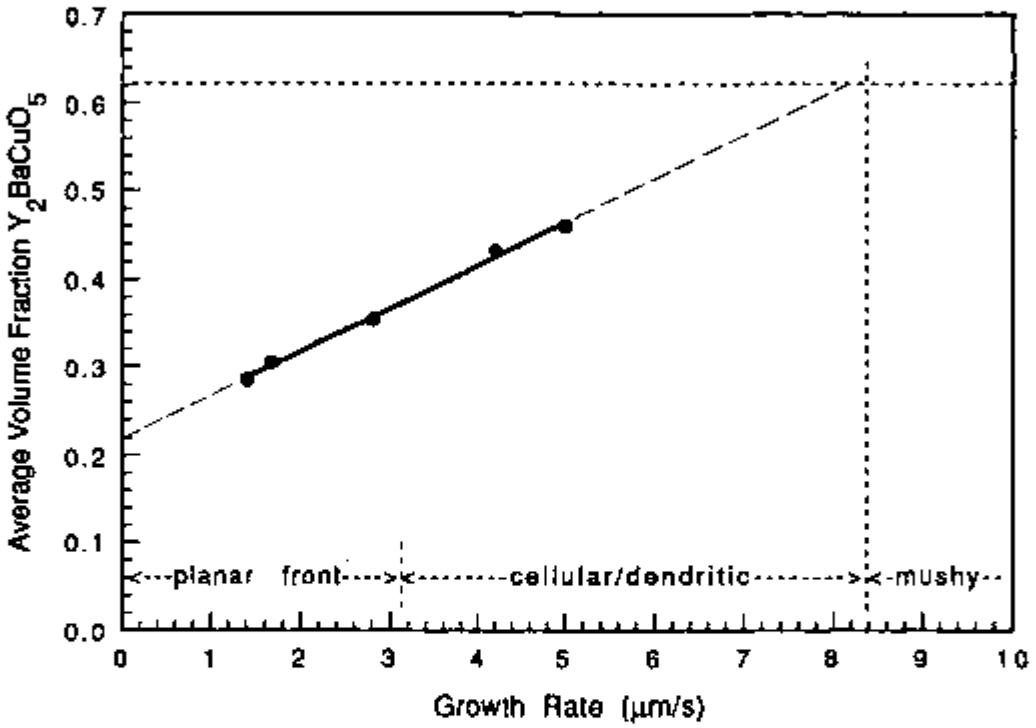

Fig. 5.18. Volume fraction of 211 in the solidified filaments versus growth rate. As the growth rate increased, so did the 211 content in the solidified material, until it became equal to the volume fraction of 211 in the zone. At this point, the reaction between 211 and liquid did not occur. The experimental line extrapolates to the 211 concentration of the precursor at zero growth rate, and intersects the vertical line representing the maximum growth rate for dendritic solidification at a volume fraction very close to the average value measured in the zone (horizontal dashed line).

The average 211 particle size in the zone and in the solidified material increased with residence time in the liquid, as shown in Fig. 5.19. The residence time was determined by dividing the zone length by the growth rate. Measurements of particle size were carried out by a line intercept method[221] in photomicrographs of LHFZ samples similar those shown in Figs. 5.17. For rod-like particles similar to 211, the method employed yields an

average transversal dimension, instead of a dimension corresponding to the average particle volume. Therefore "particle size" is loosely used here to represent average transversal dimensions.

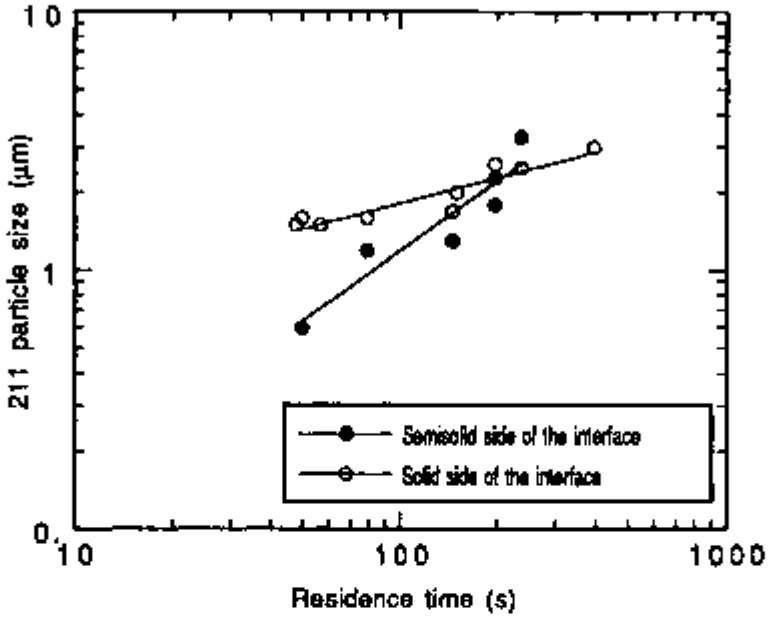

Fig. 5.19. Measurements of 211 particle size close to the solidification interface in both the semisolid and solidified materials.

The particle size in the solidified material follows a 1/3 power dependence with residence time. The average particle size in the zone, however, has a 0.9 power dependence. The causes for the different dependencies are probably related to the non-equilibrium conditions of the zone, especially at high growth velocities and temperatures. Recent coarsening experiments by Rigby *et al.*[207] and Izumi *et al.*[208] apparently support the previous hypothesis. These investigators found that the temporal exponent for coarsening of 211 particles in barium cuprate liquids was equal to the classical value of 1/3, in spite of the large volume fraction of 211 in their samples (~0.62). As discussed in Chapter 4, previous experimental, as well as theoretical work have demonstrated that the classical equation for coarsening is still applicable to solid-liquid systems in which the solid content is large. However, the rate constant for coarsening, K, increases with the volume fraction of solid.

Fig. 5.19 also shows that at shorter residence times, the average particle size becomes larger upon solidification. The apparent increase in the average

particle size may be the result of a preferential consumption of the finer particles by the peritectic reaction. As the residence time increases, most of the finer particles are consumed by coarsening before they reach the solidification interface. Thus, the peritectic reaction has to take place with a coarser and narrower particle size distribution and its net effect is a reduction of particle size.

5.3.3 *Microstructures from the Cellular/Dendritic and Mushy Regimes*

Cellular/dendritic morphologies produced highly textured polycrystalline materials with large aspect ratio grains. The aspect ratio of the grains decreased and the amount of barium cuprate and copper oxide in the samples increased with increasing growth rate. High magnification views of microstructures produced in the cellular/dendritic regime are shown in Fig. 5.20. Cellular growth is suggested in Fig. 5.20 (a) by the elongated 123 grains, which are parallel to the growth direction and contain a dispersion of 211 particles that is apparently bi-modal. It is very likely that the finer particles seen in the picture were produced at the decomposition interface and the larger particles are those that were added to the precursor as excess Y_2BaCuO_5. These particles have also coarsened significantly during their traject through the semisolid zone, because they are larger than the average size of the 211 particles contained in the precursor. Cellular growth is also evident in Fig. 5.20 (b) which is a high magnification view of the microstructure of the sample shown in Fig. 5.15 (a). An example of dendritic morphology is illustrated in Fig. 5.20 (c), which is from a sample solidified at a growth rate near the upper limit for this regime. It is difficult to distinguish grain boundaries in Fig. 5.20 (c).

Microstructures from the "quenched" regime (Fig. 5.16) are similar to the microstructure of the quenched semisolid melt and consist of a dispersion of 211 in a matrix of $BaCuO_2$ and CuO (the white phase in Fig. 5.21).

5.3.4 *Microstructures Produced by Plane Front Growth*

Crystalline Structures

Observation of quenched specimens with differential interference contrast has shown that during solidification, incipient twinning started to occur less

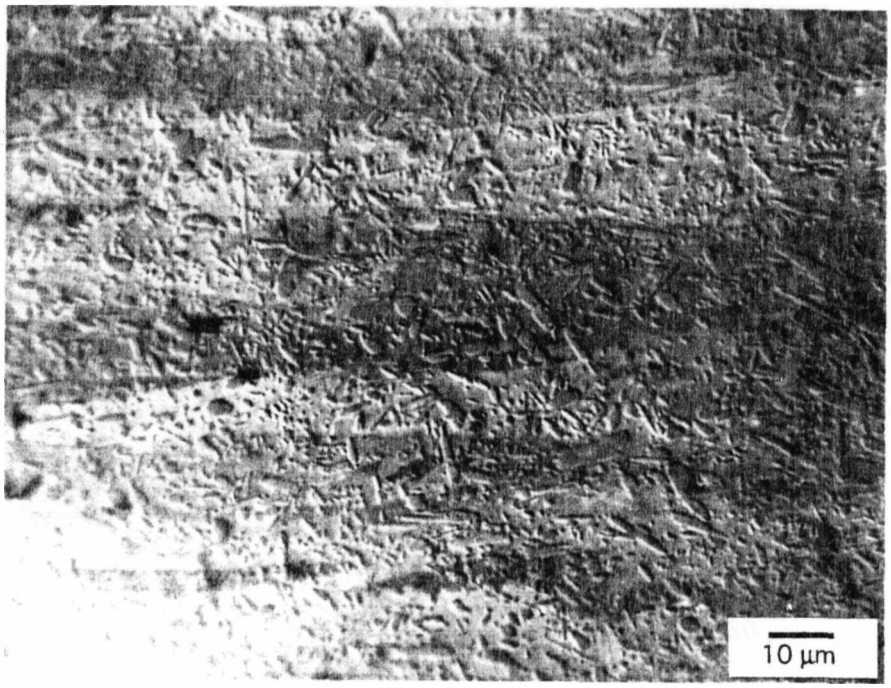

Fig. 5.20 (a). High magnification view of dendritic microstructure (type b1) in a filament of nominal composition 123 + 22.8 wt.% 211. Sample 019. Differential interference contrast.

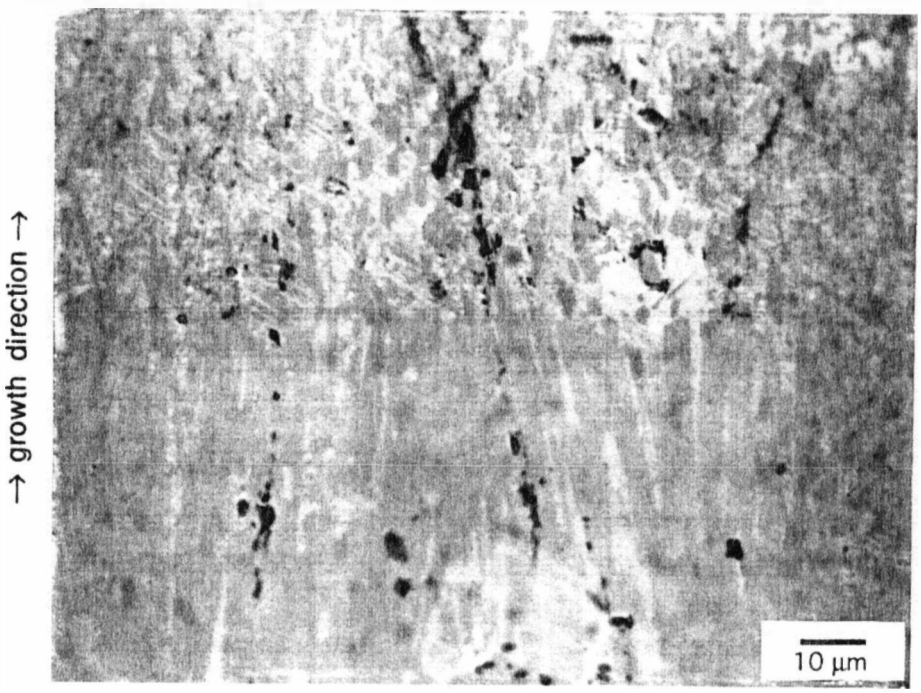

Fig. 5.20 (b). High magnification view of the cellular microstructure (type b2) of a filament solidified from a precursor which contained only the 123 phase. Sample 083. Polarized light.

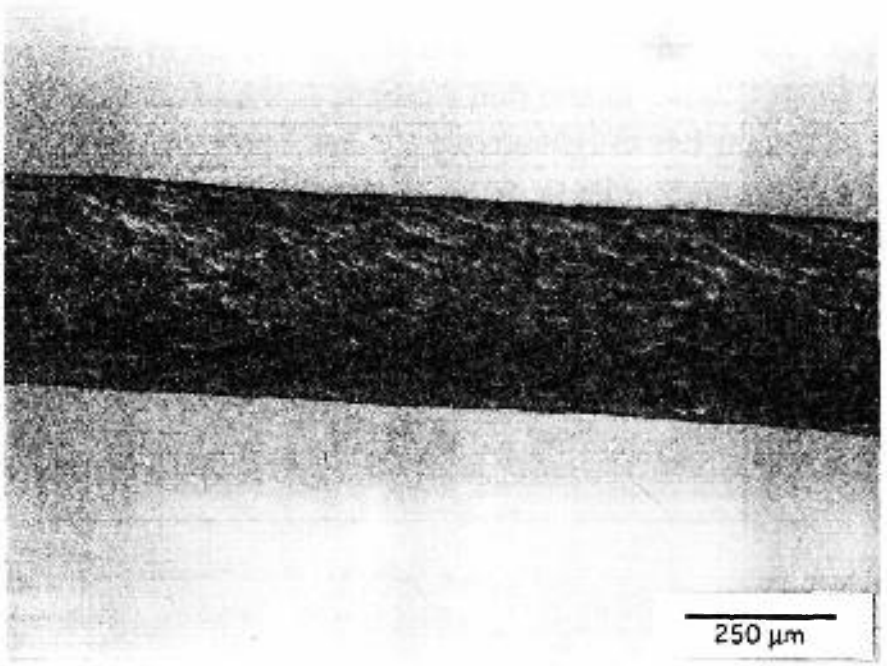

Fig. 5.20 (c). Typical microstructure produced by dendritic solidification at high velocity. Sample composition 20 wt.% 211.

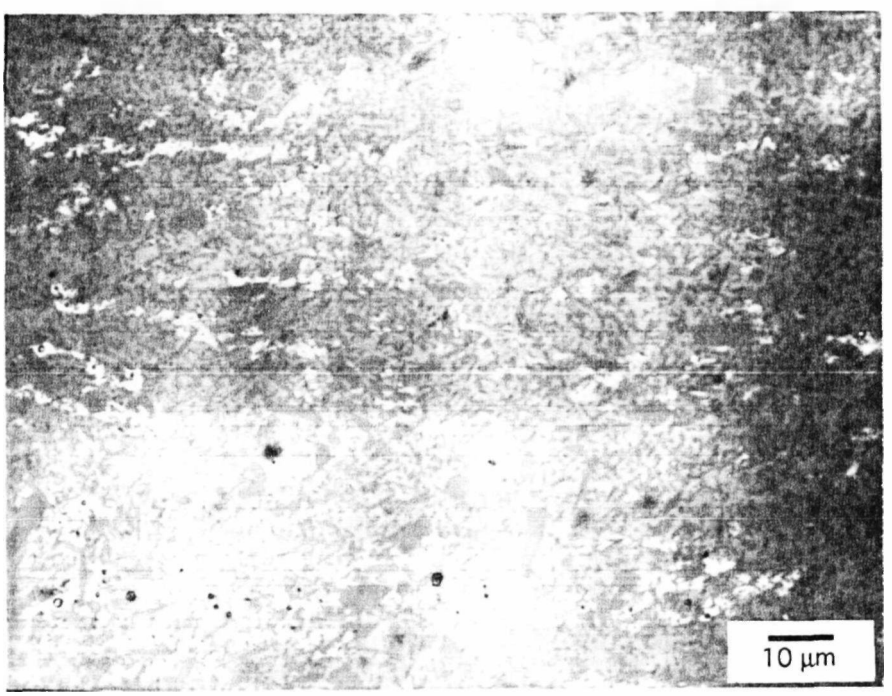

Fig. 5.21. Microstructure of a filament solidified at high velocity (type d). The amount of 123 is nil. The microstructure consists of a dispersion of 211 particles (darker phase) in barium cuprate. The dispersed white phase is CuO. See also Fig. 5.16. Sample 054. Polarized light.

than one zone length away from the growth front. Incipient twinning takes place when 123 is rapid cooled and is revealed by the development of a fine tweed-like microstructure that coarsens into sets of parallel twins uppon subsequent annealing.[222-223] Because of coarsening, tweed microstructures were easier to observe in LHFZ filaments grown at slower rates, as shown in Fig. 5.22. In that sample, fully developed sets of parallel twins could already be

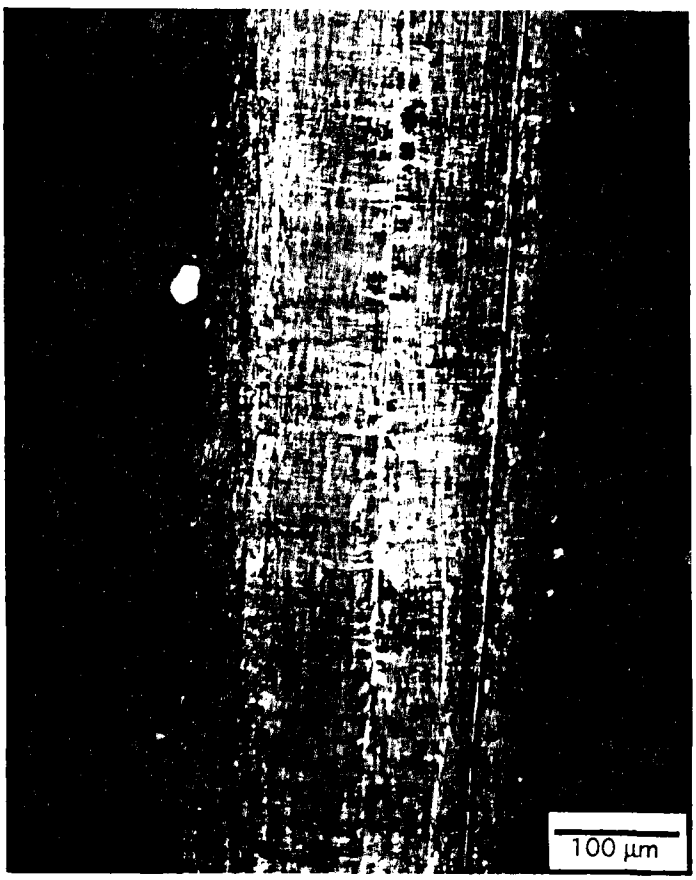

Fig. 5.22. Tweed microstructure formed by incipient twinning during plane front solidification. As grown sample. Differential interference contrast.

seen in the vicinity of grain boundaries at higher magnifications. According to Fig. 2.4, the tetragonal to orthorhombic phase transformation starts at a temperature of about 677°C in 1 atm O_2. Zone lengths and temperature gradients are of the order of 1°C/µm and 300 µm, respectively. Therefore, the tetragonal to orthorhombic transformation should start at about one diameter below the solidification interface, as indeed observed.

Low Growth Rate Range

Below about 1.7 μm/s, some distinct microstructural features were identified in the LHFZ samples. Microstructures of samples solidified in this range of growth rates are shown in Figs. 5.23 (a) and (b). In Fig. 5.23 (a) the growth rate and the maximum zone temperature were 1.39 μm/s and 1150°C, respectively. A high-angle grain boundary is clearly visible in the micrograph. Low-angle grain boundaries (or platelet boundaries) with spacings roughly equal to the particle size can also be distinguished. The top grain also contains a number of cracks formed on cooling by thermal and phase transformation stresses. In the layered 123 structure, the formation of cracks is usually favored along the basal, or *ab* planes. Therefore, in textured samples of this material, the traces of both the plane of the crack and the *ab* planes always coincide. Plate boundaries were observed only in the sample of Fig. 5.23 (a); this is probably because that sample was grown at high temperature and slow rate.

Elongated 211 particles with a preferential orientation along the growth direction were observed at lower growth rates. This is illustrated in Fig. 5.23 (b), which is from a sample grown at 1.11 μm/s with a maximum zone temperature of 1120°C. The unidirectional diffusion flux near the solidification interface and screening effects similar to those mentioned in section 4.2.4 (Fig. 4.2) are probably responsible for the morphological changes of the 211 particles at this growth rate. Some possible reasons to explain the morphological changes that occur in the 211 particles in this range of growth velocities may include the unidirectional flux near the solidification interface and the screening effects mentioned earlier in section 4.2.4 (Fig. 4.2). Another possible cause could be the directional formation of 211 at the melting interface, analogous to the directional formation of another high-temperature phase that is discussed in Chapter 6.

Intermediate Growth Rate Range

This regime corresponds to the interval 1.7 μm/s $< R \leq$ 3.11 μm/s. Similar intragranular microstructures were produced over this range of growth rates. The aspect ratio of the 211 particles apparently did not depend on growth rate within this interval. Figs. 5.24 (a) and 5.24 (b) illustrate typical microstructures of filaments grown at from precursors containing 22.8 wt.%

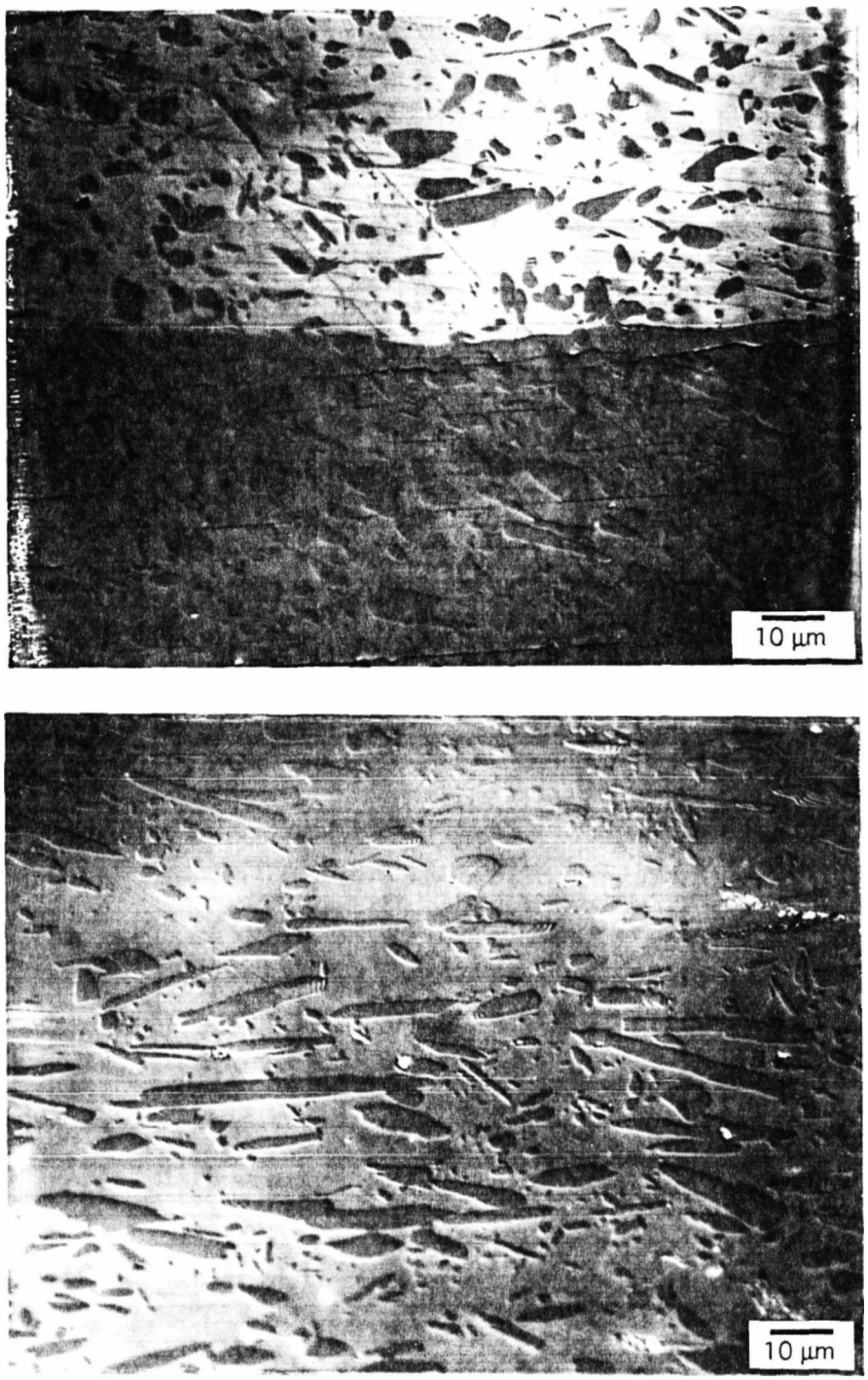

Fig. 5.23. Microstructure of samples solidified with plane front in the lower growth rate range. Top: R = 1.39 μm/s; 22.8 wt.% 211 (sample 020). Bottom: R = 1.11 μm/s; 20 wt.% 211 (sample 134); T_{max} = 1150°C (both samples). Highly elongated 211 particles, nearly parallel to the growth direction, were observed in the lower limit for planar front growth (bottom). Platelet boundaries and cracks are clearly visible in the top, but not in the bottom picture. Ledges on the particles' surface are also visible (bottom). These ledges were formed by partial dissolution of the particles near the solidification front. Differential interference contrast.

and 20 wt.% 211, respectively. Filaments grown from MIT precursors had narrower distributions of particle size compared to commercial filaments. Clean two-phase microstructures like those shown in Fig. 5.24 were obtained when the maximum temperature during growth was adjusted between 1140 - 1150°C.

Samples grown at 1120°C, had also an intragranular dispersion of CuO in addition to 211, as illustrated in Fig. 5.24 (c). This was caused by a marked enrichment in the copper content within the zone, described in section 5.3.1. Apparently, the invariant reactions that occur between the liquid and the particles during their traject through the zone contributed in some way to shape the 211 particles, as well as the particle size distribution. This is suggested by the subtle changes in particle size and morphology observed in the micrographs of Figs. 5.24 and 5.25. Fig. 5.20 is very interesting in the sense that it clearly shows a bi-modal distribution of 211 particles. The large 211 particles apparently are those added as excess to the precursor, since they are present in amounts that are similar to the 211 content of the precursor. Even though the sample of Fig. 5.20 was grown in the cellular regime, and hence at rates faster than the samples of Figs. 5.24 and 5.25, it had much larger particles, in the average, than the samples of Fig. 5.24 and 5.25. It seems that in the planar front regime, at the same time that the particle size increases with residence time, the particle size distribution is narrowed down. Insulating films along grain boundaries were also a common feature in multigrained samples solidified within this growth rate interval, as shown in Fig. 5.25 These films became progressively thicker as the growth rate decreased.

5.3.5 Phase Chemistry

In the upper limit for planar front growth, the excess volume fraction of 211 in the solidified material reached almost 13 vol.%, albeit no significant amounts of Ba-Cu oxides could be detected in the microstructure. Moreover, the good agreement between measured and nominal compositions suggested that the "missing" amounts of barium and copper were distributed between the 211 and 123 phases. The 211 particles also appeared rimmed when imaged in the backscattered electron mode, indicating the presence of a layer of different composition around the particles. Microprobe measurements of the composition of 211 particles were possible only in samples containing large

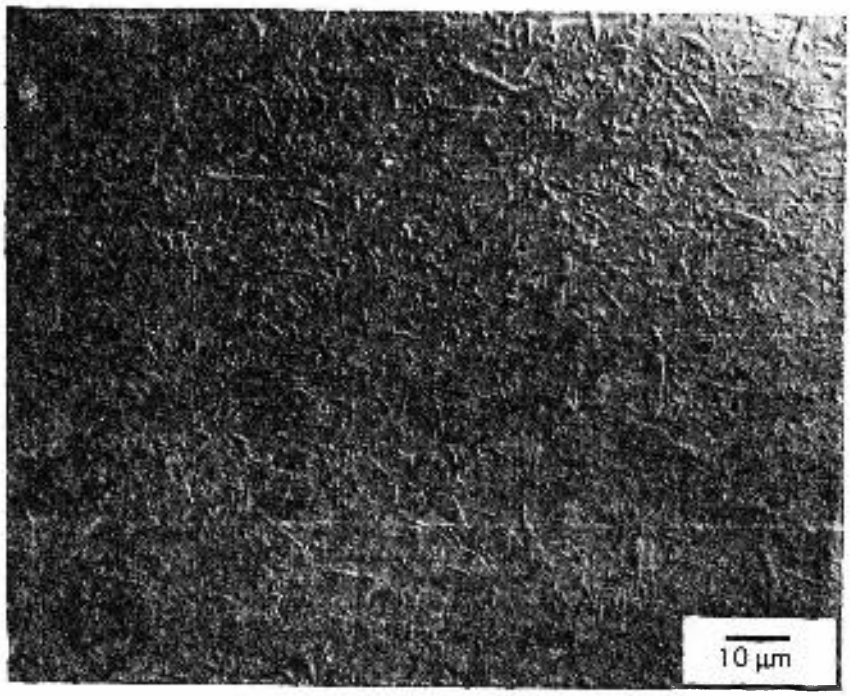

Fig. 5.24 (a)

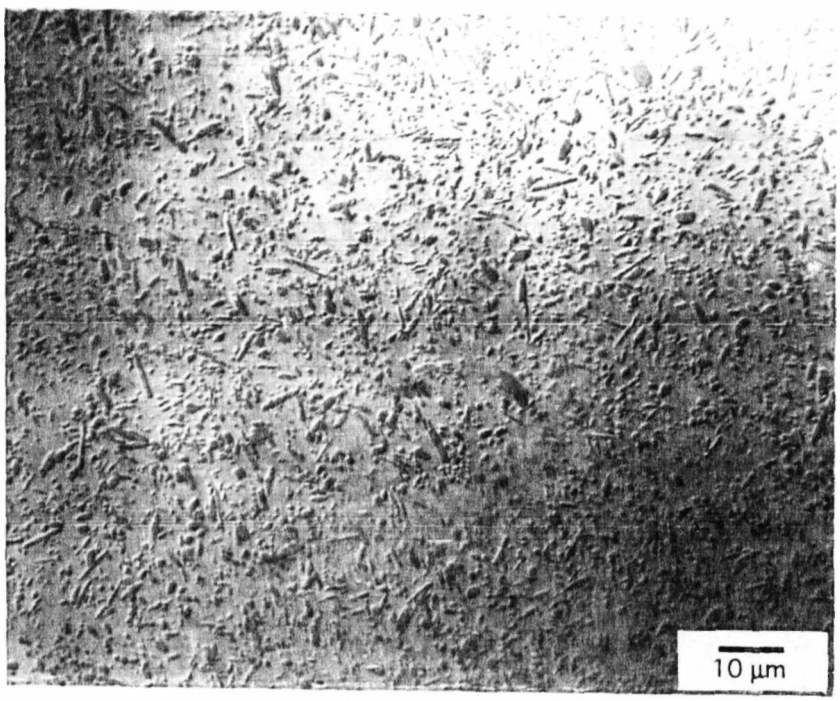

Fig. 5.24 (b)

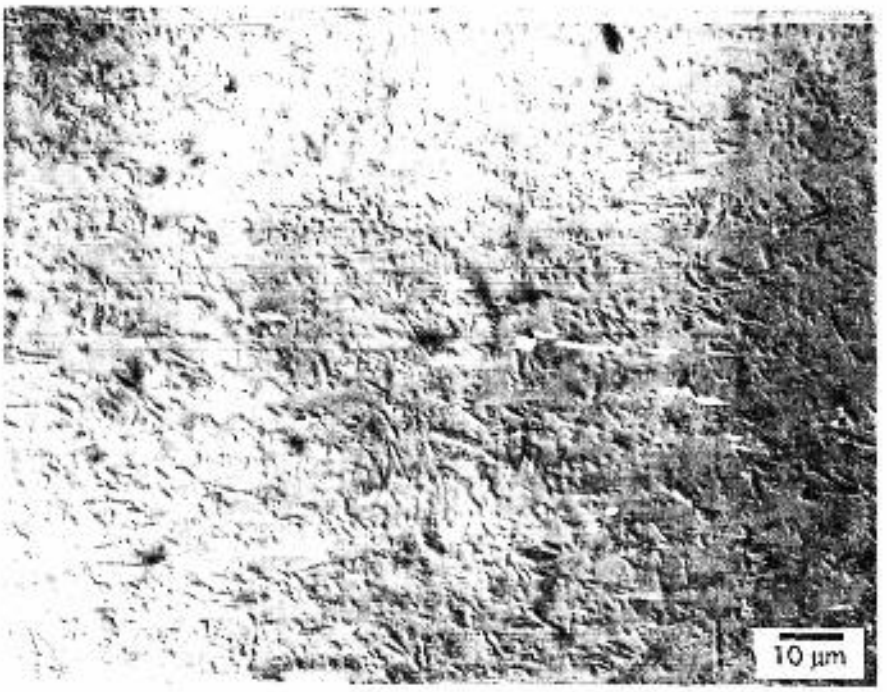

Fig. 5.24 (c)

Fig. 5.24. Typical microstructures of filaments solidified with plane front at 2.78 μm/s (intermediate growth rate regime). (a) 22.8 wt.% 211; (b) and (c) 20 wt.% 211. Slight differences in the particle size distribution are due to the different methods used to fabricate precursors. (c) also contains a dispersion of CuO particles (see text for explanation).

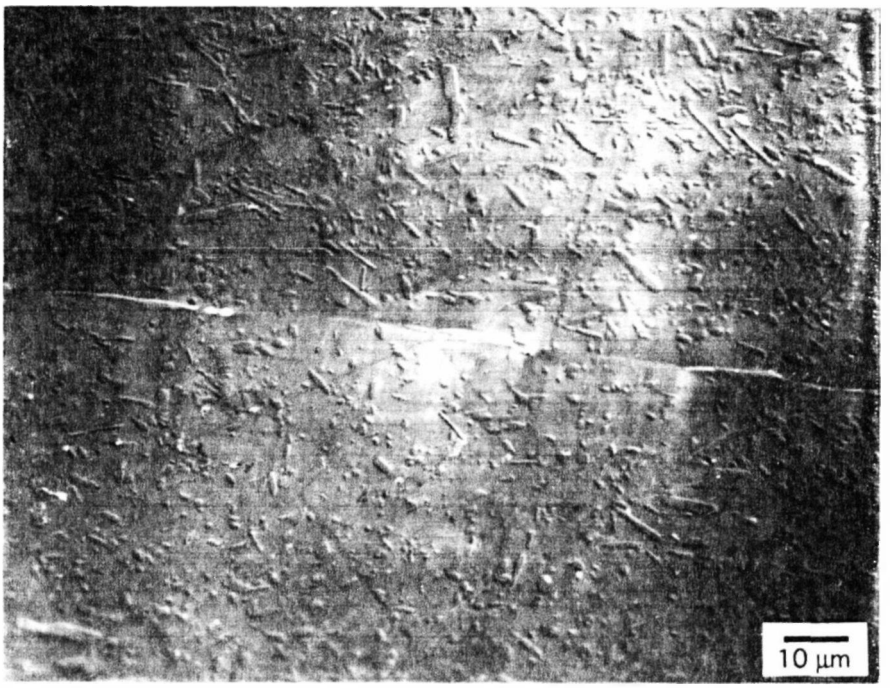

Fig. 5.25. Thick insulating films were commonly observed in grain boundaries of samples solidified at low velocities. Sample grown at 1.7 μm/s (Sample 023).

particles, such as that of Fig. 5.23 (a). Shown in Fig. 5.26 are the results of a composition scan performed across one of the grains of the sample of Fig. 5.23 (a), with a beam size of 1 μm. The scan was started with the electron beam positioned on a large 211 particle. The composition of that particle correspond to the point at the far right of the plot. Valleys and peaks occurred when both the matrix and a 211 particle were sampled by the probe. Plateaus between valleys and peaks correspond to the composition of the matrix, or 123. From the data of Fig. 5.26, the average matrix composition was determined to be $Y_{1.015}Ba_{2.047}Cu_3O_y$. The average 211 composition was determined by probing large particles within the same grain.

The resulting data points (Fig. 5.27) indicated that the particles were consistently rich in copper and depleted in yttrium, with the average composition expressed by $Y_{1.997}BaCu_{1.017}O_y$. The measured 211 volume fraction in the solidified portion of that sample was 28 vol. %. Therefore, from the former value and the measured compositions, the average oxide concentrations in the sample were determined to be 14.39 % Y_2O_3, 36.09 % BaO and 49.51 % CuO, on a molar basis, respectively. These numbers were in good agreement with the nominal concentrations of 13.86 % Y_2O_3, 35.57 % BaO and 50.57 % CuO, considering errors in volume fraction measurements (± 1%), and CuO losses by evaporation. Similar compositional variations were reported by Hojaji *et al.*[224] in melt processed samples containing excess yttrium. In their samples, the 123 matrix around 211 particles was also enriched in yttrium.

The present data suggests that the higher 211 content in the solidified material relatively to the precursor is accomodated by minor changes in both the compositions of the matrix and the particles.

5.3.6 Growth Orientation

Several microstructural features confirmed that the growth axis was parallel to the basal, or *ab* planes. In annealed samples solidified at low growth rates, the incipient twins shown in Fig. 5.22 developed into sets of mutually perpendicular twins. In $YBa_2Cu_2O_{7-\delta}$ twin boundaries lie along {110} planes; therefore, perpendicular sets of twins can only be imaged along the [001] direction. The observation of perpendicular twins in the plane of polishing, which was parallel to the filament axis, means that the [001] axis was also

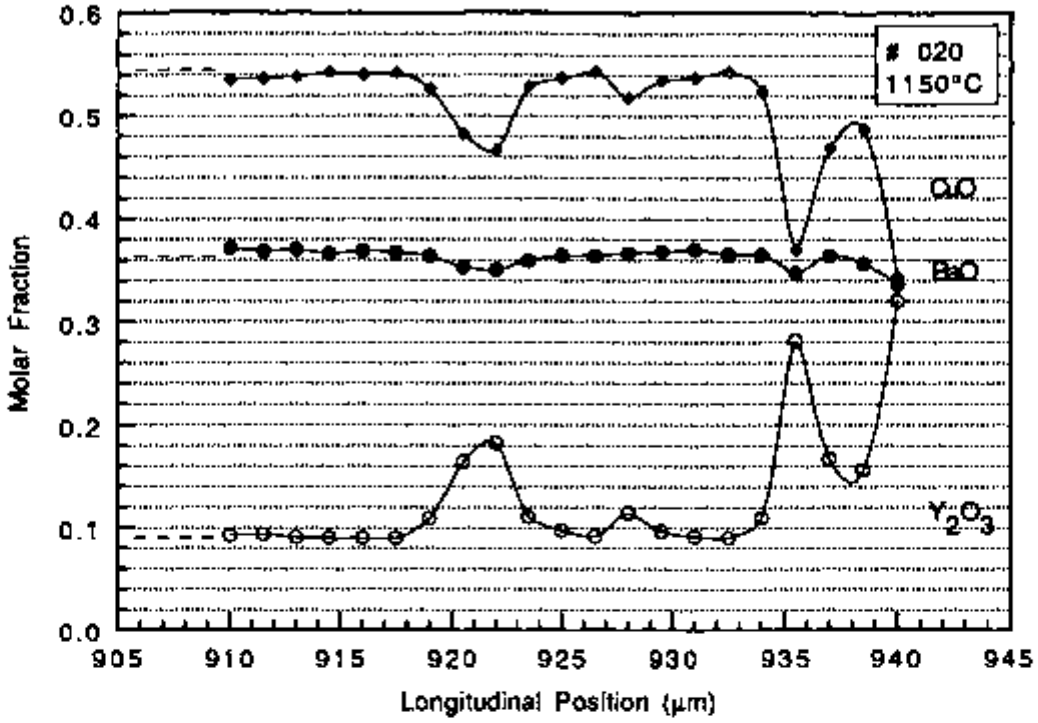

Fig. 5.26. Intragranular EPMA scan (Sample 020).

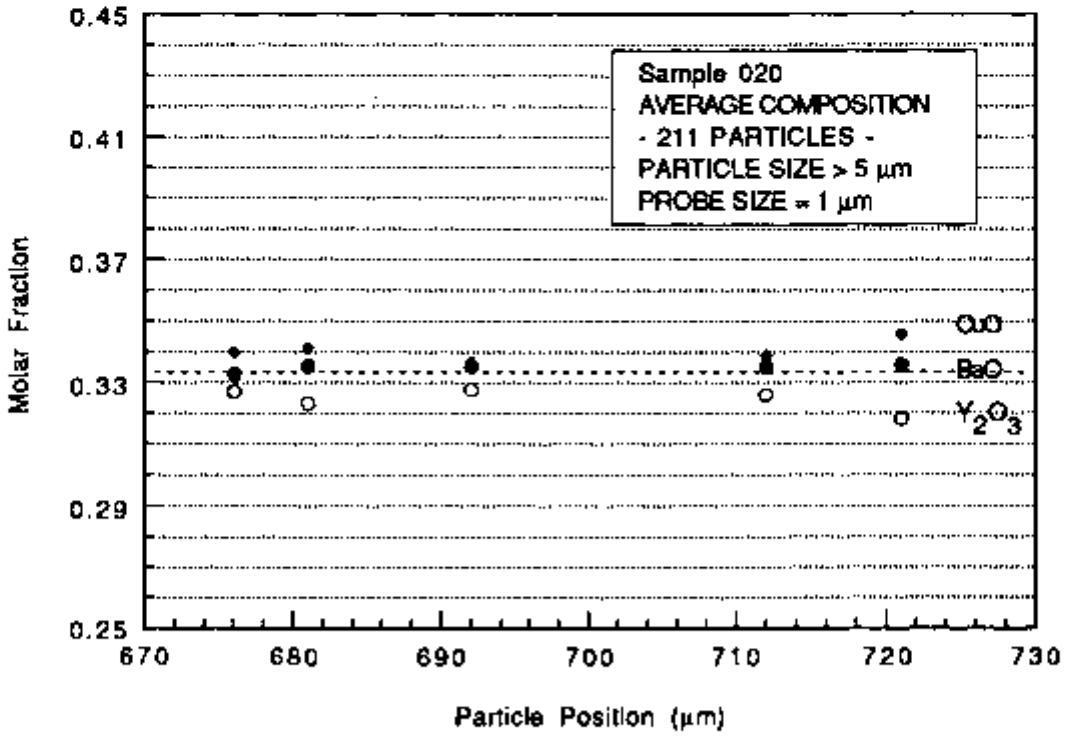

Fig. 5.27. Composition of 211 particles

perpendicular to the axis of the filaments or, equivalently, that the *ab* planes are parallel to the growth direction.

Cracks formed on cooling or during the metallographic preparation of filaments containing one or a few grains which usually run parallel or at small angles to the growth direction (Fig. 5.28). This observation and the fact that the fracture stress is much lower along the basal planes of 123, also confirmed that the filament is oriented along the basal planes.

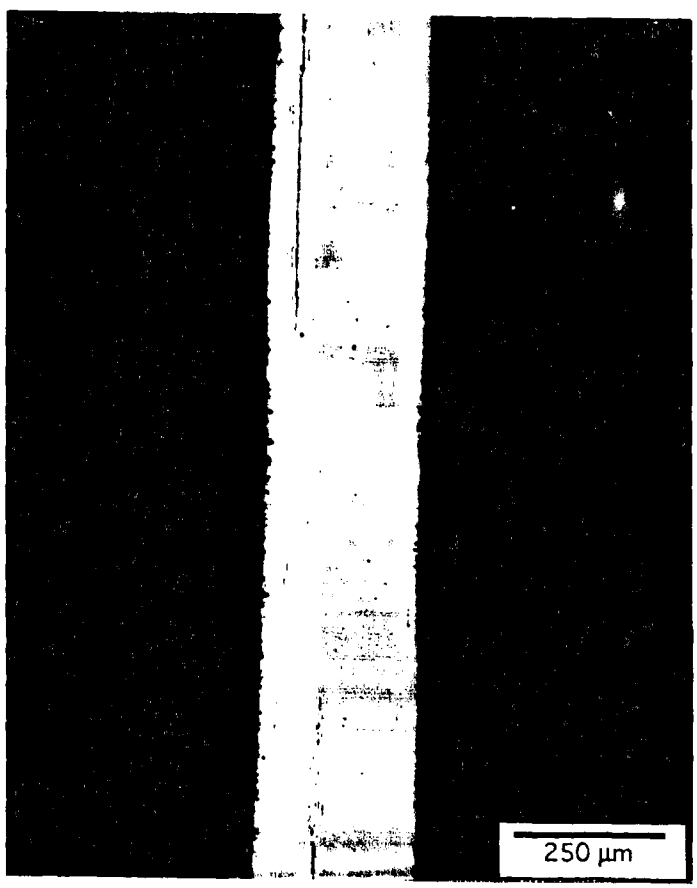

Fig. 5.28. Longitudinal section of a single-grained filament (Sample 029). Cracks were invariably found to run at very low angles to the growth direction in multigrained samples or parallel to the the axis of single-grained filaments.

Due to the difficulty in obtaining X-ray pole figures from such small diameter samples, transmission electron microscopy was used to determine the orientation of a single-grained filament. The metallographic specimen of Fig. 28 (a) was unmounted, glued to a TEM sample holder and thinned down to 20 μm by mechanical dimpling followed by ion beam milling for electron transparency. Fig. 5.29 shows a TEM image of the specimen, which exhibits a high twin density characteristic of orthorhombic $Y_2BaCu_3O_{7-\delta}$. The twins make an angle of 45° with the vertical direction of the micrograph, which is parallel to the growth axis, suggesting that the growth direction is [100].

5.3.7 *Low Angle Grain Boundaries/Platelets*

The individual grains in melt-processed 123 consist of thin platelets bounded by the basal (001) plane and stacked along the c-axis, which is parallel to the platelet thickness. To reflect the fact that the grains in melt-processed materials are composed of platelets with similar crystallographic orientation, they are commonly referred to in the literature as "domains".[11] Fig. 31 is a transversal fracture surface of an LHFZ filament containing a few domains.

Within an individual domain (or grain), the platelets are oriented such that the *c* axis is perpendicular or nearly perpendicular to the growth direction, which is normal to the plane of the picture [Fig. 5.31 (b)]. In their bi-crystals experiments, Babcock *et al.*[50] have demonstrated that boundaries formed at the intersection of mutually perpendicular sets of *ab* planes are not weak linked. A boundary of this kind is shown in Fig. 5.31 (b).

Platelet boundaries were assumed to be low angle boundaries by Jin *et al.*[87] However, Alexander *et al.*[170] have found no misorientation between adjacent platelets. These authors have also determined that platelet boundaries are filled with crystalline barium-copper oxide rich phases. Thus, they should behave as insulators, since their average thickness is of the orders of tens of nanometers. If this were the case, the magnetization of the samples should decrease with decreasing platelet thickness. Jin *et al.*[87] did not find any change in the behavior of their samples even when the plate thickness was reduced by one order of magnitude, and proposed that the platelets are not weakly coupled. Their data are reproduced in Fig. 5.31 and show that the plate thickness is roughly equivalent to the 211 particle size. Results from LHFZ samples apparently agree with their measurements.

Fig. 5.29. Twins in a single-grained orthorhombic LHFZ filament (Sample 029). The plane of the TEM foil was parallel to the filament axis. The twins are observed at a 45° angle to the growth direction (arrow), suggesting that the growth direction was [100].

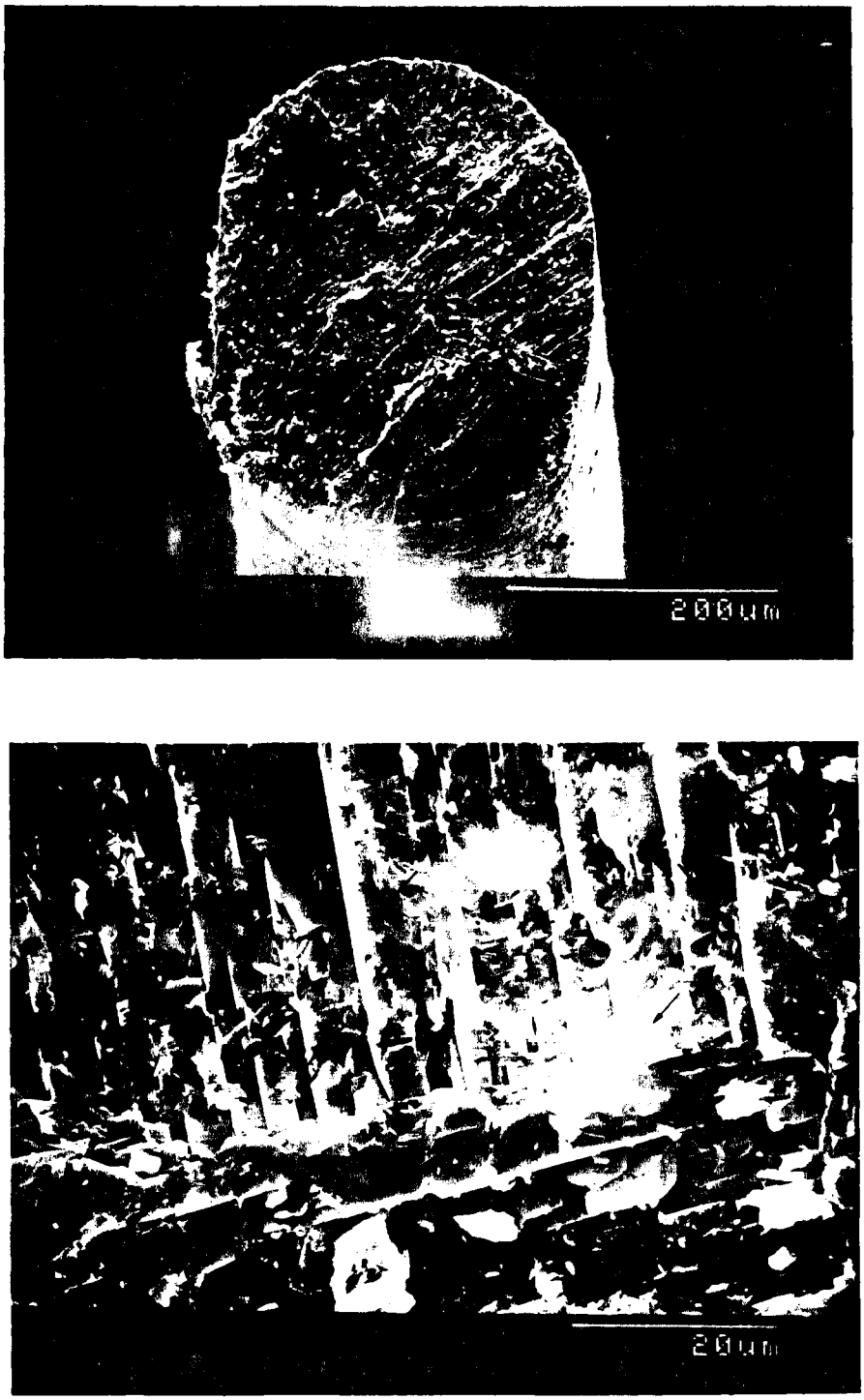

Fig. 5.30. (Top) Fractured cross section of a filament containing a few domains. (Bottom) The intragranular structure, composed by thin platelets stacked along the c-axis is shown in more detail in this micrograph. Also evident is the high density of bridges between platelets, which are indicated by arrows. Because of the existence of such bridges, each domain acts effectively as a single-crystal, providing non weak-linked paths for the flow of current. When more than one domain is present at steady-state growth, the misorientations among individual domains are given by rotation of individual platelet stacks about the [100] axis.

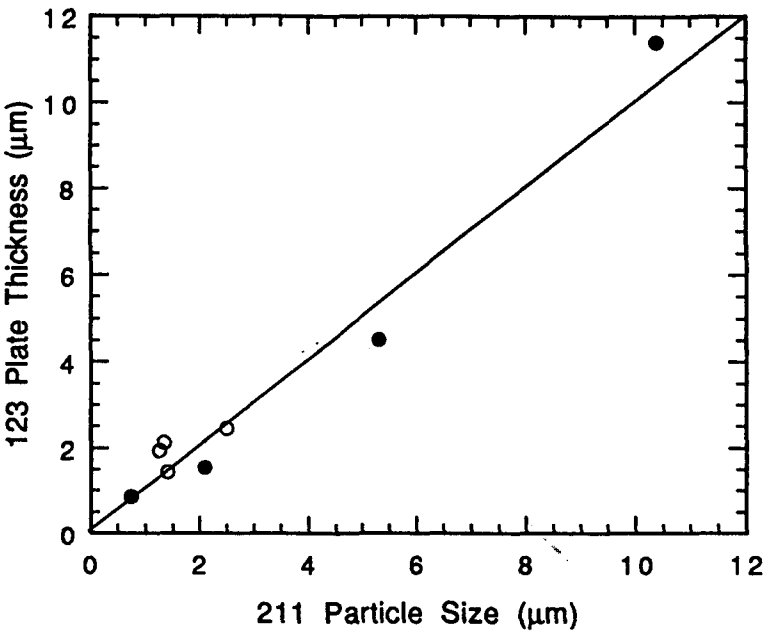

Fig. 5.31. Measurement of platelet spacing in 123 domains show that the plate thickness is roughly equivalent to the 211 particle size. Filled circles correspond to the measurements of Jin et al.[87] and open circles are from the present work.

Platelet boundaries can be easily identified in metallographic sections of samples solidified at low cooling rates ($GR < 0.01°C/s$),[11,170] but are generally not visible in LHFZ samples, which are solidified at much higher cooling rates ($GR > 1°C/s$). Apparently, the Ba-Cu oxide films between the platelets in the LHFZ samples are very thin or do not form at all.

Microtwins are also apparent along the fracture surfaces of LHFZ filaments, as shown in Fig. 5.32, which is from a filament grown at 2.78 μm/s (sample 080). The twin band spacing in Fig. 5.32 is about 88 nm; similar spacings were determined in the TEM micrograph of Fig. 5.29, which corresponds to a sample grown under similar conditions.

Alexander *et al.*[170] have observed that a common feature in the structure of melt processed 123 is the termination of a plate boundary within another platelet, as illustrated schematically in Fig. 5.33. Based on TEM observations, these investigators have proposed that the platelets are simply portions of a single crystal (the domain) and not components of a brick-wall structure, proposed earlier in the literature.[225,226]

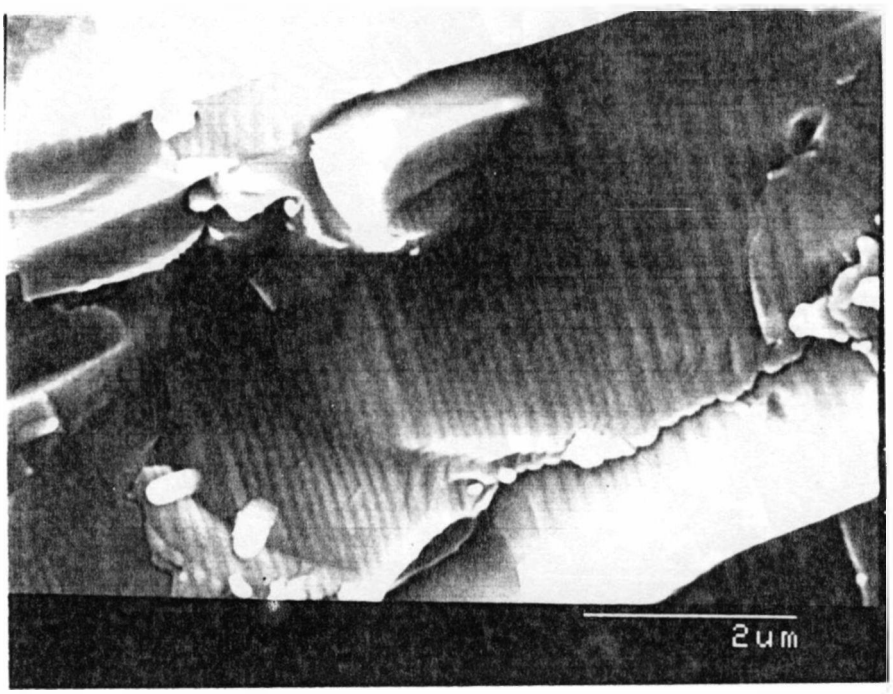

Fig. 5.32. High resolution SEM image of the fracture surface of a filament grown at 2.78 µm/s, annealed at 460°C. in flowing oxygen for 40 h. The filament contains a high density of microtwins.

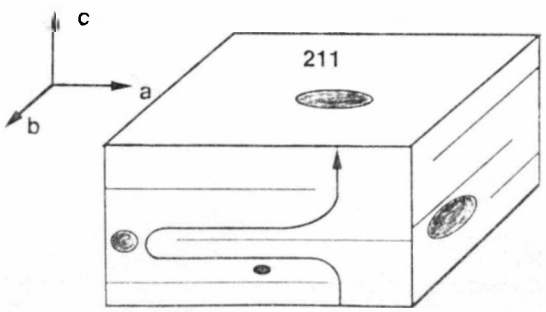

Fig. 5.33. Schematic model for current flow parallel to the c-axis solely through single-crystalline material within a domain of melt-processed 123 (From ref. 170).

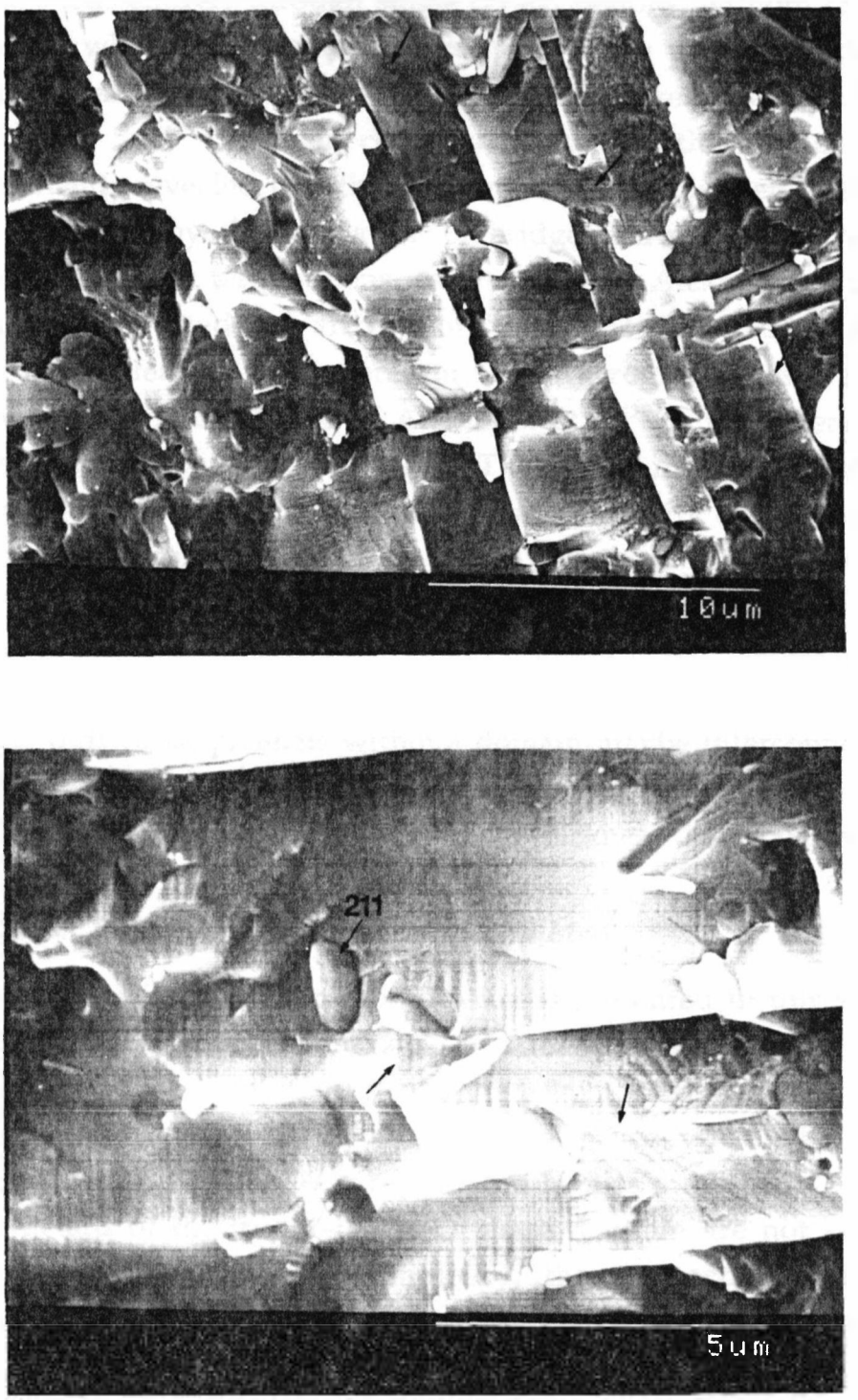

Fig. 5.34. High-resolution SEM fractographs of filaments grown at 2.78 µm/s, showing links across plates (bridges) formed during growth when a plate boundary met a 211 particle. Bridges are indicated by arrows. 211 particles are frequently seen emerging from underneath the bridges. The bottom picture also shows deformed plates meeting at a grain boundary.

One important characteristic of such a structure is that current can flow along the *c*-axis entirely through single crystal regions, without crossing plate boundaries, which may be weakly coupled. The present microstructural observations also suggest the existence of the current paths schematically shown in Fig. 5.33. However, close examination of the fracture surfaces of LHFZ filaments revealed that the interconnection of platelets within a single domain occurred by the formation of bridges across boundaries and not because of boundary terminations, as proposed by Alexander *et al.*[170] These bridges are indicated by arrows in Figs. 5.31 and 5.34. A common microstructural feature in the present SEM micrographs, as well as in the TEM and optical micrographs of Alexander *et al.*[170] is the emergence of 211 particles from underneath the bridges. The optical micrograph of Alexander *et al.* also shows that the plate boundary has continuity away from a particle or group of particles.

Many published micrographs of melt textured 123, particularly those from the work of Raveau,[227] McGinn,[156] and Alexander *et al.*[170] suggest that lateral growth of 123 platelets may occur in the volume surrounding a 211 particle. Therefore, individual platelets within a domain maybe interconnected due to the very presence of 211 particles. These interconnections may explain the independence of the magnetization on plate thickness described by Jin *et al.*[87]

5.4 Peritectic Solidification from a Semisolid Melt

A simple model for peritectic solidification is presented in this section. The model is based on experimental observations described in the preceding sections, as well as on results obtained in a complementary study of directional solidification of 123 (γ) by the electrically-heated floating zone technique (EFHZ); The model is reproduced here as published.[89]

Many details of the true Y-Ba-Cu-O phase diagram are not known in the melting range.[116] Thus, for simplicity, the peritectic solidification is considered for the case of a binary system. The treatment that follows refers to Fig. 5.1 as if it were a true binary diagram.

The principal assumption of the present model is that the peritectic reaction takes place by diffusional transport through the liquid. Dissolution of the 211 (α) particles occurs in the liquid just ahead of the solidification interface and solute then diffuses to the interface where it is consumed by

growth of the crystal. This interpretation follows directly from microstructural observations of the solidification interface, illustrated in Fig. 5.17. Yttrium gradients into the liquid phase near 211 grains have actually been measured on quenched samples by EDS analysis.[229]

The average α interparticle distance is taken as 2ℓ and the alloy is assumed to be slightly hypo-peritectic, so that some α phase is always retained in the final structure. The solute diffusion profile in the growth direction (x) ahead of the interface varies with time and location y perpendicular to the growth direction. This profile is sketched in Fig. 5.35 (b), along the line AA' of Fig. 5.35 (a). In the following, this curve will be taken as representative of the time averaged solute profile in front of the solidification interface. The curve is drawn assuming diffusion to the interface over an average distance ℓ, with liquid compositions at $x = 0$ and at $x = \ell$ determined as follows.

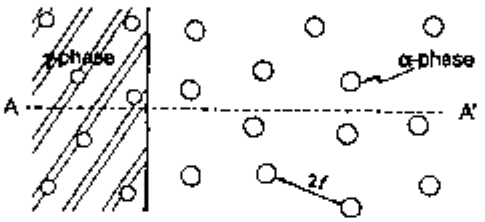

(a)

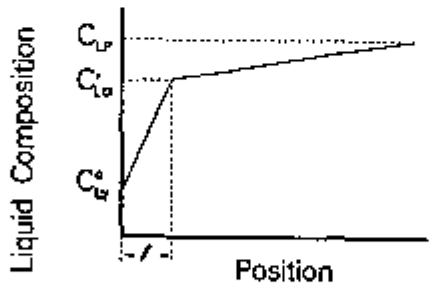

(b)

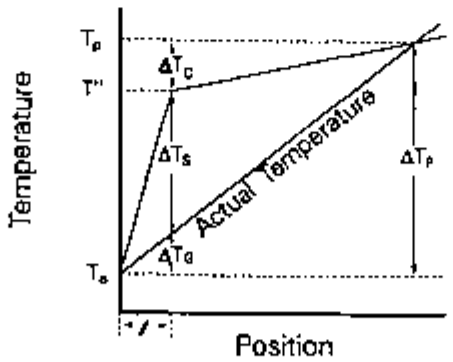

(c)

Fig. 5.35. Peritectic solidification model; (b) Solute diffusion profile in front of the advancing γ interface; (c) Temperature distribution in the liquid ahead of the solidification interface.

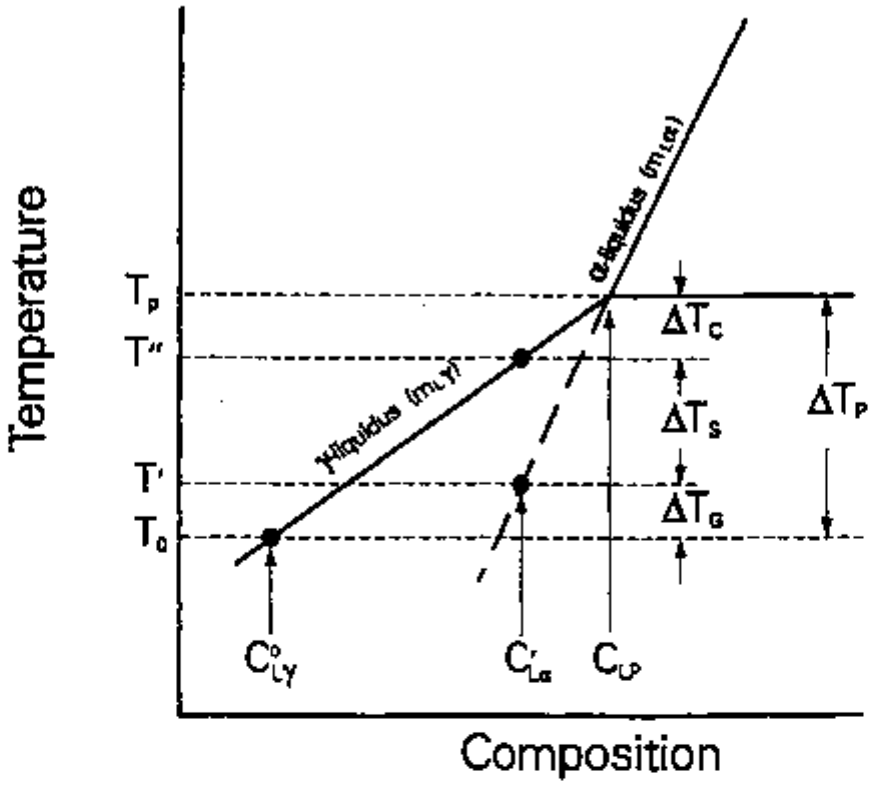

Fig. 5.36. Enlarged section of the phase diagram of Fig. 5.2 in the region of the peritectic.

Interfacial equilibrium is assumed between the α particles and their surrounding liquid. The particles are also considered large enough so that the effects of radius of curvature on melting point are negligible. When the particles are sufficiently small, the radius of curvature effect could provide a significant driving force for mass transport during the solidification of γ. The case where the radius of curvature of the α phase comprises the driving force for the peritectic reaction has been treated in detail by Izumi *et al.* [168]

The interfaces are faceted in the actual case of solidification of 123. Thus, they are not in equilibrium with the melt. Actually, faceting may be essential to achieving the plane front solidification observed in 123. Nonetheless, it is assumed that the undercooling at the faceted interface is small compared with the solutal undercoolings to be described below, and that the equilibrium partition ratio also applies at the γ interface.

Fig. 5.36 is an expanded portion of the phase diagram of Fig. 5.1, in the region of the peritectic. The dashed line represents the metastable extension

of the α liquidus. The temperature of the γ interface, T_0, is undercooled an amount ΔT_p below the peritectic temperature, T_p, where

$$\Delta T_p = \Delta T_C + \Delta T_s + \Delta T_c, \tag{5.3}$$

In the above expression, ΔT_C is the depression of the integrated temperature resulting from the temperature gradient, G. The maximum "constitutional supercooling" ahead of the interface is represented by ΔT_s, the temperature difference between the equilibrium liquidus and the actual temperature at $x = \ell$. ΔT_c is the temperature depression resulting from the deviation in solute concentration at the α interface from that of the peritectic liquid composition, c_{Lp}. These quantities are shown diagramatically in both Figs. 5.35 (c) and 5.36. From Fig. 5.35 (c),

$$\Delta T_C = (T' - T_0) = G\ell. \tag{5.4}$$

The solute content in equilibrium with the γ interface (at $x = 0$, $T = T_0$) is $c^0_{L\gamma}$, and that at $x = \ell$ and T' in equilibrium at the α particles is $c'_{L\alpha}$. These quantities are shown in Figs. 5.35 (b) and 5.36. These two points define the solute distribution curve of type 5.35 (b) for $x < \ell$. For $x > \ell$ the curve is given by the equilibrium α liquidus. Equating solvent rejected from the growing γ interface with that diffusing into the liquid gives

$$-R(c_{s\gamma} - c^0_{L\gamma}) = -D_L\left[\frac{c'_{L\alpha} - c^0_{L\gamma}}{\ell}\right], \tag{5.5}$$

where R is the growth rate and D_L is the diffusion coefficient of solute in the liquid. The slope of the equilibrium γ liquidus and metastable α liquidus are both assumed to be constant and are denoted by $m_{L\gamma}$ and $m_{L\alpha}$, respectively. A relation between interface undercooling (ΔT_p) and growth rate, R, can be derived by assuming $c_{s\gamma} - c^0_{L\gamma} \approx c_{s\gamma} - c_{Lp}$ and by substituting relationships for $c^0_{L\gamma}$ and $c'_{L\alpha}$ into Eq. (5.5). Linear liquidus lines, as shown in Fig. 5.36, result in $c^0_{L\gamma} = c_{Lp} - \Delta T_p / m_{L\gamma}$ and $c'_{L\alpha} = c_{Lp} - (\Delta T_p - \Delta T_C)/m_{L\alpha}$. Substitution of these expressions into Eq. (5.5) and making use of Eq. (5.4) gives

$$\Delta T_p = \left[\frac{R\ell}{D_L}(c_{s\gamma} - c_{Lp}) - \frac{G\ell}{m_{L\alpha}}\right]\frac{m_{L\gamma}m_{L\alpha}}{m_{L\alpha} - m_{L\gamma}}. \tag{5.6}$$

Thus, ΔT_p is linearly proportional to R when G is sufficiently small. Similarly, the following relation can be written between R and ΔT_s

$$\Delta T_s = m_{L\gamma}\frac{R\ell}{D_L}(c_{s\gamma} - c_{L\beta}) - G\ell. \tag{5.7}$$

The quantity ΔT_s is the constitutional supercooling at $x = \ell$; it is the maximum constitutional supercooling in the semisolid region. In solidification of this type, there must always be finite constitutional supercooling in front of the growing interface in order to create the compositional driving force for diffusion from the particle surface to the crystal interface. Apparently, the surface energy relationships and faceting effect permit interface stability with some finite amount of undercooling ΔT_s (or, alternately stated, with some finite gradient of undercooling) $\Delta T_s / \ell$. Thus, if some specific maximum constitutional supercooling is assumed, Eq. (5.7) provides a description of the important variables which influence maximum growth rate, R_{max} for plane front solidification. The equation may therefore be written:

$$R_{max} = \frac{D_L}{\ell(c_{s\gamma} - c_{L\beta})}\left[\frac{(\Delta T_s)_{max} + G\ell}{m_{L\gamma}}\right]. \tag{5.8}$$

The significance of temperature gradient, G, depends on the relative magnitude of $G\ell$ and $(\Delta T_s)_{max}$. Since ℓ is of the order of the particle dimension, Eq. (5.8) indicates that the maximum growth rate is relatively insensitive to temperature gradient.

An interesting feature of this type of solidification is that the total depression of the interface temperature, ΔT_p, may be much greater than the constitutional supercooling, ΔT_s, when $m_{L\alpha} \rightarrow m_{L\gamma}$. This may be seen by combining Eqs. (5.7) and (5.8):

$$\Delta T_p = \left[\frac{m_{L\alpha}}{m_{L\gamma} - m_{L\alpha}}\right]\Delta T_s + G \tag{5.9}$$

At values of $R > R_{max}$ cell, dendrites, or new grains are expected to form as was experimentally observed in this study. On the basis of established solidification principles, it is expected that at $R > R_{max}$, where cells or dendrites

form, the "tip" of the solidifying front should cease to dropping rapidly with increasing R.[180] The temperature of the "root" of the solidification interface should, however, continue to drop, ultimately reaching (in this case) the eutectic temperature of approximately 1173 K. These expectations are in qualitative agreement with experimental results presented in Ref. 89.

5.5 Discussion

5.5.1 Peritectic Solidification From Semisolid Melts

Despite the difference of more than two orders of magnitude between the temperatures in the EHFZ and LHFZ methods, the maximum velocity for continuous growth of 123 crystals increased only by a factor of 3 (Fig. 5.10). Comparison of results from different studies has to be done with caution because of the wide variations of experimental parameters and configurations. Nonetheless, the growth velocities required to produce large 123 crystals in the EHFZ experiments reported in Ref. 89 are similar to those observed by others.[161,169,157]

The preceding theoretical analysis suggests the fundamental importance of growth rate for semisolid solidification of 123 crystals. The model assumes that the composition gradient between the crystal interface and 211 particles is responsible for a significant portion of the interfacial undercooling. The magnitude of the total temperature depression of the interface is intimately related to phase equilibria in the region of the peritectic, as described in Eq. (5.9). Reference to the simple binary diagram of Fig. 1 shows that the liquidus slopes must be large for small c_{L_p}. Thus, Eq. (5.9) predicts a large value of ΔT_p for systems in which the solute is sparingly soluble. Studies of high temperature phase equilibria in the Ba-Y-Cu-O system[116] have reported yttrium concentrations in the liquid that range from 2 to 4 mol %. Additionaly, many studies report that the slope of the 211 liquidus is large compared with that for 123 near the peritectic temperature.

Growth of 123 crytals at the solidification front requires that yttrium be supplied at a sufficient rate to the interface. Eq. (5.5) describes the mass balance restriction. The supply of yttrium is provided by dissolution of 211 in the liquid ahead of the groth front. Since yttrium is only sparingly soluble in the liquid, it seems likely that, at sufficiently high growth rates, its transport to the interface is the rate limiting step.

The predictive power of Eqs. (5.8) and (5.9) can be verified by suitable approximation of the diffusivity and phase equilibria. Estimates for the yttrium diffusivity in the liquid were obtained from the coarsening data shown in Fig. 5.19, since measured values were not found in the reviewed literature. Ostwald ripening of ceramic grains in contact with liquids at high temperature has been used to estimate diffusivities in liquids.[197] As discussed in Chapter 4, both experimental and theoretical work have demonstrated that the classical equation for coarsening is still applicable to solid-liquid systems in which the solid content is large. However, the rate constant for coarsening, K, increases with the volume fraction of solid. To account for this effect, the modified version of the classical equation for coarsening by volume diffusion[199] will be employed here:

$$r^3 - r_0^3 = \alpha(\varphi)\frac{8DcM^2\gamma}{9\rho^2RT}(t - t_0), \qquad 5.10$$

where the parameter $\alpha(\varphi) = K(\varphi)/K(0)$ takes into account the volume fraction dependence. The volume fraction of 211 in the semisolid zone is $\varphi = 0.62$. For this value, the theoretical treatment of Brailsford and Wynblatt[199] predicts that $\alpha \approx 4.2$. An approximate value for $K(\varphi)$ can be obtained from measurements of particle size in the zone of a LHFZ sample grown under conditions closer to "static" coarsening experiments, that is, at low growth rates. In the low growth rate range, at 1.39 μm/s, it took 236 s for the particle size to increase from the initial value of ~ 1 μm to about 3.3 μm. The corresponding value of $K(\varphi)$ is, therefore, 1.58×10^{-19} m^3/s. This value agrees well with that determined by Rigby *et al.*[207] for YEr-211 at 1367 K, which is 4.0×10^{-19} m^3/s. The other quantities needed to estimate the diffusivity of yttrium are the 211 density (6.19 g/cm^3) and molecular weight (458.68 g), the average zone temperature (~1400 K), the solubility of yttrium in the liquid and the interfacial energy. A liquid composition of 1.5 mole% 211 at the peritectic temperature is consistent with the phase equilibria studies discussed in Chapter 2. This composition is equivalent to ~ 93 mole/m^3, if the density of the barium cuprate liquid is taken as 5.3 g/cm^3. A reasonably good estimate of the interfacial energy is 1.0 J/m^2.[228] Substitution of the previous numbers in the expression for the rate constant gives a value of 7.9×10^{-10} m^2/s for the diffusivity of yttrium in the barium cuprate liquid.

Estimates of the liquidus slopes, $m_{L\alpha}$ and $m_{L\gamma}$ are also required to use Eqs. (5.6) and (5.8). The freezing range over which 123 is in equilibrium with liquid is approximately 100 K[116] while the composition varies from c_{L_β} to the eutectic composition, $c_{e\gamma}$. The eutectic is known to contain only very small amounts of yttrium.[127] A rough estimate of $m_{L\gamma}$ is therefore, 100/(93 - 0.0) or 1.1 K m^3/mole. The liquidus slope of the high temperature phase, 211, is more difficult to estimate. Phase equilibria results[116] do indicate that the liquidus composition varies significantly from c_{L_β} only when the temperature is much greater than the peritectic temperature. This is consistent with a comparatively large value of $m_{L\alpha}$ or $m_{L\alpha} >> m_{L\gamma}$. Therefore, the term $m_{L\alpha}/(m_{L\alpha}-m_{L\gamma})$ is close to unity.

Equation (5.6) indicates that the total interface undercooling is linearly proportional to the growth rate, R, at sufficiently small values of $G\ell$. This was indeed observed in Ref. 89 for growth rates where large facets are present at the solidification interface. Measurement of $\Delta T_p/R$, in Ref. 89 yielded a value of 1.1×10^5 K s/m. With the approximations above it is possible to compare the measured slope with the calculated value of the slope. Diffusion length scales are assumed to be of the same order of magnitude as the particle size in the EHFZ samples (ℓ = 10 μm), and the concentrations $c_{e\gamma}$ and c_{L_β} are taken as 4.8×10^3 and 93 mole/m^3, respectively. Finally, if $m_{L\alpha}/(m_{L\alpha}-m_{L\gamma})$ is close to unit, substitution in Eq. (5.6) predicts that $(\Delta T_p/R)_{calc}$ is 0.7×10^5 Ks/m. The calculated value differs from the measured value by 36%; this difference is small, considering the number of approximations involved in the calculation.

The data of Fig. 5.10 indicate a slight temperature gradient dependence of the maximum growth rate for planar growth. This second order dependence is predicted by Eq. (5.8). Diffusion length scales of the order of 1 μm suggest, however, that the term $G\ell$ is small, even for the large temperature gradients used in this study, since $\Delta T_G \approx (1 \times 10^{-6}\ \text{m})(10^6\ \text{K/m}) = 1$ K. Thus, the increase in interface stability of LHFZ samples over those prepared by low temperature gradient techniques cannot be completely attributed to the effect of temperature gradient. The filaments for LHFZ were richer in 211 than the rods used in the EHFZ experiments reported by Cima *et al.*[89] and contained much smaller initial 211 particle size. Secondly, by LHFZ it is possible to achive very short zone lengths in small diameter filaments which means that the particles have a very short residence time in the liquid. Thus, coarsening

was much less significant in the LHFZ experiments. These factors combine to effectively reduce the characteristic diffusion distance in the LHFZ samples which in turn requires a large growth rate to produce the same degree of undercooling, as predicted by Eq. (5.9) in the limit of small $G\ell$. Equation (5.9) also suggests that the ratio of maximum growth rate between the LHFZ and the EHFZ samples should be in the inverse ratio of the 211 particle sizes for each case or approximately (10 μm)/(3 μm) ≈ 3.3. The maximum growth rates for the two techniques indeed differ by a factor of 3, as shown in Fig. 5.10.

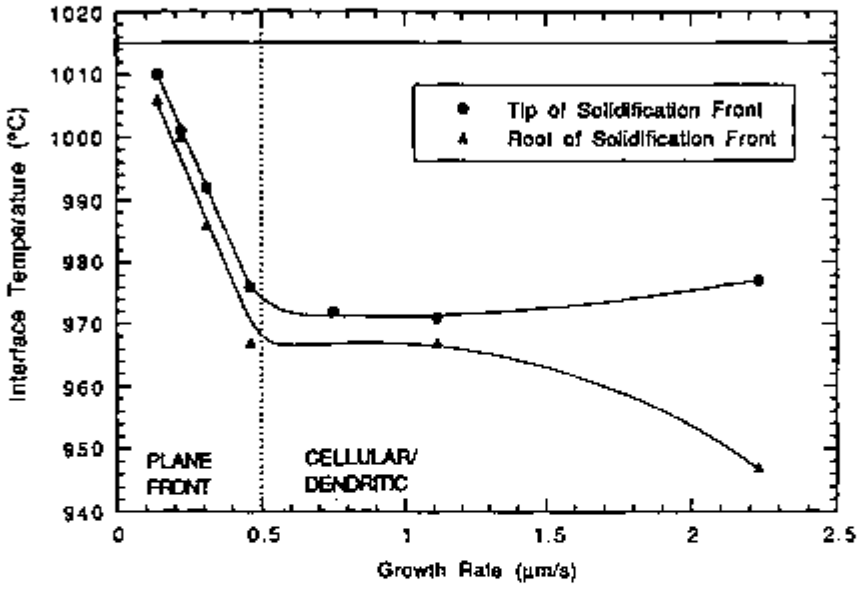

Fig. 5.37. Undercooling at the growth front during EHFZ solidification of 123. From Cima *et al.*[89]

In Fig. 5.37, from Cima *et al*,[89] the interface temperature during solidification of 123 by the EHFZ technique is plotted against the growth rate. The magnitude of the undercooling shown in Fig. 5.37 is large, given what is known about the phase equilibria in the Y-Ba-Cu-O system. Equation (5.9) indicates that $\Delta T_s \approx \Delta T_p$ when $m_{L\alpha} \gg m_{L\gamma}$ and $G\ell$ is small. Thus $(\Delta T_s)_{max}$ is of the order of $(\Delta T_p)_{max}$, which is about 48 K[89,220]. This is a substantial fraction of the freezing range over which 123 is in equilibrium with liquid, known to be approximately 100 K.[116] The highly faceted morphology of the 123 crystals is consistent with the large undercooling required to nucleate new 123 grains ahead of the solidification interface. The data in Fig. 5.37 also indicate that 211 particles do not act significantly as nucleation sites for the growth of 123

crystals. Otherwise, nucleation would occur at temperatures much closer to the peritectic temperature.

5.5.2 *Growth Parameters and Filament Microstructures*

Fig. 5.38 attempts to summarize the most important relations among the many variables associated with LHFZ growth of superconducting filaments. Variables that can be controlled independently include the chemistry, nature of phases and size of the precursor, power density distribution in the beam, growth rate, oxygen pressure and growth method. Variables represented within the dashed circle are those related to the semisolid zone and variable dependencies are indicated by arrows. This simple picture helps to understand why there are so much discrepancies among literature results for melt processed 123 and why sometimes results are irreproducible.

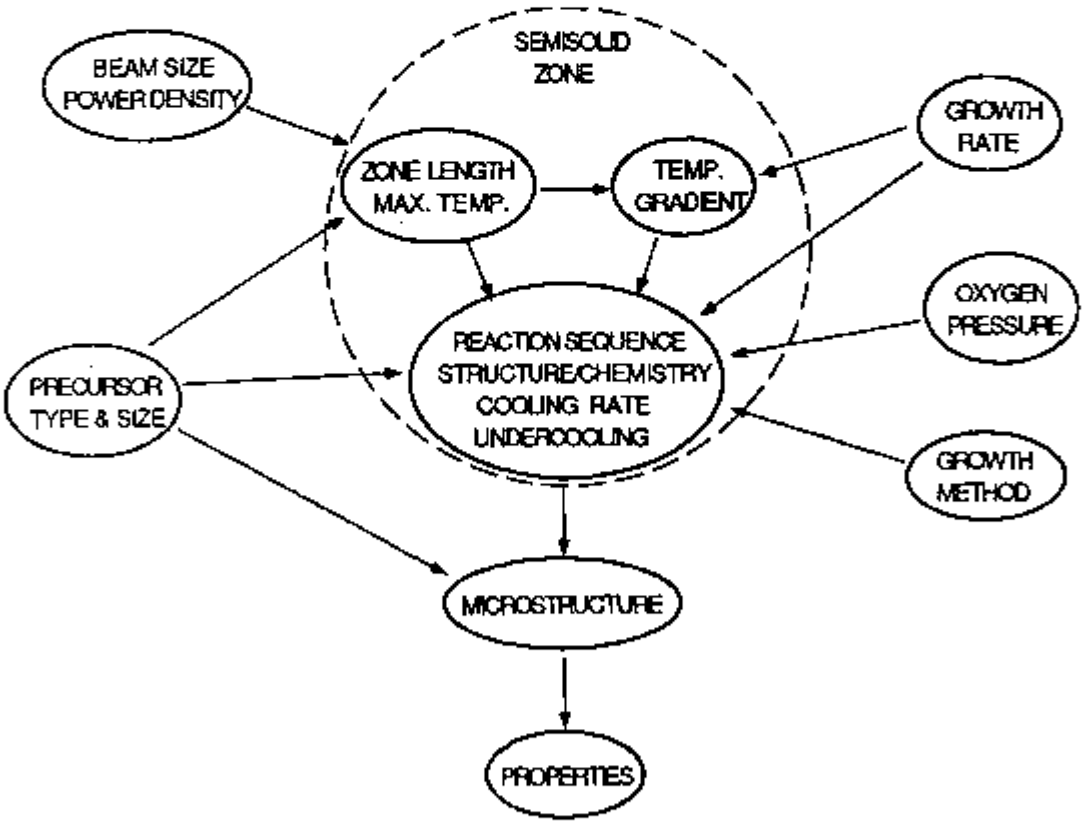

Fig. 5.38. Relations among growth parameters in directional solidification of 123 filaments by the laser-heated floating zone technique.

In LHFZ growth of 123, the semisolid zone is not "structureless", as in conventional floating zone solidification of materials that melt congruently. Thus, one must be aware that, in addition to the growth rate, temperature gradient and oxygen pressure, the solidification microstructures also reflect the thermal history of the semisolid material. Growth parameters that affect the structure of the zone include reaction sequence within the zone and characteristic time scales for the reactions, oxygen pressure, and growth method. In the case when the precursors contain addition of high-temperature phases, say 211, the structure of the precursor is not completely destroyed by partial melting and will dictate, to some extent, the solidification microstructures obtained under a given set of growth parameters. Solidification microstructures will also be affected by the porosity of the precursor, since the latter also influences the morphology, reaction sequence and chemistry of the semisolid zone. For example, if the 123 plus 211 precursors are fully dense or contain closed porosity, barium cuprate liquid cannot infiltrate the precursor. Y_2BaCuO_5 phase will not be in contact with liquid at temperatures below the peritectic temperature, and two invariant reactions, p2 and e3 (Table 2.2), will not occur. This will result in a zone composition profile that is different from that obtained in porous samples

The important point here is to select precursors, growth parameters and growth method so as to gain control over the structure, nature and chemistry of the semisolid material right ahead of the solidification interface. In this way, it might be possible to simultaneously change morphology, size, density and orientation of non-superconducting inclusions and crystalline defects from the micrometer down to the nanometer range *during* the solidification process.

5.6 Conclusions

The present investigation revealed a new mechanism for peritectic solidification, previously not observed in peritectic systems. Semisolid solidification of $YBa_2Cu_3O_{6+\delta}$ is accompanied by several phenomena that are not encountered in conventional solidification. First, the peritectic reaction occurs by dissolution of the high-temperature phase (Y_2BaCuO_5) into the liquid followed by reprecipitation on the 123 crystal surface. This interpretation is the result of direct microstructural observation of quenched

solidification interfaces. The reaction effectively stops once the crystal engulfs the high temperature phase since the contribution of solid-state diffusion is negligible. Thus, the peritect reaction does not proceed by the more conventional mechanism in which the reaction occurs at the interface between the high-temperature phase and the liquid.

Secondly, the high-temperature phase particles must become supercooled very close to the crystal interface in order to create the concentration gradient needed to drive mass transport and thereby sustain the reaction. Consideration of mass transport restrictions and thermodynamic driving force shows that the largest constitutional undercooling is a small distance ahead of the interface. This condition in classical solidification would normally cause a planar solidification interface to become unstable since small perturbations would grow. The situation with $YBa_2Cu_3O_{6+\delta}$ is, however, much different. Apparently, the highly faceted crystal interface prevents the growth of such perturbations and the growth becomes limited by the undercooling that will cause nucleation of new crystals ahead of the interface. The concepts above can be expressed quantitatively and be used to show that the maximum growth rate at which a planar interface can be sustained is inversely proportional to the Y_2BaCuO_5 particle size. This model quantitatively predicts the relationship between interface undercooling and growth rate when reasonable values of the physical parameters are used. The magnitude of the temperature gradient has only a minor effect on the maximum growth rate for planar front solidification as was observed experimentally. Analysis indicates that production of single crystal filaments of $YBa_2Cu_3O_{6+\delta}$ using simple planar growth may be limited to growth rates of the order of 3 μm/s using 1 μm particles of Y_2BaCuO_5. Such low growth rates mean that other growth morphologies must be developed that can be produced faster, yet lead to microstructures that are not weak linked and present high flux creep strength.

Chapter 6
Directional Phase Formation on Melting Via Peritectic Reaction

6.1 Introduction

This work concerns the structure of Y-Ba-Cu-O filaments directionally melted and solidified in low oxygen pressures by the laser heated float zone technique. Peritectic γ ($YBa_2Cu_3O_{7-\delta}$) and hypo-peritectic γ plus 20 wt.% α (Y_2BaCuO_5) compositions were investigated. Within a wide range of growth rates, similar microstructures were obtained for both compositions. It will be shown that the growth front morphologies observed in quenched semisolid zones of peritectic and hypo-peritectic specimens are rather unusual. Incongruent melting of the lower temperature phase resulted in aligned growth of rods or plates of a high-temperature phase, ε, (Y_2BaO_4) in the liquid phase, *on heating*. This is the first time such structures are reported in ceramic systems with peritectic reactions.

The following sequences of peritectic reactions were observed on melting in compositions near 123:

$$\gamma \rightarrow \alpha + L \rightarrow \delta + L \qquad (P_{O_2} > 10^3 \text{ Pa}) \qquad (1)$$

$$\gamma \rightarrow \alpha + L \rightarrow \varepsilon + L \rightarrow \delta + L \qquad (8 \text{ Pa} < P_{O_2} < 10^3 \text{ Pa}) \qquad (2)$$

$$\gamma \rightarrow \varepsilon + L \rightarrow \delta + L \qquad (P_{O_2} < 8 \text{ Pa}) \qquad (3)$$

In the above reactions, α and δ (Y_2O_3) phases comprised equiaxed particles. Rod-like ε was formed upon incongruent melting of α at $8 \text{ Pa} < P_{O_2} < 10^3$ Pa. At oxygen pressures below about 8 Pa, α was no longer formed and the oriented ε phase formed directly from γ, and was plate-like in morphology. The reactions $\alpha \rightarrow \varepsilon + L$ and $\gamma \rightarrow \varepsilon + L$ were not observed in the system Y-Ba-Cu-O prior to this work.

So far as it was possible to determine, the only previous report in the literature of formation of a directional structure on heating by a peritectic reaction is that by Hillert and Uhrenius[230]. These authors rapidly heated a

single phase specimen of the intermetallic Γ phase from the peritectic Fe-Zn system.[231] On heating, Γ decomposed forming a rod-like aligned structure of a higher temperature phase and liquid, which was preserved by quenching.

In Chapter 5, it was shown that in the solidification of γ from semisolid melts, the peritectic reaction occurs by dissolution of the high temperature phase, α, in the liquid ahead of the growth interface, and subsequent reprecipitation on the γ crystal surface. Solute diffusion in the liquid is the limiting mass transfer process. Solidification rates at which a plane front can be sustained are limited by diffusion distance, hereby α particle size. Thus, coarsening of α particles during the time they remain in contact with the liquid can result in reduction of permissible solidification rate. Another problem arises due to the pronounced temperature dependence of the liquid surface tension,[232] which will lead to surface tension driven flow of liquid, especially if large temperature gradients are applied.

Both the foregoing problems can be minimized by introducing a dispersion of fine α particles in the polycrystalline precursors, slightly displacing the overall composition towards α along the tie line joining α to γ[89,151,184] (Fig. 2.16), and by minimizing the time a given location is in the semi-solid temperature region. A higher volume fraction of α in the semisolid hypo-peritectic compositions can reduce liquid flow and decrease diffusion length scales in the semisolid zone during directional solidification. This was the basic motivation for using filaments containing excess α in the solidification experiments described in the previous chapter. Another solution to the above problems, in principle, would be to solidify from a wholly different melt structure, with the precursor phase being different in form and perhaps composition. Thus, the forms and types of phases studied on melting in this chapter have potential practical interest in the production of high temperature superconducting materials.

Temperature-P_{O_2} conditions for the stability of γ, α, ε and δ were determined from metallographic, X-ray, and electron microprobe analysis of quenched and as-solidified specimens. This information provided a qualitative picture of the P_{O_2} dependent changes in the related pseudo-binary phase diagram, and of the expected growth morphologies in pressure range between 8 Pa and ~10^6 Pa.

Directional growth of the ε phase from α was modelled in a simple way. The α-particles ahead of the ε interface dissolve in the superheated liquid and solute transport for ε growth is assumed to be limited by diffusion along the growth direction over distances equal to half the rod or plate spacing. A relation between superheating at the growth interface and growth rate was derived from the present model. Some possibilities for making use of such aligned structures in the growth of the superconducting compound γ are discussed.

6.2 *Experimental Procedures*

Polycrystalline filaments fabricated according to the description provided in Chapter 3 were used as feed materials in the directional solidification experiments reported here. Details about the solidification technique are the same described in chapter 5, except that only method 2 (Fig. 5.3) was used in this case.

Phase-pure γ and γ + 20 wt.% α filaments, hereafter referred to as peritectic and hypo-peritectic samples, respectively, were used as feed materials for the solidification experiments.

Filaments a few centimeters long were gripped by chucks and precisely aligned before being inserted in the crystal grower chamber. The chamber was evacuated to 30 Pa, pressurized to 0.13 MPa with oxygen and then evacuated again. Absolute oxygen pressures were maintained within the range 6 to 70 Pa in all but a few experiments. After adjusting the oxygen pressure in the chamber, two opposing 900-μm diameter beams were focused onto the fibers to produce hot zones with lengths varying between 500 and 1500 μm. Fibers were pulled downwards through the hot zone at nominal rates from 1.1 to 32.2 μm/s. Temperature control during growth was achieved by adjusting the laser power according to the readings provided by an optical micropyrometer. The zone was first scanned with the pyrometer to locate the position that corresponded to the maximum temperature reading. The laser power was then adjusted to obtain the desired temperature reading in that location. Power values typically between 1.2 and 1.5 W were needed to attain a maximum temperature of 1473°C in the molten zone. Since these values

were in the very bottom of the scale, some problems with power fluctuations were encountered during growth. The power oscillations are reflected by variations in the reported maximum zone temperatures, which are uncorrected for emissivity. Growth was interrupted by closing the beam shutter after obtaining the desired filament length. This effectively quenched the phases present in the partially molten zone as discussed next.

As-grown filaments were kept in sealed vials containing a desiccant, to prevent the reaction of their component phases with the atmosphere. Metallographic sections were prepared by grinding resin-mounted filaments in a diamond impregnated metal disk and fine polishing down to 1/4 μm with diamond paste and metallographic cutting fluid as a lubricant. Care was taken during grinding to ensure that the filaments were cut through their mid-sections. After the preparation was completed, the samples were stored in desiccators.

Back-scattered SEM and optical microscopy were used for metallographic observation. Phase identification was performed by EDS and electron-probe microanalysis in longitudinal sections and by X-ray diffraction of powdered samples. To avoid reaction during preparation of specimens for X-ray diffraction, the filaments were ground in the presence of collodium.

6.3 *Results*

6.3.1 *Growth front morphologies and structure of hypo-peritectic and peritectic samples*

The structure of the quenched semisolid zone of a hypo-peritectic sample is shown in the longitudinal section of Fig. 6.1. Isotherm movement is upward. This structure was common to all samples solidified within the pressure range of 8 to 10^3 Pa O_2. The dark region in the top of the micrograph corresponds to the porous polycrystalline feed, which contains γ and α grains. The central region was partially liquid at the time of quench and the bottom portion corresponds to the directionally solidified material.

Close examination of the quenched zone reveals the occurrence of three characteristic interfaces before the maximum temperature in the zone is reached. The first interface (Location 1) separates the polycrystalline feed from

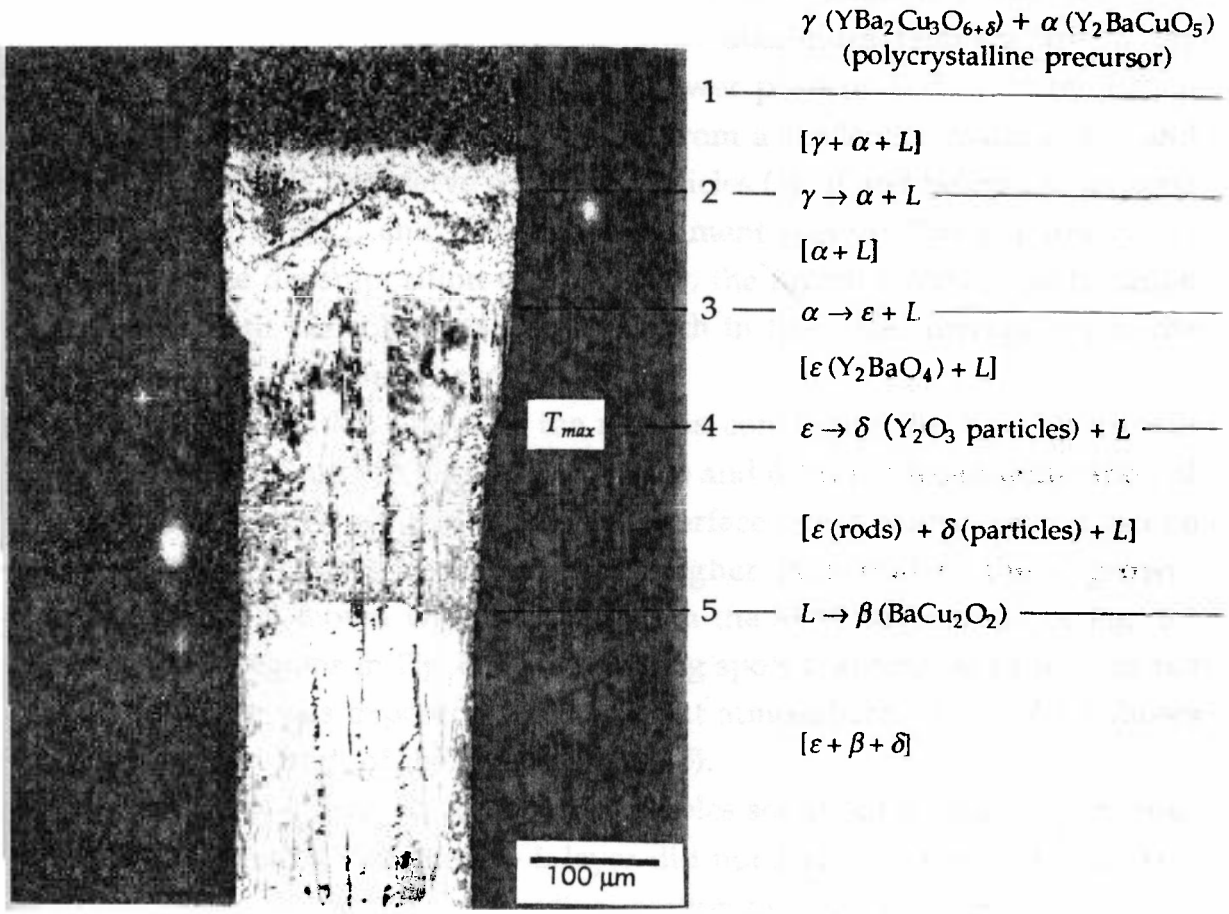

Fig. 6.1. Longitudinal section through the quenched semisolid zone of a sample directionally solidified at R = 8.33 µm/s; P_{O_2} = 333 Pa; T_{max} = 1270°C. Isotherm movement is upwards. The micrograph shows that rods of a high-temperature phase, ε, grow in the liquid, on heating, from a semisolid mixture of $\alpha + L$. This growth morphology produced an aligned microstructure consisting of ε rods or plates parallel to the growth direction and embedded in a matrix of β. In this sample, the temperature of the superficial layers of the zone exceeded that for incongruent melting of ε and particles of δ were formed by the reaction $\varepsilon \rightarrow \delta + L$.

the hot zone and indicates the onset of liquid phase sintering in the precursor location. Below this interface there is a layer approximately 40 μm thick, composed by γ, α, and intergranular liquid. The second interface, Location 2, marks the peritectic isotherm $\alpha \rightarrow \gamma + L$. At the third interface (Location 3), α decomposes peritectically with growth of a new aligned phase (ε). The temperature of this interface is below the maximum temperature in the semisolid zone, which occurs at the still lower position indicated by T_{max} at Location 4. Thus, ε is growing on heating from a semisolid mixture of α and L. It is also possible to observe equiaxed particles (δ), at and below the location corresponding to T_{max}, and close to the filament surface. These particles resulted from the decomposition of ε. Finally, the fourth interface, at Location 5, coincides with the solidus isotherm, which in this case corresponds to the solidification of β by the reaction $L \rightarrow \beta$.

Higher magnification views of the regions containing the ε and β growth interfaces are presented in Figs. 6.2 (a), 6.2 (b) and 6.2 (c). Close examination of Fig. 6.2 (b) reveals that the $\varepsilon + L$ / $\alpha + L$ interface is not sharp, since α can be seen coexisting with ε at temperatures higher than that of the ε growth interface. This is shown with more detail in the SEM micrograph of Fig. 6.2 (b). The black regions in Fig. 6. (b) are etching spots that formed as soon as the polished surface was exposed to the ambient atmosphere. Fig. 6.2 (c) shows the solidification front of the matrix phase (β).

Observation of quenched zones from samples solidified at oxygen pressures below 8 Pa, revealed that the $\alpha + L$ layer did not form in those samples. This is shown in Fig. 6.3 by the longitudinal section of a sample solidified at 7 Pa O_2. In this case, directional growth of ε occurred directly upon melting of γ.

Typical longitudinal sections of peritectic and hypo-peritectic samples are shown in Fig. 6.4. These microstructures are similar to those obtained in directional solidification by either plane front growth of eutectic alloys or cellular growth of hypo-peritectic alloys. Fig. 6.4 also shows that the morphology of the ε-phase changed with composition and oxygen pressure. In hypo-peritectic and peritectic samples solidified at higher oxygen pressures (8 to 10^3 Pa), the morphology of ε was basically rod-like [Figs. 6.4 (a) and (b)]. Below 8 Pa O_2, plates of ε were observed in peritectic samples [Figs. 6.4 (c) and (d)].

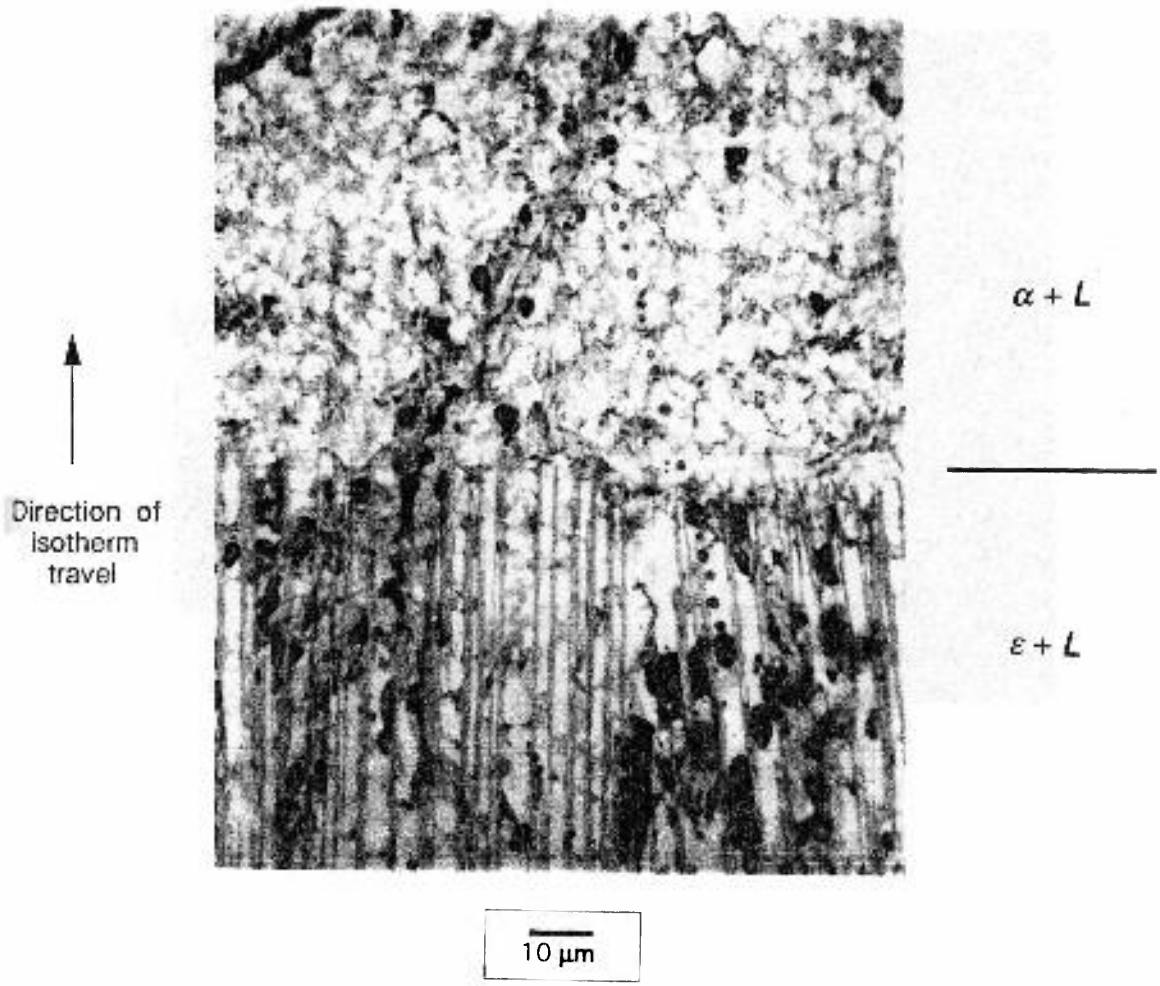

Fig. 6.2. (a) High magnification view of the ε growth front. Aligned growth of ε (bottom portion) occurs from a semisolid mixture of α and liquid of approximate composition Ba:2Cu:yO.

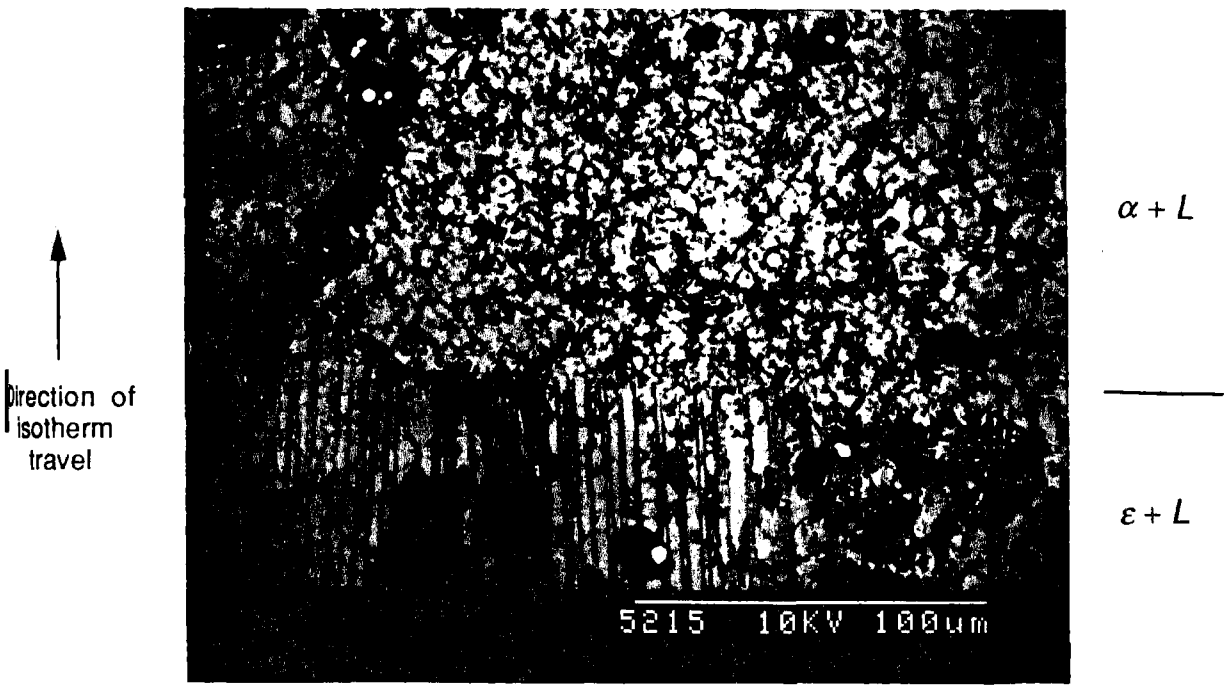

Fig. 6.2. (b) Back-scattered SEM micrograph of the field containing the region shown in Fig. 6.2 (a). The arrows shows α particles coexisting with ε rods at temperatures higher than that of the ε interface.

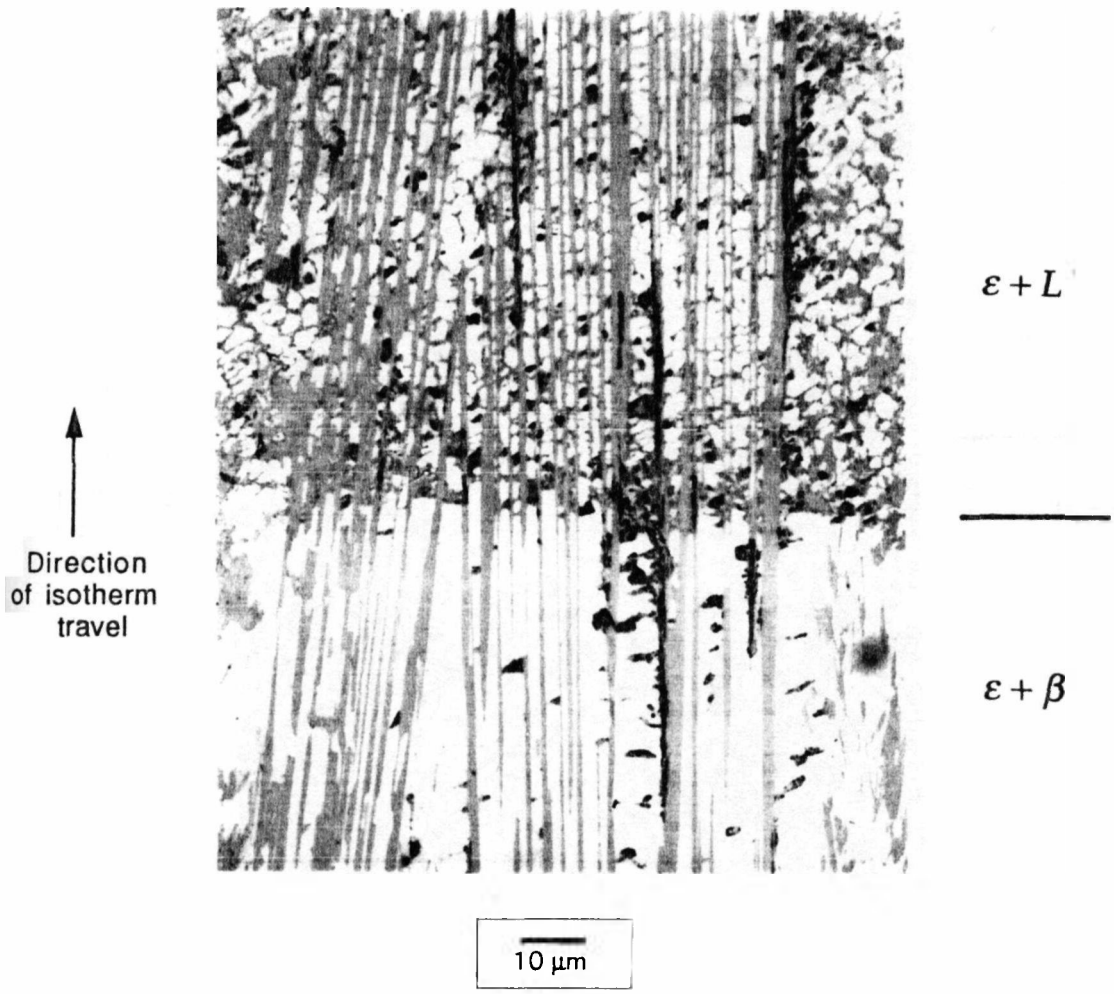

Fig. 6.2. (c). Higher magnification view of the β solidification front.

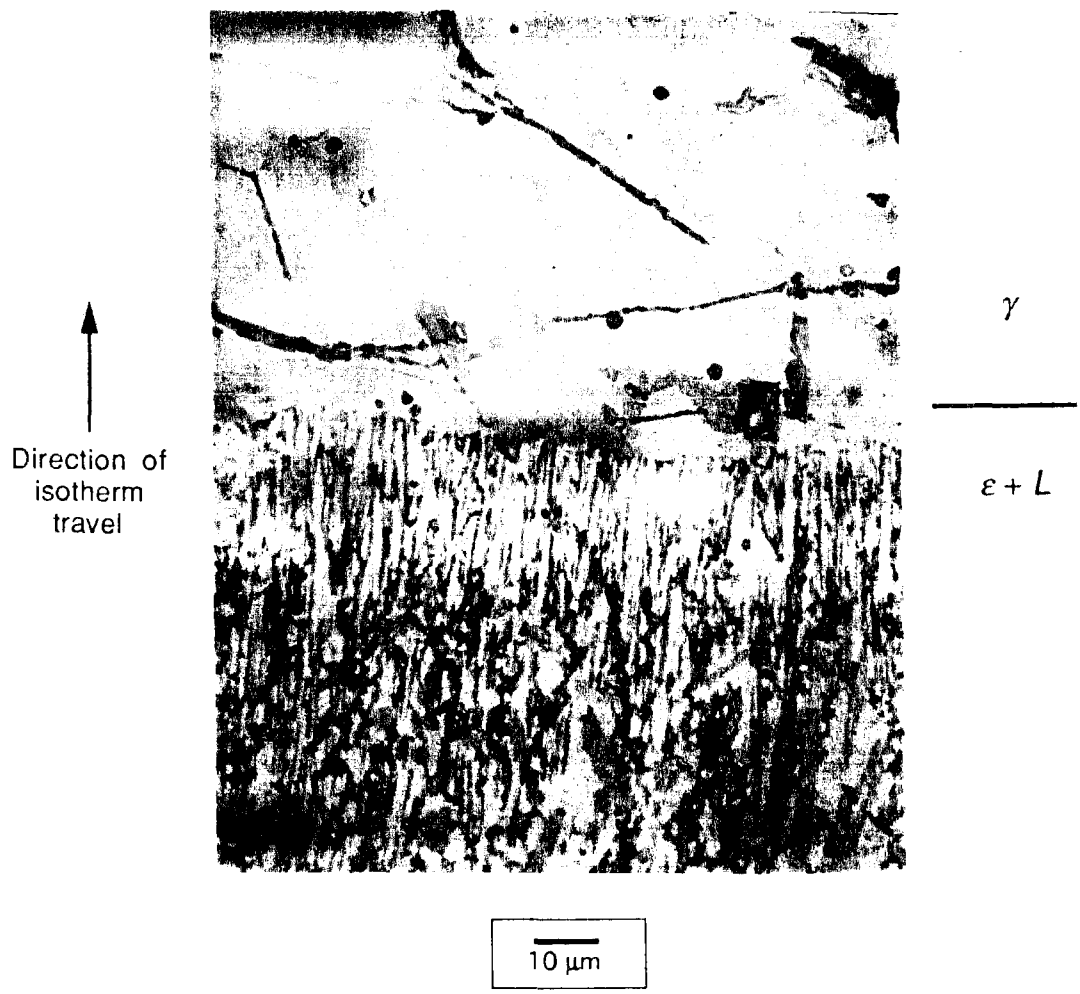

Fig. 6.3. Quenched ε growth front in a sample of overall composition γ. Rods of ε formed in the liquid directly by incongruent melting of the γ phase.

Measurements of rod or plate spacing were carried out as a function of solidification time in the quenched semisolid zone, Fig. 6.5 (a), and of growth rate, Fig. 6.5 (b). Measurements were on longitudinal sections of as-solidified $\varepsilon + \beta$ filaments.

6.3.2 Phase Identification in Directionally Solidified Samples

The phases present in the quenched semisolid zone and in the as-solidified samples were identified by EDS, X-ray diffraction and EPMA. Characteristic EDS spectra were obtained for the rods (ε), the matrix (β) and the equiaxed par ticles (δ) indicated in Fig. 6.1. The spectra showed that ε was poor in copper, L was poor in yttrium and δ contained almost no copper or barium. This is shown in Fig. 6.6 (for the ε rods) by SEM backscattered and characteristic X-ray images of the longitudinal section of a hypo-peritectic sample. Compositions and atomic ratios for the three phases were determined by microanalysis and are given in Table 6.1. EPMA results permitted the identification of ε, β and δ as Y_2BaO_4, $BaCu_2O_2$, and Y_2O_3, respectively. Two samples were prepared for X-ray diffraction and their patterns indicated a good match for the ε-phase peaks. The $BaCu_2O_2$ reflections, however, did not match exactly the peak positions given in the literature for this phase.[233,234] Since $BaCu_2O_2$ hydrolizes extremely fast and is also unstable in the presence of CO_2[234], it is likely that this phase was degraded by reaction with the atmosphere during the preparation of X-ray specimens.

6.3.3 Phase Equilibria in the System Y-Ba-Cu-O at Low Oxygen Partial Pressures

Phase equilibria in the system Y-Ba-Cu-O as a function of oxygen pressures are not very well known at low oxygen pressures. Results of reviewed work[16,36,94,95,103-105,108,109] are summarized in Fig. 6.7, which shows considerable disagreement in the position of important invariant reaction lines over several decades of oxygen pressure. The results of Lay and Renlund[105] for the invariant reaction $\gamma \rightarrow \alpha + L$ are in basic agreement with those of Lindemer *et al.*[109] but only at high oxygen partial pressures.

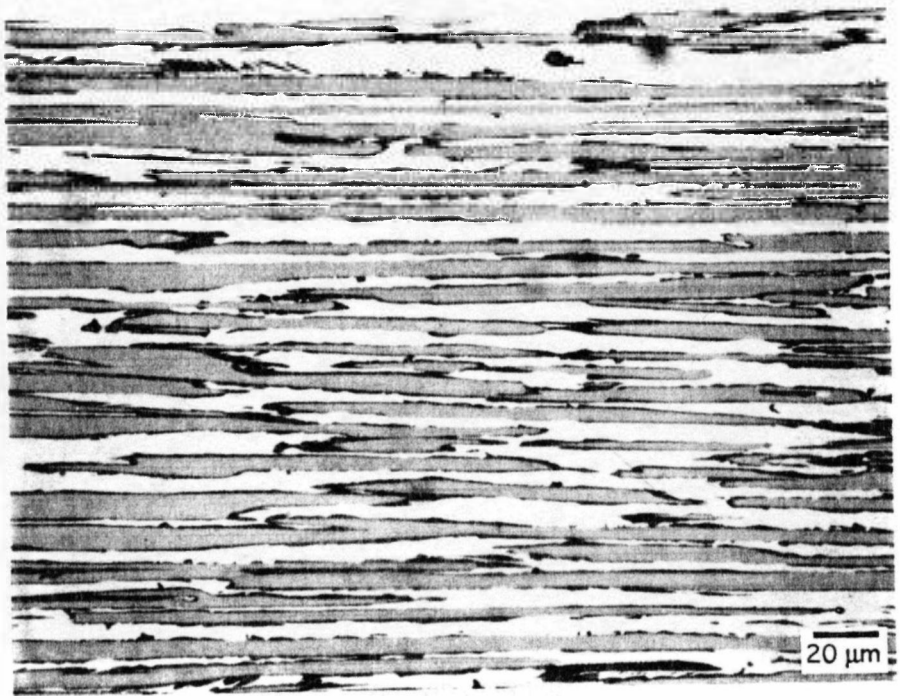

growth direction →

Fig. 6.4 (a)

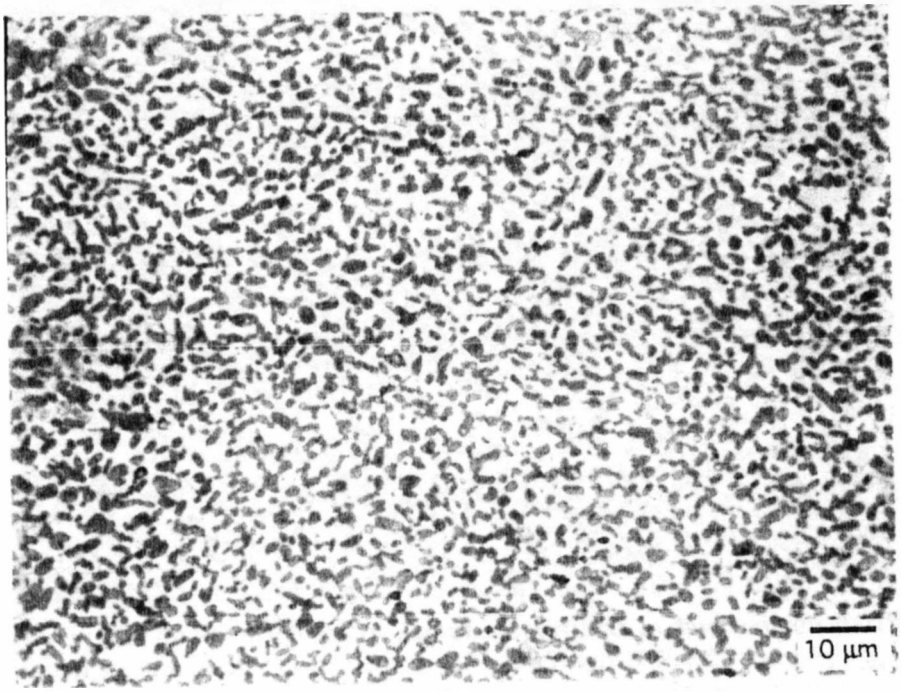

growth direction ⊙

Fig. 6.4 (b)

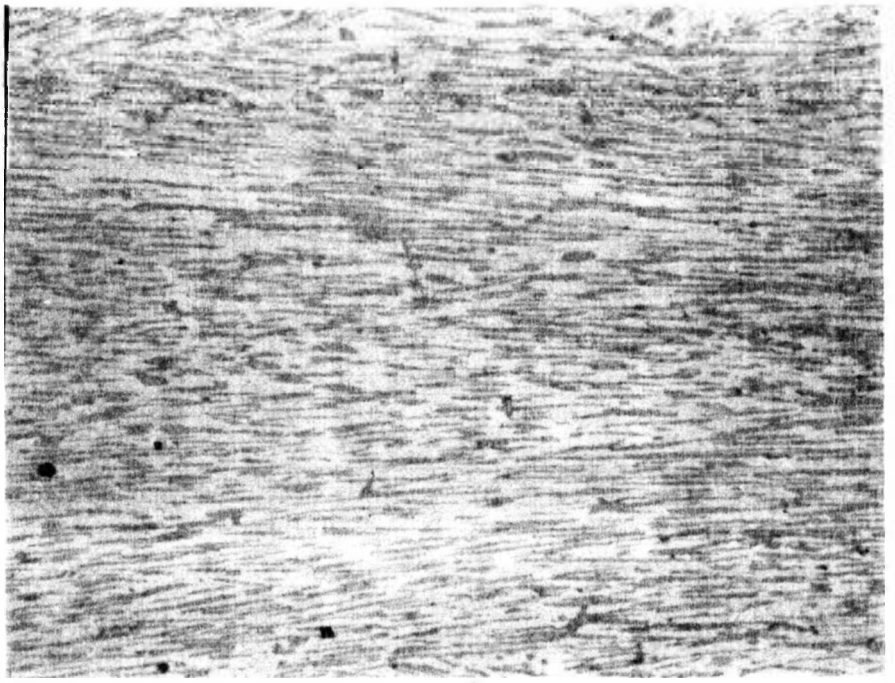

Fig. 6.4 (c)

growth direction

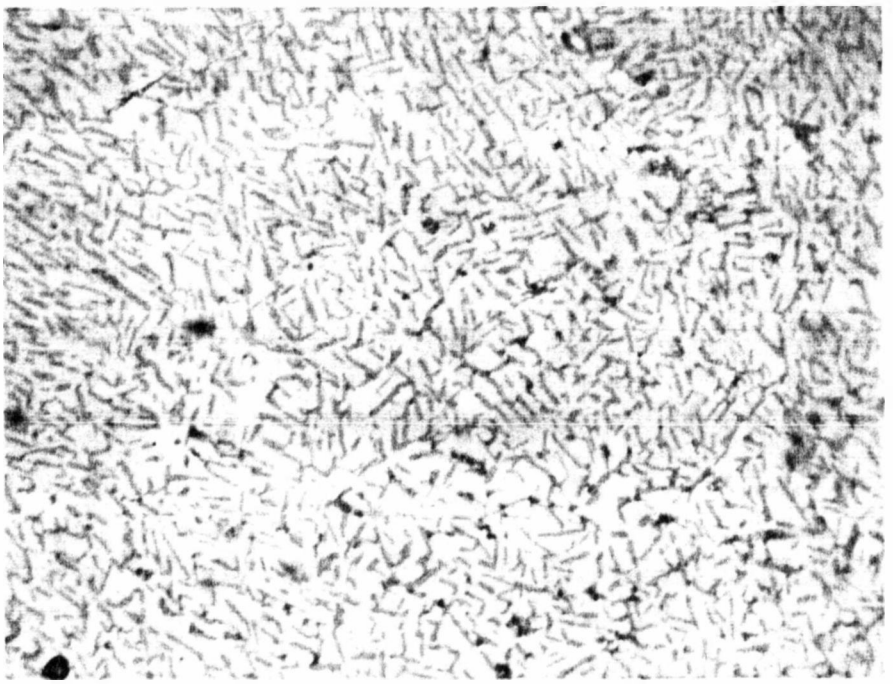

Fig. 6.4 (d)

Fig. 6.4. Typical microstructures of samples solidified in low oxygen partial pressures. (a) Longitudinal section of a hypo-peritectic sample grown at R = 2.78 μm/s; T_{max} = 1250°C; P_{O_2} = 67 Pa. (b) Transversal section of a hypo-peritectic sample grown at R= 5.56 μm/s; T_{max} = 1210°C; P_{O_2} = 11 Pa. (c) Longitudinal section of a peritectic sample grown at R = 8.33 μm; T_{max} = 1210°C; P_{O_2} = 8 Pa. (d) Transversal section of a peritectic sample grown at R = 13.89 μm/s; T_{max} = 1185°C; P_{O_2} = 8 Pa.

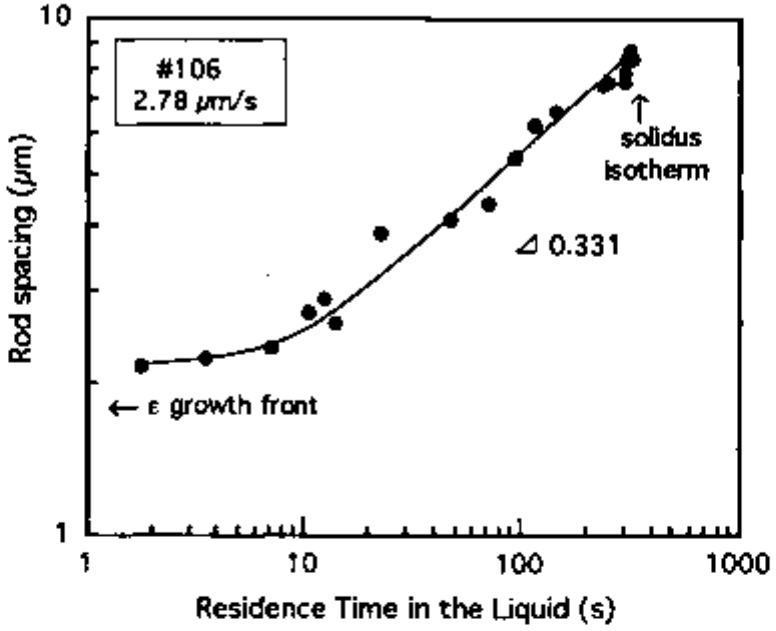

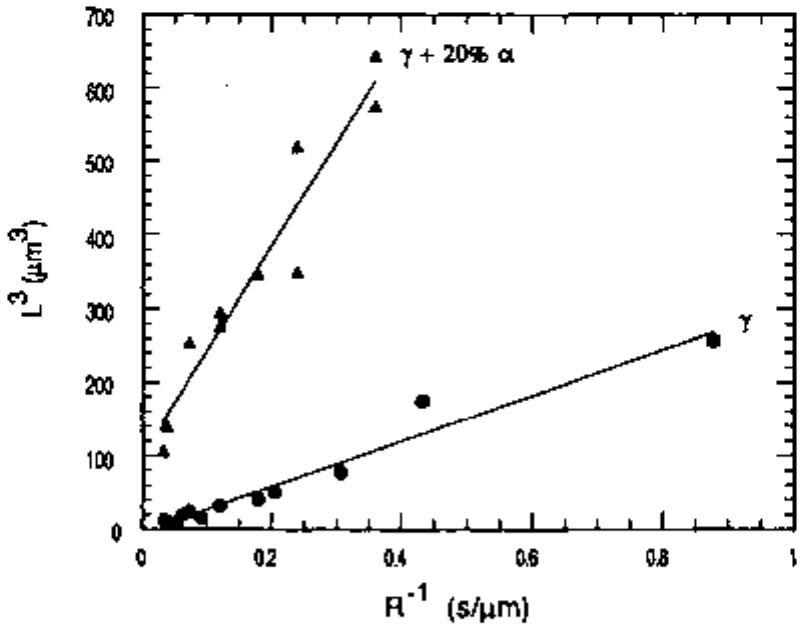

Fig. 6.5. (a) Rod spacing dependence on residence time in the semisolid zone. (b) Rod or plate spacing dependence on growth rate. Top curve: hypo-peritectic compositions; botom curve: peritectic compositions.

Above 94 Pa O_2, the sequence of equilibrium reactions reported by Lindemer *et al.*[109] and Lay and Renlund.[105] is $\gamma \rightarrow \alpha + L \rightarrow \delta + L$. Below 94 Pa O_2, Lindemer *et al.*[109] found that the equilibrium reaction on heating was $\gamma \rightarrow \alpha + \beta + \eta$, where α, β and η represent the phases Y_2BaCuO_5, $BaCu_2O_2$ and $YBa_3Cu_2O_{6+\delta}$. Ahn *et al.*[95,104] and Beyers and Ahn[16] identified that invariant reaction earlier by oxygen titration experiments. The former authors found that at 850°C, the reaction occurred at about 41 Pa O_2 in compositions near $YBa_2Cu_3O_{6+\delta}$. The line representing that equilibrating reaction is included in Fig. 6.7, with some other conflicting results. Lindemer *et al.*[109] reported that below 100 Pa O_2 no liquid phase was formed upon decomposition of γ. This observation is in contradiction with the present results.

A boundary between the phase fields $\alpha + L$ and $\varepsilon + L$ was determined from the present results and is included in Fig. 6.7. The procedure employed to obtain the data is graphically summarized in Fig. 6.8. Knowing the P_{O_2} for a given sample, the temperature of the melting interface, T_p, which corresponds to the reaction $\gamma \rightarrow \alpha + L$, was determined using the results of Lay and Renlund[105]. This temperature was subtracted from the maximum temperature in the zone to give ΔT_{max} the maximum temperature difference in the zone. The distances from the melting interface to the maximum temperature location in the zone (x_1) and from the ε growth front to the melting interface (x_2) were measured on micrographs. The temperature gradient was then estimated by $G = \Delta T_{max} / x_1$. Finally, the temperature of the ε growth front, T'_p, which corresponds to the reaction $\alpha \rightarrow \varepsilon + L$, was determined as $T'_p = T_p + Gx_2$.

In some samples the maximum temperature in the surface of the zone was higher than the decomposition temperature of ε and δ particles were produced by the reaction $\gamma \rightarrow \alpha + L$ in the superficial layer of the sample. The presence of δ particles along the surface was determined by metallographic observations of quenched zones. The micrograph presented in Fig. 6.9 corresponds to a location in the zone where the temperature during growth was maximum. The decomposition of ε to δ at the T_{max} location is indicated by the presence of δ particles. A set of T_{max}-P_{O_2} data points corresponding to the field of stability of $\delta + L$ was generated from similar observations. The points, which are included in Fig. 6.7, agreed well with the results of Lay and

Renlund[105], which were obtained under equilibrium conditions. This agreement suggests that the departure from equilibrium in our experiments was small.

According to the present results, between ~8 and ~10^3 Pa O_2, the equilibrium reactions on heating, , are:

$$\gamma \rightarrow \alpha + L \rightarrow \varepsilon + L \rightarrow \delta + L,$$

and, below ~8 Pa O_2, they are:

$$\gamma \rightarrow \varepsilon + L \rightarrow \delta + L.$$

The microstructural observations of quenched samples and the phase relations during directional solidification of $YBa_2Cu_3O_{6+\delta}$ of peritectic composition suggest that the growth morphologies may be classified according to the oxygen pressure, into three distinct regions. In the range of oxygen pressures above 10^3 Pa, only $\alpha + L$ are formed on heating into the semisolid region; the superconducting phase, γ, then grows by peritectic reaction on directional solidification. Growth of the superconducting phase, γ, occurs in the range of oxygen pressures above 10^3 Pa. In the intermediate pressure range, from ~8 to ~10^3 Pa O_2, $\alpha + L$ first form on heating and on further heating aligned rod- or plate-like structures are formed by the peritectic reaction $\alpha \rightarrow \varepsilon + L$. The directionally solidified material formed on cooling is then $\varepsilon + \beta$. In the low pressure range, below ~8 Pa O_2, the starting material forms ε directly by the peritectic reaction $\gamma \rightarrow \varepsilon + L$.

The foregoing observations are summarized in Fig. 6.10, which provides a qualitative overall picture of the relation between growth morphologies obtained by directional solidification and the phase equilibria in the system Y-Ba-Cu-O. Pseudo-binary representations of the phase diagram are also sketched in Fig. 6.10 for the three distinct ranges of oxygen partial pressure. The phase diagrams are not meant to quantitatively represent the phase equilibria in the Y-Ba-Cu-O system. Rather, they simplify the qualitative change in reactions at high temperature with P_{O_2}. Corresponding metastable extensions of the liquidus lines are included in the diagrams to indicate that the growth of γ and ε occurs from undercooled and superheated liquids, respectively.

Table 6.1. Chemical composition of the component phases of as-solidified samples.

Sample	Composition	Microstructural Feature [a]	Composition (mol%)[b] Y_2O_3	BaO	CuO	Atomic Ratios Y:Ba	Cu:Ba	Compound
106	γ+20wt.% α	ε rod	49.10	47.83	3.07	2.05	0.06	Y_2BaO_4
109	γ+20wt.% α	ε rod	47.99	48.47	3.53	1.98	0.09	Y_2BaO_4
123	γ+20wt.% α	ε rod	48.38	48.13	3.49	2.01	0.07	Y_2BaO_4
157	γ	ε rod	46.90	48.95	4.15	1.92	0.08	Y_2BaO_4
106	γ+20wt.% α	β matrix	0.04	31.65	68.31	0.0025	2.16	$BaCu_2O_2$
109	γ+20wt.% α	β matrix	0.08	33.44	66.48	0.0032	1.99	$BaCu_2O_2$
123	γ+20wt.% α	β matrix	0.02	30.90	69.09	0.0008	2.24	$BaCu_2O_2$
157	γ	β matrix	0.10	34.20	65.78	0.0060	1.92	$BaCu_2O_2$
109	γ+20wt.% α	δ particles [c]	96.80	0.42	2.78	460.95	6.62	Y_2O_3
109	γ+20wt.% α	L [d]	0.04	34.17	65.80	0.002	1.93	$BaCu_2O_2$
109	γ+20wt.% α	α particles [e]	25.77	36.66	37.58	1.41	1.03	Y_2BaCuO_5

(a) See micrographs of Figs. 6.1, 6.2, 6.3, and 6.6 for feature location.
(b) Average of 4 or 5 measurements for rods and matrix and 2 measurements for particles.
(c) Particles produced by decomposition of ε-rods at the maximum temperature location.
(d) Liquid in the semisolid material close to the decomposition interface.
(e) Particles in the semisolid material close to the γ decomposition interface.

(a) Backscattered electron image

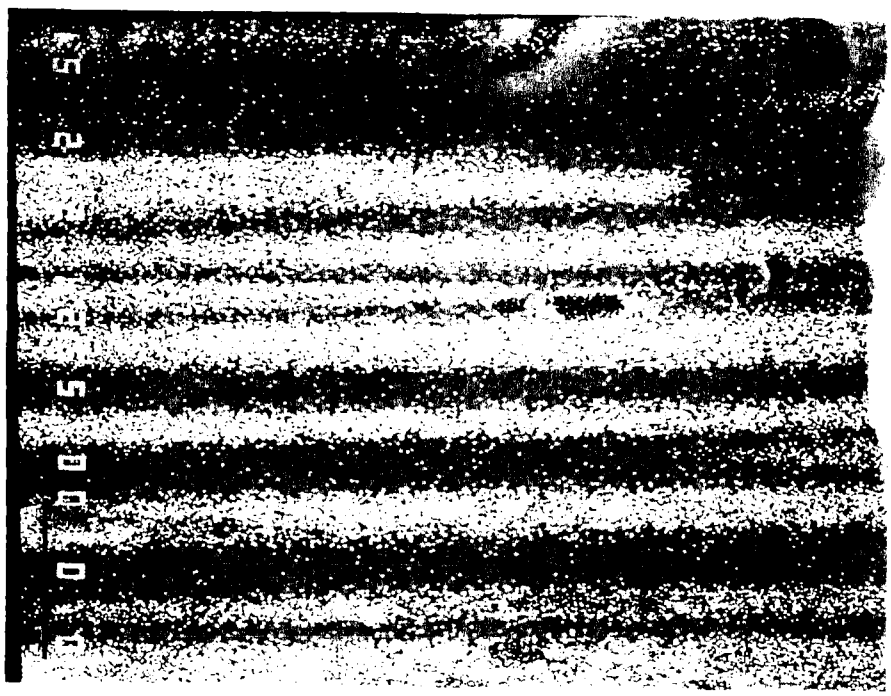

(b) Y Lα image

Fig. 6.6. (a) Backscattered SEM micrograph of a sample grown in low P_{O_2}. The dark bands are ε rods. (b) Yttrium distribution. (c) Barium distribution. (d) Copper distribution.

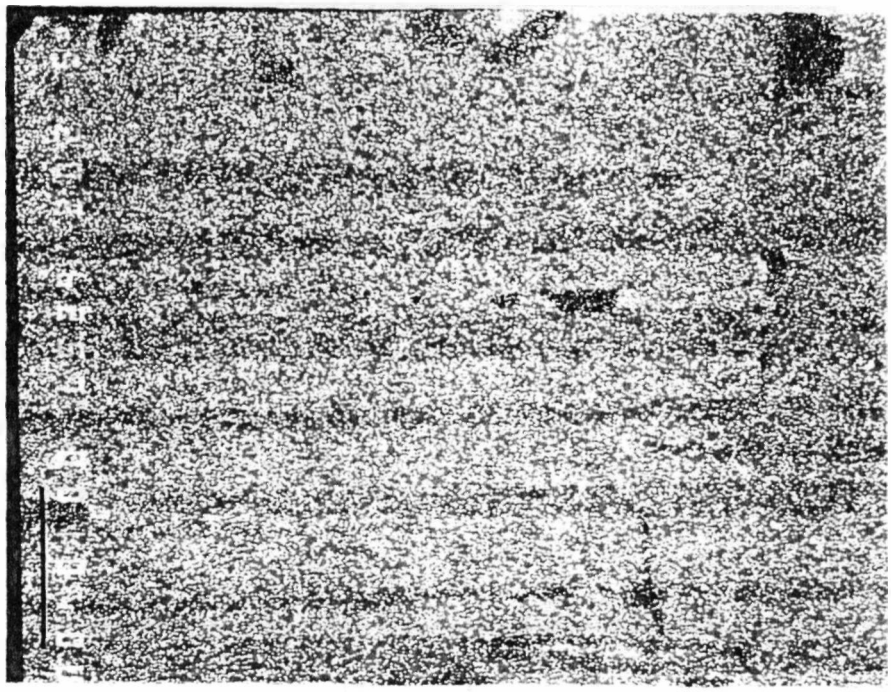

Fig. 6.6 (c). Ba Lα image

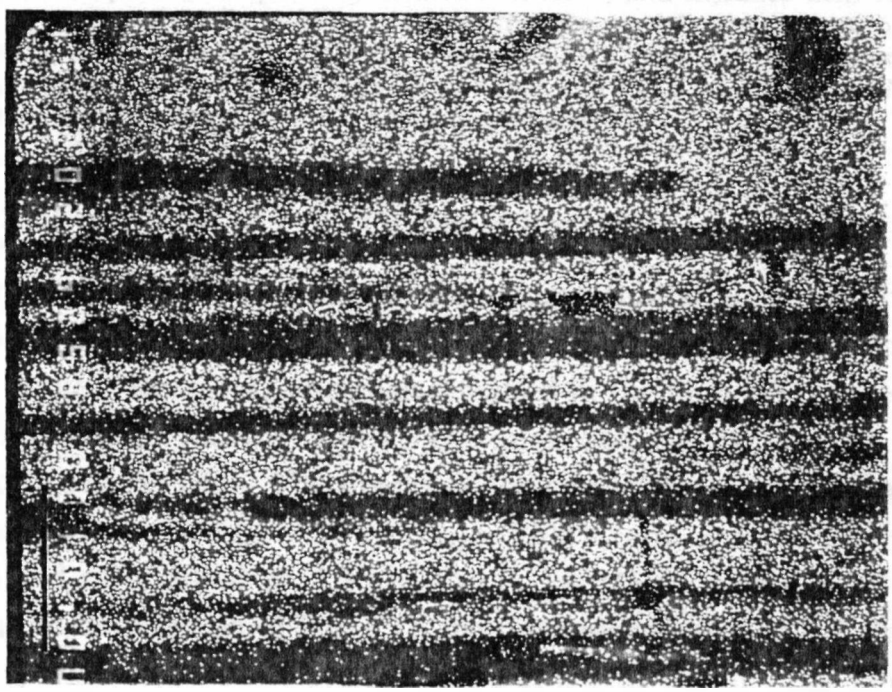

Fig. 6.6 (d). Cu Kα image

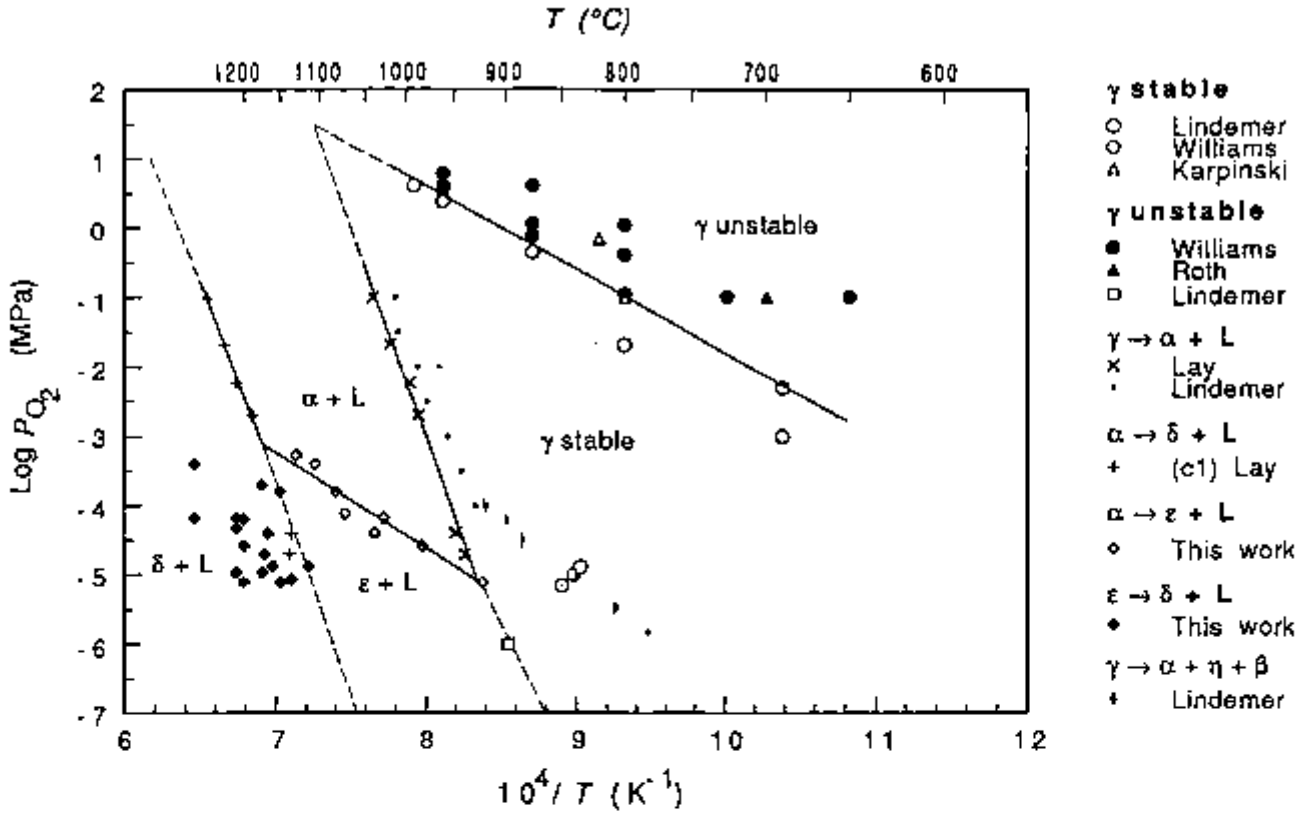

Fig. 6.7. The data as presented in this figure is based on results from the literature for the stability of phase pure γ compiled by Lindemer *et al.*[109], and includes their results for the reaction $\gamma \rightarrow \alpha + L$ and for the stability of γ at low oxygen partial pressures. Also included are the lines for the invariant reactions $\gamma \rightarrow \alpha + L$ and $\alpha \rightarrow \delta + L$ from Lay and Renlund[105] and the results of the present work for the reactions $\alpha \rightarrow \varepsilon + L$ and $\varepsilon \rightarrow \delta + L$. Data of Williams, Roth and Karpinski are from References 103, 92 and 36, respectively.

6.3.4 *Growth of γ from $(\varepsilon + \beta)$ Composite Precursors*

Filaments with aligned $(\varepsilon + \beta)$ microstructures similar to those presented in Figs. 6.5 (a) and (b), were prepared in the intermediate and low oxygen pressure ranges (Fig. 6.11), and then remelted in the high P_{O_2} range at 1.3 atm. O_2. A longitudinal section through the quenched zone of such a filament is presented in Fig. 6.11 (a). The precursor (shown in the top of the micrograph) was initially grown at P_{O_2} = 27 Pa, T_{max} = 1200°C and R = 8.3 μm/s and then remelted and resolidified at 1.3 atm O_2, T_{max} = 1150°C and R = 2.8 μm/s. As shown in the micrograph of Fig. 6.11, the precursor phases, $\varepsilon + \beta$, decomposed on heating to produce a semisolid mixture of α plus liquid. The sequence of

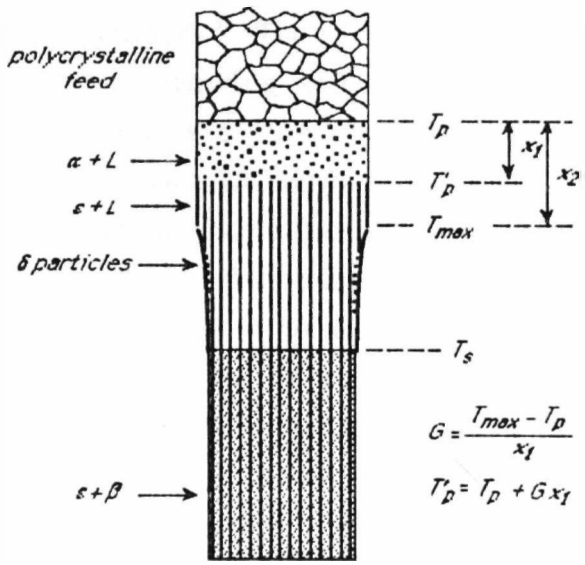

Fig. 6.8. Schematic structure of a quenched semisolid zone illustrating the procedure for determining the temperature of the ε growth front.

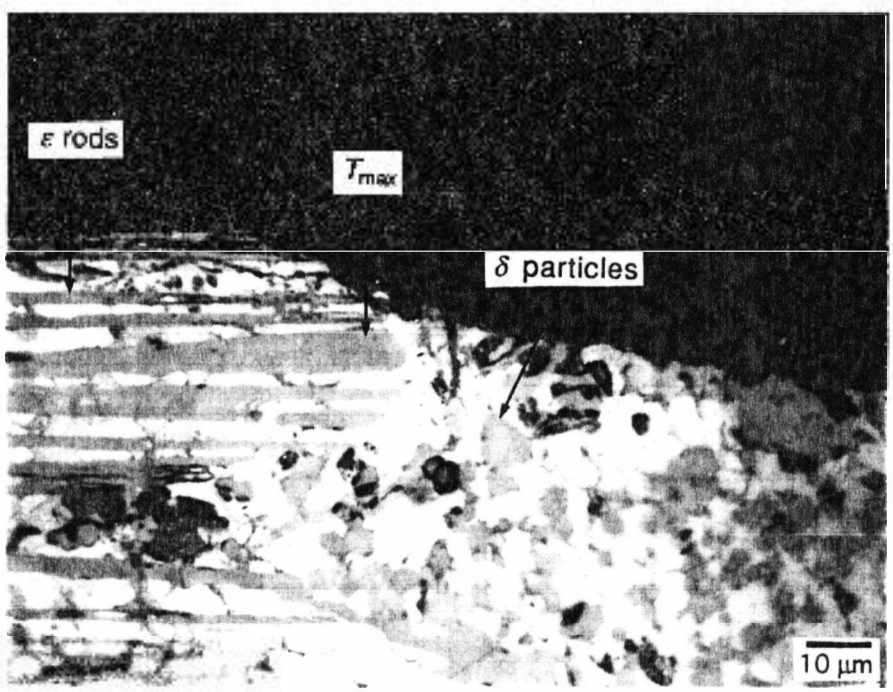

Fig. 6.9. This micrograph shows the decomposition of ε rods to δ particles at the maximum temperature location in the zone, which exceeded the incongruent melting temperature of ε.

events from this point on was similar to that encountered during growth of γ from polycrystalline precursors.[89] The bottom portion of Figure 6.11 (a) shows a single-grained γ filament growing with plane front. The microstructure of the γ crystal, which contains a fine dispersion of particles of the high-temperature phase α, is shown in Figure 6.12.

Fig. 6.11 (b) shows that the longitudinal composition profiles across the semisolid zone of Fig. 6.11 (a) are qualitatively similar to the profiles determined in samples grown from $\alpha + \gamma$ precursors. The shape of the concentration curves as well as the micrograph of Fig. 11 (a) suggest that Cu-rich oxide liquid from the zone also reacted with the product phases from the reaction between α and β, namely, α and γ.

The remelting experiment just described may also point to the origin of the discrepancies among the present results and those of Lindemer *et al.*[109] In the remelting experiment described above, the temperatures of the interfaces located in the top of the zone were also measured, in addition to the maximum temperature. Due to the inherent difficulties in precisely locating the position of the interfaces, the measurements of interface temperature may have an error of up to 30°C, but this error does not invalidate the present analysis. The measurement of temperatures and relative interface positions in the micrograph of the quenched zone allowed the estimation of the temperature of the isotherm at which ε started to decompose. A value of 773°C was obtained. A temperature of 880°C was measured at the interface where the decomposition of ε was completed. These two temperatures indicated that, at 1.3 atm O_2, the conversion of $\varepsilon + \beta$ to $\alpha + L$ was essentialy completed in about 2 min, with a heating rate of 75°C/min. The temperature range (773-880°C) and the fast rate of this reaction may explain the findings of Lindemer *et al.*[109] and Ahn *et al.*[16,95,104] It is possible that in their experiments, the oxygen partial pressure was not prevented from rising on quenching the samples equilibrated at low P_{O_2}. Apparently, during quenching, the partial reaction of ε with β produced the phases α, β and η. These may be intermediate products of the reaction between ε and β, instead of products of the decomposition of γ.

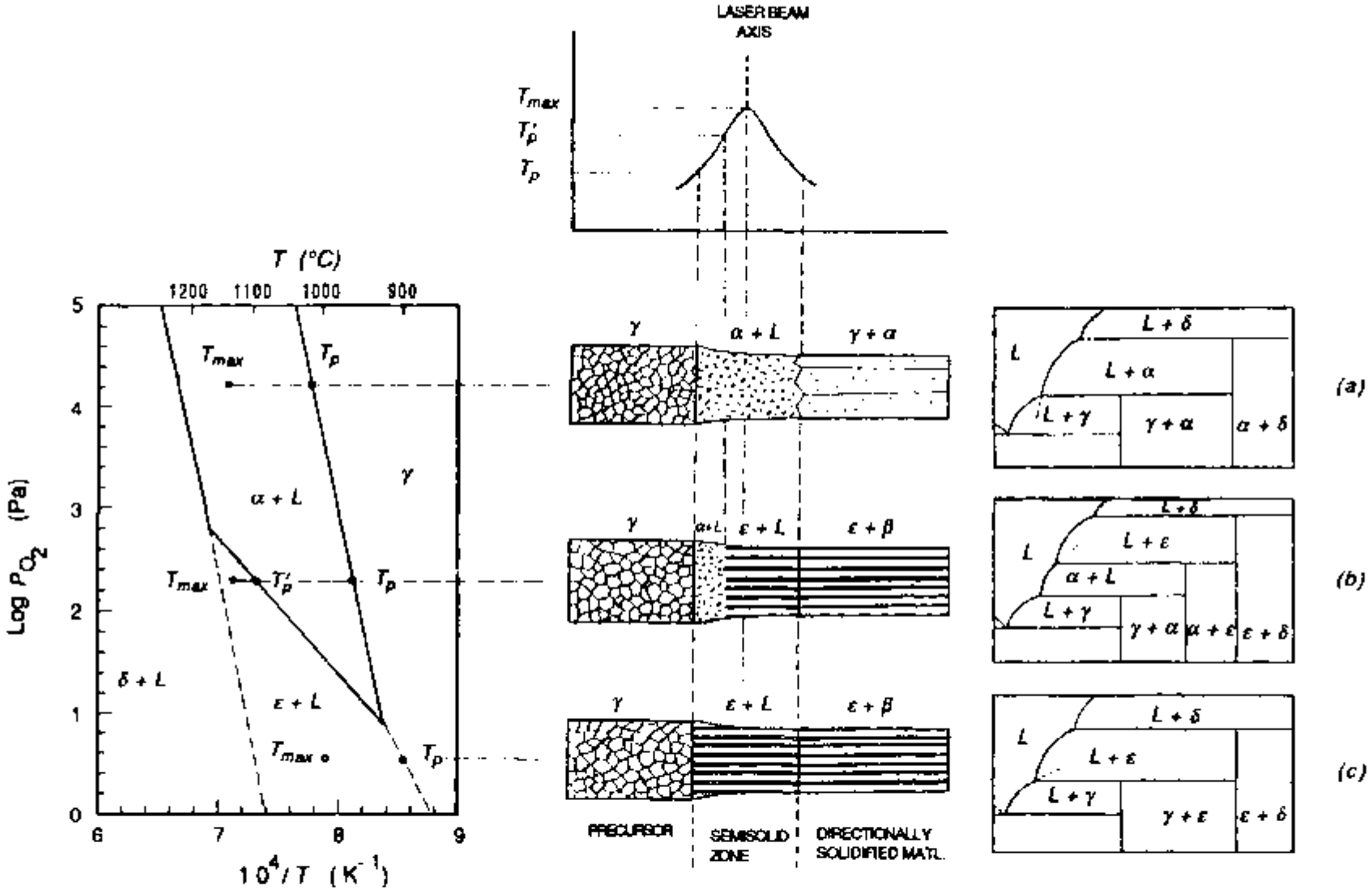

Fig. 6.10. Qualitative picture of the influence of oxygen partial pressure on solidification morphologies obtained in directional solidification of γ, as well as on pseudo-binary diagrams.

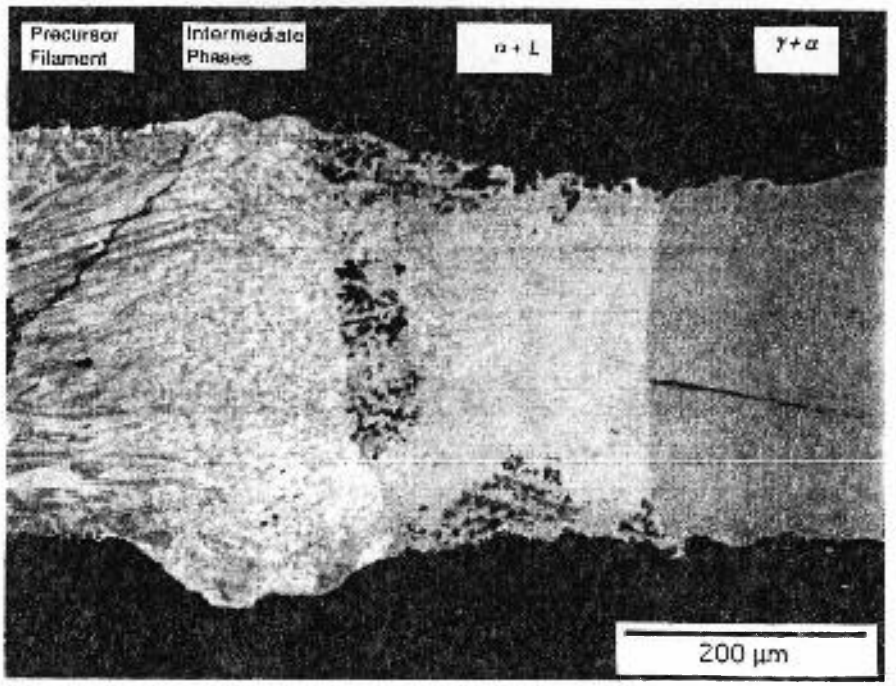

(a)

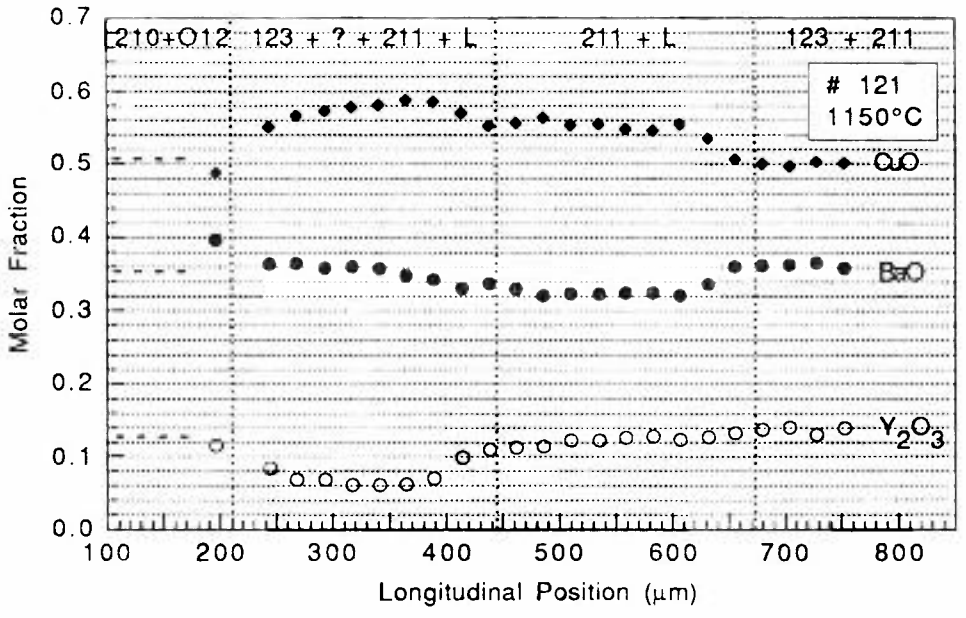

(b)

Fig. 6.11. (a) The use of $(\varepsilon + \beta)$ precursor filaments for the growth of $(\gamma + \alpha)$ crystals by directional solidification at high P_{O_2}, resulted in quenched zones like the one shown above. The region above the zone corresponds to the $(\varepsilon + \beta)$ precursor. As the temperature increased (from top to bottom), the precursor started to decompose until a semisolid mixture of $(\alpha + L)$ was formed. The bottom region is the $(\gamma + \alpha)$ crystal. (b) Average composition along the quenched zone.

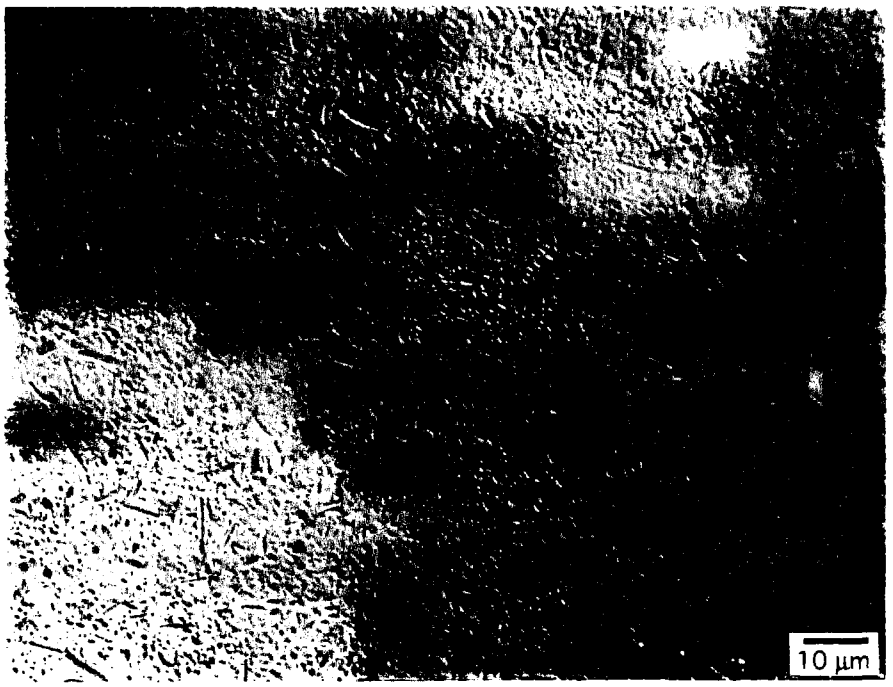

Fig. 6.12. Microstructure of the composite filament shown in Fig. 6.11 (a). Finer α particles were obtained by LHFZ growth of ($\gamma + \alpha$) composites from ($\varepsilon + \beta$) precursors.

6.4 Directional Formation of ε on Heating

A simple model is proposed in this section for directional phase formation of ε from a superheated semisolid melt, $\alpha + L$. The model is developed for solidification of ε in the intermediate range of oxygen pressures (8 to 10^3 Pa O_2). It incorporates concepts which are contained in a previous model developed for the growth of γ from undercooled semisolid melts.[89] Based on the information currently available,[16,36,94,103-105,108,116] the phase diagram employed in this analysis is assumed to be qualitatively the pseudo-binary diagram depicted in Fig. 6.10 (b).

Following experimental observations, plates or rods of ε are assumed to grow on heating from a semisolid mixture of $\alpha + L$. Solute for the growth of ε is provided by dissolution of α particles just ahead of the ε growth front. The transport of solute to ε growth front is assumed to occur by diffusion along the direction of growth, x, over a distance ℓ, which is half the ε rod or plate spacing, Fig. 6.13. The liquid composition along the x direction is

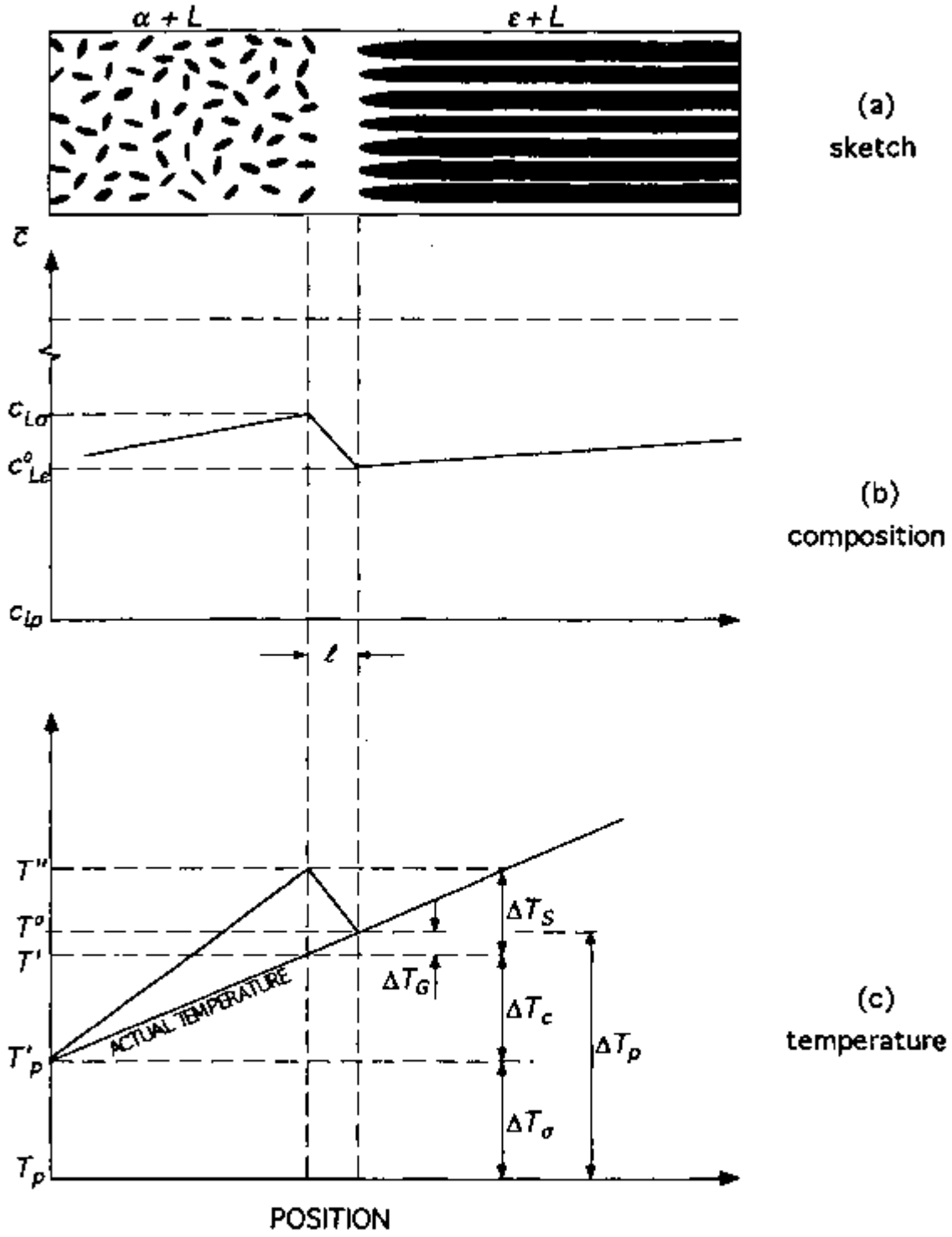

Fig. 6.13. (a) Solidification model. (b) Liquid composition. (c) Temperature distribution in the liquid ahead of the ε growth front. Growth is from right to left.

represented in Fig. 6.13 (b). These compositions relate to the expanded section of the assumed phase diagram, Fig. 6.14, as discussed below.

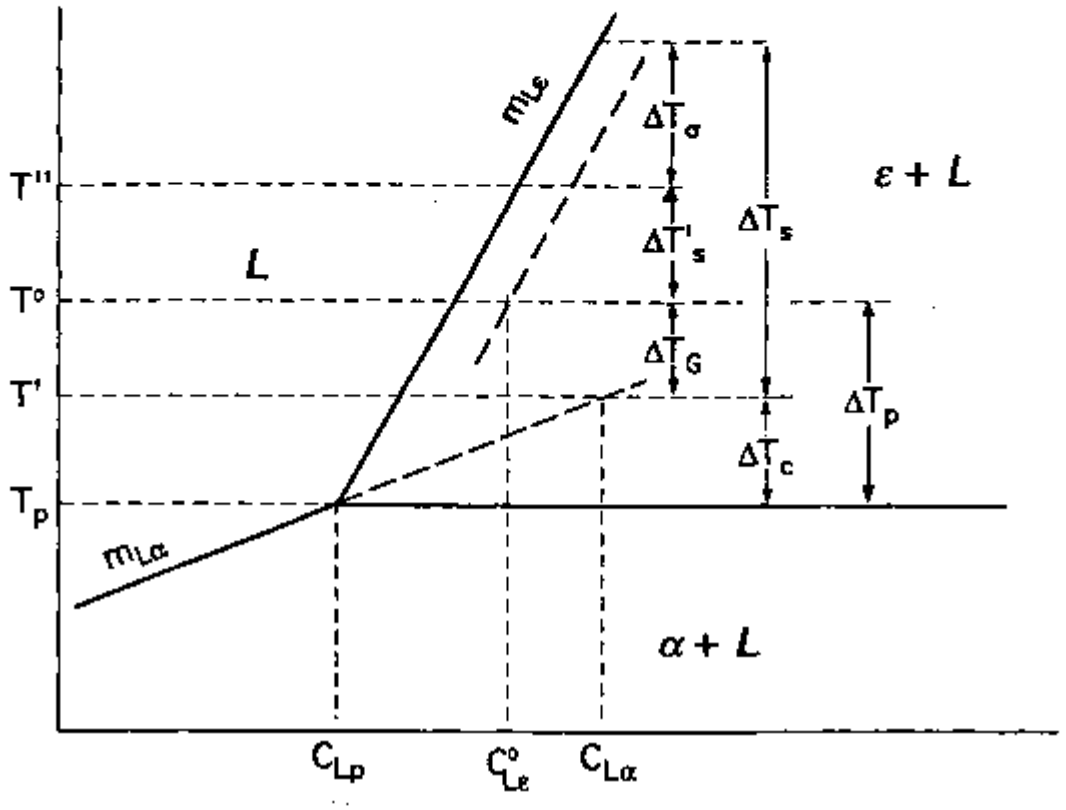

Fig. 6.14. Enlarged section of the phase diagram considered in Fig. 6.13 (b), showing the metastable liquidus lines.

The peritectic reaction on heating, $\alpha \rightarrow \varepsilon + L$, occurs at a temperature $T_p + \Delta T_p$, superheated with respect to the peritectic temperature, T_p. This superheating may be expressed by a sum of two components as

$$\Delta T_p = \Delta T_G + \Delta T_C \tag{6.1}$$

In the above equation, the term ΔT_G is a superheating component which results from the imposed temperature gradient, G. The term ΔT_C takes into consideration the increase in temperature caused by a deviation in solute concentration at the α interface from that of the metastable liquid composition, c'_{Lp}. These quantities are shown schematically in Figs. 6.13 (c) and 6.14, together with another important superheating term, ΔT_S. This term

represents the maximum "constitutional superheating" ahead of the interface and is expressed by the difference between the equilibrium liquidus and the actual temperature at $x = \ell$.

Two other temperature differences are shown in Figs. 6.13 and 6.14. ΔT_σ represents the depression of the ε liquidus due to surface tension effects at the rod or plate tips. Microstructural observations of the quenched zones indicate that the α particles in front of the ε front are larger than 1 μm. Therefore, the size effect on the melting point of the α phase is expected to be small and will not be considered here. ΔT_D represents the difference of the equilibrium liquidus temperatures at $x = 0$ and $x = \ell$, corresponding to the solute gradient for diffusional transport.

The equilibrium solute contents at the ε interface ($x = 0$, $T = T^0$) and at the α interface ($x = \ell$, $T = T'$) are $c_{L\varepsilon}^0$ and $c_{L\alpha}$, respectively. These concentrations and temperatures are indicated in Figs. 6.13 (b) and 6.14. The quantities $(c_{L\varepsilon}^0, T^0)$ and $(c_{L\alpha}, T')$ define the solute concentration curve shown in Fig. 6.13 (b) for $x < \ell$. For $x > \ell$, the solute concentration follows the equilibrium α liquidus. Mass balance for solute at the ε growth front yields:

$$R(c_{L\varepsilon}^0 - \bar{c}) = -D_L \frac{(c_{L\alpha} - c_{L\varepsilon}^0)}{\ell} \tag{6.2}$$

where R is the growth rate, D_L is the diffusion coefficient of solute in the liquid, and $\bar{c}$ is the average initial composition. If constant slopes for the equilibrium ε liquidus, $m_{L\varepsilon}$, and the metastable α liquidus, $m_{L\alpha}$, are assumed, the following relations can be obtained (Fig. 6.14):

$$\Delta T_\bullet = \Delta T_\sigma + \Delta T_D + \Delta T_C \tag{6.3}$$

$$\Delta T_D = m_{L\varepsilon}(c_{L\alpha} - c_{L\varepsilon}^0), \tag{6.4}$$

and

$$\frac{\Delta T_\varepsilon}{m_{L\alpha}} = \frac{\Delta T_\sigma + \Delta T_D + \Delta T_p}{m_{L\varepsilon}} \tag{6.5}$$

From Fig. 6.13 (c),

$$\Delta T_C = (T^0 - T') = G\ell \tag{6.6}$$

Substitution of $c^0_{L\varepsilon} - \bar{c} \approx c_{L_p} - \bar{c}$ and equations (6.1) plus (6.3) to (6.6) into equation (6.2), yields the following relation between the interface superheating, ΔT_p, and the growth rate, R:

$$\Delta T_p = \left[\frac{R}{D_L}(\bar{c} - c_{L_p}) + \frac{G}{m_{L\alpha}}\right]\frac{m_{L\alpha}m_{L\varepsilon}}{m_{L\varepsilon} - m_{L\alpha}}\ell + \frac{m_{L\alpha}}{m_{L\varepsilon} - m_{L\alpha}}\Delta T_\sigma \qquad (6.7)$$

The depression of the ε liquidus temperature, ΔT_σ can be expressed as $\Delta T_\sigma = \frac{A}{d}$, where A is a constant that includes the Gibbs-Thomson coefficient for the ε phase and d is half the transversal dimension of the ε rods (or plates) This dimension can be related to the rod or plate spacing and the volume fraction of the ε-phase, v_ε by $d^2 \approx v_\varepsilon \ell^2$ Replacing this relation into the expression for ΔT_σ gives

$$\Delta T_\sigma = \frac{A}{\sqrt{v_\varepsilon}\ell} \qquad (6.9)$$

Proceeding as above and using equation (6.9), the following relation can be written between the maximum "constitutional superheating", ΔT_s, and the growth rate, R:

$$\Delta T_s = \left[G + m_{L\varepsilon}\frac{R(\bar{c} - c_{L_p})}{D_L}\right]\ell + \left[\frac{A}{\sqrt{v_\varepsilon}}\right]\frac{1}{\ell} \qquad (6.10)$$

Equation (6.10) relates maximum "constitutional superheating", ΔT_s and growth rate. It is of the same form of that given by the Jackson-Hunt analysis[216] for the undercooling and growth rate at the eutectic growth front.

6.5 Discussion

It is interesting to note that aligned growth of α on heating was not obtained by the peritectic reaction

$$\gamma \rightarrow \alpha + L\ (3\,BaCuO_2 \cdot 2\,CuO),$$

which occurs at oxygen partial pressures above approximately 8 Pa. The decomposition of γ by the above reaction leads to the formation of randomly oriented α particles even at high values of the ratio G/R.[89,169]

Rod-like morphologies were obtained for the ε phase in all hypo-peritectic specimens (γ plus 20 wt.% α), in spite of the volume fraction of the high-temperature phase, ε, being larger than 0.4. In metallic or organic eutectics, such large volume fractions normally result in lamellar morphologies,[183,235,236] ε-plates were obtained in peritectic specimens solidified in the low range of oxygen pressures (P_{O_2} < 8 Pa), where the equilibrating reaction on melting is $\gamma \rightarrow \varepsilon + L$.

The reaction sequence that occurs in hypo-peritectic specimens may partially explain the larger inter-rod spacings obtained in these specimens (Fig. 6.6). For this composition, the sequence of reactions on heating is:

$$\alpha + \gamma \rightarrow \alpha + L \rightarrow \varepsilon + L$$

The first step of the above reactions shows that the decomposition of γ generates an additional volume of the α phase. This excess amount will be precipitated onto the α particles in contact with the γ phase prior to decomposition of the latter. The resulting semisolid mixture will be coarser than that formed by the decomposition of phase pure γ, *i.e.*, the α interparticle spacing will be larger. Thus, ε nuclei will be formed in discrete volumes spaced farther apart along the interface, since ε nucleates from α, and the average nuclei spacing will also be larger. Hence, it is expected that larger α interparticle spacings in hypo-peritectic specimens will also lead to larger rod spacings during the growth of ε.

Due to the peculiar nature of ε growth, the rods or plates stay in contact with the liquid phase until it solidifies to form the β phase, at an isotherm located more than half zone length away from the ε growth front. Therefore, it is expected that the rod or plate spacing will increase due to coarsening of ε during the time they stay in contact with the liquid phase. Coarsening will effectively stop once β forms by solidification of the inter-rod liquid. This increase in spacing was suggested by micrographs of quenched zones, similar

to that presented in Fig. 6.3 (a). Measurements of rod spacing were taken in quenched zones at regular intervals along the growth axis, from the ε growth front to the solidus interface. Typical coarsening plots like that shown in Fig. 6.5 (a) were obtained by plotting the data on a log-log scale. The curve of Fig. 6.5 (a), which is non-linear at short times, becomes linear at longer times, with a slope of 0.331. These results confirmed that the rod or plate spacing was controlled by coarsening of ε within the semisolid zone.

Therefore, straight lines were obtained by plotting the cube of the rod or plate spacing against the inverse of growth rate, which is proportional to the residence time of ε in the semisolid zone. The results are given in Fig. 6.5 (b), and show that, in addition to larger spacings, the rods in the hypo-peritectic specimens also coarsened at faster rates compared to the plates in the peritectic specimens. This is indicated by a larger slope in the case of hypo-peritectic samples. One possible reason for faster coarsening in hypo-peritectic compositions is the larger ε content of these specimens. Theoretical predictions, confirmed by experimental work[193], indicate that in solid-liquid systems, the rate constant for coarsening increases with volume fraction of the solid phase. The magnitude of the increase in the rate constant observed in the present experiments is consistent with the theoretical predictions. Another observation relates to the intercept of the curve corresponding to the hypo-peritectic specimens. The spacing value corresponding to the intercept is about 4.7 μm, which is of the order of the α interparticle spacing ahead of the ε growth front (Fig. 6.3).

The predictive power of Eq. (6.10) could be verified by measuring initial rod or plate spacings at the ε growth front location. However, these measurements were very difficult to obtain. Because of small filament diameters, the volumes enclosing the ε interface, as well the microstructural size scales were very small. As mentioned earlier, the material in the quenched zone was also extremely susceptible to chemical attack by the atmosphere; this is illustrated by the dark spots in Figs. 6.3 (a) and 6.3 (b). Therefore, chemical attack easily obscured the already fine interfacial features, preventing representative measurements of rod spacing from being taken at the ε growth front, either optically or by SEM. The microstructural size scale can be enlarged, however, by simultaneously increasing the diameter and α

particle size in the precursor ($\alpha + \gamma$) filaments. This will also allow growth at very slow rates, which is difficult to perform with small diameter filaments due to instabilities generated in the zone by liquid migration against the temperature gradient. The term ΔT_σ decreases as the transversal dimension of the rods or plates is increased. When this term is sufficiently small, Eq. (6.10) predicts a linear relation between the inverse of rod or plate spacing (at the ε growth front) and the growth rate. Additional experiments could be performed with modified precursors to test the validity of Eq. (6.10) and the former hypothesis.

The rod- or plate-like aligned microstructures observed to form on melting in the experiments reported here, present interesting possibilities for the growth of the superconducting compound γ. The ability to control the rod spacing means that the yttrium distribution in the solidified material can be finely modulated. If such materials are used as precursors for the growth of the superconducting phase γ, fine compositional modulations would then provide shorter diffusion lengths and could be exploited for the introduction of periodic compositional variations in the γ crystals, which may led to enhanced flux pinning in melt processed superconductors.

6.6 Conclusions

Directional phase formation on melting via peritectic reaction was observed to occur in the system Y-Ba-Cu-O at low oxygen partial pressures. This is the first report of directional phase growth on melting in ceramic systems with peritectic reactions.

The following reaction was observed on melting at $P_{O_2} > 8$ Pa

$$\gamma(YBa_2Cu_3O_{6+\delta}) \rightarrow \alpha(Y_2BaCuO_5) + L$$

where α phase comprised equiaxed particles. At 8 Pa $< P_{O_2} < 10^3$ Pa, the above reaction occurred and at higher temperatures, the following reaction also occurred to produce a rod-like ε phase, oriented in the growth direction:

$$\alpha\ (Y_2BaCuO_5) \rightarrow \varepsilon\ (Y_2BaO_4) + L$$

At pressures below about 8 Pa, the low temperature reaction observed was

$$\gamma \rightarrow \varepsilon + L$$

In this case, the oriented ε phase formed directly from γ, and was plate-like in morphology. The last two peritectic reactions were unknown prior to this work.

Growth of aligned rods or plates occurred from a superheated semisolid mixture of α particles and liquid ($BaCu_2O_2$), which was formed at lower temperatures by the incongruent melting of the γ phase ($YBa_2Cu_3O_{6+\delta}$) in the precursor. On cooling, solidification of the inter-rod liquid, presumably at a large degree of undercooling, suppressed the formation of γ. This resulted in the growth of composite filaments with structures very similar to directionally solidified eutectics. These structures consisted of aligned rods or plates of ε in a matrix of β ($BaCu_2O_2$).

Boundaries for the phase field ε (Y_2BaO_4) + L were located by determining relative positions and temperatures of interfaces in quenched specimens of composition 1:2:3.

A simple solidification model predicted a relation between superheating and growth rate that is analogous to that derived in the Jackson-Hunt analysis for the undercooling and growth rate during directional solidification of eutectics. Rod spacing in fully solidified samples decreased with increasing growth rate and was strongly affected by coarsening during solidification.

The sequence of transformations $\alpha + \gamma \rightarrow \varepsilon + \beta \rightarrow \alpha + \gamma$ obtained in directional solidification through suitable changes of oxygen partial pressure can be effectively used to refine, and perhaps to introduce new microstructural characteristics in $\alpha + \gamma$ composites, which may be used to enhance flux pinning in γ.

The present results illustrate a solidification case in which the solidification microstructure is controlled by the heating rate.

Chapter 7
Electrical and Magnetic Properties of Textured and Single-Crystalline LHFZ Filaments

7.1 Introduction

This chapter presents a summary of the electrical and magnetic properties of LHFZ filaments. Sample fabrication and microstructural characterization were described in detail in Chapters 5 and 6.

7.2 Experimental

7.2.1 Sample Preparation

The samples consisted of 5 to 15 mm long segments of filaments solidified under steady state. The solidified filaments had no longitudinal composition gradients and average composition very close to that of the precursor. In spite of the overall appearance of the microstructure being the same within a given growth rate range, some degree of variation in the intragranular microstructures, and hence in the superconducting properties is to be expected. Possible causes for the variation in intragranular microstructures are discussed below. Growth parameters and other sample characteristics are given in Table 5.2.

All samples were annealed in flowing oxygen, prior to the magnetization and current density measurements. During the thermal treatment, heating and cooling rates were maintained at 1°C/min, to minimize or avoid microcracking caused by thermal stresses. Most samples were annealed at 460°C for 40 h. Some samples were also given high temperature treatments at 800°C, before being oxygenated at 460°C. Contamination during annealing was prevented by lining the small ceramic boats that supported the samples with MgO single crystal plates.

The preparation of samples for direct critical current measurements consisted of the following steps:

(a) Polishing the filament surface until shiny with emery paper (800 grit size);
(b) Rinsing with acetone;
(c) Placing the sample on a glass substrate and applying an aluminum mask;

(d) Depositing 5 to 10 μm thick silver electrodes by evaporation;
(d) Annealing the sample with Ag electrodes in air at 450 °C for 30 min;
(e) Glueing the sample to a saphire substrate using cryogenic varnish;
(f) Soldering silver foil I-V leads to the silver electrodes with In metal.

The mounting procedure is sketched in Fig. 7.1. The cryogenic varnish allowed some movement of the sample, thus preventing its premature fracture by the action of Lorentz forces during the passage of current.

The preparation of samples for resistivity measurements was similar to the above description, except that ultrasonically bonded aluminum wires were used in place of soldered silver foil leads.

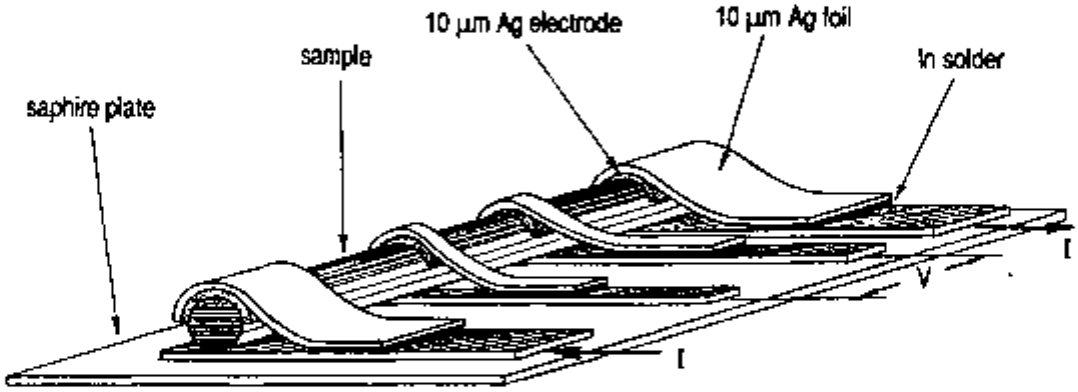

Fig. 7.1: Sample mounting for direct critical current density measurements.

7.3 Results and Discussion

7.3.1 Critical Temperature Determination

DC Measurements

Well annealed samples exhibited almost perfect metallic behavior at high temperatures, which extrapolated to near zero resistance at 0 K, as illustrated in Fig. 7.2. The data correspond to a sample oxygenated at 500°C for 40 h, then annealed at 800°C for 12 h and finally re-oxygenated at 460°C for 20 h. The critical temperature (zero resistance) was ~ 92.5 K. This value compares well with conventionally melt-processed materials, which display critical temperatures in the range 89 - 90 K.

Contactless Measurements

Shown in Fig. 7.3 are results of critical temperature determinations obtained in a SQUID magnetometer (model MPMS, Quantum Design, San Diego, CA). All curves correspond to samples containing 20 wt. % 211, and grown at 2.78 μm/s. Curves (1), (2) and (3) were measured with the applied field parallel to the growth direction and correspond to samples 094, 121 and 091, respectively (see Table 5.2). Curve (4) also corresponds to sample 094, but is for field perpendicular to the growth direction. Sample 91 was dopped with 1 wt.% Pt,

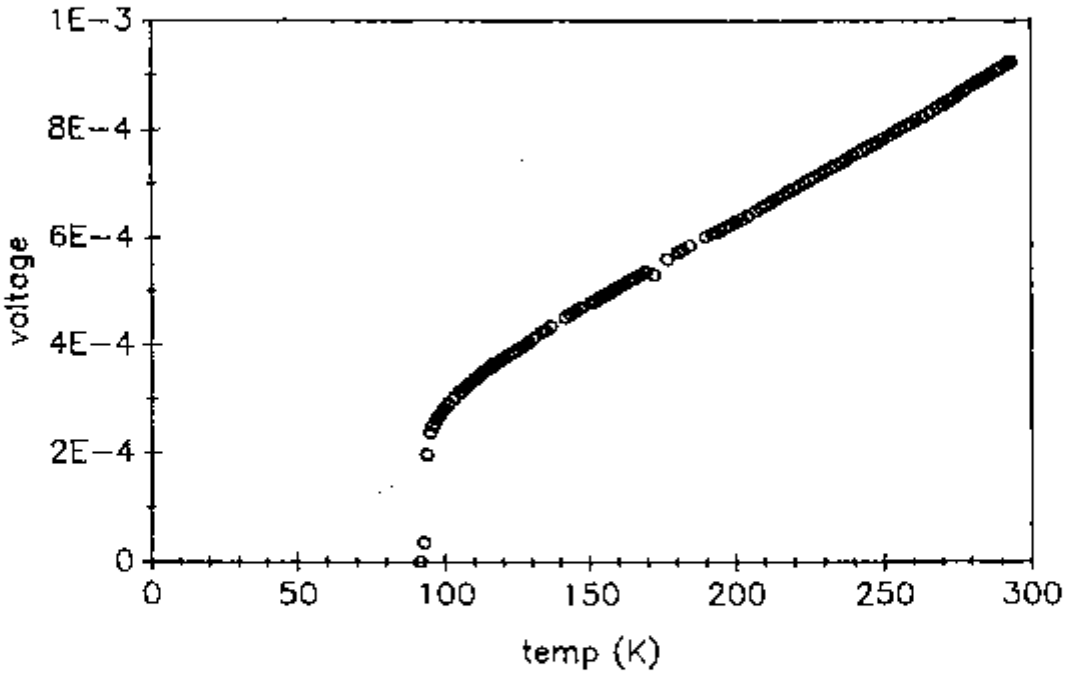

Fig. 7.2. Temperature-resistance characteristics along the growth direction of a single-grained LHFZ filament solidified at R = 2.78 μm/s (sample 029).

and sample 121 was grown from a precursor containing 210 and 012, instead of 123 and 211. Fabrication and characteristics of the latter sample are described in Chapter 6. Curve (4) is also for sample 094, but the applied field was perpendicular to the growth direction. The critical temperature for the onset of superconductivity (T_{co}) did not depend on precursor type, addition of Pt or sample orientation, and was about 92 K for all samples. However, the curve for sample 121 has a much broader transition. This and the presence of kinks in that curve, suggested that it was composed by a mixture of phases with different critical temperatures. It would be worthed to investigate this

hypothesis further, since solidification of these filaments with a controlled assemblage of superconducting (and also non-superconducting) phases may provide materials with enhanced flux pinning. A kink around 85 K is also discernible in curve (3), which is for the sample with 1 % Pt. Kinks were generally observed at ~ 81 and 85 K in other similar measurements. It is

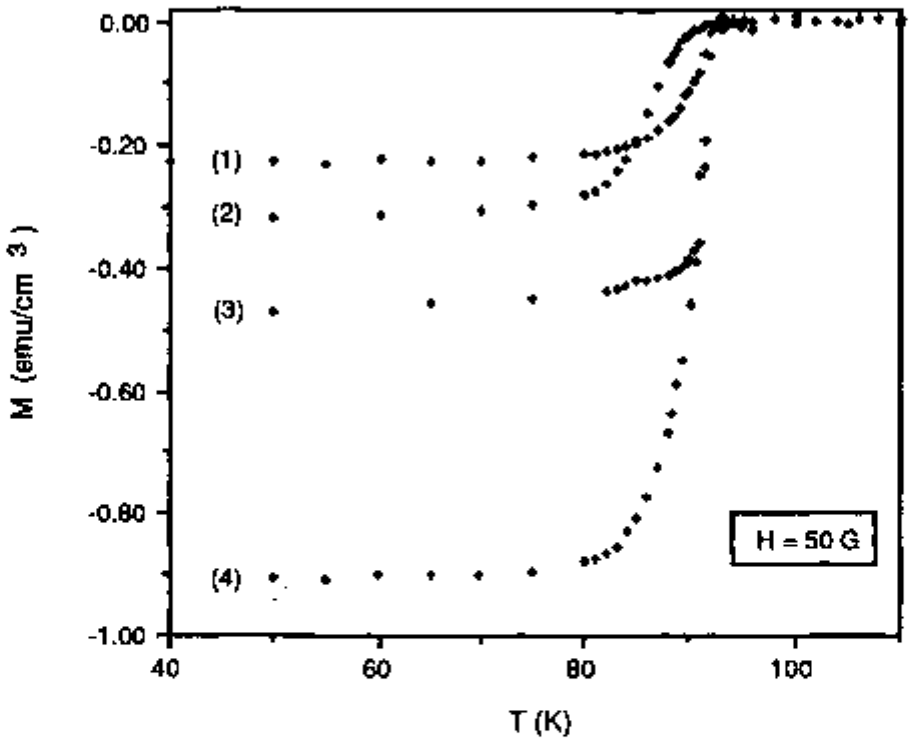

Fig. 7.3. Longitudinal magnetic moment of LHFZ samples. Measurements performed on cooling in an applied field of 50 G.

possible that during the solidification of LHFZ filaments, the formation of minor amounts of 123.5 (T_{c0} ~ 91 K)[237] and 124 (T_{c0} ~ 81 - 82.5 K)[38,250] was favored by the combination of relatively high pressures (1.3 atm O_2) and growth rates. An increase in the diamagnetic signal by a factor of 4 occurred when the sample orientation with respect to the applied field was changed from parallel ($H \perp c$) to perpendicular ($H \parallel c$). This increase is consistent with magnetization measurements reported below as a function of orientation with respect to the applied field.

7.3.2 *Magnetization Hysteresis and Magnetization Current Densities*

Bean's Model

Critical current densities were estimated using the Bean critical-state model[238] for isotropic superconductors. Its extension to anisotropic superconductors did not result in very different magnetic formulae.[239,240] However, the application of these formulas requires the determination of current densities along the crystallographic axes, what is experimentally difficult. For this reason, the simpler expressions due to Bean will be used here. In the Bean model, transport currents, *dc* bias field, lower critical field and surface barriers are all taken to be zero. The applied *dc* field and the full-penetration field are H_a and H_p, respectively. H_p is a function of the critical current density J_c and the cylinder radius r. The magnetization per unit volume of superconductor, M, is equal to the half-width of the hysteresis loop ($\Delta M/2$) for $H_a \geq H_p$. The geometry of interest here is that of a long cylinder of diameter d oriented parallel to H_a. For this case, magnetization and current density are related by the following equation:

$$J_c = \frac{30\Delta M}{d}, \tag{7.1}$$

Approximate solutions for H_a perpendicular to the cylinder axis have also been discussed by Goldfarb *et al.*[241] and references therein. The solution considered by Goldfarb differs from the above expression only by a factor of $\pi/4$. Since the solution is approximate and corrections for demagnetization were not made, Eq. (7.1) was also used to estimate critical current densities in the transverse orientation.

Eq. (7.1) can be applied to high-temperature superconductors provided that the following conditions are satisfied: (1) the sample is homogeneous and has dimensions consistent with the model; (2) flux vortices are well pinned. This is generally true in high-*Tc* superconductors at low temperatures; (3) the contribution from surface barriers and reversible magnetization is small. This conditions often is found at low temperatures where the hysteresis loop is symmetric at high fields; (4) The magnetization should be taken at fields larger than H_p, for which M is not a strong function of the applied field. Estimates of J_c from M at $H_a = 0$ are likely to have larger errors.

The former conditions are seldom satisfied simultaneously. However, for homogeneous samples, such as single crystals and samples with contiguous oriented grains, such as the present specimens, the basic critical-state model can be applied.[241]

Effect of Growth Rate

Fig. 7.4 shows the magnetization current density (J_c) of LHFZ filaments as a function of growth rate. J_c increased with growth rate in the planar front regime. At the transition from planar to cellular/dendritic growth, the data suggests the existence of a discontinuity in J_c and the trend is reversed as the growth rate increases past the transition value. To obtain the data of Fig. 7.4, all growth parameters but the growth rate were kept constant or within narrow limits. Parameters included in the former category were oxygen pressure, zone length, filament composition and diameter and precursor microstructure. Modest, 20 to 30°C reductions in temperature were necessary during growth at slow rates to maintain the zone stability. However, even temperature reductions of 50°C did not produce noticeable changes in zone length.

A number of factors may contribute to the observed J_c increase in planar front samples. Probably, the most important ones are those related to the concentration of defects and to the platelet structure.

Point and line defects potentially capable of enhancing flux pinning, as well as stacking faults, are likely to be more numerous at faster growth rates. Additionaly, the solid 211 particles in the semisolid zone coarsened to a lesser extent at faster rates. The finer particles promoted the stability of the zone during growth and reduced the extent of microcracking in the solidified material. The occurrence of cleaner grain and platelet boundaries also appeared to be related to the presence of smaller particles. Another important effect of fine 211 particles may be the formation of a larger number of platelet bridges (Section 5.3.7).

Surprisingly large currents were determined in the cellular/dendritic regime, considering the substantial decrease in the volume fraction of 123 that occurred with increased growth rate (Fig. 5.18), as well as the polyphase nature of the samples. In the cellular/dendritic regime, the grains are weak-linked; thus, instead of sample diameter, the grain size would be the proper length scale to use in Bean's model in order to estimate the intragranular J_c.

Reasonably good estimates of grain size in dendritic samples were difficult to make, because of the "fuzzy" appearance of the boundaries. Thus, as a matter of consistency, all current density calculations were carried out using the sample diameter. Nonetheless, an average grain size of 15 μm was estimated for the cellular sample of Fig. 5.15. Intragranular J_c values similar to the planar front samples were calculated for the cellular/dendritic samples, when the grain size of 15 μm was used in conjunction with Bean's model.

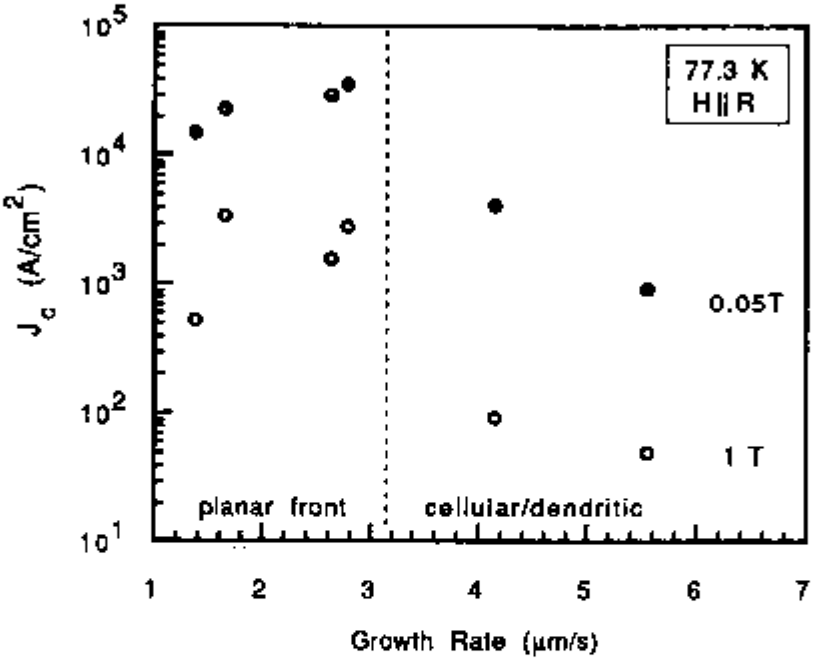

Fig. 7.4 Magnetization critical current density versus growth rate. Points in the planar front regime are average results. Points in the cellular/dendritic regime are from single samples.

Fig. 7.5 illustrates the field dependence of the magnetization current densities of LHFZ filaments solidified from precursors containing 22.8 wt.% 211. The top three data sets correspond to the best values measured at the given growth rate and the two lower sets are for single samples. At low fields, the cellular/dendritic samples showed a stronger field dependence of J_c than the planar front samples. The trend was reversed at fields of about 1 T. Arrests were also observed in the three lower curves and were probably caused by the increased flux pinning that resulted when lower order parameter regions were driven normal by the applied field. These arrests

could be eliminated by subjecting the samples to additional heat treatment in flowing oxygen.

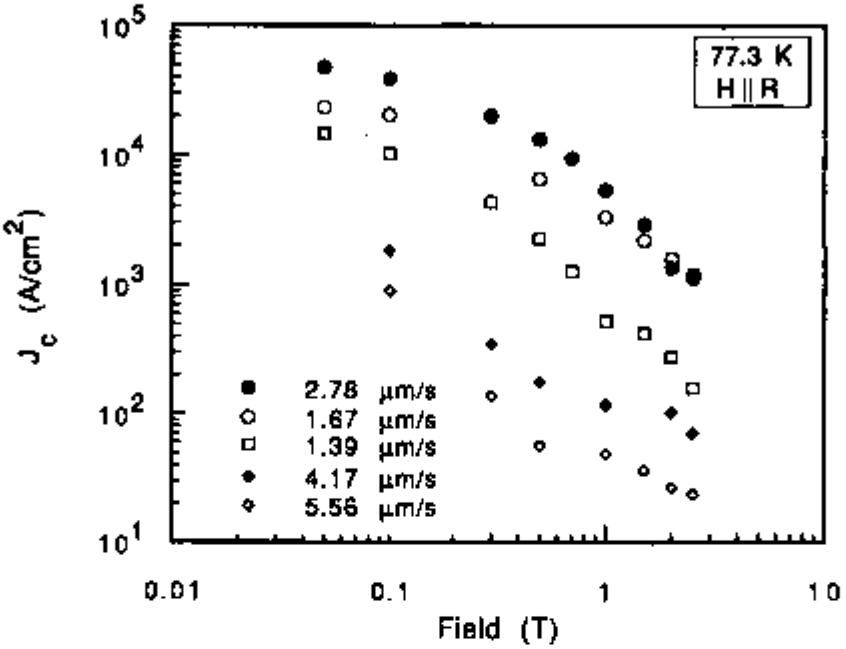

Fig. 7.5 Field and growth rate dependence of magnetization current densities of LHFZ filaments. The results are from samples of composition 123 plus 22.8 wt.% 211.

Anisotropic Behavior

The anisotropic behavior of LHFZ filaments is illustrated in Figs. 7.6 and 7.7. Fig. 7.6 shows half of the magnetization hysteresis loop of a sample that contained 2 grains. Critical current densities calculated from the data of Fig. 7.6 are shown in Fig. 7.7.

As described in Chapter 5, the orientation of the filaments is such that the *c* axis is perpendicular (or nearly perpendicular) to the growth direction. Therefore, a field applied parallel to the growth direction is perpendicular to the *c* axis (or parallel to the *ab* planes). In this orientation the magnetization of the crystal is the lowest. The sample of Fig. 7.6 contained two grains that run along its entire length; thus, for $H \perp R$, the field was applied at an arbitrary angle with respect to the *c* axis. The anisotropy of the crystals, expresssed by the ratios $J_c^{H\|R} / J_c^{H\perp R}$ or $J_c^{H\|c} / J_c^{H\perp c}$ (when the sample orientation

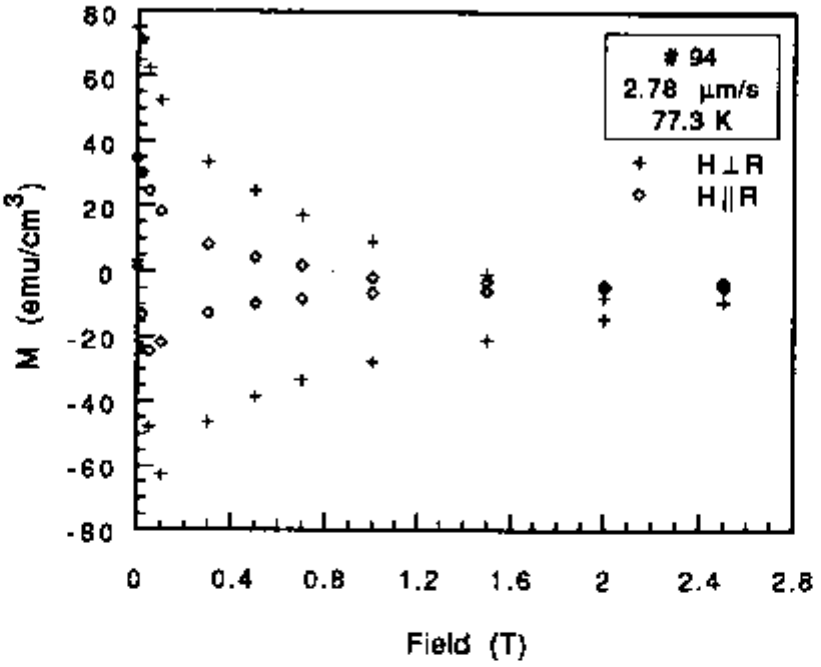

Fig. 7.6 Magnetization loops of a bi-crystal sample.

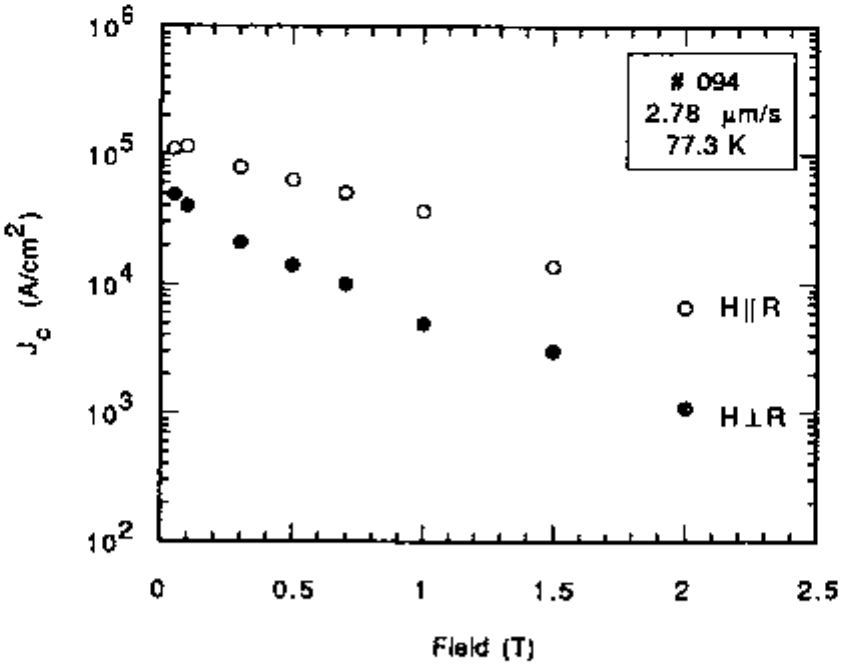

Fig. 7.7 Magnetization current densities calculated from the width of the magnetization hysteresis loops of Fig. 7.6.

was known) was determined on a few samples, including that of Fig. 7.6. The ratios increased with applied field, ranging from 2 to 10 at a field of 1 T and decreased with temperature. Measurements on single crystals by other investigators[23,239] yielded higher anisotropy ratios, i.e., 30 to 40 at H = 1 T.

The anisotropic magnetization behavior was also investigated on a single-grained sample with the applied field perpendicular to the growth direction (filament axis). The single-grained nature of the specimen was determined a priori by observing portions of its extremities under crossed polarizers. The sample was inserted in the magnetometer chamber and magnetization loops were determined after each incremental rotation of the sample about its axis.

The results (Fig. 7.8) showed the existence of maxima and minima space 90° apart; thus, confirming the single-grained nature of the sample. The maxima and minima of the magnetization curves correspond to angular positions at which the field was injected parallel and perpendicular to the *c*-axis, respectively. Current flows exclusively along the Cu-O (basal) planes when the field is parallel to the *c*-axis and along the *c*-direction, across the basal Cu-O planes, when the field is perpendicular to the *c*-axis. .

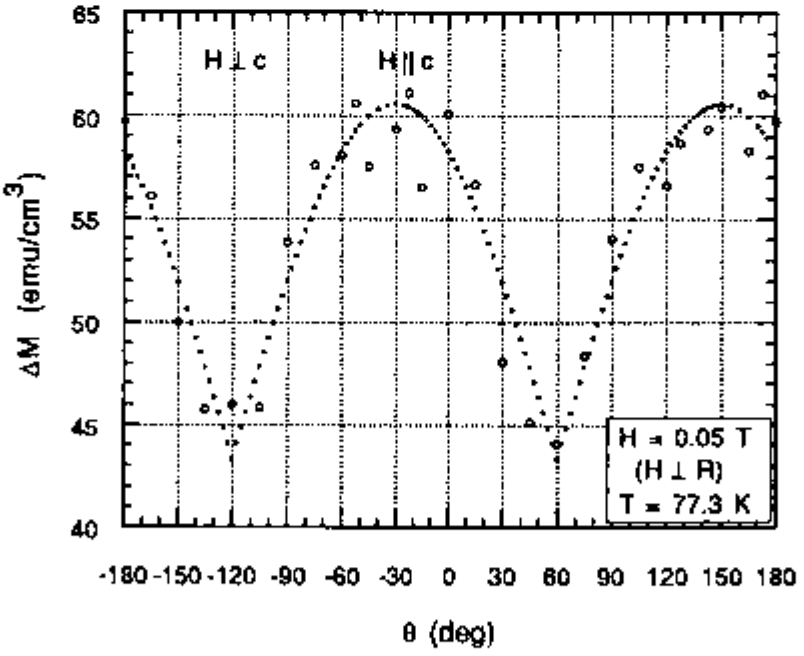

Fig. 7.8 Difference in magnetization as a function of the angle θ between the applied field H and the filament axis. ΔM values were obtained from the M-H hysteresis loops. The measurements were started at $\theta = 0°$.

The magnetization moment measured with $H \parallel c$ was larger than that measured with $H \perp c$ by a factor of about 1.3. This difference is in reasonable agreement with previous results from similar experiments on melt-textured domains[242,243] and filaments.[244] However, as discussed below, the form of the angular dependence is different than that found in the previous experiments.

Teshima *et al.*[245] have investigated the direction of the magnetization in *c*-axis oriented 123 films prepared by laser ablation. They concluded that in their samples, the magnetic moment induced by the applied field was parallel to the *c*-axis direction. In their experiments, as well as in the present work, measured M values correspond to the longitudinal moment, that is, the component of the magnetization parallel to the applied field. Thus, if the magnetic moment is induced along the c direction, the measured values should vary as $|\cos\theta|$, where θ is the angle between the c axis and the magnetic field. This dependence was indeed observed in their films and confirmed by the present experiments. Fig. 7.8 shows that the experimental points (open circles) are well fitted by an expression of the form $\Delta M = A + B\,|\cos(\theta + 30°)|$, with A = 43.34 emu/cm^3 and B = 17.21 emu/cm^3. This curve is represented by the dotted line in Fig. 7.8.

Temperature Dependence

Shown in Fig. 7.9 are magnetization hysteresis loops for the same specimen of Fig. 7.8. At 1 T, the width of the hysteresis loop increased by more than 2 orders of magnitude when the temperature was decreased from 77.3 K to 4.2K. A substantial increase in flux pinning was observed at 50 K and below, particularly at high fields. This is shown in Fig. 7.10 by the weak dependence of J_c on the applied field. At 77.3 K, J_c decreased rapidly with increasing field. A several-fold decrease in both the magnetization and the current density was observed when the field orientation was changed from parallel to perpendicular to c, but the form of the field dependence remained unchanged.

Fig. 7.10 shows that at $T \leq 50$K, very little change in current density occurred as the field was increased up to 0.1 T. At a field between 0.1 and 0.5 T there was an initial drop in the J_c values, which then remained fairly constant (at 50 and 30 K) or slightly decreased (at 10 and 4.2 K) as the field continued to

increase. This observations suggests the existence of at least two categories of pins in the material.

One of the main requisites for the pins to be effective is that their sizes have to be comparable to the fluxon diameter, which is approximately given by 2ξ. As discussed in Chapter 2, the penetration depth (λ) and the coherence length (ξ) follow a -1/2 dependence of the lower and upper critical field, respectively. However, little changes occur in H_{c1} and H_{c2} below 50 K, because of the nature of their temperature dependence, which is approximately given by $H_c(T) = H_c(0)\,[1 - (T/T_c)^2]$. Therefore, the temperature dependence of both the coherence length and the penetration depth is also weak below 50 K. This means that in this temperature range, the flux pinning characteristics of the material does not change markedly, as was indeed observed. Apparently, a good correspondence between the densities, as well as the diameters of fluxons and pins was achieved below 50 K.

A slight increase in the pinning strength, revealed by the initial increase in current density with field, was observed to occur at 4.2 K. This observation

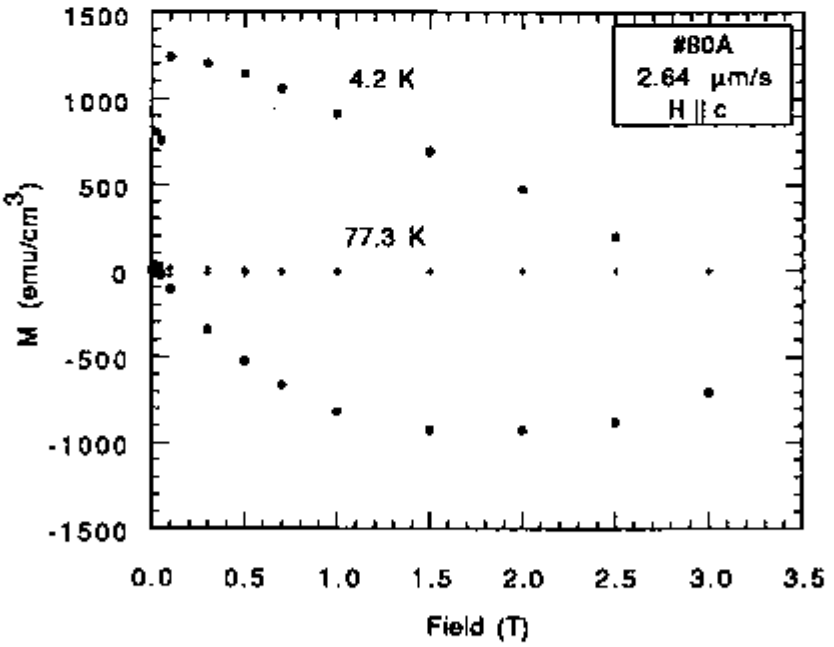

Fig. 7.9 Magnetization loops of a single-grained filament at 4.2 and 77.3 K. Measurements performed with the applied field perpendicular to the growth direction (filament axis).

suggests that at low fields the pins are superconducting regions with lower H_{c2} and T_c than the matrix. As these regions are driven normal by the increasing

field, their pinning strength initially increases with field up to a maximum, which occurs when they become fully normal.

As the field increases, so does the fluxon density [m^{-2}], which is given by H/Φ_0, where Φ_0 is the fluxoid quantum. One should expect the flux pinning to decrease as the field is increased past the value at which the fluxon density equals the pin density. This is probably the cause of the decrease in J_c with increasing field shown in Fig. 7.10. However, the measured field dependences were weak, suggesting that in this temperature and field range other pins also became effective.

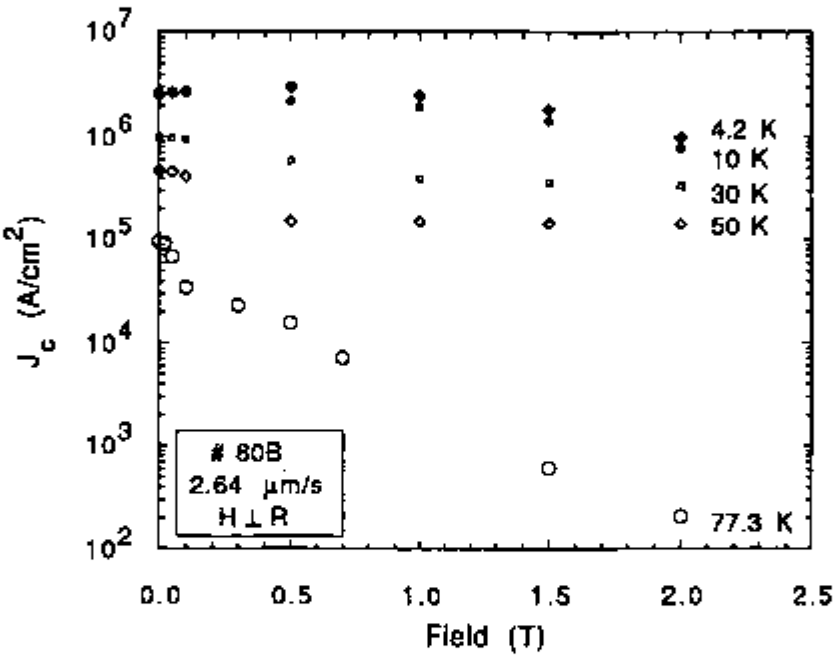

Fig. 7.10. Temperature dependence of the magnetization current density of a single-grained filament

At 77.3 K, different field dependencies of J_c were observed at low and high fields. The current densities measured at 77.3 were much lower than at 50 K and decreased markedly with increasing field over the entire range investigated. This was probably caused by weak flux pinning, due to the combination of a large coherence length with the inadequate nature, size and geometry of the existing defects. The enhancement of flux pinning in this temperature range will certainly require a very good understanding of the defect nature, as well as of the detais of the interactions between fluxons and

defects. However, the magnitude of the decrease in current density that occurs at 77.3 K suggests that one will not be able to produce large increases in the current densities at high temperatures solely by introducing defects in the material. This is so because flux creep is strong at 77.3 K. The pinning energy (δE) depends on the volume of fluxon core pinned (δV), as well as on the thermodynamic critical fields of matrix (H_c^m) and defect (H_c^d):

$$\delta E = -\frac{1}{2}\mu_0\left[(H_c^m)^2 - (H_c^d)^2\right]\delta V \qquad (7.2)$$

Therefore, the maximization of the pinning energy requires the simultaneous increase of H_c^m and δV. An additional gain in pinning energy will be achieved if the defects are non-superconducting, in which case $H_c^d = 0$. Increases in both the upper critical field and T_c have been reported to occur when a small fraction of La is substituted for Ba in compounds of nominal composition $YBa_{2-x}La_xCu_3O_{7-\delta}$.[246] Significant increases in flux pinning have also been reported to result from defects introduced by phase decomposition.[61,247] as well as from the combination of atomic substitution and phase decomposition.[248] Thus, the combination of chemical substitution, phase decomposition and melt processing seems to be a very attractive route for to increase flux pinning in cuprate superconductors.

Recently published current density results for high-quality single crystals grown by the flux method[59,249] are very similar to the LHFZ filaments in magnitude and behavior with respect to temperature and field. These results support a previous hypothesis[170] that the platelet domains are indeed single crystals.

7.3.3 Direct Critical Current Density Measurements

To minimize Joule heating at the electrical contacts, which is a major obstacle to accurate determinations of critical current densities in high-T_c superconductors, the samples were tested with short current pulses. The measurements were performed with the samples immersed in liquid nitrogen.

Two samples were measured using a high-speed power supply capable of delivering up to 50 A at up to 15 V (Kepco ATE-15-50M). The first sample was

tested by 10 ms pulses, generated at 3 s intervals, with 0.5 A increase between pulses. The voltage accross the samples was measured on a scale of 0 - 1 V. Maximum voltage readings did not exceed 5 mV up to 10.9 A. At 11.4 A, the voltage spiked above 1 V and the sample bursted. The second sample underwent a number of different pulses. The observed noise levels were proportional to the current amplitude, and between 30 and 40 A, the typical noise level was 15 mV. The noise was in the form of a +15 mV spike during the rising edge of the current pulse, some lower voltage oscillations, and then a comparable negative spike on the falling edge of the pulse. This noise pattern was attributed to the way the sample was set up for measurement. Apparently, an air-core transformer was created between the current and voltage leads by the way the wires were wrapped around the liquid nitrogen container. This could explain the observed voltage spikes. At around 40 A, the current was increased by about 0.1 A/pulse. At 41.65 A, noise levels were still at 13 mV, as before. The maximum recorded voltage spike was about 121 mV during the 41.75 pulse. At 41. 85 A, the sample bursted with a flash of light. Based on these observations it was concluded that the sample critical current was at least 41.75 A.

The other two samples were measured with a 100 A power supply using pulse widths of 1 ms. The voltage across the sample was measured by means of a digital oscilloscope. Details of the measurement system are shown in Fig. 7.10. Before evaluating the samples, the measurement system was investigated with a copper bar. A voltage of 110 μV was obtained with a current pulse of 22 A in a copper bar of 5 μΩ, just as expected. Voltage waveforms from sample 138 are presented in Fig, 7.11 and the measured voltage as a function of the applied current is shown in Fig. 7.12. As illustrated in Fig. 7.12, a sudden rise in voltage occurred near the critical current. The evolution with the voltage curve with applied current was similar to the two previous samples. The critical current of sample 138 was determined to be 39 A with a criterion of 10^{-10} cm (Fig. 7.12).

Fig. 7.13 illustrates the voltage waveforms and the voltage-current curve for sample 130. Significant reduction in the noise level was obtained by simply averaging the voltage waveforms, as shown in Fig. 7.13. A slight downward deviation was observed in the V-I curve as the transmitted current increased. The origin of this behavior could not be identified, but it

was possible to conclude that the critical current of the sample was at least 59A, the current at which the sample bursted.

The results are presented in Table 7.1 as a lower limit for the critical current density of the samples. It is believed that large heat generation at the electrodes prevented the attainment of the actual critical current density in the four samples tested. The direct measurements, which are for current transmitted along the *ab* planes apparently agree with magnetization measurements in the transverse orientation ($H \parallel c$), also included in Table 7.1. However, this agreement may be fortuitous, since the magnetization measurements are also lower limits, because demagnetization factors were neglected. Nonetheless, the Bean critical-state model can predict well the transport current density of single-grained filaments.

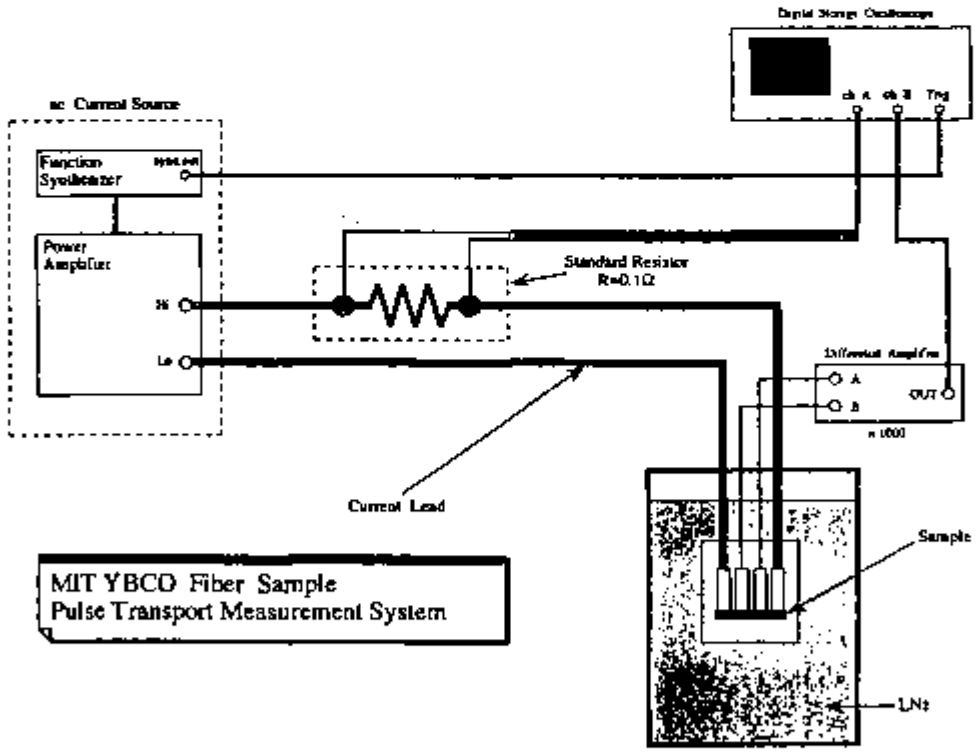

Fig. 7.11. Sketch of the pulsed, direct critical current measurement system.

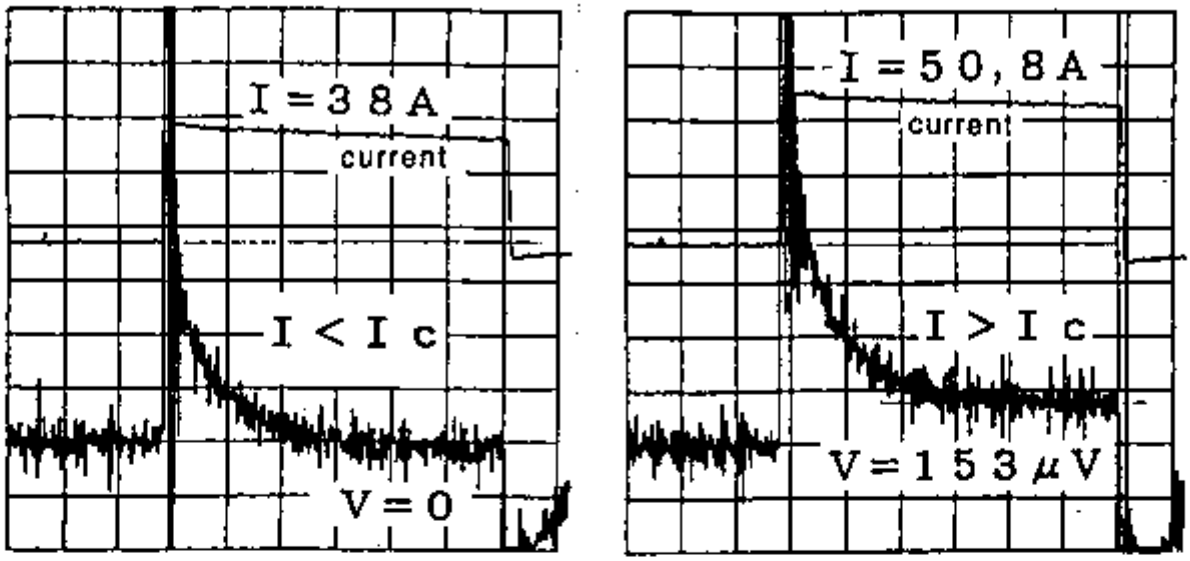

Fig. 7.12. Voltage waveforms from sample 138.

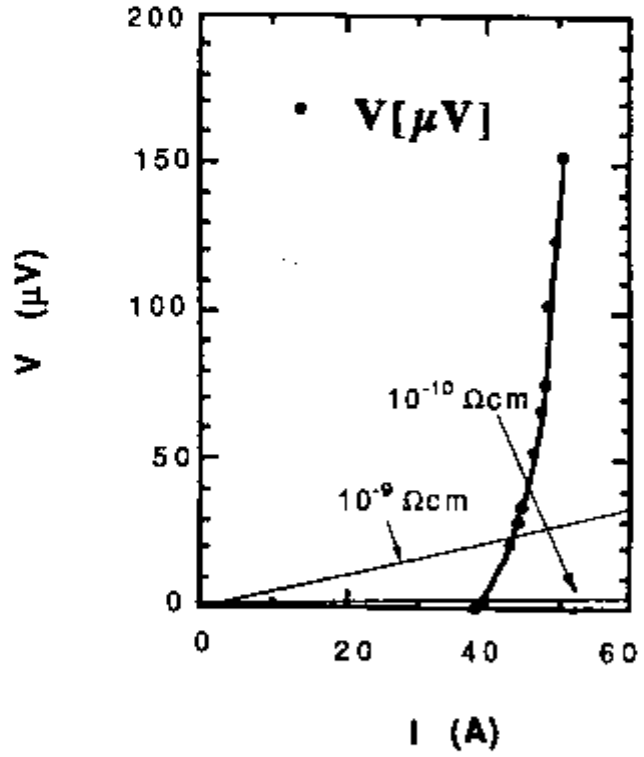

Fig. 7.13. Voltage-current curve from sample 138.

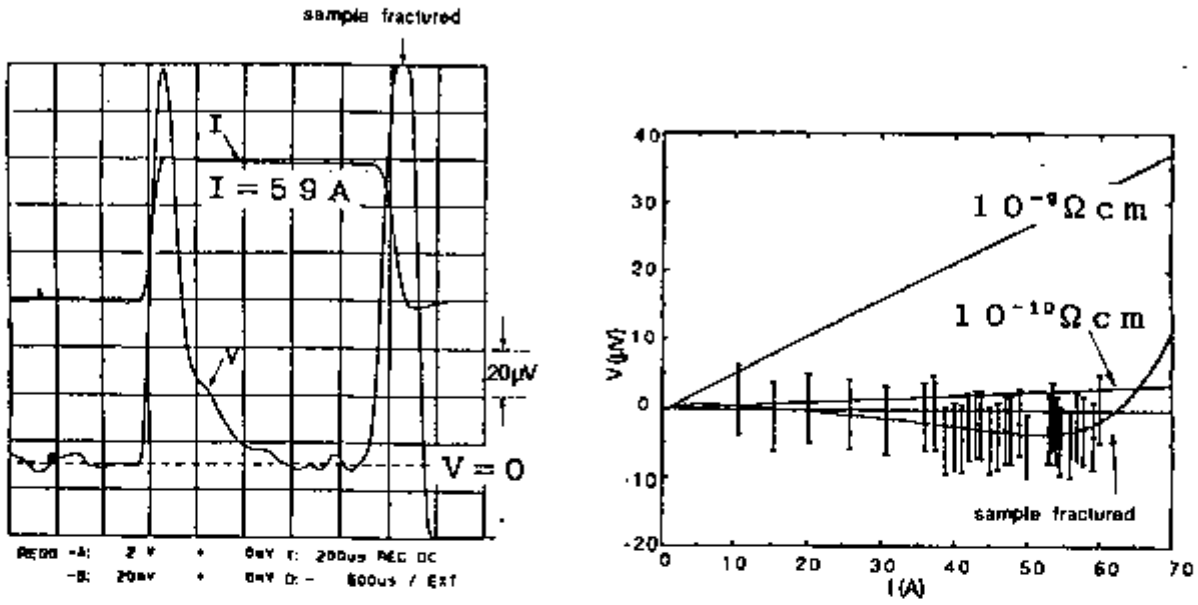

Fig. 7.14. Voltage waveform curves and V-I curves for sample 130.

Table 7.1. Summary of magnetization and transport current density results (all samples were solidified at 2.78 μm/s, except sample 080, which was grown at 2.64 μm/s).

Sample	Diameter (μm)	Critical Current Density (A/cm²) J_c^{abc} (Magnetization) $H = 0.05$ T; $T = 77.3$ K	J_c^{ab} (Transport) Self-field; $T = 77.3$ K
		H ∥ R	J ∥ R
033[b]	240	3.2×10^4	$\geq 2.4 \times 10^4$
138[a]	260	2.6×10^4	$\geq 7.2 \times 10^4$
129[b]	220	3.7×10^4	$\geq 1.1 \times 10^5$
130[a]	248	5.3×10^4	$\geq 1.2 \times 10^5$
		H ⊥ R	
080[a]	200	9.5×10^4	
091[a]	200	1.1×10^5	
094[b]	348	1.2×10^5	

([a]) 1 grain
([b]) 2 grains

7.4 Summary

In the planar front regime, higher solidification velocities produced filaments with higher critical current densities. A sharp decrease in critical current density occurred at the transition from planar to cellular/dendritic growth. Within the latter regime, the critical current density decreased as the solidification velocity increased.

The results suggested that the anisotropic behavior of LHFZ filaments can be characterized by three different values of current density, depending on the relative orientation of the filament with respect to the applied magnetic field. The highest current values of current density were measured with the applied field oriented parallel to the *c* axis and perpendicular to the filament axis. In this orientation, the shielding currents flow exclusively along the basal *ab* planes.

Both indirect and direct methods yielded current density values in excess of 10^5 A/cm^2 at 77.3 K and along the basal planes. These values were about twice the values determined with the field oriented parallel to the filament axis ($H \parallel R$). Magnetization current densities increased rapidly with decreasing temperature, reaching values in excess of 10^6 A/cm^2 at low fields below about 30 K.

At 50 K and below, LHFZ filaments displayed good flux pinning characteristics, as evidenced by the weak field dependence of the current density. At 77.3 K, the rapid decrease of the critical current density with applied field, over the entire field interval investigated, revealed a decrease in the flux pinning capabilities. However, at 77.3 K, the critical current of LHFZ filaments exceeds the typical value of good polycrystalline materials by more than 2 orders of magnitude at low fields, and by more than 3 orders of magnitude at 1 T.

Chapter 8
Conclusions

1.

A plastic extrusion process was developed to fabricate polycrystalline superconducting filaments for the directional solidification experiments reported here. The filaments were composed of an inter-dispersion of the superconducting phase, $YBa_2Cu_3O_{7-\delta}$ and 20 wt.% of the high-temperature phase Y_2BaCuO_5. The filament fabrication process relied on the addition of octanol based solutions of a binder, poly-vinyl butyral and a plasticizer, di-butyl phthalate, to the mixture of 123 and 211 oxide powders. Controlled evaporation of solvent yielded a plastic mass with adequate rheological properties for extrusion into 300 - 400 μm diameter filaments. Filament density varied between 70 and 100%, depending on composition. After binder burn out and sintering, the filaments contained no extraneous phases, such as oxycarbonates or low melting point cuprates.

2.

The morphology of Y_2BaCuO_5 (211), the high-temperature phase formed by incongruent melting of $Y_2BaCu_3O_{7-\delta}$ (123), was investigated by quenching experiments. 123 samples prepared from different powders resulted in 211 particles with different size and morphology. This was attributed to different kinds and levels of contaminants in the starting powders. The average 211 particle size was larger in the samples prepared from powder containing lower nominal levels of contaminants. The addition of 1.1 wt. % Pt to the samples caused a significant reduction in 211 particle size, as well as marked changes in particle morphology. Needle-like 211 particles were observed to form in samples containing platinum. The needles appeared to radiate from a common origin, probably a common nucleation center. It appears that the addition of platinum leads to formation of barium platinate or quaternary oxides of platinum, which may act as heterogeneous nucleation centers for the nucleation of the 211 phase. The results suggested that dopping may be an efficient method to obtain fine 211 particles during semisolid processing of 123.

3.

Single-crystalline or textured 123 filaments were succesfully grown by the laser-heated floating zone technique in 1.27 atm O_2. Liquid was found to migrate out of the zone, down the temperature gradient, especially at high values of the latter. Liquid migration was prevented by the addition of about 23 vol.% of the high-temperature phase 211. The stability of the zone increased with the density and the amount of 211 particles in the precursor. Steady state peritectic solidification of the superconducting compound 123 was obtained in temperature gradients of the order of 10^6 °C/m in the range of growth rates from 1 to 8 μm/s.

4.

Besides the peritectic reaction $211 + L \rightarrow 123$ that occurs at the 123 solidification front, other invariant reactions also occurred within the floating semisolid zone. The longitudinal liquid composition profile within the zone was affected by growth method, composition, nature and density of the precursor, as well as by the occurrence of the previous invariant reactions.

5.

Depending on growth rate and temperature gradient, three types of growth morphologies of the growing 123 phase were observed in this work: "faceted plane front", "cellular/dendritic" and "quenched". A fourth type of morphology, "equiaxed/blocky" has also been also reported in the literature for growth at low temperature gradients and relatively fast solidification velocities.

6.

The volume fraction of 123 in the solidified filament decreasead linearly with growth rate in the planar and cellular/dendritic regime, up to 8 μm/s. Past that value, the cooling rates were fast enough to prevent the formation of 123 by the peritectic reaction at the growth front, and the semisolid mixture of 211 and L was simply quenched at the metastable solidus interface.

7.
Generally, microcracking was not observed in samples grown with planar front, which contained 30 to 35 vol.% of fine 211 particles. Residual inclusions composed by barium cuprate and/or copper oxide were difficult to find in these samples. Samples solidified with cellular/dendritic morphologies were multiphase.

8.
The 211 particles coarsened while in contact with the liquid during their traject through the zone. At growth rates below 1.4 μm/s, the 211 particles displayed a preferred orientation along the growth direction.

9.
Insulating films were detected along grain boundaries, especially at low solidification velocities. The thickness of grain boundary films decreased with increasing growth rate. At rates close to the upper limit for plane front growth, insulating films along grain boundaries could no longer be detected by optical microscopy. Whenever present, these films appeared to be discontinuous.

10.
In samples solidified with planar front morphology, the intra-granular structure consisted of stacks (domains) of thin, *ab*-oriented 123 plates, with thickness similar to the 211 interparticle spacing. Platelet boundaries could be observed in fracture surfaces by scanning electron microscopy, but not by optical microscopy in polished sections, except at very slow growth rates. Apparently, the plate boundaries are much cleaner in LHFZ filaments than in conventionally melt processed samples.

11.
This work confimed previous observations which have indicated that the 123 plate domains are essentially single crystals. SEM fractographs revealed that the plate structure contains a large density of interconnections, which formed at the positions where the plate boundaries met with 211 particles during

planar front growth. These interconnections allow for non weak-linked current flow along the *c*-direction.

12.
The mechanism for steady-state peritectic solidification of 123 with planar front was identified for the first time in this work. The mechanism is quite different from that encountered in conventional solidification. In the latter case the reaction initially occurs at the interface between the high-temperature phase and the liquid and then proceeds by diffusion through the solid reaction layer that separates the high-temperature phase from the surrounding liquid. In 123, the peritectic reaction occurs by dissolution of the 211 phase into the liquid, transport of solute by diffusion through a distance roughly equal to the 211 particle size, and reprecipitation on the 123 crystal surface. This interpretation resulted directly from microstructural observations of quenched interfaces in samples solidified by the laser-heated floating zone technique.

13.
The high-temperature 211 particles must become supercooled very close to the crystal interface in order to create the concentration gradient needed to drive mass transport and thereby sustain the reaction. Considerations of mass transport restrictions and thermodynamic driving forces showed that the largest constitutional supercooling is a small distance ahead of the interface. This condition in classical solidification would normally make a planar front unstable, since perturbations would grow. In the case of 123, the highly faceted crystal interface apparently prevents the growth of such perturbations and the limiting factor for planar front growth is the amount of undercooling that will cause nucleation of new crystals ahead of the interface.

14.
A solidification model was developed to interpret the experimental observations. The model predicts, in agreement with experiment, that growth rate of the low temperature solid phase has a strong effect on the ability to obtain the desirable faceted plane front and that the effect of the

temperature gradient is small. Interparticle spacing of the high-temperature phase (211) is also predicted to have a strong effect.

15.

The present experiments revealed that the production of single-crystalline filaments of 123 is limited to growth rates of 3.1 μm/s using about 1 μm 211 particles and temperature gradients of the order of 10^6 °C/m.

16.

This work revealed, for the first time, the formation of aligned structures in ceramic systems by directional phase formation on melting via peritectic reaction in filaments of phase pure 123 and 123 plus 20 wt.% 211. The following sequences of peritectic reactions were observed on heating in compositions near 123:

$$\gamma \rightarrow \alpha + L \rightarrow \delta + L \qquad (P_{O_2} > 10^3 \text{ Pa})$$
$$\gamma \rightarrow \alpha + L \rightarrow \varepsilon + L \rightarrow \delta + L \qquad (8 \text{ Pa} < P_{O_2} < 10^3 \text{ Pa})$$
$$\gamma \rightarrow \varepsilon + L \rightarrow \delta + L \qquad (P_{O_2} < 8 \text{ Pa})$$

where γ, α, δ, and ε represent the phases 123, 211, 200 and 210. In the above reactions α and δ phases comprised equiaxed particles. Rod-like ε was formed by incongruent melting of α following the second reaction series above. Below 8 Pa, α was no longer formed and the oriented ε phase formed directly from γ, and was plate-like in morphology. The reactions $\alpha \rightarrow \varepsilon + L$ and $\gamma \rightarrow \varepsilon + L$ were not observed in the system Y-Ba-Cu-O prior to this work.

17.

Growth of aligned rods or plates occurred from a superheated semisolid mixture of α particles and liquid, which was formed by incongruent melting of the γ phase in the precursor. On cooling, formation of γ was suppressed by solidification of the liquid phase to form β ($BaCu_2O_2$). This resulted in the growth of composite filaments with structures very similar to directionally solidified eutectics.

18.

Boundaries for the phase fields ε + L and δ + L were located by determining relative positions and temperature of interfaces in quenched specimens of composition 1:2:3. The laser-heated technique was found to be an interesting and effective technique for the study of phase equilibria as a function of oxygen partial pressure in reactive oxide systems.

19.

A simple solidification model predicted a relation between superheating and growth rate that is analogous to that derived in the Jackson-Hunt analysis for the undercooling and growth rate during directional solidification of eutectics. The dependence of the ε rod or plate spacing on growth rate, however, is not the same as that found by Jackson and Hunt. This is because the ε phase grows directionally *in* rather than *from* a liquid phase. The rods or plates coarsen before reaching the solidus interface, and the spacing is largely controlled by coarsening.

20.

Growth of γ plus α composites from $\varepsilon + \beta$ precursors was demonstrated for the first time. The sequence of transformations

$$\alpha + \gamma \xrightarrow{P'_{O_2}} \varepsilon + \beta \xrightarrow{P''_{O_2}} \alpha + \gamma,$$

where $P'_{O_2} < 10^3$ Pa and $P''_{O_2} > 10^3$ Pa, was also demonstrated to be an effective tool for microstructural control in $\gamma + \alpha$ composites.

21.

A qualitative picture was proposed to explain the effects of oxygen partial pressure on the solidification morphologies, as well as on the pseudo-binary phase diagrams of 123.

22.

In the planar front regime, higher solidification velocities produced filaments with higher current densities. A sharp decrease in current density occurred at the transition from planar to cellular/dendritic growth. Within the latter regime, the critical current density decreased as the solidification velocity

increased. This was attributed to the substantial decrease in the volume fraction of the superconducting phase in filaments solidified with dendritic front.

23.

The anisotropic behavior of single-crystalline LHFZ filaments is similar to that reported previously for *c*-axis oriented thin films fabricated by laser-ablation.

24.

Current densities in excess of 10^5 A/cm^2 at 77.3 K and along the basal *ab* planes were obtained by both direct and indirect methods. The magnetization current densities increased rapidly with decreasing temperature, reaching values in excess of 10^6 A/cm^2 at low fields. Below 50 K, LHFZ filaments displayed good flux pinning characteristics, as evidenced by the weak field dependence of the current density. At 77.3 K, the rapid decrease of critical current density with applied field, over the entire field interval investigated, suggested weak flux pinning in the solidified structure.

Chapter 9
Suggestions for Future Work

9.1 Precursor Filaments

Important microstructural attributes of LHFZ filaments, such as microchemistry, nature of defects and platelet structure are imposed by the characteristics of the semisolid zone. In chapters 5 and 6 it was demonstrated that the structure and chemistry of the semisolid zone are strongly dependent on the structure as well as on the chemistry and nature of the phases contained in the precursor. Therefore, it will be appropriate to investigate in more depth the relations between the nature of the semisolid zone and of the precursor and the resulting microstructure. This will require different types of filaments with controlled microstructure.

Precursor filaments composed by 210 plus 012 are particularly attractive since the 210 rod spacing, and hence the spatial distribution of Y, Ba, and Cu can be varied through changes in growth rate. The easy interconversion of 210 plus 012 and 123 plus 211 can also be exploited to produce composite filaments containing submicrometric dispersions of 211 in 123 by directional solidification. For the same reason, materials produced via sol-gel routes could also be exploited for the production of composite 123 plus 211 filaments.

9.2 Flux Pinning Enhancement Via Solidification Processing

9.2.1 Growth Rate Oscillations

In directional solidification, the amount of solute (or solvent) carried forward ahead of the solidification interface is given by the area under its concentration profile, which is proportional to the characteristic distance D/R.[214,251] Referring to the concentration profiles of Figs. 5.7 and 5.8, if during steady state growth the value of R is increased, D/R and the amount of copper ahead of the solidification interface must decrease; the solid that forms immediately after the increase of speed must have a higher Cu concentration during the transition from steady state growth at lower R to steady state at

higher R. In the same manner, the copper concentration in the solid following a decrease in speed must be lower than the steady state value. Therefore, growth rate oscillations during steady state will cause the solute content in the solid to oscillate with the same periodicity.[214] Due to the particularities of crystal growth during directional solidification of 123, it is very likely that periodic changes in solute concentration be acommodated as non-superconducting inclusions in the 123 crystals. A further aspect worthed investigating is the relation between the growth rate oscillations and the density of point, line and surface defects, as well as their orientation relatively to the crystal. The proposed approach may also be combined with other techniques presently used for flux pinning enhancement, such as phase decomposition and chemical substitution.

9.2.2 *Copper-rich Compositions*

Fig. 2.19 reproduces the 123-CuO section of the pseudo-ternary BaO-Y_2O_3-CuO phase diagram for oxygen pressures below 1 atm, proposed by Lindemer *et al.*[109] In that pressure range, the diagram show complicated melting relations, which involve at least two solid phases. The field 123 plus CuO extends over the entire composition range, between 879 and 964°C. Consideration of that diagram suggests that it may be possible to obtain unique microstructures by solidification in this composition range by following two distinct paths:

(1) At the composition p1, 123 and CuO are formed by the reaction of 211 with liquid. Under large temperature gradients and adequate growth rates, it could be possible, at least in principle, to solidify single crystals of the 123 compound containing CuO in the form of thin platelets. If the size scale of these platelets is sufficiently small, short post-solidification heat treatments could be employed to convert the 123 plus CuO sample into 123 plus 124 and then into 123 plus CuO again, similarly to an age-hardening type process. If the microstructural size scales are such that the previous reactions can be completed in reasonable time, three basic types of pinning centers could be introduced in the material, making the flux pinning effective over the whole temperature range (4 to 80 K). The first class would include the intrinsic 123 pinning sites, which are effective in the low temperature range as shown in Fig. 7.10. The second class would include pinning centers that may be

effective in the mid-temperature range, such as stacking faults and their associated dislocations, for example. The third class must include defects with relatively larger length and cross section. This is so, because in the high-temperature range the coherence length becomes very large and small defects are ineffective because they do not pin large volumes of fluxon core; therefore the total pinning force is small to prevent flux creep. These defects could be the non-superconducting CuO platelets formed during the solidification process and/or intentionally added impurity phases. Possibly, the introduction of such defects must be done in such a way that they have a definite orientation with respect to the crystal axes.

(2) This approach is proposed after the recent results of Karpinski *et al.*[111] for the stability of the compounds 123, 123.5 and 124 over the range of oxygen pressures from 0.01 MPa to 1000 MPa (0.1 to 10,000 atm), which are shown in Fig. 2.20. The diagrams of Karpinski *et al.* indicate that the phase 123.5 decomposes incongruently above about 10 atm O_2 at the stoichiometric composition (20 atm O_2 at the 124 composition). Their P_{O_2}-temperature conditions suggest that, as the oxygen pressure increases, the 123 plus CuO field in Fig. 2.20 becomes narrower, and eventually disappears. This may allow the direct solidification of 123.5 from a semisolid mixture of 211 plus liquid of overall composition p1, in very modest oxygen pressures (possibly between 5 and 10 atm) and without the formation of CuO platelets. Below 5 atm, if the temperature range for the stability of the 123 plus CuO field is small enough, the formation of CuO could be also be suppressed if the the undercooling is such that the solid in equilibrium with the liquid p1 becomes 123.5. In any case, if both 123 and 123.5 could be formed simultaneously during directional solidification, it would be possible to obtain intergrowth structures which are important from the point of view of flux pinning. In addition, the decomposition of the 123.5 phase by post-solidification annealing could also be used to introduce non-superconducting defects in the crystal.

9.2.3 *Chemical Substitution*

Neumeier[246] have recently reported increases of 2 K in the critical temperature and 50% in the upper critical field (H_{c2}) of 123 when a minor amount of La is

substituted for Ba. An earlier paper by Tallon *et al.*[248] reported a 17-fold increase in the intragranular J_c of polycrystalline 123 at 77 K and 0.75 T, when La substitution was combined with the phase decomposition technique. These results, viewed in the context of Fig. 2.15 suggest that the judicious combination of directional solidification with second phase addition, chemical substitution and phase decomposition may yield significant increases in the current density levels of 123 at 77 K and high fields.

Bibliography

1 C. Michel, L. Er-Rakho, and B. Raveau, J. Solid State Chem. **39**, 161 (1981).

2 C. Michel, L. Er-Rakho, and B. Raveau, J. Solid State Chem. **42**, 176 (1982).

3 C. Michel and B. Raveau, J. Solid State Chem. **43**, 73 (1982).

4 C. Michel, L. Er-Rakho, and B. Raveau, Mat. Res. Bull. **20**, 667 (1985).

5 J. G. Bednorz and K. A. Müller, Z. Phys. B **64**, 189 (1986).

6 W. K. Wu, J. R. Ashburn, C. J. Torng, P. H. Hor, R. L. Meng, L. Gao, Z. J. Huang, Y. Q. Wang, and C. W. Chu, Phys. Rev. Lett. **58**, 908 (1987).

7 M. Maeda, Y. Tanaka, M. Fukutomi, and A. Asano, Jpn. J. Appl. Phys. **27**, L209 (1988).

8 Z. Z. Sheng and A. M. Hermann, Nature **332**, 55 (1988).

9 G. Burns, *High-Temperature Superconductivity*, Academic Press, CA (1992), p. 57.

10 Ibid. 9 p. 112.

11 D. M. Kroeger and A. Goyal, J. Met. **44**, 42 (1992).

12 A. W. Williams, G. H. Kwei, R. B. Von Dreele, A. C. Larson, I. D. Reistrick, and D. L. Bish, Phys. Rev. B **37**, 7960 (1988); R. Beyers and T.M. Shaw, Solid State Physics **42**, H. Ehrenreich and D. Turnbull (eds.), Academic Press, Boston, MA (1989), p. 140.

13 E. D. Specht, C. J. Sparks, A. G. Dhere, J. Brynestad, O. B. Cavin, D. M. Kroeger, and H. A. Oye, Phys. Rev. B **37**, 7426 (1988).

14 T. B. Lindemer, J. F. Hunley, J. E. Gates, A. L. Sutton, J. Brynestad, J. Am. Ceram. Soc. **72**, 1775 (1989).

15 D. de Fontaine, G. Ceder, M. Asta, Nature **343**, 544 (1990).

16 R. Beyers and B. T. Ahn, Annu. Rev. Mater. Sci. **21**, 335 (1991).

17 T. A. Friedman, M. W. Rabin, J. Giapintzakis, J. P. Rice, and D. M. Ginsberg, Phys. Rev. B **42**, 6217 (1990).

18 Ibid. 9, p. 84.

19 J. B. Torrance, A. Bezinge, A. I. Nazzal, T. C. Huang, S. S. Parkin, D. T. Keane, S. L. LaPlaca, P. A. Horn, and G. A. Held, Phys. Rev. B **40**, 8872 (1989).

20 C. Kittel, *Introduction to Solid State Physics*, Wiley, NY (1986) p. 346.

21 L. Krusin-Elbaum, R. L. Greene, F. Holtzberg, A. P. Malozemoff, and Y. Yeshurun, Phys. Rev. Lett. **62**, 217 (1989).

22 Ibid. 9, p. 153.

23 U. Welp, W. K. Kwok, G. W. Crabtree, K. G. Vandervoort, and J. Z. Liu, Appl. Phys. Lett. **57**, 84 (1990).
24 D. H. Wu and S. Sridhar, Phys. Rev. Lett. **65**, 2074 (1990).
25 Ibid. 9, p. 155.
26 U. Welp, M. Grimsditch, H. You, W. K. Kwok, M. M. Fang, G. W. Crabtree, and J. Z. Lin, Physica C **161**, 1 (1989).
27 L. Civale, T. K. Worthington, and A. Gupta, Phys. Rev. **B** 43, 5425 (1991).
28 Ibid. 9, p. 167.
29 Ibid. 9, p. 27
30 W. L. Johnson, *Physical Metallurgy*, R. W. Cahn and P. Haasen (eds.), North-Holland, NY (1983), p. 1774
31 H. W. Zandbergen, R. Gronsky, K. Wang, T. Thomas, Nature **331**, 596 (1988).
32 A. F. Marshall, R. W. Barton, K. Char, A. Kapitulnik, B. Oh, Phys. Rev. B **37**, 9353 (1988).
33 J. Karpinski, E. Kaldis, E. Jilek, S. Rusiecki, B. Bucher, Nature **336**, 660 (1988)
34 J. Karpinski, E. Kaldis, S. Rusiecki, E. Jilek, P. Fischer, J. Less-Common Met. **150**, 207 (1989).
35 J. Karpinski, E. Kaldis, and S. Rusiecki, J. Less-Common Met. **150**, 207 (1989)
36 J. Karpinski, S. Rusiecki, E. Kaldis, B. Bucher, E. Jilek, Physica C **160**, 449.
37 D. E. Morris, J. H. Nickel, J. Y. T. Wei, N. G. Asmar, J. S. Scott, Phys. Rev. B **39**, 7347 (1989).
38 D. E. Morris, N. G. Asmar, J. H. Nickel, R. L. Sid, J. Y. T. Wei, and J. E., Post, Physica C **159**, 287 (1989).
39 R. J. Cava, J. J. Krajewski, W. F. Peck, B. Batlogg, L. W. Rupp , Nature **338**, 328 (1989).
40 D. M. Pooke, R. G. Buckley, M. R. Presland, J. L. Tallon, Phys. Rev. B **41**, 6616 (1990).
41 J. S. Ho and C. T. Chang, Appl. Phys. Lett. **58**, 2426 (1991).
42 L. Bonoldi, M. Sparpaglione, and L. Zini, Appl. Phys. Lett. **61**, 964 (1992).
43 S. Ohara, M. Matsuda, Y. Watanabe, and M. Takata, Appl. Phys. Lett. **59**, 603 (1991)
44 S. Jin, H. M. O'Bryan, P. K. Gallagher, T. H. Tiefel, R. J. Cava, R. A. Fastnacht, and G. W. Kammlott, Physica C **165**, 415 (1990).

45 R. S. Liu, R. Janes, M. J. Bennett, and P. P. Edwards, Appl. Phys. Lett. **57**, 920 (1990)
46 S. Jin and J. E. Graebner, Mat. Sci. Eng. **B7**, 243 (1991).
47 D. Dimos, P. Chaudhari, and J. Mannhart, Phys. Rev. B **41**, 4038 (1990).
48 Ibid. 9, p. 154
49 Ibid. 20, p. 350.
50 S. Babcock, X. Y. Cai, D. L. Kaiser, and D. C. Larbalestier, Nature **347**, 167 (1990).
51 S. Babcock, MRS Bull. **17**, 20 (1992).
52 K. B. Alexander, D. M. Kroeger, J. Bentley and J. Brynestad, Physica C **180**, 337 (1991).
53 S. E. Babcock, T. F. Kelly, P. J. Lee, J. M. Seuntjens, L. A. LaVanier, and D. C. Larbalestier, Physica C **152**, 25 (1988).
54 D. M. Kroeger, A. Choudhury, J. Brynestad, R. K. Williams, R. A. Padget, and W. A. Coghlan, J. Appl. Phys. **64**, 331 (1989).
55 A. P. Clarke, R. B. Schwarz, and J. D. Thompson, J. Less-Common Met. **168**, 1 (1991).
56 A. Umezawa, G. W. Crabtree, J. Z. Liu, H. W. Weber, W. K. Kwok, L. H. Nunez, T. J. Moran, and C. H. Sowers, Phys. Rev. B **36**, 7151 (1987).
57 R. B. Van Dover, E. M. Gyorgy, L. F. Schneemeyer, J. W. Mitchell, K. V. Rao, R. Puzniak, and J. V. Waszczak, Nature **342**, 55 (1989).
58 L. Civale, T. K. Worthington, L. Krusin-Elbaum, A. D. Marwick, F. Holtzberg, J. R. Thompson, M. A. Kirk, and R. Wheeler, J. Met. **44**, 60 (1992).
59 J. L. Vargas and D. C. Larbalestier, Appl. Phys. Lett. **60**, 1741 (1992).
60 S. Jin, T. H. Tiefel, S. Nakahara, J. E. Graebner, H. M. O'Bryan, R. A. Fastnacht, and G. W. Kammlott, Appl. Phys. Lett. **56**, 1287 (1990).
61 R. Ramesh, S. Jin, S. Nakahara, and T. H. Tiefel, Appl. Phys. Lett. **57**, 1458 (1990).
62 S. Jin, G. W. Kammlott, S. Nakahara, T. H. Tiefel, and J. E. Graebner, Science **253**, 427 (1991).
63 N. Imanaka, F. Saito, H. Imai, and G. Adachi, Jpn. J. Appl. Phys. **28**, L580 (1989).
64 D. Lee and K. Salama, Jpn. J. Appl. Phys. **29**, L2017 (1990).
65 P. McGinn, N. Zhu, W. Chen, M. Lanagan, and U. Balachandran, Physica C **167**, 343 (1990).

66 S. Reich and V. M. Nabutovsky, J. Appl. Phys. **68**, 668 (1990).
67 O. Ishii, T. Konaka, M. Sato, and Y. Koshimoto, Jpn. J. Appl. Phys. **29**, L 1075 (1990).
68 X-G. Zeng, H. Kuriyaki, and K. Hirakawa, Jpn. J. Appl. Phys. **29**, L 2020 (1991)
69 S. Jin, J. E. Graebner, T. H. Tiefel, and G. W. Kammlott, Appl. Phys. Lett. **56**, 186 (1990).
70 W. D. Wilber and R. D. Finnegan, J. Appl. Phys. **67**, 5073 (1990).
71 Y. H. Kao, Y. D. Yao, L. Y. Jang, F. Xu, A. Krol, L. W. Song, and C. J. Sher, A. Darovsky, J. C. Phillips, J. J. Simmins, and R. L. Snyder, J. Appl. Phys. **67**, 353 (1990).
72 N-L. Wu and Y. C. Chang, Jpn. J. Appl. Phys. **29**, L563 (1990).
73 R. E. Loehman, A. P. Tomsia, J. A. Pask, and A. H. Carim, Physica C **170**, 1 (1990).
74 A. K. Gangopadhyay and T. O Mason, Physica C **178**, 64 (1990).
75 M. Itoh, H. Ishigaki, T. Ohyama, T. Minemoto, H. Nojiri, and M. Motokawa, J. Mater. Res. **6**, 2272 (1991).
76 L. S. Yeou and K. W. White, J. Mater. Res. **7**, 1 (1992).
77 S. Reich, D. Veretnik, I. Feiner, and U. Yaron, J. Appl. Phys **72**, 4805 (1992).
78 N. Ogawa, I. Hirabaiashi, and S. Tanaka, Physica C **177**, 101 (1991).
79 N. Imanaka, F. Saito, H. Imai, and G. Adachi, J. Appl. Phys. **67**, 915 (1990).
80 J. Shimoyama, J. Kase, S. Kondoh, E. Yanagisawa, T. Matsubara, M. Suzuki, and T. Morimoto, Jpn. J. Appl. Phys. **29**, L1999 (1990).
81 P. McGinn, W. Chen, N. Zhu, L. Tan, C. Varanasi, and S. Sengupta, Appl. Phys. Lett. **59**, 120 (1991).
82 C. J. Kim, K. B. Kim, K. W. Lee, C. T. Lee, G. W. Hong, I. S. Chang, and D. Y. Won, Mat. Lett. **11**, 241 (1991).
83 L. T. Romano, O. F. Schilling and C. R. Grovenor,Physica C **178**, 41 (1991).
84 S. Jin, T. H. Tiefel, R. A. Fastnacht, and G. W. Kammlott, Appl. Phys. Lett. **60**, 3307 (1992).
85 A. Goyal, S. J. Burns, and P. D. Funkenbusch, Physica C **168**, 405 (1990).
86 S. Jin, T. H. Tiefel, and G. W. Kammlott, Appl. Phys. Lett. **59**, 540 (1991).
87 S. Jin, G. W. Kammlott, and T. H. Tiefel, Physica C 181, 57 (1991).

88 L. T. Sagdahl, T. Lægreid, K. Fossheim, M. Murakami, H. Fujimoto, S. Gotoh, K. Yamaguchi, N. Koshizuka, and S. Tanaka, Physica C **172**, 495 (1991).

89 M. J. Cima, A. M. Figueredo, M. C. Flemings, M. Nakade, H. Ishii, H. D. Brody, and J. S. Haggerty, J. Appl. Phys. **72**, 179 (1992).

90 K. G. Frase and D. R. Clarke, Adv. Ceram. Mat. **2**, 295 (1987).

91 T. Aselage and K. Keefer, J. Mater. Res. **3**, 1280 (1988).

92 R. S. Roth, G. J. Rawn, F. Beech, J. D. Whitler, J. O Andersson, *Ceramic Superconductors II*, M. F. Yan (ed.), Am. Ceram. Soc., Westerville, OH (1988), p. 13.

93 K. Oka, K. Nakane, M. Ito, M. Saito, and H. Unoki, Jpn. J. Appl. Phys. **27**, L1065 (1988).

94 J. E. Ullman, R. W. McCallum, and J. D. Verhoeven, J. Mater. Res. **4**, 752 (1989).

95 B. T. Ahn, V. Y. Lee, R. Beyers, T. M. Gür, and R. A. Huggins, Physica C **162-164**, 883 (1989).

96 J. Karpinski, S. Rusiecki, E. Kaldis, B. Bucher, and E. Jilek, Physica C **160**, 449 (1989).

97 M. Maeda, M. Kadoi, and T. Ikeda, Jpn. J. Appl. Phys. **28**, 1417 (1989).

98 F. Licci, P. Tissot, and H. J. Scheel, J. Less Comm. Met. **150**, 201 (1989).

99 T. Wada, N. Suzuki, A. Ichinose, Y. Yaegashi, H. Yamauchi, and S. Tanaka, Appl. Phys. Lett. **57**, 81 (1990).

100 M. R. Chandrachood, D. E. Morris, and A. P. B. Sinha, Physica C **171**, 187 (1990).

101 J. M. Liang and L. J. Chen, Appl. Phys. Lett. **57**, 2142 (1990).

102 V. F. Shamrai, Y. V. Efimov, O. G. Karpinskii, A. A. Babareko, G. M. Leitus, T. M. Frolova, E. A. Myasnikova, A. M. Postnikov, M. E. Salvelyeva, and Y. L. Lipikhin, J. Less Comm. Met. **162**, 181 (1990).

103 R. K. Williams, K. B. Alexander, J. Brynestad, T. J. Henson, D. M. Kroeger, T. B. Lindemer, G. C. Marsh, and J. O. Scarbrough, J. Appl. Phys. **67**, 6934 (1990).

104 B. T. Ahn, V. Y. Lee, R. Beyers, T. M. Gür, and R. A. Huggins, Physica C **167**, 529 (1990).

105 K. W. Lay and G. M. Renlund, J. Am. Ceram. Soc. **73**, 1208 (1990).

106 T. B. Lindemer, F. A. Washburn, C. S. MacDougall, and O. B. Cavin, Physica C **174**, 135 (1991).

107 Y. Sawai, K. Ishizaki, M. Takata, Y. Narukawa, Physica C **176**, 147 (1991).
108 R. K. Williams, K. B. Alexander, J. Brynestad, T. J. Henson, D. M. Kroeger, T. B. Lindemer, G. C. Marsch, J. O. Scarbrough, and E. D. Specht, J. Appl. Phys. **70**, 906 (1991).
109 T. B. Lindemer, F. A. Washburn, C. S. MacDougall, R. Feenstra, and O. B. Cavin, Physica C **178**, 93 (1991).
110 T. B. Lindemer, F. A. Washburn, and C. S. MacDougall, Physica C **196**, 390 (1992).
111 J. Karpinski, E. Kaldis, H. J. Schwer, K. Conder, E. Jilek, *Controlled Growth of Single- and Poly-Crystals of High Temperature* Superconductors, Proc. Int. Workshop on Superconductivity, ISTEC and MRS (1992), p. 187.
112 R. S. Roth, J. P. Cline, and J. J. Ritter, *Controlled Growth of Single- and Poly-Crystals of High Temperature Superconductors*, Proc. Int. Workshop on Superconductivity, ISTEC and MRS (1992), p. 45.
113 A. Mawdsley, J. L. Tallon, and M. R. Presland, Physica C **190**, 437 (1992).
114 W. Zhang, and K. Osamura, Physica C 190, 396 (1992).
115 K. Conder, J. Karpinski, E. Kaldis, S. Rusiecki, and E. Jilek, Physica C **196**, 164 (1992).
116 J. D. Whitler and R. S. Roth, *Phase Diagrams for High-Tc Superconductors*, Am. Ceram. Soc., Westerville, OH (1991).
117 L. Zhang, J. Chen, H. M. Chan, and M. P. Harmer, J. Am. Ceram. Soc. **72**, 1997 (1989).
118 E. K. Chang, E. F. Ezell, and M. J. Kirschner, Supercond. Sci. Technol. **3**, 391 (1990).
119 T. M. Shaw, D. Dimos, P. E. Batson, A. G. Schrott, D. R. Clarke, and P. R. Duncombe, J. Mater. Res. **5**, 1176 (1990).
120 T. B. Lindemer, C. R. Hubbard, and J. Brynestad, Physica C **167**, 312 (1990).
121 K. Borowiec, J. Przyluski, and K. Kolbrecka, J. Am. Ceram. Soc. **74**, 2007 (1991).
122 E. A. Cooper, A. K. Gangopadhyay, and T. O Mason, J. Mater. Res. **6**, 1393 (1991).
123 J. R. Verkouteren, Mater. Lett. **8**, 59 (1989).
124 M. Murakami, M. Morita, K. Doi, K. Miyamoto, and H. Hamada, Jpn. J. Appl. Phys. **28**, L399 (1989).

125 D. E. Morris, A. G. Markelz, B. Fayn, J. H. Nickel, Physica C **168**, 153 (1990).
126 M. Nevriva, E. Pollert, L. Matejkova, and A. Triska, J. Crystal Growth **91**, 434 (1988).
127 K. Fischer, R. Hergt, and D. Linzen, Cryst. Res. Technol. **23**, 1169 (1988).
128 K. N. R. Taylor, P. S. Cook, T. Puzzler, D. N. Mattews, G. J. Russell, and P. Goodman, J. Crystal Growth **88**, 541 (1988).
129 F. Garzon and I. Raistrick, J. Electrochem. Soc. **136**, 2753 (1989).
130 B. N. Sun, R. Boutellier and H. Schmid, Physica C **157**, 189 (1989).
131 M. J. V. Menken, K. Kadowaki, and A. A. Menovsky, J. Crystal Growth **96**, 1002 (1989).
132 T. Wolf, W. Goldacker, B. Obst, G. Roth, and R. Flükiger, J. Crystal Growth **96**, 1010 (1989).
133 B. N. Sun, P. Hartman, C. F. Woensdregt, and H. Schmid, J. Crystal Growth **100**, 605 (1990).
134 M. Nevriva, E. Pollert, J. Heitmanek, S. Durcok, M. Simeckova, and P. Diko, Physica C **179**, 253 (1991).
135 B. N. Sun, K. N. R. Taylor, B. Hunter, D. N. Mattews, S. Ashby, and K. Sealey, J. Crystal Growth **108**, 473 (1991).
136 T. Wolf, *Controlled Growth of Single- and Poly-Crystals of High Temperature Superconductors*, Proc. Int. Workshop on Superconductivity, ISTEC and MRS (1992), p. 123.
137 P. Fischer, Physica C **196**, 105 (1992).
138 A. Drake, F. Gencer, M. Aindow, Y. Feng, and J. S. Abell,*Controlled Growth of Single- and Poly-Crystals of High Temperature Superconductors*, Proc. Int. Workshop on Superconducivity, ISTEC and MRS (1992), p. 248.
139 F. Holtzberg and C. Feild, T. Wolf, *Controlled Growth of Single- and Poly-Crystals of High Temperature Superconductors*, Proc. Int. Workshop on Superconductivity, ISTEC and MRS (1992), p. 25.
140 L. F. Schneemeyer, J. V. Waszczak, T. Herzog, S. H. Glarum, and T. Siegrist, T. Wolf, *Controlled Growth of Single- and Poly-Crystals of High Temperature Superconductors*, Proc. Int. Workshop on Superconducivity, ISTEC and MRS (1992), p. 49.

141 Y. Hidaka, T. Wolf, *Controlled Growth of Single- and Poly-Crystals of High Temperature Superconductors*, Proc. Int. Workshop on Superconductivity, ISTEC and MRS (1992), p. 29.
142 R. Liang, P. Dosanjh, D. A. Bonn, D. J. Baar, J. F. Carolan, and D. N. Hardy, Physica C **195**, 51 (1992).
143 D. L. Kaiser, F. Holtzberg, B. A. Scott, and T. R. McGuire, Appl. Phys. Lett. **51**, 1040 (1987).
144 D. L. Kaiser, F. Holtzberg, M. F. Chisholm, and T. K. Worthington, J. Crystal Growth **85**, 593 (1987).
145 H. J. Scheel, P. Niedermann, J. Crystal Growth **94**, 281 (1989).
146 J. Takada, H. Kitaguchi, A. Osaka, Y. Miura, K. Takahashi, M. Takano, Y. Ikeda, Y. Bando, N. Yamamoto, Y. Oka, and Y. Tomii, Jpn. J. Appl. Phys. **26**, L1707 (1987).
147 S. Jin, J. Met. **44**, 7 (1991).
148 S. Jin, T. H. Tiefel, R. C. Sherwood, M. E. Davis, R. B. van Dover, G. W. Kammlott, R. A. Fastnacht, and H. D. Keith, Appl. Phys. Lett. **52**, 2074 (1988).
149 T. Matsushita, B. Ni, M. Murakami, M. Morita, K. Miyamoto, M. Saga, S. Matsuda, and M. Tanino, Jpn. J. Appl. Phys. **28**, L1545 (1989).
150 M. Murakami, M. Morita, and N. Koyama, Jpn. J. Appl. Phys. **28**, L1125 (1989).
151 M. Murakami, M. Morita, K. Doi, K. Miyamoto, Jpn. J. Appl. Phys. **28**, L1189 (1989).
152 S. Jin, R. C. Sherwood, E. M. Gyorgy, T. H. Tiefel, R. B. van Dover, S. Nakahara, L. F. Schneemeyer, R. A. Fastnacht, and M. E. Davis, Appl. Phys. Lett. **54**, 584 (1989).
153 P. J. McGinn, W. Chen, and M. A. Black, Physica C **161**, 198 (1989).
154 K. Salama, V. Selvamanickam, L. Gao, and K. Sun, Appl. Phys. Lett. **54**, 2352 (1989).
155 P. J. McGinn, W. Chen, N. Zhu, U. Balachandran, and M. T. Lanagan, Physica C **165**, 480 (1990).
156 P. McGinn, W. Chen, N. Zhu, M. Lanagan, and U. Balachandran, Appl. Phys. Lett. **57**, 1455 (1990).
157 H. Wang, H. Herman, H. J. Wiesman, Y. Zhu, Y. Xu, R. L. Sabatini, and M. Suenaga, Appl. Phys. Lett. **57**, 2495 (1990).
158 K. No, D.-S. Chung, J.-M. Kim, J. Mater. Res. **5**, 2610 (1990).

159 T. Goto and Y. Kino, Jpn. J. Appl. Phys. **29**, L2030 (1990).
160 D. Shi, H. Krishnan, J. M. Hong, D. Miller, P. J. McGinn, W. H. Chen, M. Xu, J. G. Chen, M. M. Fang, U. Welp, M. T. Lanagan, K. C. Goretta, J.T. Dusek, J.J. Picciolo, and U. Balachandran, J. Appl. Phys. **68**, 228 (1990).
161 D. Shi, M. M. Fang, J. Akujieze, M. Xu, J. G. Chen, and C. Segre, Appl. Phys. Lett. **57**, 2606 (1990).
162 V. Selvamanickam, C. Partsinevelos, A. V. McGuire, and K. Salama, Appl. Phys. Lett. **60**, 3313 (1992).
163 K. Yamaguchi, M. Murakami, H. Fujimoto, S. Gotoh, T. Oyama, Y. Shiohara, N. Koshizuka, and S. Tanaka, J. Mater. Res. **6**, 1404 (1991).
164 J. Chunlin, F. Zhanguo, Z. Guofan, Z. Gulyi, B. Welmin, Z. Zhongxian, G. Shuquant, Supercond. Sci. Technol. **4**, 49 (1991).
165 A. Goyal, P. D. Funkenbusch, D. M. Kroeger, and S. J. Burns, Physica C **182**, 203 (1991).
166 S. Hu, H. Hojaji, A. Barkatt, M. Boroomand, M. Hung, A. C. Buechele, A. N. Thorpe, D. D. Davis, S. Alterescu, J. Mater. Res. **7**, 808 (1992).
167 T. Izumi and Y. Shiohara, J. Mater. Res. **7**, 16 (1992).
168 T. Izumi and Y. Nakamura, and Y. Shiohara, J. Mater. Res. **7**, 1621 (1992).
169 Y. Shiohara, T. Izumi, and Y. Nakamura, *Controlled Growth of Single- and Poly-Crystals of High Temperature Superconductors*, Proc. Int. Workshop on Super-conductivity, ISTEC and MRS (1992), p. 53.
170 K. B. Alexander, A. Goyal, D. M. Kroeger, V. Selvamanickam, and K. Salama, Phys. Rev. B **45**, 5622 (1992).
171 M. Ullrich, D. Müller, K. Heineman, L. Niel and H. C. Freyhardt, Physica C **198**, 181 (1992).
172 W. Ruikun, R. Hongtao, X. Ling, H. Qing, W. Chaoqun, and Y. Dingan Supercond. Sci. Technol. **3**, 344 (1990).
173 J. P. Zhou, S. X. dou, H. K. Liu, A. J. Gouch, M. H. Apperley, N. Savvides, and C. C. Sorrell, Supercond. Sci. Technol. **2**, 212 (1989)
174 R. J. Pollard, D. G. McCartney, N. McN Alford, and T. Button, Supercond. Sci. Technol. **2**, 169 (1989).
175 R. L. Meng, C. Kinalidis, Y. Y. Sun, L. Gao, Y. K. Tao, P. H. Hor, and C. W. Chu, Nature **345**, 326 (1990).
176 W. G. Pfann, *Zone Melting*, Wiley, New York, (1958).
177 D. Gazit and R. S. Feigelson, J. Crystal Growth **91**, 318 (1990).
178 R. S. Feigelson, D. Gazit, D. K. Fork, T. H. Gebale, Science **240**, 1642 (1988)

179 D. Gazit, P. N. Peszkin, L. V. Moulton, and R. S. Feigelson, J. Crystal Growth **98**, 545 (1989).
180 H. D. Brody, J. S. Haggerty, M. J. Cima, and M. C. Flemings, J. Crystal Growth **96**, 225 (1989).
181 Z. Lu, L. V. Moulton, R. S. Feigelson, R. J. Raymakers, and P. N. Peszkin, J. Crystal Growth **106**, 732 (1990).
182 M. J. Cima, X. P. Jiang, H. M. Chow, J. S. Haggerty, M. C. Flemings, H. D. Brody, R. A. Laudise, and D. W. Johnson, J. Mater. Res. **5**, 1834 (1990).
183 M.C. Flemings, *Solidification Processing*, McGraw-Hill, New York (1974).
184 J. D. Hodge, L. J. Klemptner, M. V. Parish, J. Mat. Sci. Lett. **10**, 1362 (1991).
185 S. R. Su, M. O'Connor, M. Levinson, and P. G. Rossoni, Physica C **178**, 81 (1991).
186 C. H. Hsu, K. G. Lloyd, J. D. Cohen, T. R. Askew, R. B. Flippen, J. T. Schwartz, J. D. Connolly Jr., and H. W. Jacobson, Mat. Lett. **11**, 74 (1991).
187 R. M. Laine, K. A. Youngdahl, R. A. Kennish, M. L. Hoppe, Z.-F. Zhang, and J. Ray, J. Mat. Res. **6**, 895 (1991).
188 S. Katayama and M. Sekine, J. Mater. Res. **6**, 1629 (1991).
189 U. Balachandran and R. B. Poeppel, Ceram. Bull. **70**, 815 (1991).
190 L. D. Woolf, W. A. Raggio, F. E. Elsner, M. V. Fisher, R. B. Stephens, T. L. Figueroa, C. H. Shearer, J. D. Rose, K. M. Schaubel, R. A. Olstad, T. Ohkawa, D. M. Duggan, M. DiMartino, and R. L. Fagaly, Appl. Phys. Lett. **58**, 534 (1991).
191 T. Goto and T. Sugishita, J. Mater. Res. **7**, 11 (1992).
192 M. V. Parish, *Controlled Growth of Single- and Poly-Crystals of High Temperature Superconductors*, Proc. Int. Workshop on Superconductivity, ISTEC and MRS (1992), p. 232.
193 P. W. Voorhees, Annu. Rev. Mater. Sci. **22**, 197 (1992).
194 G. W. Greenwood, Acta. Metall. **4**, 243 (1956).
195 I. M. Lifshitz, V. V. Slyozov, J. Phys. Chem Solids **19**, 35 (1961).
196 C. Wagner, Z. Elektrochem. **65**, 35 (1961).
197 H. Fischmeister and G. Grimvall, Mater. Sci. Res. **6**, 119 (1973).
198 A. J. Ardell, Acta Metall. **20**, 61 (1972).
199 A. D. Brailsford and P. Wynblatt, Acta Metall. **27**, 489 (1979).
200 C. H. Kang and D. N. Yoon, Metall. Trans. A **12**, 65 (1981).
201 S. S. Kang and D. N. Yoon, Metall. Trans. A **13**, 1405 (1982).

202 P. W. Voorhees and M. E. Glicksman, Metall. Trans. A **15**, 1081 (1984).
203 S. K. Battacharyya and K. C. Russell, Metall. Trans. A **7**, 453 (1976).
204 N. Akaiwa, S. C. Hardy, and P. W. Voorhees, Acta Metall. **39**, 2931 (1991).
205 A. N. Niemi and T. H. Courtney, J. Mater. Sci. **16**, 226 (1981).
206 P. W. Voorhees, G. B. McFadden, R. F. Boisvert, and D. I. Meiron, Acta Metall. **36**, 207 (1988).
207 K. Rigby, M. J. Cima, M. C. Flemings, and J. S. Haggerty, 3rd Quarterly Report: Critical Current Enhancement of Directionally Solidified HTSC Materials: Microstructural Control, Materials Processing Center, M.I.T., (1992).
208 T. Izumi, Y. Nakamura, and Y. Shiohara, J. Mater. Res. **8**, (1993).
209 D. R. Uhlman and G. A. Chadwick, Acta Metall. **9**, 835 (1961).
210 S. Mizoguchi, Y. Ueshima, T. Matsumiya and H. Kajioka, Solidification Processing 1987: Proc. of the 3rd. Int. Conference, Dept. Metallurgy, U. of Sheffield, Sheffield, September 1987, p. 75.
211 J. K. Chuang, D. Reinisch, and K. Schwerdtfeger, Metall. Trans. A **6**, 235 (1975).
212 H. E. Hyman, C. McCullough, C. G. Teri, and R. Mehrabian, Metall. Trans. A **22**, 1647 (1991).
213 W. J. Boettinger, Metall. Trans. 5, 2023 (1974).
214 B. Chalmers, *Physical Metallurgy*, Willey & Sons, New York, (1959).
215 J. D. Livingston, Mat. Sci. Eng. **7**, 61 (1971).
216 K. A. Jackson and J. D. Hunt, Trans. TMS-AIME **236**, 1129 (1966).
217 M. Hillert, *Solidification and Casting of Metals*, The Metals Society, London (1979, p. 81.
218 B. F. Oliver and B. Kamad, J. Less Common Met. **168**, 81 (1991).
219 J. S. Haggerty and W. P. Menashi, NASA-CR-72811 ADL 71997, February 1971.
220 Y. Nakamura, T. Izumi, and Y. Shiohara, *Controlled Growth of Single- and Poly-Crystals of High Temperature* Superconductors, Proc. Int. Workshop on Superconductivity, ISTEC and MRS (1992), p. 261.
221 E. E. Underwood, *Quantitative Stereology*, Addison-Wesley, Reading, MA (1970). pp. 5-45.
222 G. Van Tendeloo, H. W. Zandbergen, and S. Amelinckx, Solid. State Comm. **63**, 389 (1987).

223 S. Ijima, T. Ichihashi, Y. Kubo, and J. Tabuchi, Jpn. J. Appl. Phys. **26**, L1790 (1987).
224 H. Hojaji, A. Barkatt, K. A. Michael, S. Hu, A. N. Thorpe, M. F. Ware, I. G. Talmy, D. A. Haught, and S. Alterescu, J. Mater. Res. **5**, 721 (1990).
225 J. Mannhart and C. C. Tsuei, Z. Phys. B **77**, 53 (1989).
226 A. P. Malozemoff, *High-Temperature Superconducting Compounds II*, S. H. Whang, A. DasGupta, and R. B. Laibowitz, TMS Publ., Warrendale, PA (1990) p. 3.
227 B. Raveau, Phys. Today, **53** (1992).
228 Y. V. Naidich, Progress in Surface and Membrane Science 14, D. A. Cadenhead and J. F. Danielli (eds.), Academic Press, New York (1981), p. 353
229 M. A. Rodriguez, B. J. Chen, and R. L. Snyder, Physica C **195**, 185 (1992).
230 M. Hillert and B. Uhrenius, Scand. J. Metallurgy **1**, 223 (1972).
231 M. Hansen and K. Anderko, *Constitution of Binary Alloys*, McGraw Hill, New York, (1958) p. 738.
232 X. P. Jiang, M. J. Cima, H. D. Brody, J. S. Haggerty, and M. C. Flemings, *Controlled Growth of Single- and Poly-Crystals of High Temperature Superconductors*, Proc. Int. Workshop on Superconductivity, ISTEC and MRS (1992), p. 259.
233 C.L. Teske and H. Müller-Buschbaum, Z. Natürforschung **27B**, 296 (1971).
234 D. Dubé, B. Champagne, P. Lambert, and Y. Le Page, Mater. Lett. 9, 353 (1990).
235 M. C. Flemings, Metall. Trans. **5**, 2121 (1974).
236 R. Elliott, Int. Metals Rev. **214**, 161 (1977).
237 J. L. Tallon and J. Lusk, Physica C **167**, 236 (1990).
238 C. P. Bean, Rev. Mod. Phys. **36**, 31 (1964).
239 E. M. Gyorgy, R. B. Van Dover, K. A. Jackson, L. F. Schneemeyer, and J. V. Waszczak, Appl. Phys. Lett. **55**, 283 (1989).
240 R. L. Peterson, J. Appl. Phys. **67**, 6930 (1990).
241 R. B. Goldfarb, M. Lelental, C. A. Thompson, Magnetic Susceptibility of Superconductors and Other Spin Systems, R. A. Hein, T. L. Francavilla, and D. H. Liebenber (Eds.), Plenum Press, New York (1992).
242 J. W. Ekin, K. Salama and V. Selvamanickam, Appl Phys. Lett. **59**, 360 (1991).
243 V. Selvamanickam, K. Forster, and K. Salama, Physica C **178**, 147 (199

244 D. K. Christen, C. E. Klabunde, D. B. Chandler, M. J. Neal, M. V. Parish, B. C. Chakoumakos, A. Goyal, and D. M. Kroeger, *Controlled Growth of Single- and Poly-Crystals of High Temperature Superconductors*, Proc. Int. Workshop on Superconductivity, ISTEC and MRS (1992), p. 181.

245 H. Teshima, A. Oishi, H. Izumi, K. Ohata, T. Morishita, and S. Tanaka, Appl. Phys. Lett. **58**, 2833 (1991).

246 J. J. Neumeier, Appl. Phys. Lett. **61**, 1852 (1992).

247 I. Felner, B. Brosh, U. Yaron, Y. Yeshurun, and E. Yacoby, Physica C **173**, 337 (1991).

248 J. L. Tallon, D. M. Pooke, R. G. Buckley, M. R. Presland, N. E. Flower, S. Gibson, and P. W. Gilberd, Appl. Phys. Lett. **59**, 1239 (1991).

249 J. L. Vargas and D. C. Larbalestier, *Controlled Growth of Single- and Poly-Crystals of High Temperature Superconductors*, Proc. Int. Workshop on Superconductivity, ISTEC and MRS (1992), p. 63.

250 G. Triscone, T. Graf, A. Junod, D. Sanchez, O. Brunner, D. Cattani, and J. Muller, Physica C **168**, 40 (1990).

251 W. A. Tiller, *The Science of Crystallization: Macroscopic Phenomena and Defect Generation*, Cambridge University Press, Cambridge, (1991), pp.155-226

252 A. M. Figueredo, M. J. Cima, M. C. Flemings, and J. S. Haggerty, in preparation for publication.

Biographical Note

The author was born in Dracena, State of São Paulo, Brazil. He attended high-school in the public school system of the city of São Paulo. In 1973, he was admitted to Universidade de São Paulo, in São Paulo, Brazil, where he was introduced to the field of materials science by an M.I.T. graduate. In March, 1978, he received a degree in mining engineering from the same university. After that, he worked for a short period as a mining engineer in the inhospitable, but beautiful Amazon region. There he found himself surrounded by destruction, deep ignorance, and all imaginable kinds of hungry mosquitoes. That was sufficient to kill his motivation to pursue a career in mining engineering. In 1979 he returned to University of São Paulo, where he worked for his M.S. degree at the Instituto de Pesquisas Energéticas e Nucleares, a research institute associated to the university. After receiving his M.S. degree he worked in the same institute for three years, before deciding to apply for admission to a Ph.D. program in the U.S. He came to the United States in 1986, to attend the Graduate School of Case Western Reserve University. In 1987 he married Neuza and decided to change Case for M.I.T. Their life in Cambridge was full of rewarding experiences, the most important being the birth of Maria in January, 1989.